UNIVERSITY OF SOUTHAMPTON

FACULTY OF ENGINEERING, SCIENCE & MATHEMATICS

School of Chemistry

High-Throughput Fabrication and Testing of Lithium Battery Materials

by

Matthew Robert Roberts MChem (Hons)

Thesis for the degree of Doctor of Philosophy

DATE 03/04/2008

ABSTRACT

A new method for the high-throughput discovery of cathode materials for lithium ion batteries has been developed. The novelty is in the method of separating the synthesis and electrode fabrication steps, which has resulted in high quality electrochemical data and standard deviation in results of approximately 6 %. This method has then been used to investigate several material systems. Investigations into $LiFePO_4$ have shown that sol-gel preparations with a sucrose to phosphoric acid ratio of 0.22 give the highest initial capacities and best rate performance. The rate capability of this material was found to be enhanced by ball milling the as synthesised material for 1 h. Further improvements in rate performance could be achieved when Mg was used as a dopant on the Fe site. Investigations of $LiFe_{1-x}Mn_xPO_4$ showed that the capacity is significantly reduced as x is increased due to a well documented reduction in conductivity. The reaction mechanism of the Fe^{2+}/Fe^{3+} redox couple was seen to change from 1 phase to a 2 phase type on increasing x. On further investigation of the $LiMnPO_4$ material Mg doping was found to alleviate the conductivity limitations and at a rate of C/7 ~60 mA h g^{-1} was observed.

To further validate the method and to demonstrate the versatility of the PoSAT technique in terms of which materials can be investigated, research into $LiCo_{1-x-y}Ni_xMn_yO_2$ is also presented. Using a novel approach to obtain thermally graded arrays optimal synthesis temperature and precursor salts were found for $LiCo_{0.33}Ni_{0.33}Mn_{0.33}O_2$. The material prepared from an aqueous mixed metal nitrate solution at 700 °C was found to show a high initial capacity ~200 mA h g^{-1} and acceptable cyclability. Using this synthesis method, investigations into the ternary system $LiCo_{1-x-y}Ni_xMn_yO_2$ were also undertaken. It was found that in materials containing y>0.5 electrochemical performance similar to $LiMn_2O_4$ was observed. The highest performance materials were seen in samples containing roughly equal (>25 % of each) amounts of each metal.

Table of Contents

Chapter 1: Introduction

Chapter 2: Experimental Techniques and Theoretical background

Chapter 3: Development and Validation

Chapter 4: Towards the optimization of LiFePO4

Chapter 5: Compositional variations $LiMPO_4$

Chapter 6: Investigations of $LiNi_{1-x-y}Co_xMn_yO_2$ cathodes

Chapter 7: Conclusions and Further Work

Appendices

Acknowledgements

I would particularly like to thank Professor John Owen who has provided me with excellent guidance throughout my studies. This includes my undergraduate education where his infectious enthusiasm influenced my choice of postgraduate study. He was also instrumental in providing me with the opportunity of visiting Japan during my PhD which was a fantastic experience and has also encouraged my participation in several international conferences. Another person who was extremely important in my education into battery systems is Dr Girts Vitins without his teaching and guidance I would have been lost during my first year. Special thanks goes to all the other members of the Owen Group during my studies in Southampton, Dr Alan Spong, Dr Thierry "Putan" Le Gall, Ken "yellows a good colour" Reiman, Dr Yasuaki "love affair" Wakizaka, Hannah "the Cuban, I would walk 500 miles" Alcock, Phil "to dust, go big or go home" Johns. Also all the other members of floor 7 during my time were extremely helpful these include Doug Offin (and honoree floor 7 member Laura Williams), Chris "I liked raya's biscuits" Vian, Xioahong Li (Helen), Maria "long island ice tea" Nestoridi and the Rusky Estonian double act Raika "the pregnant one" Jerohova and Katika "time to take a tea" Kuleshova. During the preparation and the writing of this thesis all the mentioned people have provided me with invaluable help or when that hasn't helped we have forgotten about it and enjoyed a few too many drinks together. I would also like to thank the chemistry department support staff who have made the process of study far easier than it might have been.

Special thanks goes to my parents who have always closely supported me and continue to do so. I have always found their encouragement to be good source of inspiration and my mums cooking a good source of expansion.

Symbols

B	factor determining the degree of line broadening	
c	number of cycles	
C_r	C-rate	h^{-1}
d_{hkl}	lattice spacing	
D	Diffusion coeffecient	$cm^2\ s^{-1}$
E	potential	V
E_a	Activation Energy	eV
F	faradays number (96487 C)	$C\ mol^{-1}$
ΔG	change in free energy	J
I	current	A
IR	current resistance	Ω
l	Particle radius	cm
m_p	mass of active material pellet	g
n	number of electrons	
Q	charge	C
Q_M	theoretical capacity	$mA\ h\ g^{-1}$
Q_S	specific Capacity	$mA\ h\ g^{-1}$
Q_{SI}	initial specific capacity	$mA\ h\ g^{-1}$
Q_{SF}	final specific capacity	$mA\ h\ g^{-1}$
Q_p	capacity of active material pellet	A h
R	resistance	Ω
t	Crystal size	nm
t_s	seconds in 1 hour	s
μ	Chemical Potential	$J\ mol^{-1}$
$\%_{CPR}$	percentage capacity retention per cycle	
λ	wavelength	cm
θ	X-ray beam angle of incidence	°
Θ_B	Bragg angle	°
τ	Particle time constant	s
σ	conductivity	$S\ cm^{-1}$

Abbreviations

AB	acetylene black
AC	alternating current
AM	active material
CP	cyclopentanone
CV	cyclic voltammetry
DEC	diethyl carbonate
DISC	direct in situ calcinations
DME	dimethoxyethane
DMC	dimethyl carbonate
EC	ethylene carbonate
EG	Ethylene glycol
FEG SEM	Field emission gun scanning electron microscope
GADDS	General area diffraction detector system
HT-TGA	high-throughput thermo gravimetric analysis
IPA	isopropanol
PC	propylene carbonate
PEO	poly(ethylene oxide)
PoSAT	Post Synthesis Array Transfer
PVD	Physical Vapour Deposition
PVdF	polyvinylidene difluoride
PVdF_HFP	polyvinylidene difluoride hexafluropropylene
PTFE	poly(tetrafluoroethylene)
LiBOB	lithium bis(oxalato)borate
LiTFSI	lithium bis(trifluoromethane sulfone imide)
MF	metal fluorides
MS	metal sulphides
PD	paste deposition
SEI	solid electrolyte interface
SEM	scanning electron microscopy
SPR	sucrose to phosphoric acid ratios
TGA	thermo gravimetric analysis
UHV	ultra high vacuum
VMP2	variable multichannel potentiostat
XPS	x-ray photoelectron spectroscopy
XRD	x-ray diffraction

Chapter 1 Introduction

Energy storage and batteries have never been of such importance as now, both in people's everyday lives and also on the political landscape. In the modern world portable electronics have become ubiquitous; in the last 25 years the number of mobile phones and laptops has increased dramatically, which has meant that people are using more batteries and demanding improvements in performance. The importance of renewable and green sources of energy like wind and solar have also become major issues in recent years; however, unstable weather conditions can temporarily disable these devices. Energy storage systems would provide us with the ability to stabilise (1) the supply of electricity and overcome some of the drawbacks of these systems. The electric vehicle market has also developed significantly in recent years with the advent of hybrid vehicles which require high power batteries.

The increase in battery use has led consumers to demand higher storage capacity, energy and power. However, a recent article in chemistry world said "We are, it seems, so near and yet so far from a new era of rechargeable battery technology. While gadget technology moves on at an alarming pace the humble battery is still playing catch up" (2).

These factors mean that a radical new approach needs to be developed to accelerate the way battery research is carried out. The application of high-throughput methodologies can help us reach the next generation of materials and meet the demands of the modern world.

1.1 Aims and Objectives

Aim

Develop a new method for the high-throughput discovery of positive electrode materials.

Objectives

- Build on the work of Spong et. al.(3-5) and devise a new method with a high degree of accuracy.
- Validate this method by comparison with a known system.
- Demonstrate the application of this method to several topical systems in current battery research.

1.2 Batteries

The Voltaic "pile" was introduced in 1800 by Alexander Volta, and is the first report of an electrochemical battery(6). Since then the field has continued to grow and develop, such that many different chemical systems have been adopted. In this section a brief introduction to the science and review of many of these systems will be given followed by a more comprehensive introduction to the topical Lithium ion battery.

1.2.1 Concepts

A battery is an electrochemical device which converts chemical energy to electrical energy(7). Figure 1-1 is a schematic showing the basic processes in a battery during discharge.

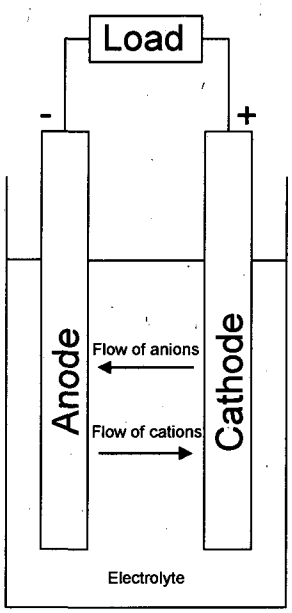

Figure 1-1 A schematic of an electrochemical cell during discharge(8).

During charge and discharge anions and cations flow between the positive and negative electrodes. This is a result of chemical reactions taking place in the cathode and anode. Below a series of equations summarise the operation in a lithium rechargeable battery where the positive electrode is $LiCoO_2$ and the negative electrode is carbon(9). This is a simplified by assuming 1 lithium is inserted per Co rather than the narrower range for reversibility, to be discussed later(10).

During discharge

At the negative electrode: $LiC_6 \rightarrow Li^+ + C_6 + e^-$

Equation 1-1

At the positive electrode: $CoO_2 + Li^+ + e^- \rightarrow LiCoO_2$

Equation 1-2

During charge

At the negative electrode: $Li^+ + C_6 + e^- \rightarrow LiC_6$

Equation 1-3

At the positive electrode: $LiCoO_2 \rightarrow CoO_2 + Li^+ + e^-$

Equation 1-4

Overall *Charged* *Discharged*

$$LiC_6 + CoO_2 \leftrightarrow C_6 + LiCoO_2$$

Equation 1-5

Here, during discharge the Li moves from the carbon to the CoO_2 and on charge the process is reversed. This system can be referred to as a "secondary battery", a "rechargeable battery", a "storage battery" or an "accumulator" (11, 12). This means that the chemical reaction that caused the discharge can be reversed by passing a current in the opposite direction. If this is not the case and it is impossible or difficult to reverse the chemical reaction in this way then the cell is referred to as a "primary"(11, 12) meaning that cells are purchased in the charged state and then after a single discharge discarded. Many of these primary systems use a liquid electrolyte

which is contained in a absorbent separator giving them the appearance of being dry and hence are often referred to as "dry cells".

1.2.1.1 Important Battery Parameters

Free Energy and Cell Voltage

When a battery is discharged there is a change in the free energy of the system as the reactants are converted into products as with any chemical reaction. This change in energy is directly related to the cell voltage(10, 12-14) shown in Equation 1-6.

$$\Delta G = -nFE$$

Equation 1-6

ΔG = Change in free energy/J

n = number of electrons

F = Faraday's constant = 96487 C

E = Potential/ V

In the particular case of the lithium ion cell, the free energy change can be expressed in terms of the chemical potential of lithium according to Equation 1-7.

$$\partial G = (\mu_{Li}^{P} - \mu_{Li}^{N})\partial n$$

Equation 1-7

∂n = small change in number of electrons/ mol

μ_{Li}^{P} =chemical potential of lithium in the positive electrode/ J mol^{-1}

μ_{Li}^{N} =chemical potential of lithium in the negative electrode/ J mol^{-1}

Equation 1-6 and Equation 1-7 can then be combined to express the potential of a cell as a function of the chemical potential shown in Equation 1-8.

$$E = \frac{-(\mu_{Li}^{P} - \mu_{Li}^{N})}{F}$$

Equation 1-8

Generally the voltage changes during discharge because the chemical potential changes with composition, for example $Li_{1-x}CoO_2$ over the range $0 < x < 0.5$ where the composition varies continuously within a single phase the discharge occurs between 4.3 and 3.6 V (15). However, some materials undergo discharge by conversion between two phases of different stiochiometry. In this case a constant potential is predicted by Equation 1-7 because of the constant chemical potential for phase equilibrium.

Whenever a voltage is quoted within this work it is referred to vs. Li.

Capacity

Capacity is one of the key measurements used to characterise a battery material. It will be one of the most common parameters that will be referred to in this thesis. Within the literature it has many forms, there is theoretical capacity and specific capacity (or more simply capacity) which can both be quoted as gravimetric and volumetric values. The following will explain these terms using the example of the commercially successful battery material $LiCoO_2$.

Theoretical capacity

Firstly, the reaction that is happening is considered, this is shown below in Equation 1-9 for the charge reaction of $LiCoO_2$(13).

Charge reaction $LiCoO_2$ $\quad LiCoO_2 \rightarrow Li_{0.5}CoO_2 + 0.5Li^+ + e^-$

Equation 1-9

In Equation 1-9 we can see that during charge 1 mole of Li is extracted from $LiCoO_2$ and 1 mole of electrons flows around the external circuit. This means that the charge that has been passed is equal to the moles of electrons multiplied by Faraday's constant (Equation 1-10).

$$Q = m \times F$$

Equation 1-10

Q= Calculated charge passed during charge / C

m = moles of electrons

F= Faradays number = 96487 C mol^{-1}

The gravimetric capacity can then calculated by dividing the charge passed by the molecular mass of the active material (Equation 1-11).

$$Q_M = \frac{mF}{M}$$

Equation 1-11

Q_M = theoretical capacity per g/ C g^{-1}

M = molecular mass/g

The above result in C g^{-1}, may be converted to the technical unit of mA h g^{-1} by dividing by 3.6. If these equations are now used to calculate the theoretical capacity of $LiCoO_2$ based on the discharged state of CoO_2 the result is 273 mA h g^{-1}.

Specific Capacity

The term specific capacity in this work will refer to the experimentally observed value of the capacity on discharge. This is calculated by measuring the charge per gram of active material followed by conversion from C g^{-1} to mA h g^{-1}

In the case of $LiCoO_2$ practically the reversible specific capacity calculated from the measured charge is ~130 mA h g^{-1}(10). This is significantly different from that calculated theoretically, this is normally explained as only 0.5 moles of Li can be extracted reversibly from 1 mole of $LiCoO_2$.

Cyclability

Cyclability is a term which only applies to secondary rechargeable batteries. It refers to how well a battery retains its capacity on cycling. This is normally observed by plotting a graph of specific capacity *vs.* cycle number and qualitatively observing the

performance. It can also be quoted as percentage capacity retention per cycle(16). This can be calculated using Equation 1-12.

$$\%_{CRP} = 100 - \frac{100(Q_{SI} - Q_{SF})}{(Q_{SI} \times c)}$$

Equation 1-12

$\%_{CPR}$ = percentage capacity retention per cycle

Q_{SI} = initial specific capacity/ mA h g^{-1}

Q_{SF} = final specific capacity/ mA h g^{-1}

C = number of cycles

Rate

C-rate

C-rate is a term which refers to how fast or slow a battery is charged or discharged. This is referred to in the "Handbook of Batteries" (13) as being based on the capacity rating of the battery, however, in all cases within this work this will be referred to based on the theoretical capacity. Firstly, the capacity of the active material under test is calculated as in Equation 1-13.

$$Q_p = m_p \times Q_T$$

Equation 1-13

Q_p = capacity of active material pellet/ A h

m_p = mass of active material pellet/ g

From this value the C-rate can be calculated using Equation 1-14.

$$C_r = \frac{I}{Q_P}$$

Equation 1-14

C_r = C-rate

I = current/ A

This gives us a rate which is the inverse of the time it takes to discharge the battery. For example, a C-rate of 0.1 means that if the full capacity of the active material pellet is discharged in 10 h. C-rate is only ever referred to for galvanostatic discharge, however, it is possible and sometimes done in this work to estimate it for cyclic voltammetry.

Rate capability

Rate capability is determined by how well a material retains its specific capacity at high rates of discharge. This is typically reported by plotting graphs of specific capacity *vs.* C-rate, current or scan rate (for cyclic voltammetry measurements).

1.2.2 Primary Systems

A primary battery is sold in the charged state and is only useful for a single discharge(12). The electrochemical reaction that takes place during discharge can be considered as irreversible(11). A summary of a few popular systems is shown below in Table 1-1. These batteries are extensively used in portable electronic equipment such as torches, cameras and watches(11). The major advantages of most primary systems are there simplicity, good self life and acceptable cost.

Table 1-1. Table of some common primary battery systems. Reproduced from New battery Technologies(17).

System	Cell Reaction			Nominal Voltage/V	Energy Density/ Wh/l
	Positive electrode	Electrolyte	Negative electrode		
Leclanché	MnO_2	$ZnCl_2$ NH_4Cl	Zn	1.5	200
Alkaline Mn Dry Battery	MnO_2	KOH (ZnO)	Zn	1.5	320
Ag_2O Zn battery	Ag_2O	KOH NaOH	Zn	1.55	450
Zn-Air Battery	O_2	KOH	Zn	1.4	1235
$Li/(CF)_n$ battery	$(CF)_n$	$LiBF_4$/ γ-BL	Li	3	400
Li/ MnO_2 battery	MnO_2	$LiCF_3SO_3$/ PC+DME	Li	3	400

1.2.3 Secondary systems

A secondary battery is one which after discharge can be recharged and used again. This is done by reversing the flow of the electrons and thus reversing the discharge reaction(11). These systems are advantageous as after an initial purchase the consumer can continue reusing the battery many times(11). These battery systems have been used in applications such as automotive ignition and extensively in the mobile electronic devices such as laptops and mobile phones.

Table 1-2 Table of some common secondary battery systems. Reproduced from New battery Technologies(17).

System	Cell Reaction			Nominal Voltage/V	Energy Density/ Wh/l
	Positive electrode	Electrolyte	Negative electrode		
Sealed Lead-Acid battery	PbO_2	H_2SO_4	Pb	2	75
Ni-Cd Battery	NiOOH	KOH	Cd	1.2	100
Ni-MH Battery	NiOOH	KOH	MH(H)	1.2	240
Li/ V_2O_5 rechargeable battery	V_2O_5	$LiBF_4$/ PC+DME	Li-Al	3	140
Li Ion Rechargeable Battery	$LiCoO_2$	$LiPF_6$/ EC+DEC	C	4	280

The lithium systems offer a significant advantage over the others in Table 1-1 as the operating voltage is much higher(14). This stems from an increase in the free energy of insertion of the lithium into the host lattice. The negative electrode typically has a small chemical potential (if Li μ_N = 0 or a small negative value in the case of

graphite)(14, 18), while the positive electrode has a highly negative chemical potential, resulting in the observed high voltages which can be calculated with Equation 1-8. A summary of some of the potentials of lithium intercalation compounds can be seen in Figure 1-2.

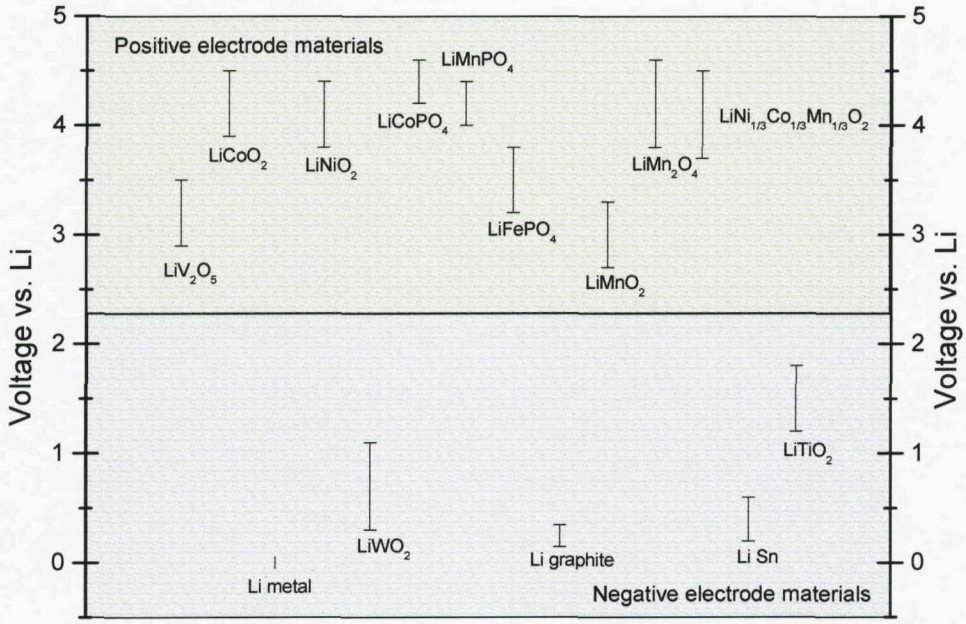

Figure 1-2 Electrochemical potential of some lithium intercalation compounds vs. metallic lithium(18, 19).

The use of this higher voltage system has led to a significant increase in the energy density both gravimetric and volumetric that can be stored from the older systems illustrated in Figure 1-3. This is one of the key reasons that lithium systems have flooded the rechargeable market in recent years. This widespread use has meant that the interest in improving these systems still further is larger than ever before.

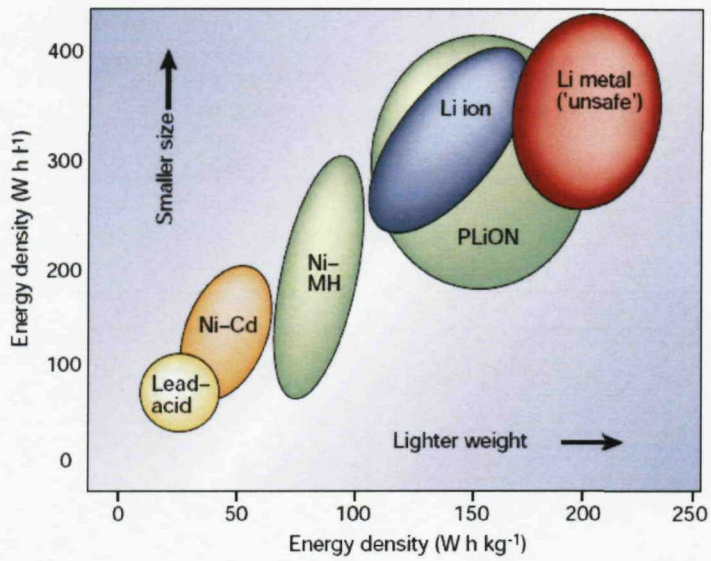

Figure 1-3 Comparison of the different battery technologies in terms of volumetric and gravimetric energy densities. Copied from reference(19).

1.3 Lithium/lithium ion secondary battery

The first commercial systems were operated using a positive electrode material (discussed in more detail later) a non-aqueous ion conducting electrolyte and a lithium metal negative electrode(10). The charging process is shown below in Equation 1-15.

$$Li(s) + A_zB_Y(s) \underset{\text{discharge}}{\overset{\text{charge}}{\rightleftharpoons}} Li_xA_zB_y(s) + (1\text{-}x)\ Li(s)$$

Equation 1-15

This reaction is remarkable as it occurs well outside the electrolyte stability window. It only occurs thanks to the formation of a passivation layer on the surface of the Li referred to as the solid electrolyte interface (SEI) (a term coined by Peled(20)). This layer protects the electrodes from further reaction whilst enabling Li ion transfer from the electrode to the electrolyte(21). The lithium metal system had significant advantages due to its light weight and stability in a number of electrolytes meaning the batteries have long shelf lives. However, there were safety issues with lithium metal; on long term cycling dendrite formation was a significant problem causing

short circuits and explosions as a result of thermal runaway(14, 21). To circumnavigate this problem a second intercalation material is now used for the negative electrode the first commercially successful example of which was carbon(10, 22). A generic example of the cell charge discharge reaction is shown below in Equation 1-16.

$$Li_xC_nM_m(s) + A_zB_Y(s) \underset{\text{discharge}}{\overset{\text{charge}}{\rightleftharpoons}} C_nM_m(s) + Li_xA_zB_y(s)$$

C_nM_n = the negative electrode: a low voltage *vs.* Li intercalation material e.g. graphite
A_zB_Y = the positive electrode: a high voltage *vs.* Li intercalation material e.g. $LiCoO_2$

Equation 1-16

The negative electrode acts as a lithium ion sink accepting lithium ions during charging and releasing them during discharge. This effect is termed a "rocking chair battery", "swing" or more general "lithium ion battery". Below in Figure 1-4 a schematic of the rocking chair battery is shown(6).

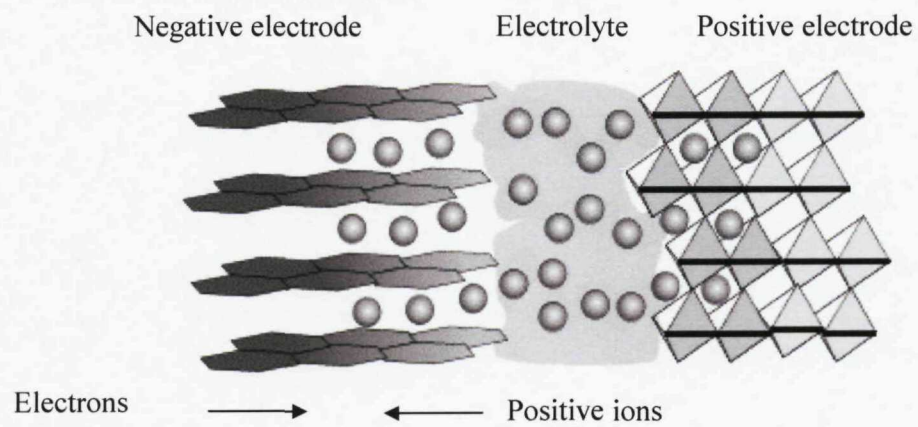

Figure 1-4 Schematic diagram of a lithium ion cell. The balls represent lithium ions that compensate the electrostatic charge due to electrons passing in and out of the electrodes while current passes in the external circuit.

The use of two intercalation materials in Li-ion batteries avoids the problem of dendrite formation, making the system safer and more reliable. However, the negative electrodes are now heavier than pure lithium, reducing the overall specific capacity of

the cell. However, the improvements in safety make this a more appropriate cell design.

Negative electrode materials

The most common negative electrode used commercially is graphitic carbon introduced by SONY(10). This material inserts 1 Li per 6 carbons to form LiC_6 at around 0.25 V vs Li and has a capacity of ~320 mA h g^{-1}(19, 23). Other negative electrode materials include alloys with Si(24), Al and Sn(25) which offer much larger capacities (> 600 mA h g^{-1}); however, the retention of capacity on cycling was poor. Recently use of the same alloys in amorphous form has shown much improved performance(26). Other possible negative electrodes are the various forms of TiO_2 and other titanates; the example of TiO_2-B has a discharge potential of 1.4 V vs. Li and a capacity of approximately 200 mA h g^{-1}(27). One significant advantage of this material is its high discharge potential means that the threat of dendrite formation and subsequent cell failure from Li plating is removed, with a graphitic electrode this can still sometimes be a problem at high rates(10).

Electrolytes

The electrolytes used in most lithium ion batteries are lithium salts dissolved in a organic solvent. However, lithium ion batteries operate well outside the stability window of most organic solvents(21). This problem is resolved as a passivation layer known as the solid electrolyte interface (SEI) forms on the surface of the negative electrode and protects against the decomposition, while, allowing ion conduction from the electrode to the electrolyte(21).

Many different salts have been used during the development of Li ion battery, however, recently $LiPF_6$,(21) LiTFSI(14) and LiBOB (28) appear most commonly within the literature. Various different organic solvents have also been examined with ethylene carbonate (EC) and dimethyl carbonate mixtures(DMC) being the most widely used(21).

Several different polymer electrolytes have also been trialed, such as polyethylene oxide (PEO)(21). The use of such electrolytes have several advantages compared with

the organic solvent electrolytes; the increased strength over the porous separator forms a physical barrier to dendrites reducing the possibility of short circuits and the low vapour pressure also reduces the chance of the cell drying out which is often a problem with liquid electrolytes. Another recent approach has been the use of ionic liquids (29)which have extremely low vapour pressure and are resistant to fire. However, problems due to extremely low diffusion coefficients significantly limit there practical application.

The composite structure of battery electrodes

Most battery electrodes are composite porous structures shown schematically below in Figure 1-5. Because many positive electrodes are poor electronic conductors a conductive additive typically acetylene black is added providing electronic pathways to allow reaction to occur(10). A polymer binder is also added which is there to hold the powder together in a film typically this material is PVdF but sometimes PTFE can also be used. Although usually the negative electrode has a high electronic conductivity a similar structure is often still used, the binder is added to provide structure as before and the conductive additive is added to provide an electronic pathway through the binder. This structure is porous to the electrolyte so the Li ions can easily diffuse to the surface of the active material particles. When the electrodes are poor electronic conductors the electrochemical reaction can only occur at those points where the active material, binder and electrolyte meet.

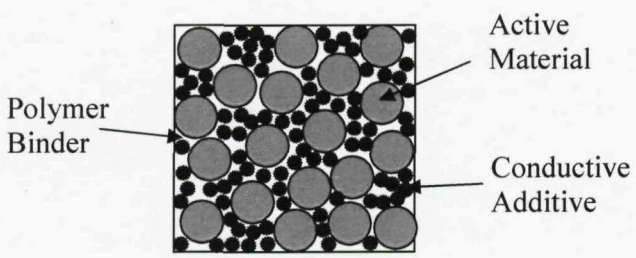

Figure 1-5 Schematic of battery electrode grey circles represent active materials, black stars represent conductive additive (AB) and the white regions represent the binder.

1.3.1 Positive Electrode Materials

1.3.1.1 A Review of the history of Positive Electrodes

Originally lithium battery systems were developed as primaries by NASA in the 1960s as a high energy power source for space development projects(17). These batteries employed metal halides or oxides as the positive material. The first commercial system was developed by Matsushita based on CF_x and MnO_2 positive material(10, 17). Following this work attempts were made at rechargeable systems using molten salts, with designs that would operate at around 450 °C; however, these systems were never successfully brought to the market place because of problems resulting from corrosion and the high temperatures of operation(30, 31) .

The first really successful Li rechargeable system was the TiS_2/Li cell developed in the late 1970's(10, 32, 33). TiS_2 is a layered material which behaves as a semi-metal, inserting up to 1 Li per Ti at a voltage of 2.1 V *vs.* Li. This system was marketed by Exxon with a LiAl negative electrode in the late 1970's. The search for new materials then moved towards researching metal oxides(10, 15, 34, 35). In the 1980s layered metal oxides were identified as a potential new positive electrode material, the first commercially successful and still the most widely employed is $LiCoO_2$(15). This was originally recognised by Goodenough et. al. (15). and brought to the market by SONY, who used a $LiCoO_2$ positive material and carbon negative to create a Lithium ion battery(36). This was followed in the 1990s with the development of the spinel material $LiMn_2O_4$ proposed by Thackeray et. al. (37). In more recent years the olivine phase of $LiFePO_4$ was suggested by Padhi et. al.(38, 39) which led Armand et. al. (40) to develop a novel carbon coating preparation to overcome the intrinsic low conductivity of $LiFePO_4$. The following section will give a more detailed discussion of the layered, spinel and olivine materials focussing mainly on those specific areas relating to the work within this thesis. Following this there will be a very brief description of other systems which are attracting significant interest at the moment.

$LiMO_2$

The general $LiMO_2$ has the α-$NaFeO_2$ structure with the lithium and transition metal ions located at octahedral 3(a) and 3(b) sites in a cubic close packed arrangement of oxygens(10, 41). The lithium, transition metal and oxygen form alternating layers which allow the lithium to diffuse in and out of the structure on cycling. The structure of $LiCoO_2$ is shown in schematics below in Figure 1-6.

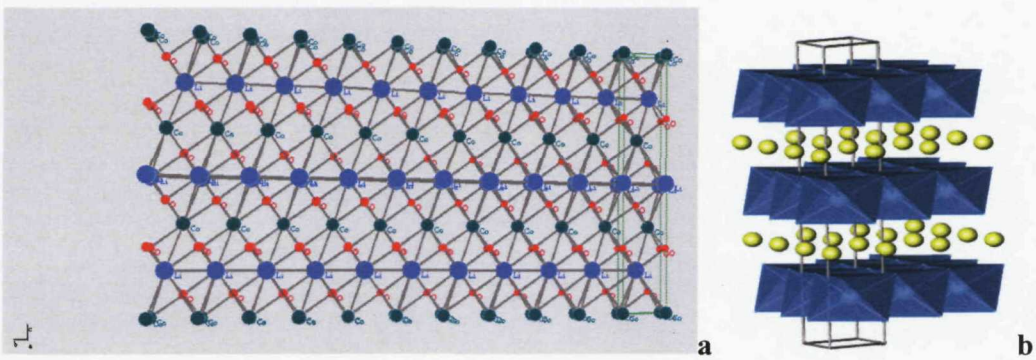

Figure 1-6 The structure of $LiCoO_2$ shown in two different ways; atoms and bonds (a) polyhedrons and Li atoms (b)(10).

The general structure shown here (Figure 1-6) has been used to form several different successful cathode materials a summary of which is presented below.

$LiCoO_2$

This was the first really successful commercial Li-ion battery material, the charge reaction proceeds as shown below in Equation 1-17(15).

$$LiCoO_2 \leftrightarrow Li_{0.5}CoO_2 + 0.5Li$$

Equation 1-17

Only 50 % of the available Li can be charged and discharged reversibly. If greater than 50 % Li is extracted large phase changes in the material occur resulting in severe capacity loss. If 100 % of the Li is removed the structure will rearrange completely to give hexagonal close packing of the oxygen in CoO_2(10). The material has a high voltage discharge at around 4 V and a capacity which is limited to 130 mA h g^{-1} by the incomplete extraction and insertion of Li.(10, 42) However, more recently some researchers have had success in increasing the amount of Li that can be utilised and thus increasing the capacity by using surface coatings(43, 44). It seems however that

even with these treatments the capacity is limited to 180 mA h g^{-1}. Nevertheless after 16 years of service since its commercialisation in 1991 $LiCoO_2$ is still the most widely used material in Li-ion cells. However, it does have significant drawbacks such as its high cost and toxicity which need to be addressed in the development of new materials.

$LiNi_{1/3}Co_{1/3}Mn_{1/3}O_2$ and other $LiNi_{1-y-z}Co_yMn_zO_2$

The $LiNi_{1/3}Co_{1/3}Mn_{1/3}O_2$ was proposed in 2001 by Ohzuku et. al.(45, 46) as a high voltage cathode (discharging around 4 V vs Li). Capacities greater than 200 mA h g^{-1} have been reported for this material in the range 2 to 4.6 V with negligible capacity loss.(46, 47) Ohzuku et. al. propose that in the $LiNi_{1/3}Co_{1/3}Mn_{1/3}O_2$ structure the Co, Ni and Mn exist in the 3+, 2+ and 4+ oxidation states respectively.(41) The charging reaction is shown below in Equation 1-18. However, the theoretical capacity of 278 mA h g^{-1} has not been observed within the potential limits of most experiments corresponding to the insertion of the 1 whole Li.

$$LiNi_{1/3}Co_{1/3}Mn_{1/3}O_2 \leftrightarrow Ni_{1/3}Co_{1/3}Mn_{1/3}O_2 + Li$$

Equation 1-18

This material has other advantages over $LiCoO_2$ *e.g.* the reduction of Co also means a reduction in cost and toxicity. However, several reports in the literature have shown that whilst structurally pure materials have been obtained it has been difficult to reproduce the electrochemical performance(48-50). The main preparation routes have been to precipitate either the metal hydroxides or metal carbonates from a solution of the metal sulphates or nitrates, although many other routes have been tried. It is apparent from these studies that the preparation of this material is sensitive to reaction conditions such as calcinations temperature(50) and time, precursor salts(47, 49, 50) and also the use of excess Li seems to be important. One of the most promising synthesis methods has been proposed by Shaju et al. who prepared a macropoous $LiNi_{1/3}Co_{1/3}Mn_{1/3}O_2$ using a dilute solution of metal acetates mixed with resorcinol and formaldehyde in a sol-gel method(47). This material shows a 99.9 % retention of

capacity per cycle compared with the best reported elsewhere of 99.83 %, it also shows a high rate capability. It is proposed that the excellent performance of this materials is a result of an optimised sample morphology(47). Other methods to improve the performance of this material have used a variety of surface treatments(51, 52) to improve the retention of capacity on cycling and also cationic substitution(53, 54). Recently Thackeray et al. (55) have shown that by washing the $LiNi_{1/3}Co_{1/3}Mn_{1/3}O_2$ in a dilute solution of NH_4PF_6 prior to testing a significant improvement in the retention of capacity on cycling can be achieved.

The $LiNi_{1/3}Co_{1/3}Mn_{1/3}O_2$ material is a member of the $LiCoO_2$-$LiNiO_2$-$LiMnO_2$ phase triangle shown below in Figure 1-7. This diagram was proposed by Koyama et al. based on first principle calculations from the superlattice model(56). The calculations show that this is not a true solid solution over the whole ternary diagram; for example it has areas of phase separation between $LiMnO_2$ and $LiCoO_2$. However, there are several areas of solid solution and formation of supperlattices indicated in Figure 1-7. Several members of this complicated phase diagram and many of the ternary edge compositions have been investigated within the literature but as yet no systematic experimental investigation has been published.

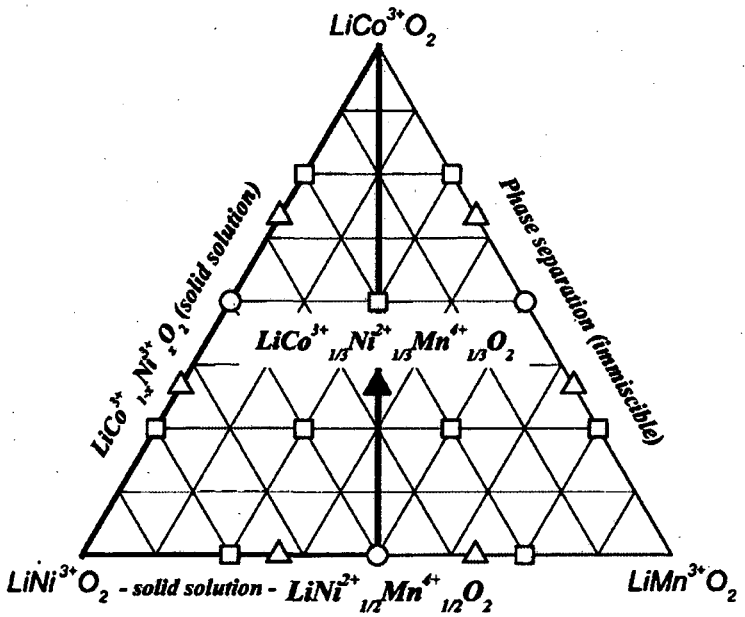

Figure 1-7 A phase triangle of $LiCoO_2$-$LiNiO_2$-$LiMnO_2$. Copied from reference(41). Superlattice structures are expected at compositions marked in squares for [2×2, in triangles for [√3×√3] R30°, and circles for the straight or zigzag models.

Other $LiMO_2$

Other materials with the same structure have been tried less successfully. $LiNiO_2$ was investigated for many years but has problems associated with Ni presence on the Li sites reducing the diffusion coefficient. Instability in the materials containing low lithium content gave unstable cells that were especially dangerous in contact with organic solvents(10). $LiMnO_2$ has also been investigated; however problems with conversion of the structure from layered to spinel during cycling has plagued its application(10).

$LiMn_2O_4$

$LiMn_2O_4$ is based on the spinel structure $MgAl_2O_4$(57) and has an anion framework of cubic close packed oxygen ions(58). The Li ions occupy the tetrahedral 8a sites while the manganese cations and oxygen anions occupy the octahedral 16d and 32e sites, respectively(59).

The reaction typically proceeds as shown in Equation 1-19, however, a second Li can be inserted into the spinel structure resulting in the charging reaction shown in Equation 1-20. When only a single lithium is inserted activity is observed at around 4 V *vs* Li, the use of the second Li results in a second plateau at around 3 V *vs* Li(10, 37, 60).

$$LiMn_2O_4 \leftrightarrow Mn_2O_4 + Li$$

Equation 1-19

$$Li_2Mn_2O_4 \leftrightarrow Mn_2O_4 + 2Li$$

Equation 1-20

This material has generated much interest but suffers from significant capacity loss at high temperatures and problems of Mn^{2+} dissolving into the electrolyte(10, 61). Several attempts have been made to improve the materials performance using cationic substitution. The theory is that by substitution with appropriate ions the average oxidation state of the manganese can be increased causing an improvement in

capacity retention on cycling(10, 59). Particular improvements have been seen when using the $LiAl_xMn_{1-x}O_{4-y}F_y$, where the anionic substitution of F^- has resulted in improved capacities without sacrificing the cycle life of the material(59). The use of new electrolytes such as LiBOB has also been suggested as a way to improve the capacity loss at high temperatures(62, 63). It has been suggested that a polymerisation of the BOB^- anion occurs on the first cycle forming a thin layer between the electrolyte and the particles which is permeable to Li but can suppress the dissolution of Mn^{2+}.

Detailed discussion of $LiMPO_4$

Interest in the $LiMPO_4$ was initiated when Padhi et. al.(38, 39) first suggested the $LiFePO_4$ and $LiFe_{1-x}Mn_xPO_4$ materials in 1997. Below a brief review of the important features of $LiFePO_4$ relating specifically to this work will be given.

$LiFePO_4$

$LiFePO_4$ has a general olivine structure of $(Mg,Fe)_2SiO_4$(57) found in the earths mantle, this has an orthorhombic crystal class(64). $LiFePO_4$ has a hexagonally close packed array of oxygen atoms with Fe (FeO_6) and P (PO_4) binding with the octahedral and tetrahedral sites respectively; this is shown in two schematics (Figure 1-8) below the first atoms and bonds (a) the other showing and polyhedrons and Li atoms(b) (10). Within this structure the phosphorus atoms occupy tetrahedral sites and the iron atoms octahedral sites. The FeO_6 octhedra are linked via corners in the bc plane and the LiO_6 octahedra form edge sharing chains on the b axis. What is clear from these two schematics is that the Li ions exists within channels which allows the extraction and insertion during charge and discharge, via the following reaction (Equation 1-21).

$$LiFePO_4 \leftrightarrow Li^+ + FePO_4 + e^-$$

Equation 1-21

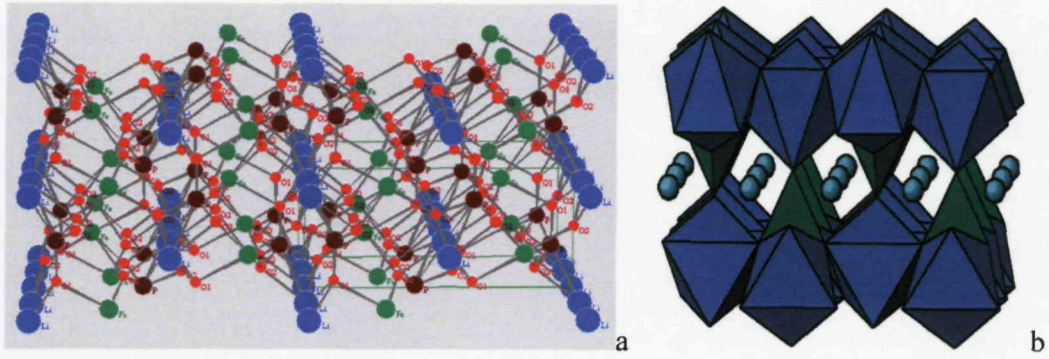

Figure 1-8 The structure of $LiFePO_4$ shown in two different ways; atoms and bonds (a) FeO_6 and PO_4 polyhedrons and Li atoms (b)

The initial work of Padhi et. al.(38, 39) showed a reversible capacity of 110 mA h g^{-1} at slow rates with a discharge potential of 3.4 V *vs.* Li. This is only about 65 % of the theoretical capacity (170 mA h g^{-1}), this reduction was attributed to both poor electronic conductivity and poor ionic conductivity(19, 64). The electronic conductivity of $LiFePO_4$(65) is only 10^{-9} S cm^{-1} compared with 10^{-3} S cm^{-1} for $LiCoO_2$(66).

Carbon Coating to Improve Conductivity

To alleviate the problem of low intrinsic electronic conductivity Ravet et. al.(40) reported that when a 1 wt. % carbon coating was used then a specific capacity of 160 mA h g^{-1} was achieved. The coating forms a conductive network (Figure 1-9) which is in close contact to the $LiFePO_4$ particles. This is far more effective than any carbon additives such as acetylene black described earlier.

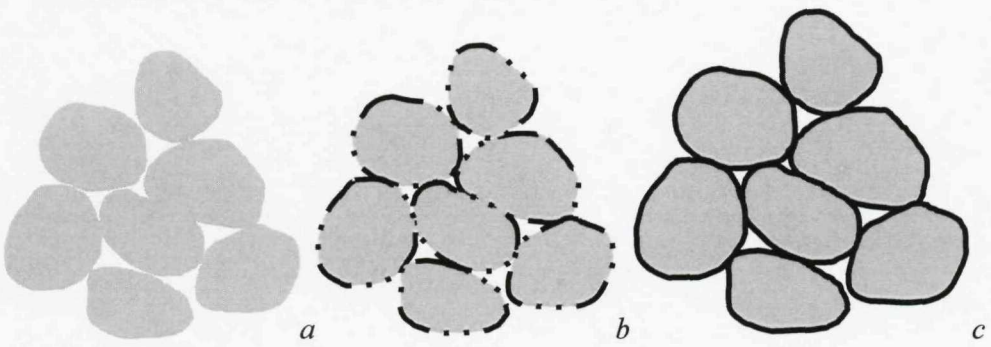

Figure 1-9 Schematic view of how carbon can be used to form a conductive network to overcome the problem of poor conductivity in $LiFePO_4$. Three states of $LiFePO_4$ are shown: *(a)* no carbon coating, *(b)* partial but insufficient carbon coating and *(c)* perfect carbon coating.

Figure 1-9 represents the percolation by carbon coating of $LiFePO_4$. Percolation is a mathematical concept which in this case models the effect of different degrees of carbon coating on the performance of $LiFePO_4$. The percolation threshold has been reached when there is a direct path through the conductive medium (the carbon coating) from the non-conductive medium ($LiFePO_4$) to the current collector (there is still acetylene black (AB) and binder to be considered within this model as well). This nicely describes what happens when the material is carbon coated, we need sufficient coating so that there are no breaks in the electronic conduction path as in Figure 1-9 (c) but not in (a) or (b). When this network is not formed (a,b) effective electronic connectivity can not be maintained by the AB alone and little or no capacity can be extracted at moderate rates. This is not a classical interpretation of percolation which is shown in Figure 1-10. Here the percolation threshold simply refers to how many of the white squares need to be replaced by blue squares to achieve a route via only blue squares from the left hand side to the right hand side of the grid(67).

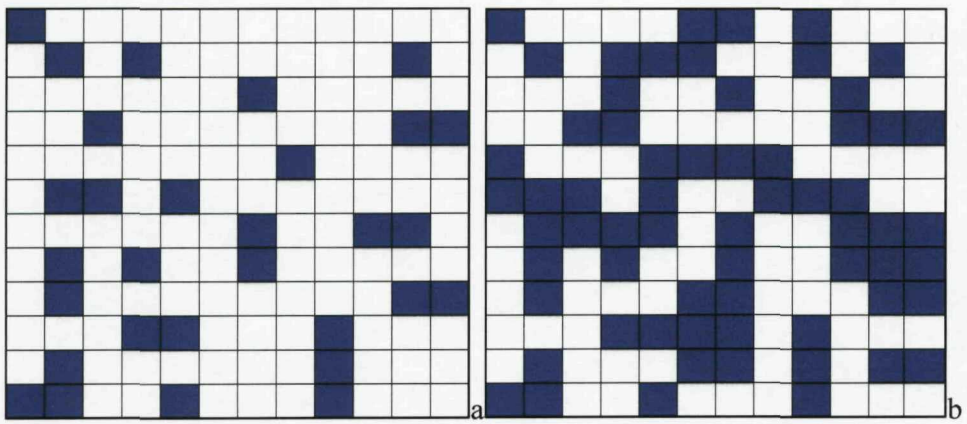

Figure 1-10 Figure showing percolating networks. (a) below percolation threshold, (b) above percolation threshold.

This carbon coating technique was very successful in overcoming the conductivity problems, at moderate scan rates (C/5) a capacity of 160 mA h g^{-1} can be extracted(68). Several methods have been reported for carbon coating $LiFePO_4$ these include solid state reaction (40, 68) or solution base methods with sucrose(68) or other carbon based additives(69-71). However, using carbon to improve the materials conductivity increases the mass and volume of the electrode composite, which has the

effect of reducing the capacity of the material. Several papers have suggested that the conductivity of the $LiFePO_4$ can be increased by placing an inactive ion on either the Li or the Fe site; this could alleviate the need for carbon coating and increase the energy density of the material.

Conductive Substitution $Li_{1-x}M_xFe_{1-y}M_yPO_4$

One of the earliest reports of conductivity improvement via substitution of inactive species on the Li was reported by Chung et. al.(64). They reported a $\sim 10^8$ increase in conductivity of $LiFePO_4$ when doping with Mg, Al, Ti, Nb, Zr or W on the Li site and also reported greatly improved electrode performance. They report that the "highly conductive doped compositions seem to be extrinsic *p*-type semiconductors", and that this is the primary reason for there greatly improved performance. However, the interpretation of these results was questioned by Ravet et. al.(72) who believe the improved conductivity is more likely to be a result of carbon residues from the precursor salts than the claimed material effect. Several other reports in the literature have suggested improved performance using the same elements(73) as Chung et. al.(64) and also other elements have been used to dope on the Li site for example; Zn(74), La(75) and Ti(76). However, all these results are still tainted with the suggestion that carbon residue may be effecting an accurate interpretation.

The study of $LiFe_{1-y}Mg_yPO_4$ materials presented by Barker et. al. (77), was one of the earliest examples of substitution of the Fe by an inactive species, they successfully synthesized the material via a carbothermal reaction and saw a capacity of 150 mA h g^{-1} at C/20 seeing what they described as "outstanding ionic reversibility". Later several publications investigating different synthesis methods and material performance reported improved capacity, conductivity and rate capability(78-81). Other papers have suggested that doping with Zr, Ti(80, 82), Cu, Zn(74, 83) may also improve the materials performance via a similar mechanism. The explanation for these improvements is varied. An increase in conductivity is reported in several papers, however, it is still unclear as to the effect of any carbon residues within these samples, the same problem as suggested by Ravet et. al.. Measurements of XPS show a weakening in Li-O interaction and thus an improved ionic diffusion in the Mg doped

samples.(84) A further explanation suggest that the inactive Mg ions acts to stabilize the structure during charge and discharge and improves the materials performance.(79)

Other Olivines $LiMPO_4$

Other systems with the same structure as $LiFePO_4$ that have also been studied include $LiCoPO_4$(85, 86),$LiNiPO_4$(85) and $LiMnPO_4$(38). One of the most extensively investgated of these is $LiMnPO_4$ this is a higher voltage material than $LiFePO_4$ with approximately the same capacity and therefore represents a route for improving the energy density of the material. However, this material has extremely low conductivity and the reported electrochemical performance has been poor. In the initial work by Padhi et. al. a capacity of only 6 mA h g^{-1} was reported(38). Improved performance up to 160 mA h g^{-1} has been reported at slow rates (C/100) for some preparations which form extremely small particles(87, 88). In the original work on $LiFePO_4$ and $LiMnPO_4$ reported by Padhi et. al.(38) the use of the solid solution $LiFe_{1-x}Mn_xPO_4$ was suggested, here whilst some capacity was seen at higher voltages typically the capacity reduced linearly with the addition of Mn, this result has also been observed by others(89). A detailed study of this material has been reported by Yamada et al.(90) who demonstrate 160 mA h g^{-1} for the composition $LiMn_{0.6}Fe_{0.4}PO_4$ at slow rates. This work has focused on resolving the reaction mechanism in the mixed metal phosphate. It is reported that the 2 phase behaviour of $LiFePO_4$ moves increasingly to a 1 phase behaviour on the substitution of Fe for Mn(91).

Other Systems

Several other systems have also been considered as positive electrode materials such as $LiMSiO_4$ (where M = Fe and Mn) results on this material were first reported by Thomas et. al.(92) and since then several other papers have been published. The advantage of this material is that it is possible to insert and extract more than 1 Li giving it a relatively high capacity. Other phosphate based materials have also been proposed such as $LiVPO_4F$(93), $Li_3V_2(PO_4)_3$ and several others.

Key Requirements of a Cathode Material

In a review paper by Whittingham(10) the key requirements for a cathode in a lithium battery were outlined these are shown below.

An ideal cathode should be developed such that:

1. The material contain a readily reducible/oxidizable ion, for example a transition metal.
2. The material react with lithium in a reversible manner.
3. The material react with lithium with a high free energy of reaction ($\Delta G = -nFE$).
    a. High capacity, preferably at least one lithium per transition metal (large n).
    b. High voltage (large E), preferably around 4 V (due to decomposition of the electrolyte).
    c. This leads to a high-energy storage.
4. The material have a high rate capability.
5. The material be a good electronic conductor, preferably a metal.
    a. This allows for the easy addition or removal of electrons during the electrochemical reaction.
    b. This minimizes the need for inactive conductive diluents, which take away from the overall energy density.
6. The material have a stable structure which does not change or degrade on cycling leading to a high retention of capacity per cycle.
7. The material be low cost.
8. The material be environmentally benign.

1.4 Combinatorial and High throughput technique

1.4.1 The Principle

The combinatorial principle was originally conceived for the simultaneous synthesis of a large number of organic molecules(94, 95). The large number of products meant that the chances of finding attractive targets were greatly improved. Below in Figure 1-11 a pictorial representation of the combinatorial principle is shown. The method shown is called the Split&Pool synthesis and employs reacting on polymer supports and simple division and recombination steps to generate a large number of samples in a single reaction vessel(96).

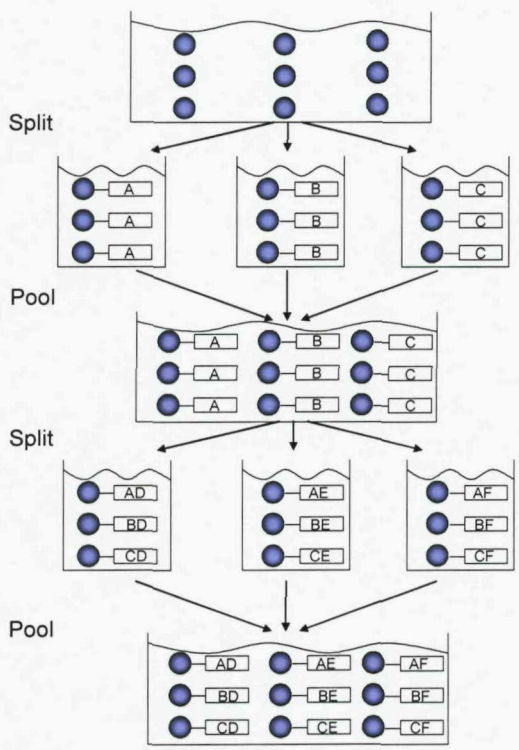

Figure 1-11. Flow chart displaying the combinatorial principle.

The first use of this principle was published by Mario Geysen in 1986(94, 95). In this study he produced a large library of compounds which were then screened for their

biological activity. This technique has now become commonplace in organic chemistry. The principles of this technique were quickly adopted by all areas of materials science (a summary is shown in Table 1-3 of many of the industries which these techniques have been applied) where often not only the composition can affect sample performance but also morphology, crystal structure, testing conditions and other parameters(96).

Table 1-3 Examples of materials explored using combinatorial and high-throughput experimentation techniques. Table partially reproduced from literature(96).

Material Explored	Reference
Heterogeneous catalysts	(97)
Homogeneous catalysts	(98)
Fuel cell anode	(99)
Enantioselective catalysts	(100)
Electrocatalysts	(101)
Polymers	(102)
Zeolites	(103)
Luminescent compounds	(104)
Magnetoresistive compounds	(105)
Metal alloy compounds	(106)
Coating materials	(107)
Fuel cell materials	(108)
Solar cell materials	(109)
Agricultural materials	(110)
Ferroelectric/dielectric materials	(111)
Structural materials	(112)
Hydrogen storage materials	(113)

The terms combinatorial, high-throughput and parallel can often be found in the literature used interchangeably. An important distinction needs to be made between combinatorial techniques and high-throughput methods. The expression combinatorial chemistry was originally coined for the organic applications described above. Here, in one pot a large number of samples are prepared simultaneously, they are not separated but analysed together at the same time. In high-throughput methods samples are

typically fabricated one at a time however very quickly. This difference is not a golden rule for deciding which is the correct term, however, it is a reasonable guide.(96)

1.4.2 Combinatorial and High-throughput approaches in battery research

The first demonstration of combinatorial techniques applied to electrochemistry was presented by Reddington et al. in 1998(101). The experiment involved the parallel electrochemical cycling of methanol fuel cell catalyst, the most active catalyst then generated the most hydrogen ions which could be observed using a fluorescent acid-base dye. Since then these concepts and ideas have been widely applied to other areas of electrochemistry(114, 115) in particular batteries and fuel cells(4, 116-118).

1.4.2.1 Standard Non-high-throughput synthesis

Before the introduction of high throughput methods in battery science, it is important to recognise what constitutes at standard method. A typical conventional method of cathode material testing is shown below in Figure 1-12.

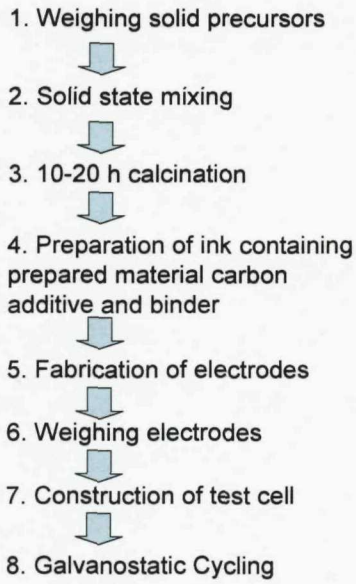

Figure 1-12 A flow chart depicting the processes involved in fabrication and test of a battery cathode using conventional methods.

The various stages in battery testing shown in Figure 1-12 are typically very labour intensive and time consuming. It may take anything from two weeks to two months from initiating the experiment until the cycling data can be analysed. The first major rate limiting step is the preparation of the active material which requires laborious grinding, long times and high temperatures. Whilst, the second is the electrochemical measurement which can often take many weeks if investigation into a materials cycling stability are being made.

1.4.2.2 Development of the Testing Equipment

Several groups have demonstrated the parallel screening of battery materials(4, 119, 120). The principle method used is a cell with many working electrodes and a single counter/reference electrode typically lithium. A selection of several cell designs from the literature is shown in Figure 1-13a-c. The potentials of the working electrodes are then controlled vs. the reference and the current of each element is monitored. This is done using the circuit shown in Figure 1-13d the critical component of which is a commercially available 16 bit, 64 channel analogue converter.

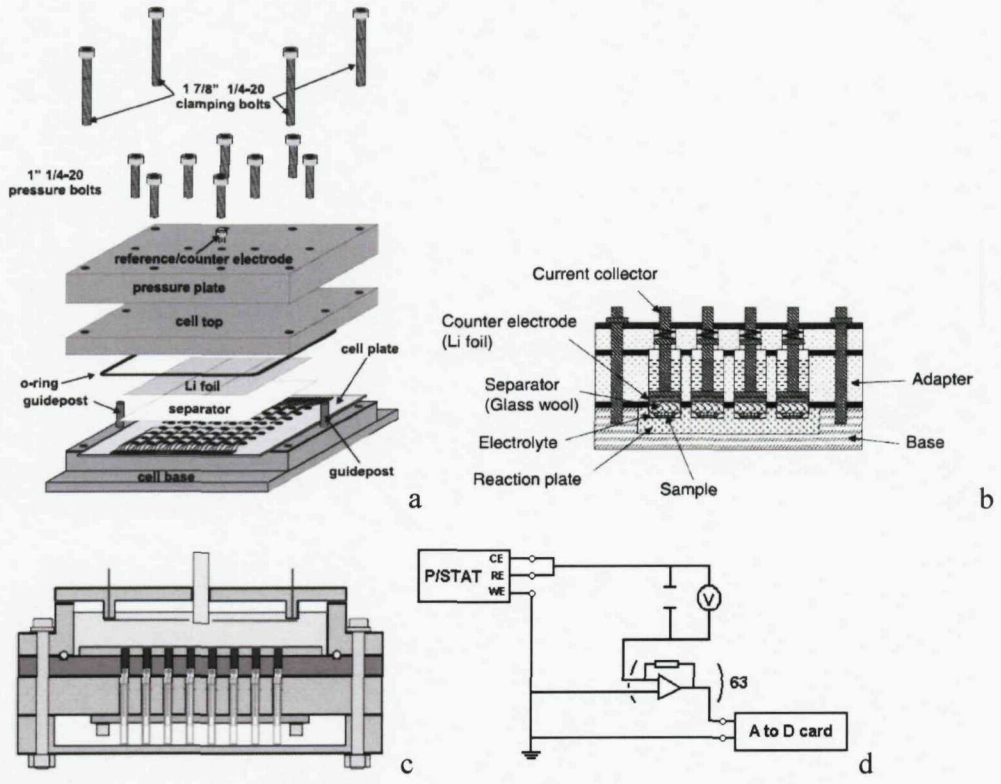

Figure 1-13 Figure of some combinatorial equipment: a (Dahn group design), b (Watanabe) and c (Owen) are cell designs used by various research groups. The circuit diagram in d (Owen) shows how the design used for the current followers used in Southampton.

1.4.2.3 Fabrication Methods

Perhaps the biggest challenge of combinatorial or high-throughput approaches to the study of battery materials is the effective synthesis of the electrodes. Below the various techniques previously used in the high throughput discovery of battery materials are summarised(121).

Physical Vapour Deposition(PVD)

This is the most developed and extensively used method of all those discussed here. Although ultra high vacuum (UHV) techniques physical vapour deposition have been used to study high purity thin films in catalyst (122), thicker films, and therefore

faster deposition rates are generally preferred for battery material testing(121). Consequently sputtering has been preferred to UHV deposition. This technique has been pioneered by Dahn et al. in Dalhousie University in Canada(116, 119, 123). The technique is to sputter a substrate with the desired metal through a mask which controls the flux of material seen over the whole substrate; this gives a graduated increase of material from one side of the substrate to the other. An example of a schematic taken from the literature(117) is shown below in Figure 1-14. The substrate was first placed behind the Si mask which produced an even layer of material. The substrate is then moved to the Sn mask and a layer of material is deposited which varies in thickness according to the masks design. This means that at various places on the substrate different values of x in $Si_{1-x}Sn_x$ can be obtained.

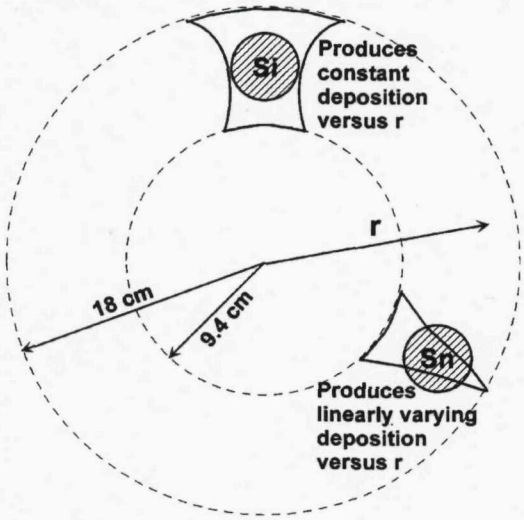

Figure 1-14 Schematic representation of the setup used inside the Dahn group sputtering chamber. Sputtering masks are used to deposit a linear range in composition *x* in a binary system such as $Si_{1-x}Sn_x$.

For more complicated systems (i.e. the deposition of several layers, typically three, however, a more recent publication has shown a method for the fabrication of quaternary compositional spreads using a more elaborate masking system(124)) multiple metal targets are used. A schematic in Figure 1-15 shows how a generic ternary mixture could be formed.

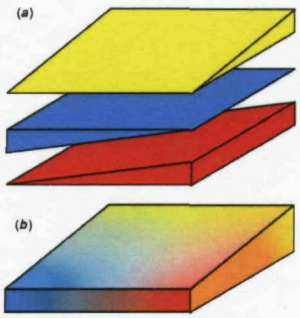

Figure 1-15 Thin layers of metals are stacked upon each other to form an atomically mixed product with variable composition. Image taken from the literature(125).

This method has been employed in the study of many different materials systems. The systems chosen for study were mainly negative electrode materials normally metallic alloys. What follows in Table 1-4 is a summary of some of the material studies explored via this method by the Dahn group and others using similar procedures.

Table 1-4 Publications investigating battery materials using Physical Vapour Deposition.

Reference	Year of Publication	Title	*Brief Description of Results*
(117)	2003	The Electrochemical Reaction of Li with Amorphous Si-Sn Alloys	Used to show that $Si_{0.66}Sn0.34$ is the most promising candidate for further study.
(123)	2003	Electrochemical Performance of SiAlSn Films Prepared by Combinatorial Sputtering	Used to show that amorphous materials of SiAlSn show high capacities and high retention of capacity on cycling.
(126)	2003	Combinatorial Synthesis and rapid characterization of $Mo_{1-x}Sn_x$ ($0 \leq x \leq 1$) thin films	Used to identify the structural phases in $Mo_{1-x}Sn_x$.
(127)	2003	A Combinatorial Study of $Li_yMn_xNi_{2-x}O_4$ Cathode Materials Using Microfabricated Solid State Electrochemical Cells	Validation of the method using a well studied technique.
(128)	2004	Combinatorial Investigations of the Si-Al-Mn System for Li-Ion Battery Applications	Identification of an optimal composition $Si_{0.38}Al_{0.52}Mn_{0.1}$ which can be melt spun and has a high capacity and retention of capacity on cycling.
(129)	2004	Study of the Electrochemical Performance of Sputtered $Si_{1-x}Sn_x$ Films	Used to identify amorphous $Si_{1-x}Sn_x$ $0 < x < 0.45$ materials that showed a high capacity and retention of capacity on cycling.
(130)	2005	Electrochemical Reaction of the SiAg Binary System with Li	SiAg does not cycle as well as SiSn, and a simple model for the structural changes that occur during extraction of Li is proposed.
(125)	2005	Electrochemical Reaction of the $Si_{1-x}Zn_x$ Binary System with Li	Compositions of $Si_{1-x}Zn_x$ have been found which show good capacity retention and over 1000 mA h g^{-1}.
(131)	2006	Combinatorial Study of $Sn_{1-x}Co_x$ ($0<x<0.6$) and $[Sn_{0.55}Co_{0.45}]_{1-y}C_y$ ($0 < y < 0.5$) Alloy	The addition of Carbon makes amorphous materials with high capacities (~700 mA h g^{-1})

		Negative Electrode Materials for Li-Ion Batteries	with long cycle life.
(132)	2006	Al-M (M=Cr, Fe, Mn, Ni) Thin Film Negative Electrode materials	Samples with more than 15 % dopant are completely inactive. Increased activity was observed at elevated temperatures.
(133)	2006	The Impact of the Addition of Rare Earth Elements to $Si_{1-x}Sn_x$ Negative Electrode materials for Li-Ion Batteries	Compositions of amorphous $Si_{1-x}Sn_x$ with Rare Earth metal dopants show high capacity and cycle life whilst also can be fabricated using melt spinning methods.
(134)	2006	Simple Model for the Capacity of Amporphous Silicon-Aluminium- Transition Metal Negative Electrode Materials	A comprehensive Si-Al-M (M=Cr, Fe, Mn, Ni) study was performed which showed patterns which allowed predictions of the performance of crystalline materials based on the performance of the amorphous material.
(135)	2006	Combinatorial Study of Tin-Transition Metal Alloys as Negative Electrodes for Lithium-Ion Batteries	It is suggested that $Sn_{1-x}V_x$ is the best candidate as a negative electrode as it is amorphous at relatively low x values and has a high capacity.
(136)	2007	Method to Predict Phase Formation and Specific Capacity for Lithium in Codeposited Silicon-Transition Metal Thin Films	Structural information about the Silicon transition metal thin films has been obtained.
(137)	2007	Tin-Transition Metal-Carbon Systems for Lithium-Ion Battery Negative Electrodes	Identification of Sn-Co-C as a candidate for negative electrode materials.
(138)	2007	Studies of $Si_{1-x}C_x$ Electrode Materials Prepared by High-Energy Mechanical Milling and Combinatorial Sputter Deposition	Commercially relevant compositions are identified.

This method has been very effective in the study of negative electrode materials as seen in table 1 and has allowed many materials to be investigated in the few short years since its inception. More recently, initial results have been reported for the study of some positive materials such as the metal fluorides. However, composition spreads of more conventional positive materials such as the oxides have not been reported, presumably due to the difficulty of preparation conditions(139, 140).

Electrodepostion

This technique uses electrodepostion as means of obtaining compositional spreads. One approach uses the Hull cell to deposit a composition spread on a single substrate (Figure 1-16). This employs the changes in current density caused by having a working electrode which is not aligned parallel with the counter electrode(121).

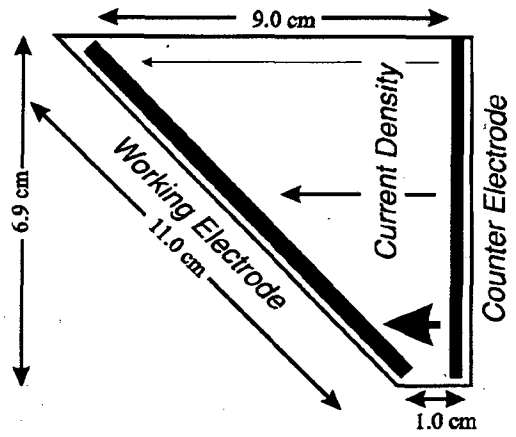

Figure 1-16 The Hull cell. This image has been reproduced from the literature(141).

Table 1-5 Publications investigating battery materials using Electrodeposition.

Reference	Year of Publication	Title	Brief Description of Results
(142)	2003	Single-Bath Electrodeposition of a Combinatorial Library of Binary $Cu_{1-x}Sn_x$ Alloys.	Sn rich high capacity. Cu rich high retention of capacity of cycling.
(143)	2003	Comparison of Electrodeposited Copper-Zinc Alloys Prepared Individually and Combinatorially.	Investigates the structure of the composition spread in the Cu-Zn system and highlights some materials for further study.
(144)	2004	Application of combinatorial methodologies to the synthesis and characterization of electrolytic manganese dioxide.	This introduces a technique for combinatorial electrodepostion and uses it to identify optimal performance EMD.
(141)	2005	Masked Electrodeposition of a Composition-Spread Library of Sn-Zn onto a 64- Channel Combinatorial Cell Plate.	Synthesis of Sn-Zn system for further study.
(145)	2005	Combinatorial Electrodeposition of Ternary Cu-Sn-Zn Alloys	A new dripped immersion plating was added to the combinatorial electrodeposition method to obtain a Cu-Sn-Zn method
(125)	2005	Electrochemical Reaction of the $Si_{1-x}Zn_x$ Binary System with Li	$Si_{0.4}Zn_{0.6}$ had a capacity of 100 mA h g^{-1} and cycled well

Solution based or Sol Gel Synthesis methods (Precursor mixtures)

Solution based or sol-gel synthesis will be discussed in greater detail in Chapter 2. However, it is a process used to synthesise the active material which typically involves the mixing of solution precursor salts (e.g. lithium acetate, iron nitrate, and

phosphoric acid for the synthesis of $LiFePO_4$) and possibly adding a chelating agent to inhibit the crystallisation of salts on drying, and maintaining a homogeneous mix of ions at the atomic level. An advantage of sol-gel for combinatorial synthesis is the one-step reaction, simplifying the process for rapid preparation in an array. By using a commercial liquid handling system this method can easily be adapted for high throughput synthesis where many precursor solutions can be rapidly prepared of different compositions. This differs from the electro-deposition and PVD methods as discrete samples of each material rather than graded compositional ranges are prepared as shown in Figure 1-17.

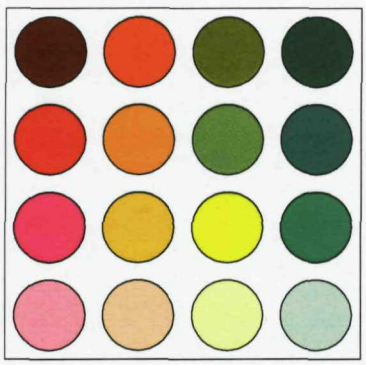

Figure 1-17 Schematic of an array of 16 discrete sol-gel samples.

Below in Table 1-6 a summary of the work done using this method, which has been extensively employed in Southampton and is discussed in further detail in 1.4.3.

Table 1-6 Publications investigating battery materials using Sol Gel Synthesis

Reference	Year of Publication	Title	Brief Description of Results
(146)	2002	Application of combinatorial process to $LiCo_{1-X}Mn_XO_2$ (0 <= X <= 0.2) powder synthesis	A structural study
(120)	2004	Combinatorial electrode array for high-throughput evaluation of electrode materials	Validation of the method
(121)	2005	High-throughput Discovery of Battery Materials	Results for $LiCo_{1-x-y}Ni_xFe_yPO_4$ are presented
(5)	2007	High Throughput Screening of the Effect of Carbon Coating in $LiFePO_4$ Electrodes	Data optimising the preparation of $LiFePO_4$ was obtained.

Paste Deposition (Ink Preparation)

Paste deposition is a technique where the active material is suspended in an ink containing binder; this can then be mixed in different ratios with an ink of acetylene black(AB), this will be discussed in more details in 1.4.3.1 along with other details of high-throughput techniques developed in Southampton(4). Another paste deposition method used was that of Chen *et al.*(26) who used bar coating technique to prepare a thickness gradient across a substrate. This was done by tilting the notch bar spreader so that the gap between substrate and bar was thicker at one end than the other. When the bar was then used to spread a slurry across the substrate the film coated was thicker on one side than the other.

1.4.3 Southampton Combi Battery Research the Early Years

Combinatorial battery research was started in Southampton in 2001 with the PhD of Alan Spong(3-5). During the first four years of this work the infrastructure was developed which allowed for the construction of the high-throughput cell and parallel electrochemical characterisation of battery electrodes. This section will review the methods of electrode fabrication and testing employed in these early years and discuss some results which highlight some of the areas that needed improvement.

1.4.3.1 Electrode Fabrication

Initial work employed two approaches; the first involves mixing inks and is known as the Paste Deposition method(3, 4, 121) the second is method for fabricating thin films of active material on the surface of an current collector via a sol gel synthesis described as direct in situ calcinations (DISC).

Paste Deposition (PD)

This technique was developed such that an active material was suspended in an ink containing binder; this was then mixed in different ratios with an ink of acetylene black(AB) to study the effect of carbon loading on electrochemical activity of active materials. The technique was successfully used by Spong et. al.(4) to study the percolation of $LiMn_2O_4$ with AB. Figure 1-18 below shows how the method worked.

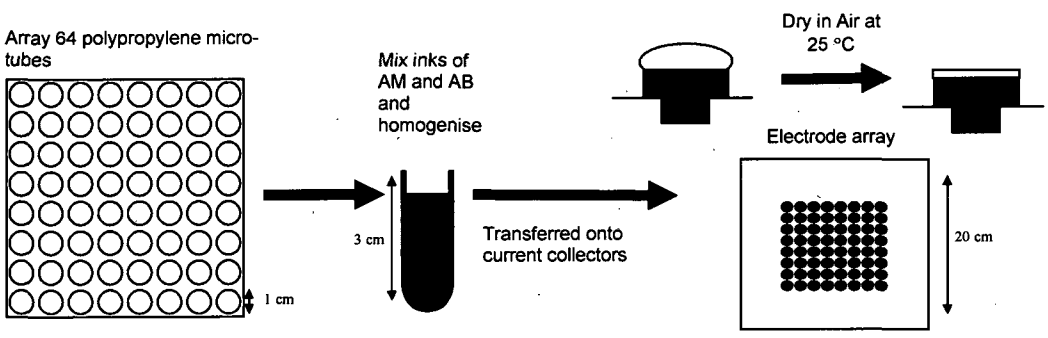

Figure 1-18 Schematic showing the paste deposition high-throughput technique.

Direct In Situ Calcination (DISC)

This method works by rapidly preparing a large number of individual precursor solutions for sol-gel preparations in an array of polypropylene micro-tubes. Small aliquots (3 μL) of each solution are then deposited onto carbon current collectors and dried to form thick films before being calcined at high temperatures (typically greater than 700 °C) (3, 121). Provided the precursor solutions were sufficiently viscous, the thick films deposited on each array element generally transformed into conductive porous monoliths after pyrolysis. Gases evolved during the pyrolysis reaction left behind a contiguous network of voids that were filled by a liquid electrolyte during cell assembly, similar to the intentional voids in most composite battery electrode structures. Below in Figure 1-19 a schematic summarises this procedure.

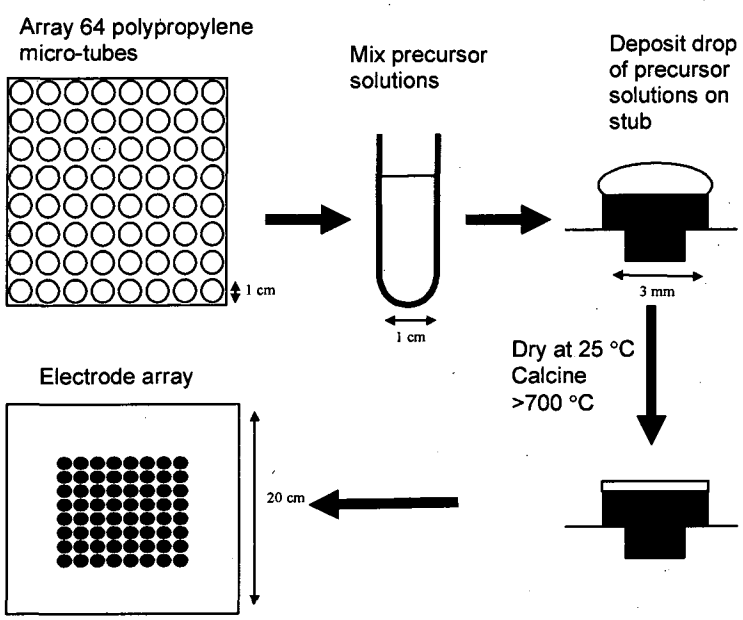

Figure 1-19 Schematic showing the DISC high-throughput technique.

1.4.3.2 Electrode testing

Once an array had been fabricated using either the PD or DISC method it was then taken forward for electrochemical characterisation using the parallel screening

equipment(4). This involved the construction of a cell which had 64 individual working electrodes and a single common counter electrode. The potential of the counter electrode was then controlled to perform cyclic voltammetry experiments such that the electrodes were charged and discharged. This was done using a commercial Variable Multichannel Potentiostat (VMP2, Princeton AppliedResearch; Biologic-Science Instruments). The current response of each working electrode was then monitored using an in-house constructed 64 channel current follower, details of which can be found in the literature(4). Below in Figure 1-20 photographs showing the electrode testing equipment are shown.

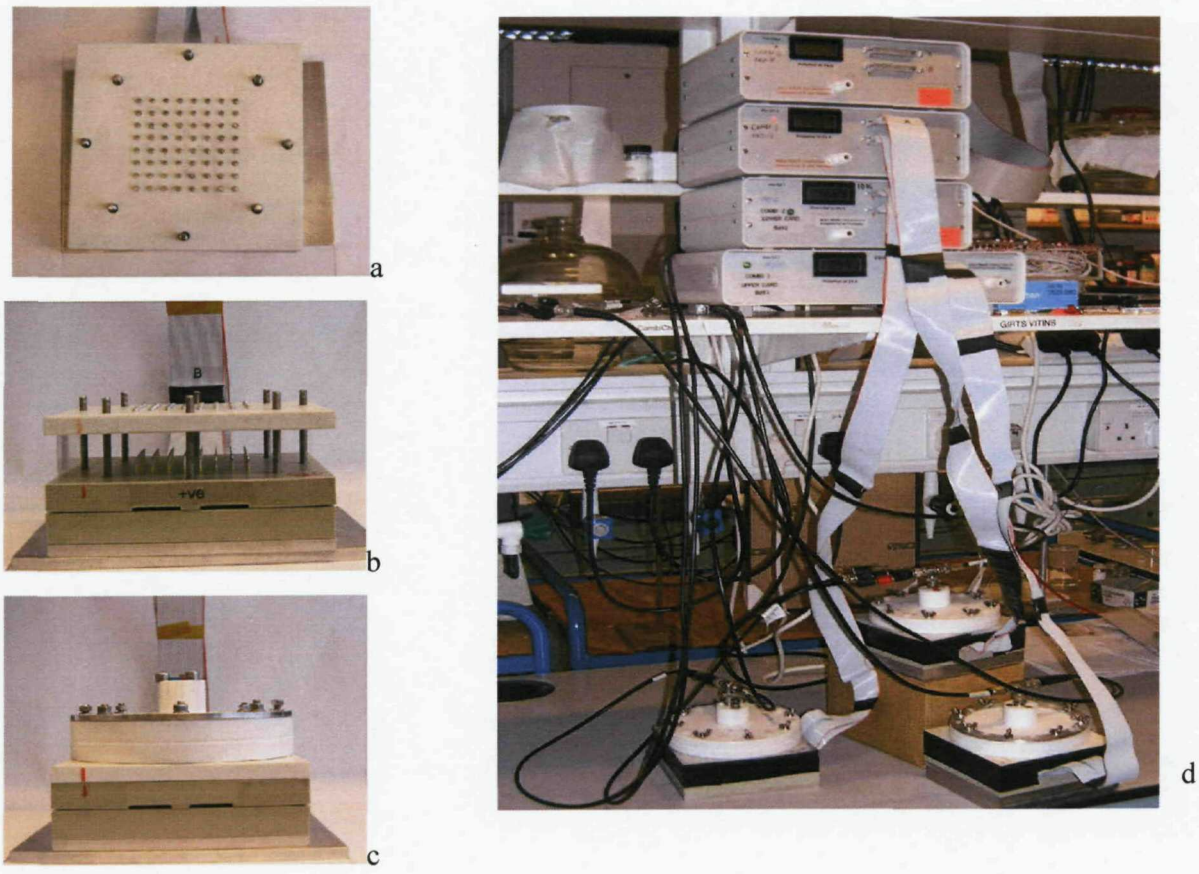

Figure 1-20 Photos showing the combinatorial setup: a) the combi array, b) the sprung connections to each electrode on a combi array, c) a closed combi cell and d) three combi cells connected to current follows recording 64 cyclic voltammograms.

1.4.3.3 A reproducibility study of the DISC method

Below in Figure 1-21 is a result of reproducibility study conducted using the DISC method(3, 5). In this study 32 identical electrodes of carbon coated $LiFePO_4$ were prepared using the DISC approach. These electrodes were the cycled between 2.5 and 4.5 V *vs.* Li and the specific capacity was calculated.

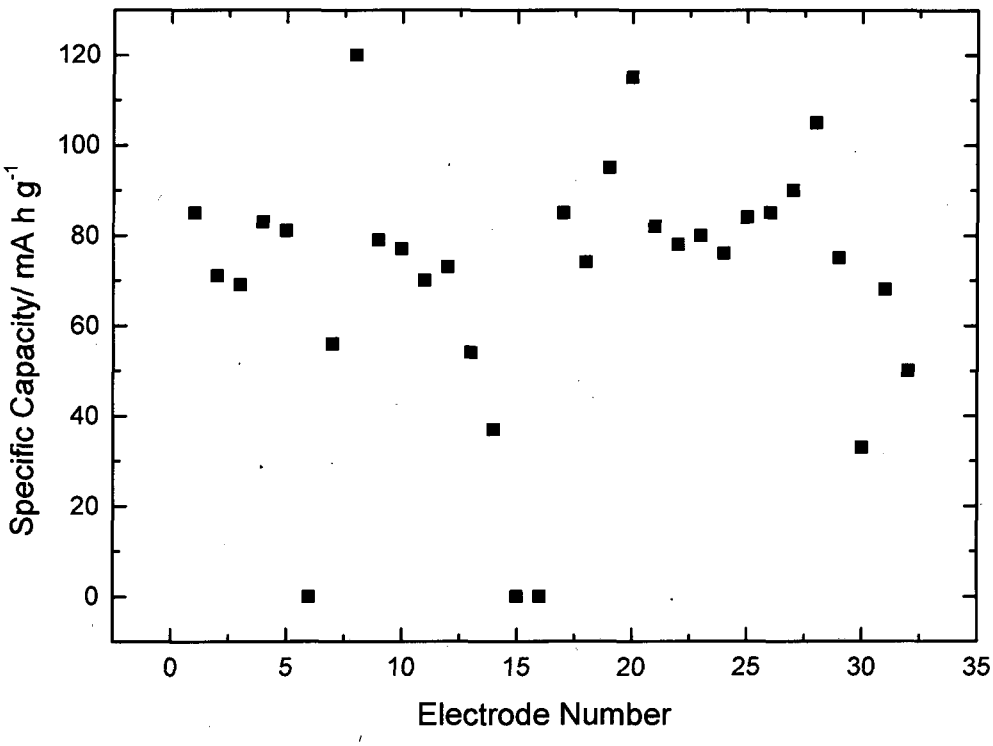

Figure 1-21 The scatter in specific capacity values for 64 identically prepared $LiFePO_4$ electrodes

The data in Figure 1-21 shows a specific capacity of around 77 mA h g^{-1} with a standard deviation of 28 mA h g^{-1} which reveals an error on the results of ±37 %.

The largest contribution to this error was identified as poor adhesion of the active material to the current collector substrate. During the calcination of the active materials there was often a large amount of gas evolution which resulted in the powder being knocked of the surface of the current collectors. A worst-case example

of this is depicted in Figure 1-22 on alumina tile. This effect led to poor knowledge of electrode weights and hence the large inaccuracies.

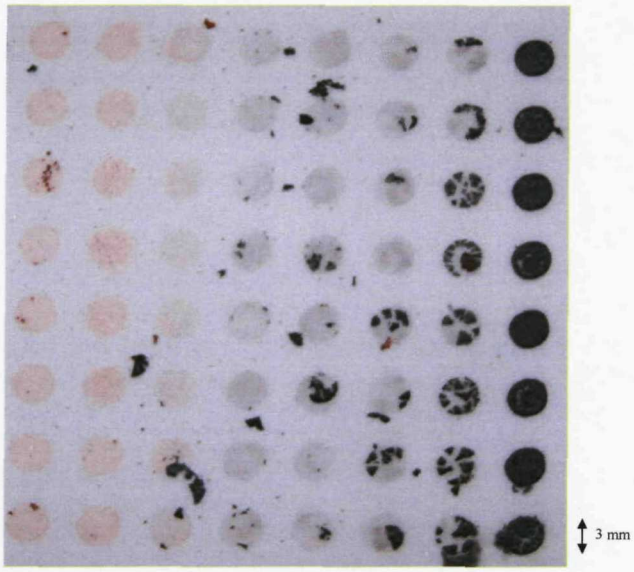

Figure 1-22 A piece of alumina tile with an array of active material samples deposited on it prepared via the DISC method.

A further effect that can be seen in Figure 1-22 is that the method produced large agglomerates of particles which were then tested rather than the thin films intended. These conditions are far from optimal for battery testing where materials are normally ground to a fine powder with the addition of AB and binder. All of the above were identified as sources of the large errors noted in Figure 1-21.

1.4.3.4 Identification of the Challenges Ahead

The current technique outlined here suffers from some key problems. The first is that there are large levels of scatter in the results reducing the possibility of detailed analysis. The second is that the quality of the obtained CVs is only sufficient to be considered a very general screening technique, and detailed analysis of the CVs can not be performed. The third is a lack of structural characterisation of the material formed during electrode preparation so that there is little confidence in any obtained results. The fourth is that only one cycle can be made using this technique, when

cyclability is one of the most important figures merit when analysing new battery materials. Much of the work in this report is involved in addressing these problems.

1.5 Chapter 1 References

1. B. V. Scrosati, C.A., *Modern Batteries: An Introduction to Electrochemical Power Sources*, p. 14, Arnold, London (1997).
2. S. Hadlington, Battery Assault, in *Chemistry World*, p. 58 (2007).
3. A. D. Spong, High-Throughput Discovery of Lithium Battery Materials, in, University of Southampton, Southampton (2005).
4. A. D. Spong, G. Vitins, S. Guerin, B. E. Hayden, A. E. Russell and J. R. Owen, *Journal of Power Sources*, **119**, 778 (2003).
5. M. R. Roberts, A. D. Spong, G. Vitins and J. R. Owen, *Journal of The Electrochemical Society*, **154**, A921 (2007).
6. B. V. Scrosati, C.A., *Modern Batteries: An Introduction to Electrochemical Power Sources*, p. 200, Arnold, London (1997).
7. D. R. Linden, T., in *Handbook of Batteries: Third Edition*, p. 2.1, McGraw-Hill, New York (2002).
8. D. R. Linden, T., in *Handbook of Batteries: Third Edition*, p. 1.7, McGraw-Hill, New York (2002).
9. P. O. Atkins, T. Rourke, J. Weller, M. Armstrong, F. Overton,T, in, p. 614, Oxford University Press, Oxford (2006).
10. M. S. Whittingham, *Chemical Reviews*, **104**, 4271 (2004).
11. D. R. Linden, T., in *Handbook of Batteries: Third Edition*, p. 1.5, McGraw-Hill, New York (2002).
12. M. Winter and R. J. Brodd, *Chemical Reviews*, **104**, 4245 (2004).
13. D. R. Linden, T., in *Handbook of Batteries: Third Edition*, p. 1.9, McGraw-Hill, New York (2002).
14. J. R. Owen, *Chemical Society Reviews*, **26**, 259 (1997).
15. K. Mizushima, P. C. Jones, P. J. Wiseman and J. B. Goodenough, *Material Research Bulletin*, **15**, 783 (1980).
16. K. M. Shaju and P. G. Bruce, *Advanced Materials*, **18**, 2330 (2006).
17. S. H. Kawauchi, T. Kawase, T., *New Battery Technologies*, Matsushita Batterry Industrial Co., Ltd. (1994).
18. D. R. Linden, T., in *Handbook of Batteries: Third Edition*, p. 34.6, McGraw-Hill, New York (2002).
19. J. M. Tarascon and M. Armand, *Nature Materials*, **414**, 359 (2001).
20. E. Peled, *Journal of The Electrochemical Society*, **126**, 2047 (1979).
21. K. Xu, *Chemical Reviews*, **104**, 4303 (2004).
22. Y. Nishi, Azuma, H. , Omaru, A. , Non aqueous electrolyte cell, in, U. S. Patent Editor (1990).
23. D. R. Linden, T., in *Handbook of Batteries: Third Edition*, p. 34.8, McGraw-Hill, New York (2002).
24. S. Bourderau, T. Brousse and D. M. Schleich, *Journal of Power Sources*, **82**, 233 (1999).
25. A. N. Dey, *Journal of The Electrochemical Society*, **118**, 1547 (1971).

26. Z. Chen, V. Chevrier, L. Christensen and J. R. Dahn, *Electrochemical and Solid-State Letters*, **7**, A310 (2004).
27. A. R. Armstrong, G. Armstrong, J. Canales, R. Garcia and P. G. Bruce, *Advanced Materials*, **17**, 862 (2005).
28. J. A. Goodenough, H. Buchanan, M., Report of the Basic Energy Sciences Workshop for Electrical Energy Storage, in, J. A. Goodenough, H. Buchanan, M. Editor (2007).
29. S. Seki, Y. Kobayashi, H. Miyashiro, Y. Ohno, A. Usami, Y. Mita, N. Kihira, M. Watanabe and N. Terada, *Journal of The Electrochemical Society*, **110**, 10228 (2006).
30. D. R. Vissers, Z. Tomczuk and R. K. Steunenberg, *Journal of The Electrochemical Society*, **121**, 665 (1974).
31. T. D. Kaun and P. Nelson, *Electrochimica Acta*, **38**, 1269 (1993).
32. M. S. Whittingham, F. R. Gamble, *Materials Research Bulletin*, **10**, 363 (1975).
33. M. S. Whittingham, *Science*, **192**, 1126 (1976).
34. M. S. Whittingham, *Journal of The Electrochemical Society*, **123**, 315 (1976).
35. J. Galy, *Journal of Solid State Chemistry*, **100**, 229 (1992).
36. K. Ozawa, *Solid State Ionics*, **69**, 212 (1994).
37. M. M. Thackeray, W. I. F. David, P. G. Bruce and J. B. Goodenough, *Materials Research Bulletin*, **18**, 461 (1983).
38. A. K. Padhi, K. S. Nanjundaswamy and J. B. Goodenough, *Journal of the Electrochemical Society*, **144**, 1188 (1997).
39. A. K. Padhi, K. S. Nanjundaswamy, C. Masquelier, S. Okada and J. B. Goodenough, *Journal of the Electrochemical Society*, **144**, 1609 (1997).
40. M. Armand, M. Gauthier, J.-F. Magnan and N. Ravet, Method for synthesis of carbon-coated redox materials with controlled size, in (2004).
41. T. Ohzuku, M. Ariyoshi, Y. Makimura, N. Yabuuchi and K. Sawai, *Electrochemistry*, **73**, 2 (2005).
42. G. G. Amatucci, J. M. Tarascon and L. C. Klein, *Journal of The Electrochemical Society*, **143**, 1114 (1996).
43. J. Cho and G. Kim, *Electrochemical and Solid-State Letters*, **2**, 253 (1999).
44. J. Cho, C.-S. Kim and S.-I. Yoo, *Electrochemical and Solid-State Letters*, **3**, 362 (2000).
45. T. Ohzuku and Y. Makimura, *Chemistry Letters*, 744 (2001).
46. N. Yabuuchi and T. Ohzuku, *Journal of Power Sources*, **119**, 171 (2003).
47. K. M. Shaju and P. G. Bruce, *Advanced Materials*, **18**, 2330 (2006).
48. K. M. Shaju, G. V. S. Rao and B. V. R. Chowdari, *Electrochimica Acta*, **48**, 145 (2002).
49. X. F. Luo, X. Y. Wang, L. Liao, X. M. Wang, S. Gamboa and P. J. Sebastian, *Journal of Power Sources*, **161**, 601 (2006).
50. L. Q. Zhang, X. Q. Wang, T. Muta, D. C. Li, H. Noguchi, M. Yoshio, R. Z. Ma, K. Takada and T. Sasaki, *Journal of Power Sources*, **162**, 629 (2006).
51. Y. Kim, H. S. Kim and S. W. Martin, *Electrochimica Acta*, **52**, 1316 (2006).
52. Y. K. Sun, S. W. Cho, S. W. Lee, C. S. Yoon and K. Amine, *Journal of the Electrochemical Society*, **154**, A168 (2007).
53. H. S. Shin, D. Shin and Y. K. Sun, *Electrochimica Acta*, **52**, 1477 (2006).
54. S. Y. Ye, Y. Y. Xia, P. W. Zhang and Z. Y. Qiao, *Journal of Solid State Electrochemistry*, **11**, 805 (2007).

55. M. M. Thackeray, S. H. Kang, C. S. Johnson, J. T. Vaughey, R. Benedek and S. A. Hackney, *Journal of Materials Chemistry*, **17**, 3112 (2007).
56. Y. Koyama, Y. Makimura, I. Tanaka, H. Adachi and T. Ohzuku, *Journal of the Electrochemical Society*, **151**, A1499 (2004).
57. A. R. West, *Solid State Chemistry and its Application*, John Wiley & Sons Ltd. (1984).
58. M. M. Thackeray, A. Dekock, M. H. Rossouw, D. Liles, R. Bittihn and D. Hoge, *Journal of the Electrochemical Society*, **139**, 363 (1992).
59. G. G. Amatucci, N. Pereira, T. Zheng and J. M. Tarascon, *Journal of the Electrochemical Society*, **148**, A171 (2001).
60. M. M. Thackeray, *Progress in Solid State Chemistry*, **25**, 1 (1997).
61. G. G. Amatucci, C. N. Schmutz, A. Blyr, C. Sigala, A. S. Gozdz, D. Larcher and J. M. Tarascon, *Journal of Power Sources*, **69**, 11 (1997).
62. D. T. Shieh, P. H. Hsieh and M. H. Yang, *Journal of Power Sources*, **174**, 663 (2007).
63. B. T. Yu, W. H. Qiu, F. S. Li and L. Cheng, *Journal of Power Sources*, **166**, 499 (2007).
64. S. Y. Chung, J. T. Bloking and Y. M. Chiang, *Nature Materials*, **1**, 123 (2002).
65. C. Delacourt, L. Laffont, R. Bouchet, C. Wurm, J. B. Leriche, M. Morcrette, J. M. Tarascon and C. Masquelier, *Journal of The Electrochemical Society*, **152**, A913 (2005).
66. H. Tukamoto and A. R. West, *Journal of the Electrochemical Society*, **144**, 3164 (1997).
67. P. B. Dean, N.F., *Proceedings of the Cambridge Philosophical Society*, **63**, 477 (1967).
68. A. D. Spong, G. Vitins and J. R. Owen, *Journal of the Electrochemical Society*, **152**, A2376 (2005).
69. R. Dominko, M. Bele, M. Gaberscek, M. Remskar, D. Hanzel, S. Pejovnik and J. Jamnik, *Journal of the Electrochemical Society*, **152**, A607 (2005).
70. R. Dominko, J. M. Goupil, M. Bele, M. Gaberscek, M. Remskar, D. Hanzel and J. Jamnik, *Journal of the Electrochemical Society*, **152**, A858 (2005).
71. J. D. Wilcox, M. M. Doeff, M. Marcinek and R. Kostecki, *Journal of The Electrochemical Society*, **154**, A389 (2007).
72. N. Ravet, A. Abouimrane, M. Armand, S. Y. Chung, J. T. Bloking and Y. M. Chiang, *Nature Materials*, **2**, 702 (2003).
73. S. T. Yang, Y. X. Liu, Y. H. Yin, H. Wang and C. W. Cui, *Journal of Inorganic Materials*, **22**, 627 (2007).
74. H. Liu, Q. Cao, L. J. Fu, C. Li, Y. P. Wu and H. Q. Wu, *Electrochemistry Communications*, **8**, 1553 (2006).
75. L. Shaohua, T. Zilong, L. Junbiao and Z. Zhongtai, *Rare Metal Materials and Engineering*, **36**, 1366 (2007).
76. G. Wang, Y. Cheng, M. M. Yan and Z. Y. Jiang, *Journal of Solid State Electrochemistry*, **11**, 457 (2007).
77. J. Barker, M. Y. Saidi and J. L. Swoyer, *Electrochemical and Solid-State Letters*, **6**, A53 (2003).
78. J. Hong, C. Wang and U. Kasavajjula, *Journal of Power Sources*, **162**, 1289 (2006).
79. T. H. Teng, M. R. Yang, S. H. Wu and Y. P. Chiang, *Solid State Communications*, **142**, 389 (2007).

80. G. X. Wang, S. Bewlay, J. Yao, J. H. Ahn, S. X. Dou and H. K. Liu, *Electrochemical and Solid-State Letters*, **7**, A503 (2004).
81. C. Wang and J. Hong, *Electrochemical and Solid-State Letters*, **10**, A65 (2007).
82. G. X. Wang, S. Bewlay, S. A. Needham, H. K. Liu, R. S. Liu, V. A. Drozd, J. F. Lee and J. M. Chen, *Journal of The Electrochemical Society*, **153**, A25 (2006).
83. J. F. Ni, H. H. Zhou, J. T. Chen and X. X. Zhang, *Materials Letters*, **59**, 2361 (2005).
84. G. X. Wang, S. L. Bewlay, K. Konstantinov, H. K. Liu, S. X. Dou and J. H. Ahn, *Electrochimica Acta*, **50**, 443 (2004).
85. F. Zhou, M. Cococcioni, K. Kang and G. Ceder, *Electrochemistry Communications*, **6**, 1144 (2004).
86. K. Amine, H. Yasuda and M. Yamachi, *Electrochemical and Solid State Letters*, **3**, 178 (2000).
87. N. H. Kwon, T. Drezen, I. Exnar, I. Teerlinck, M. Isono and M. Graetzel, *Electrochemical and Solid State Letters*, **9**, A277 (2006).
88. H. S. Fang, L. P. Li and G. S. Li, *Chemistry Letters*, **36**, 436 (2007).
89. J. Yao, S. Bewlay, K. Konstantionv, V. A. Drozd, R. S. Liu, X. L. Wang, H. K. Liu and G. X. Wang, *Journal of Alloys and Compounds*, **425**, 362 (2006).
90. A. Yamada, Y. Kudo and K. Y. Liu, *Journal of the Electrochemical Society*, **148**, A747 (2001).
91. A. Yamada, Y. Kudo and K. Y. Liu, *Journal of the Electrochemical Society*, **148**, A1153 (2001).
92. A. Nyten, S. Kamali, L. Haggstrom, T. Gustafsson and J. O. Thomas, *Journal of Materials Chemistry*, **16**, 2266 (2006).
93. J. Barker, M. Y. Saidi and J. L. Swoyer, *Journal of the Electrochemical Society*, **150**, A1394 (2003).
94. H. M. Geysen, Meloen, R.H., Barteling, S.J.,, *Proceedings of the National Academy of Sciences of the United States of America-Biological Sciences*, **81**, 3998 (1984).
95. H. M. Geysen, Rodda, S.J., Mason, T.J., *Molecular Immunology*, **23**, 709 (1986).
96. R. A. Potyrailo and W. F. Maier, *Combinatorial and High-Throughput Discovery and Optimization of Catalysts and Materials*, p. , Taylor and Francis Group (2007).
97. A. Holzwarth, H. W. Schmidt and W. F. Maier, *Angewandte Chemie*, **37**, 2644 (1998).
98. A. C. Cooper, L. H. McAlexander, D. H. Lee, M. T. Torres and R. H. Crabtree, *Journal of the American Chemical Society*, **120**, 9971 (1998).
99. P. Strasser, Q. Fan, M. Devenney, W. H. Weinberg, P. Liu and J. K. Norskov, *Journal of Physical Chemistry*, **107**, 11013 (2003).
100. M. T. Reetz, M. H. Becker, K. M. Kuhling and A. Holzwarth, *Angewandte Chemie*, **37**, 2647 (1998).
101. E. Reddington, *Science*, **280**, 1735 (1998).
102. S. Brocchini, K. James, V. Tangpasuthadol and J. Kohn, *Journal of the American Chemical Society*, **119**, 4553 (1997).
103. R. Lai, B. S. Kang and G. R. Gavalas, *Angew Chem Int Ed Engl*, **40**, 408 (2001).

104. E. Danielson, M. Devenney, D. M. Giaquinta, J. H. Golden, R. C. Haushalter, E. W. McFarland, D. M. Poojary, C. M. Reaves, W. H. Weinberg and X. D. Wu, *Science*, **279**, 837 (1998).
105. G. Briceno, H. Chang, X. Sun, P. G. Schultz and X. D. Xiang, *Science*, **270**, 273 (1995).
106. A. G. Ramirez and R. Saha, *Applied Physics Letters*, **85**, 5215 (2004).
107. B. Chisholm, R. Potyrailo, J. Cawse, R. Shaffer, M. Brennan, C. Molaison, D. Whisenhunt, B. Flanagan, D. Olson, J. Akhave, D. Saunders, A. Mehrabi and M. Licon, *Progress in Organic Coatings*, **45**, 313 (2002).
108. R. Z. Jiang, C. Rong and D. Chu, *Journal of Combinatorial Chemistry*, **7**, 272 (2005).
109. H. Hansel, H. Zettl, G. Krausch, C. Schmitz, R. Kisselev, M. Thelakkat and H. W. Schmidt, *Applied Physics Letters*, **81**, 2106 (2002).
110. D. W. S. Wong and G. H. Robertson, in *Chemicals Via Higher Plant Bioengineering*, p. 91 (1999).
111. H. Chang, C. Gao, I. Takeuchi, Y. Yoo, J. Wang, P. G. Schultz, X. D. Xiang, R. P. Sharma, M. Downes and T. Venkatesan, *Applied Physics Letters*, **72**, 2185 (1998).
112. J. C. Zhao, *Advanced Engineering Materials*, **3**, 143 (2001).
113. C. H. Olk, *Measurement Science & Technology*, **16**, 14 (2005).
114. E. Lindner, Z. L. Lu, H. A. Mayer, B. Speiser, C. Tittel and I. Warad, *Electrochemistry Communications*, **7**, 1013 (2005).
115. W. Markle, B. Speiser, C. Tittel and M. Vollmer, *Electrochimica Acta*, **50**, 2753 (2005).
116. J. R. Dahn, S. Trussler, T. D. Hatchard, A. Bonakdarpour, J. R. Mueller-Neuhaus, K. C. Hewitt and M. Fleischauer, *Chemistry of materials*, **14**, 3519 (2002).
117. L. Y. Beaulieu, K. C. Hewitt, R. L. Turner, A. Bonakdarpour, A. A. Abdo, L. Christensen, K. W. Eberman, L. J. Krause and J. R. Dahn, *Journal of the Electrochemical Society*, **150**, A149 (2002).
118. S. Guerin, B. E. Hayden, C. E. Lee, C. Mormiche, J. R. Owen, A. E. Russell, B. Theobald and D. Thompsett, *Journal of Combinatorial Chemistry*, **6**, 149 (2004).
119. V. K. Cumyn, M. D. Fleischauer, T. D. Hatchard and J. R. Dahn, *Electrochemical and Solid-State Letters*, **6**, E15 (2003).
120. K. Takada, K. Fujimoto, T. Sasaki and M. Watanabe, *Applied Surface Science*, **223**, 210 (2004).
121. R. A. Potyrailo and W. F. Maier, in *Critical Reviews in Combinatorial Chemistry*, R. A. Potyrailo and W. F. Maier Editors, p. 279, Taylor and Francis Group (2007).
122. S. Guerin, B. E. Hayden, D. Pletcher, M. E. Rendall and J. P. Suchsland, *Journal of Combinatorial Chemistry*, **8**, 679 (2006).
123. T. D. Hatchard, J. M. Topple, M. D. Fleischauer and J. R. Dahn, *Journal of The Electrochemical Society*, **6**, A129 (2003).
124. V. Chevrier and J. R. Dahn, *Measurement Science and Technology*, **17**, 1399 (2006).
125. T. D. Hatchard, M. N. Obrovac and J. R. Dahn, *Journal of The Electrochemical Society*, **152**, A2335 (2005).
126. A. Bonakdarpour, K. C. Hewitt, T. D. Hatchard, M. D. Fleischauer and J. R. Dahn, *Thin Solid Films*, **440**, 11 (2003).
127. J. F. Whitacre, W. C. West and B. V. Ratnakumar, *Journal of The Electrochemical Society*, **150**, A1676 (2003).

128. M. D. Fleischauer and J. R. Dahn, *Journal of The Electrochemical Society*, **151**, A1216 (2004).
129. T. D. Hatchard and J. R. Dahn, *Journal of The Electrochemical Society*, **151**, A1628 (2004).
130. T. D. Hatchard and J. R. Dahn, *Journal of The Electrochemical Society*, **152**, A1445 (2005).
131. J. R. Dahn, R. E. Mar and A. Abouzeid, *Journal of The Electrochemical Society*, **153**, A361 (2006).
132. M. D. Fleischauer, M. N. Obrovac, J. D. McGraw, R. A. Dunlap, J. M. Topple and J. R. Dahn, *Journal of The Electrochemical Society*, **153**, A484 (2006).
133. J. R. Dahn, R. E. Mar, M. D. Fleischauer and M. N. Obrovac, *Journal of The Electrochemical Society*, **153**, A1211 (2006).
134. M. D. Fleischauer, M. N. Obrovac and J. R. Dahn, *Journal of The Electrochemical Society*, **153**, A1201 (2006).
135. A. D. W. Todd, R. E. Mar and J. R. Dahn, *Journal of The Electrochemical Society*, **153**, A1998 (2006).
136. M. D. Fleischauer, R. Mar and J. R. Dahn, *Journal of The Electrochemical Society*, **154**, A151 (2007).
137. A. D. W. Todd, R. E. Mar and J. R. Dahn, *Journal of The Electrochemical Society*, **154**, A597 (2007).
138. A. Timmons, A. D. W. Todd, S. D. Mead, G. H. Carey, R. J. Sanderson, R. E. Mar and J. R. Dahn, *Journal of The Electrochemical Society*, **154**, A865 (2007).
139. J. Dahn and R. Mar, Combinatorial Study of LiF:Ni Nanocomposites for Positive Electrode Materials in Li-Ion Batteries, in *ECS Meeting Abstracts*, p. 339, ECS (2006).
140. J. R. Dahn, in *58th Annual Meeting of the International Society of Electrochemistry*, Banff (2007).
141. S. D. Beattie and J. R. Dahn, *Journal of the Electrochemical Society*, **152**, C549 (2005).
142. S. D. Beattie and J. R. Dahn, *Journal of the Electrochemical Society*, **150**, C457 (2003).
143. S. D. Beattie and J. R. Dahn, *Journal of the Electrochemical Society*, **150**, C802 (2003).
144. M. Devenney, S. W. Donne and S. Gorer, *Journal of Applied Electrochemistry*, **34**, 643 (2004).
145. S. D. Beattie and J. R. Dahn, *Journal of the Electrochemical Society*, **152**, C542 (2005).
146. I. Yanase, T. Ohtaki and M. Watanabe, *Solid State Ionics*, **151**, 189 (2002).

Chapter 2 Experimental Techniques and Theoretical background

2.1 Chemicals

The chemicals used for active material preparations were all obtained from Aldrich unless otherwise stated in the experimental details and of greater than 98 % purity. All solutions were prepared volumetrically. The reaction gases used for synthesis were of high purity and obtained from BOC. The electrolyte solutions for high-throughput measurements were prepared volumetrically from battery grade $LiPF_6$ (≥99.99 %, Aldrich) and propylene carbonate (Aldich, ReagentPlus®, 99%), before use the solvents were dried by placing in sealed jar with molecular sieve for 5 days. Electrolyte solutions for small cell testing were comprised of $LiPF_6$ and ethylene carbonate/dimethyl carbonate (EC/DMC) (1 : 1vol)(Merk, Battery Grade).

2.2 Material Synthesis

2.2.1 Solid State Preparation

The method of solid state preparation is well used in inorganic chemistry(1). The precursor materials are ground using a pestle and mortar to a homogeneous mixture (Figure 2-1), before being heated to temperatures normally exceeding 500 °C. The resultant powder is then sometimes re-ground and re-heated to ensure a homogeneous product. The reactions proceed slowly as the diffusion coefficient of the ions are small; this means that good mixing and high temperatures are required to make sure pure products are obtained.

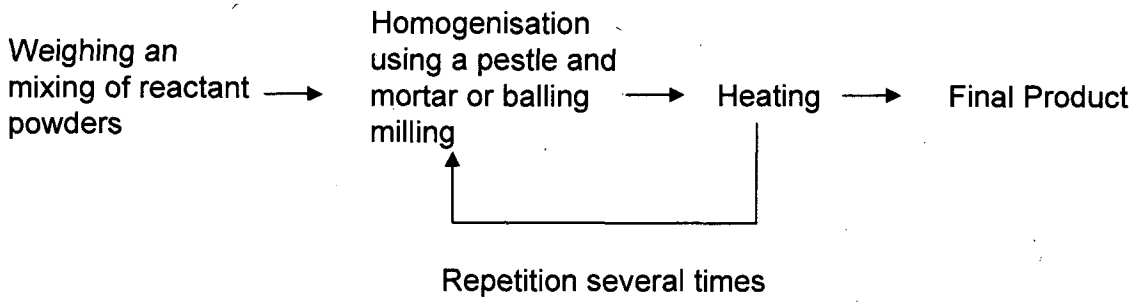

Figure 2-1 The solid state synthesis method.

2.2.2 Sol-Gel

The Sol- Gel method has been employed to prepare inorganic materials, glasses and ceramics(1, 2). This method typically involves mixing solutions containing metal ions with the addition of a chelating agent, a hydrolysis reaction then follows to form a gel containing intimately mixed ions. This is then followed by calcinations to form the final product. A scheme for this is shown in Figure 2-2.

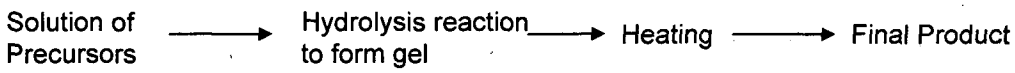

Figure 2-2 The sol-gel method.

The chelating agent is a ligand which forms a bond with the reactant ions, binding materials in a well mixed matrix. During heat treatment the ligand molecule is typically decomposed to a gas leaving a matrix of well mixed ions which then rearrange to form the inorganic target structure. However, as the mixing is on the atomic level the diffusion distances required for reactions to occur are much smaller and therefore the reactions occur much faster. Normally this negates the need for repeated regrinding and reheating of the reactants to form a pure product.

Within the work reported here a slight variation on the Sol-Gel method has been used to form $LiFePO_4$. Instead of the addition of a chelating agent, sucrose is added to a solution of precursors containing the relevant ions (LiAc, $Fe(NO_3)_3$, and H_3PO_4). On drying this

forms a homogeneous precursor which can be heat treated to form the $LiFePO_4$. The sucrose is believed to act in three ways; firstly, to suppress the crystallisation of the individual salts; secondly, to reduce the Fe^{3+} to Fe^{2+} and thirdly, to provide a carbon coating on the surface of the $LiFePO_4$(3). This method is particularly useful when applied to high-throughput studies as the solutions can be easily mixed using automated equipment and by addition of other ions interesting compositional studies can easily be undertaken.

2.2.3 Automated Mixing

An automated liquid handler was used to mix precursor solutions for sol-gel preparations in an array of micro-crucibles. In Figure 2-3 a photo of the automated liquid handler and an array of plastic micro-tubes used to contain the mixtures of precursors are shown. This automated liquid handler can be used to produce arrays much faster than by hand.

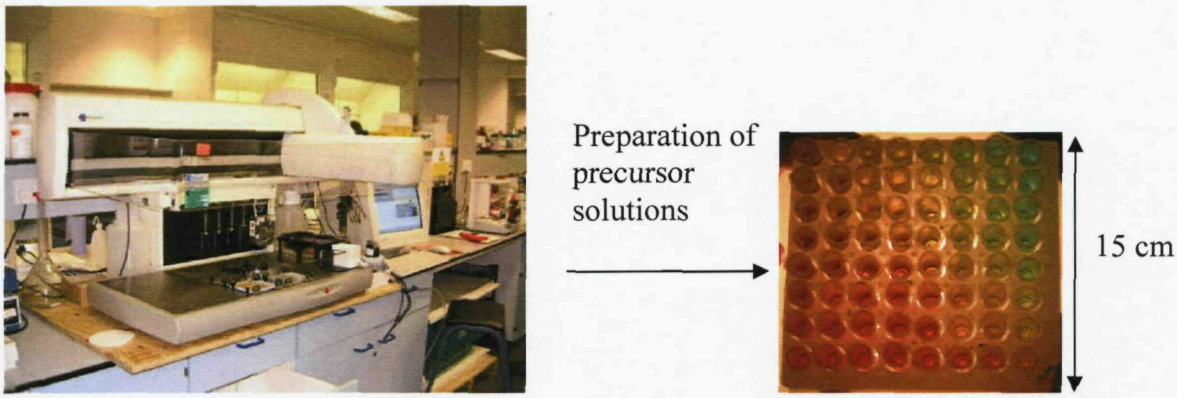

Figure 2-3 Photo of the automated liquid handler and an array of plastic microtubes used to contain the mixtures of precursors solution.

2.3 Electrode Fabrication

2.3.1 Ball Milling

Ball milling is a method used extensively in materials science to reduce particle size or homogenise several powders.(4) This has been used in battery science to prepare the active materials.(4) Ball milling works by placing a powder in a sealed container with small balls; vibration of this container then causes the balls to move, hitting each other and the sides of the container, this abrasive action acts to reduce the particle size of the active material. The milling time can affect the performance of the active materials as reported by Tarascon et al.(4)

2.3.2 PTFE Pellet Electrodes

This preparation is a dry method the solid active material is ground to a powder, mixed with acetylene black (Shawinigan Black, 100%-compressed, Chevron) and poly(tetrafluoroethylene) (AB, PTFE, Type: 6C-N, DuPont) and worked into a solid lump using a pestle and mortar. This solid piece of electrode is then rolled into a film using a rolling mill (Minimill, Durston), the resulting ~60 μm thick film is then cut into ∅ 1.13 cm with surface area of 1 cm^2 circles using a standard size cork borer. Each pellet is then weighed (~5-15 mg) and dried at 120°C under vacuum using a glass oven (Buchi).

2.3.3 PVdF-HFP ink preparation

When using this method an ink is formed from the active material and acetylene blank suspended in a solution of cyclopentanone (CP, Aldrich, 99+%) and PVdF-HFP (Aldrich) binder. This ink can then be coated on a substrate, once the CP has evaporated an electrode material is left. This can be done using a bar coating method, however, in the work presented here this method is typically used for the preparation of combinatorial electrodes and will be discussed in more detail later.

2.4 Electrochemical Testing

2.4.1 Electrochemical Techniques

Electrochemical techniques provide an extremely important method for the characterisation of battery materials. What follows is a description of some of the key methods used to study batteries in this thesis.

The basic setup used for all battery testing is shown below in Figure 2-4. The cathode or positive electrode material was always the material under study, and its performance was measured versus an anode made of lithium foil. The lithium has a stable potential even when the current is flowing and can therefore be used as a reference counter electrode. The electrolyte is typically a Li salt dissolved in an organic liquid.

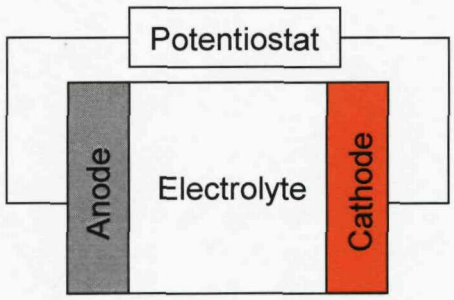

Figure 2-4 Generic setup of a battery electrochemical setup.

Cyclic Voltammetry

Cyclic voltammetry is a method by which we study oxidation and reduction processes which result from the flow of electrons. In the setup shown in Figure 2-4 the potential is controlled relative to the anode and swept between two voltage limits. At certain potentials oxidation and reduction processes will occur resulting in the flow of a current. The various parameters which can be controlled are the potential limits and the scan rate.

By changing the potential limits only the redox couples of interest may be viewed such that any undesirable side reactions may be removed.

In the introduction several figures of merit were introduced which can be used to characterise a materials performance; all these can be obtained via Cyclic voltammetry. The specific capacity can be calculated from the integral of the current versus time. By calculating the specific capacity from many cycles and different scan rates the cyclability and rate performance can also be respectively determined. The cyclic voltammogram (CV) also shows the potential of the redox reaction and hence we can calculate the reaction energy. We can also obtain a lot of information about the processes controlling the reaction from the shape of the CV, this will be discussed in much greater detail in later chapters.

Galvanostatic Cycling

Whilst cyclic voltammetry has been widely applied to the study of materials in this work, the battery industrial standard is galvanostatic cycling. The CV method was chosen because for high-throughput measurements as it is experimentally easier to control the potential of 64 electrodes in parallel while observing the current than the opposite. When a cell is charged and discharged under a galvanostatic regime a constant current is applied to the cell which results in the cell potential changing as the reduction or oxidation processes occur. When a specific potential limit is reached the flow of the current is inverted and the reverse reactions occur. By repeating this process cycling data is built up about the material. Control of the current magnitude will vary the charge and discharge time and give information about the rate capability of a material. This technique is only reported here if bulk sample testing is used once materials of interest have been identified.

AC impedance

AC impedance is the third electrochemical technique which has been used in this thesis. Its application was only used once and therefore will be reviewed only briefly. This

method involves the application of different frequencies of an alternating current or voltage and the measurement of the voltage or current response. This gives information about the resistance and capacitances within a system and allows an equivalent circuit model to be constructed. The application in this work is to the measurement of the electronic conductivity in inorganic materials.

2.5 Powder X-ray Diffraction

When an inorganic material is prepared x-ray diffraction is used to extract information about this structure, firstly to confirm sample purity but also the dimensions and other structural characteristics. When a beam of x-rays is directed at atoms or ions within a sample it will interact with electrons and causes scattering. In the ordered structure within inorganic materials the distances between the ions (a few Ångstroms) is comparable to wavelength of x-rays (for the K_α radiation of a copper target the wavelength is 1.54 Å). This means that when the x-rays interact with these ordered structures the scattering is not random but along specific diffraction angles which are a result of constructive and destructive interference.(1) This is depicted in Figure 2-5.

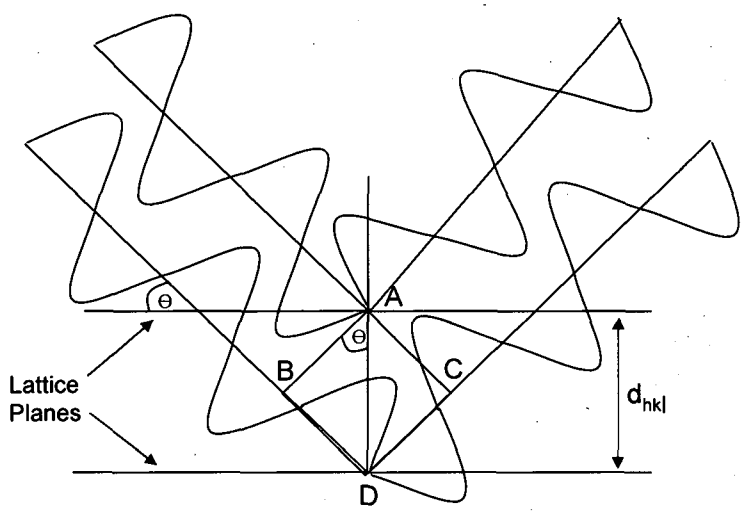

Figure 2-5 Derivation of Bragg's Law. Reproduced from reference(1).

Here the scattering of the beam at points A and D corresponds to constructive interference at that specific diffraction angle (θ). Constructive interference like this only happens when the distance travelled by the lower x ray beam is exactly a whole integer of wavelengths, indicated below in Equation 2-1.(1)

$$pathdifference = BD + DC = 2d_{hkl}.\sin\theta = n\lambda$$

Equation 2-1

λ = wavelength

n = positive integer (usually 1)

d_{hkl} = lattice spacing

θ = X-ray beam angle of incidence

This is known as the Bragg equation and provides a simple model for understanding the interaction of x-rays and electronic structure. The equation tells us that if a beam of x-rays (with a specific λ) hits a structure at a certain angle (θ) when the spacing between parallel atomic layers (d_{hkl}) is right constructive interference will occur and a diffraction maxima will be observed. As the angle then changes the interference between the x-rays will no longer be constructive and soon completely destructive inference will occur. This will result in peaks of maximum intensity at specific θ values corresponding to the various different d spacing's between parallel planes in the large crystal structure. When recording an XRD pattern a single wavelength of x-rays is used to sweep through a range of angles of incidence from θ_1 to θ_2. Structural information such as unit cell parameters and d spacing's can then be extracted by peak indexing discussed as an appendix or Retivield refinement both of which are used within this thesis. In the Retivield method a trial structure of the material under study is proposed, and the XRD pattern expected calculated.(1) The calculated XRD pattern is then compared to an experimentally recorded pattern. The parameters of the original proposed structure are then altered and the pattern is re-calculated and re-compared with the recorded pattern, this process is undertaken many times until a good fit between experimental and calculated patterns is

seen. The parameters of the structure used to form the best fit model are then taken as the correct values.

When characterising battery materials it is common to investigate the effect of substituting one ion for another for example in $LiFe_{1-x}Mn_xPO_4$. In materials where a solid solution (a single crystal structure exist for a certain range of ionic substitution) exists a change in the lattice parameters is often observed. If the change is a linear increase or decrease between the unit cell parameters of the solid solution end members this corresponds to a Vegard's shift.(5) By extracting the unit cell parameters using x-ray diffraction this effect can be studied.

2.6 Experimental Infrastructure

2.6.1 Test Cells

Small Cell Galvanostatic Cycling

Small cell testing was used to characterise single sample bulk preparations and was always used with galvanostatic cycling. The cell construction was built in house and is shown below in Figure 2-6. A cell is made by sandwiching a separator (diameter 1.2 cm, glass fibre filter paper *GF/F, Whatman*) with a small piece of lithium (1 cm) and the active material. This is then sealed using a metal base and lid which act as current collectors separated by a compressed viton ring. Springs and pistons are included in the design to ensure good contact between electrodes and electrolyte. This cell can then be connected to a potentiostat and tested using galvonstatic testing.

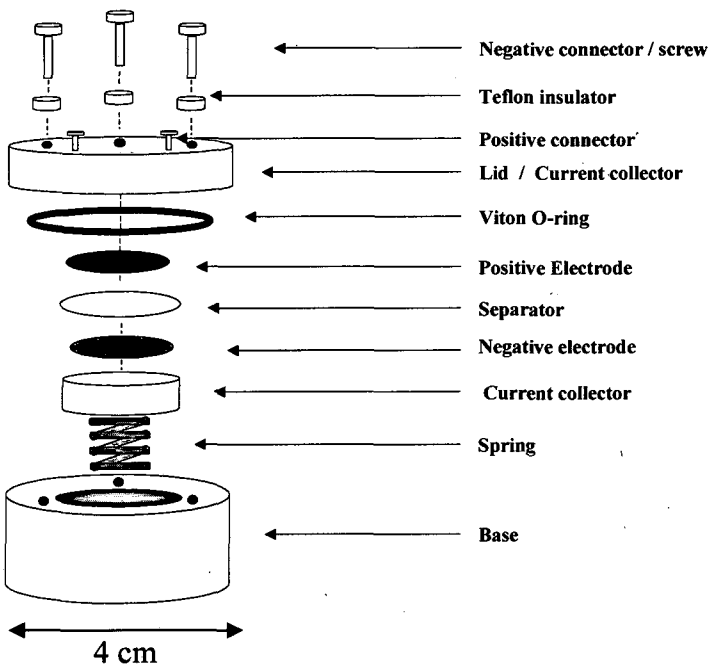

Figure 2-6 A schematic representation of a small cell for the electrochemical testing of battery materials. (6)

High-Throughput Cell Testing

The cell is constructed as shown in Figure 2-7. It is designed with a single piece of lithium metal as the negative electrode, this is separated from the 64 positive electrode materials by a piece of glass fiber filter paper soaked in electrolyte *(GF/F, Whatman)*. This construction means that the 64 positive electrodes share a common counter electrode. Each of the 64 positive electrodes is individually connected to the current follower using spring loaded contacts. The spring loaded contacts ensure that all the electrodes are level with the lithium. It can be difficult to close the cell as the electrodes are loose and liable to fall out and cause a short circuit, this problem has been solved by using a system of wedges and clamps.

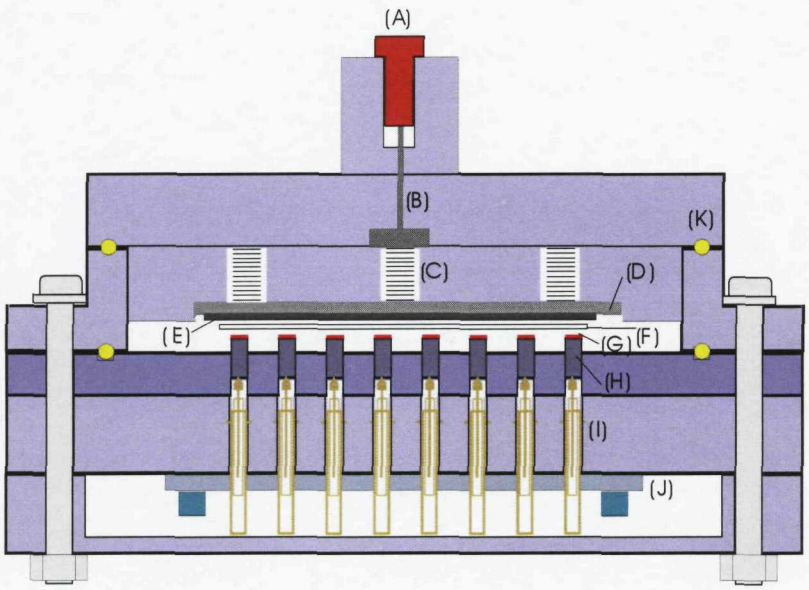

Figure 2-7 A schematic diagram showing the structure of a combinatorial cell. The label refers to the following: A. Negative electrode connector, B. Stainless steel contact, C. Spring contact, D. Stainless steel current collector, E. Lithium metal, F. Glass separator, G. Electrode material, H. Aluminium working electrode, I. spring contact and J. Printed circuit board.(7)

2.6.2 Instruments

Variable Multi-channel Potentiostat (VMP): This VMP (Princeton Applied Research; Biologic-Science Instruments) is a 16-channel potentiostat which can be used to apply most electrochemical techniques. Crucially for this work all channels can perform galvanostatic cycling, cyclic voltammetry and ac impedance. This instrument was used to investigate bulk materials using the small cell design and galvanostatic cycling. For high high-throughput measurements a single channel was used to control the potential of the counter electrode while the combinatorial current followers were used to measure the currents.

Combinatorial Current followers: The application of these instruments was discussed in the introduction. These instruments were built in house by Tom Young.

Furnace: The Furnace used for all preparations was a ∅ 9 cm tube furnace (Lenton). The atmosphere of this furnace could be controlled using a flow of gas through the tube. Typically preparations were conducted in argon, oxygen or air.

Glove Box: To construct batteries under inert conditions an argon-filled glove box was used (H2O,O2< 1 ppm; Unilab from MBraun).

Scanning Electron Microscopes: Depending on the resolution required two different instruments were used. Normally the Phillips XL-30E Environmental SEM microscope was used however, if higher magnifications were required the JSM 6500F thermal field emission scanning electron microscope was sometimes required.

Ball miller: A Retsch MM200 ball miller was used for milling samples. Any milling reported here was performed using stainless steel milling containers with 1 mm diameter stainless steel balls. IPA was added as a solvent when wet milling was performed.

Vibrating table: An IKA VIBRAX VXR BASIC vibrating table was used for agitation of solutions and ball milling of arrays.

Vortex mixer: A Fischer "Whirlimix" Vortex mixer was used to agitate the solutions to ensure homogeneity.

Bulk sample X-ray Diffractometer: The Siemens D5000 diffractometer was used for measurement of XRD patterns for phase identification and Rietveld refinements of bulk prepared samples. This uses a CuK(1 radiation x-ray source.

High-throughput XRD Equipment: To structurally characterize the samples prepared via high-throughput routes a different XRD instrument was used. The Bruker AXS C2 diffractometer is shown below in □ REF _Ref164765200 \h □ * MERGEFORMAT □Figure 2-8, this instrument has been specifically designed for this purpose.

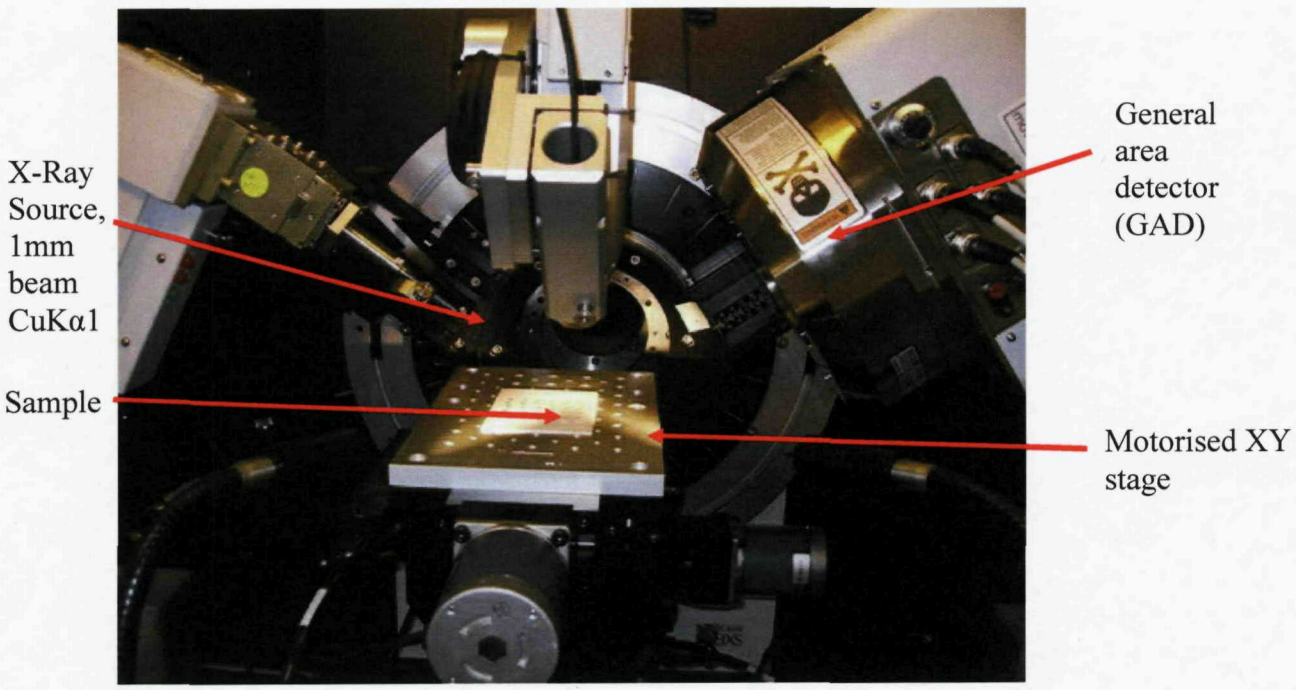

Figure 2-8 Bruker AXS C2 diffractometer.

This *Bruker AXS C2* measurement is fully automated, the operator simply places the array of high-throughput samples on a movable x, y, z stage. The sample locations are then imputed into the controlling software (GADDS) and then each sample is sequentially measured. To speed up measurements it also uses a general area detector to measure the diffracted x-rays. This works by recording the whole 2θ range of diffracted patterns simultaneously. In general an acquisition time of 20 minutes was used for each sample, so to record diffraction patterns for the whole array it took approximately 22 hours. This uses a $CuK_{\alpha 1}$ radiation x-ray source.

2.7 Chapter 2 References

1. Weller. M.T, *Inorganic Materials Chemistry*, Oxford University Press (1994).

2. P. O. Atkins, T. Rourke, J. Weller, M. Armstrong, F., in, p. 614, Oxford University Press, Oxford (2006).

3. A. D. Spong, G. Vitins and J. R. Owen, *Journal of the Electrochemical Society*, **152**, A2376 (2005).

4. J.-M. Tarascon, M. Morcrette, J. Saint, L. Aymard and R. Janot, *Comptes Rendus Chimie*, **8**, 17 (2005).

5. A. R. West, *Solid State Chemistry and its Application*, John Wiley & Sons Ltd. (1984).

6. T. Le Gall, K. H. Reiman, M. C. Grossel and J. R. Owen, *Journal of Power Sources*, **119**, 316 (2003).

7. A. D. Spong, G. Vitins, S. Guerin, B. E. Hayden, A. E. Russell and J. R. Owen, *J. Power Sources*, **119**, 778 (2003).

Chapter 3 Development and Validation

The DISC approach has demonstrated the concept of high-throughput cathode studies; however, the results show poor reproducibility. This chapter initially reports a quantitative study of the problems with DISC and PD methods and then introduces the second generation of high-throughput methods; Post Synthesis Array Transfer (PoSAT).

3.1 Assessing the State of DISC and PD

3.1.1 The Effect of Electrode Mass

To characterise electrode materials one of the key figures of merit used is specific capacity calculated using Equation 3-1. The accuracy of this measurement relies on accurate knowledge of the electrode mass.

$$Q_s = \frac{Q}{3.6 \times m}$$

Equation 3-1

Q_s =Specific Capacity/ mA h g^{-1}

Q = Charge/ coulombs

3.6 = conversion factor to translate coulombs into mA h

m = mass/g

In the DISC and PD work the mass of all the electrodes was assumed to be uniform. The effect of this assumption had been quantified previously by Spong(1) using an array of identical $LiMn_2O_4$ electrodes prepared via the PD method. This showed that there was a 15 % standard deviation on the specific capacities.

To reduce this scatter two methods are investigated; the first is to increase the electrode size thus reducing sampling errors by increasing the mass of the electrode, this assumes

the problem is a standard rather than a percentage error; a second approach is to weigh the electrodes.

3.1.1.1 Experimental Details

A new array was constructed where the electrode diameter was increased from 3 to 6 mm. A single ink containing 6 % solids was then prepared; the solid fraction containing 80 % $LiMn_2O_4$, 10 % AB and 10 % PVdF-HFP in CP. 14 μL of this ink (an increase from 4 μL used on the 3 mm stub) was deposited on to each electrode on the array, the volatile component was then removed at 80 °C for 12 h. The electrodes were then weighed using a computer monitored balance. The combinatorial test cell was constructed as described in Chapter 2 and the electrodes were cycled between 3.2 and 4.5 V at 0.05 mV s^{-1}.

3.1.1.2 Results and Discussion

The array of CVs in Figure 3-1 show extremely good reproducibility. The two peaks seen at around 4.1 V is characteristic of the $LiMn_2O_4$ behavior.(2, 3) The three channels with flat lines are due to a known wiring problem.

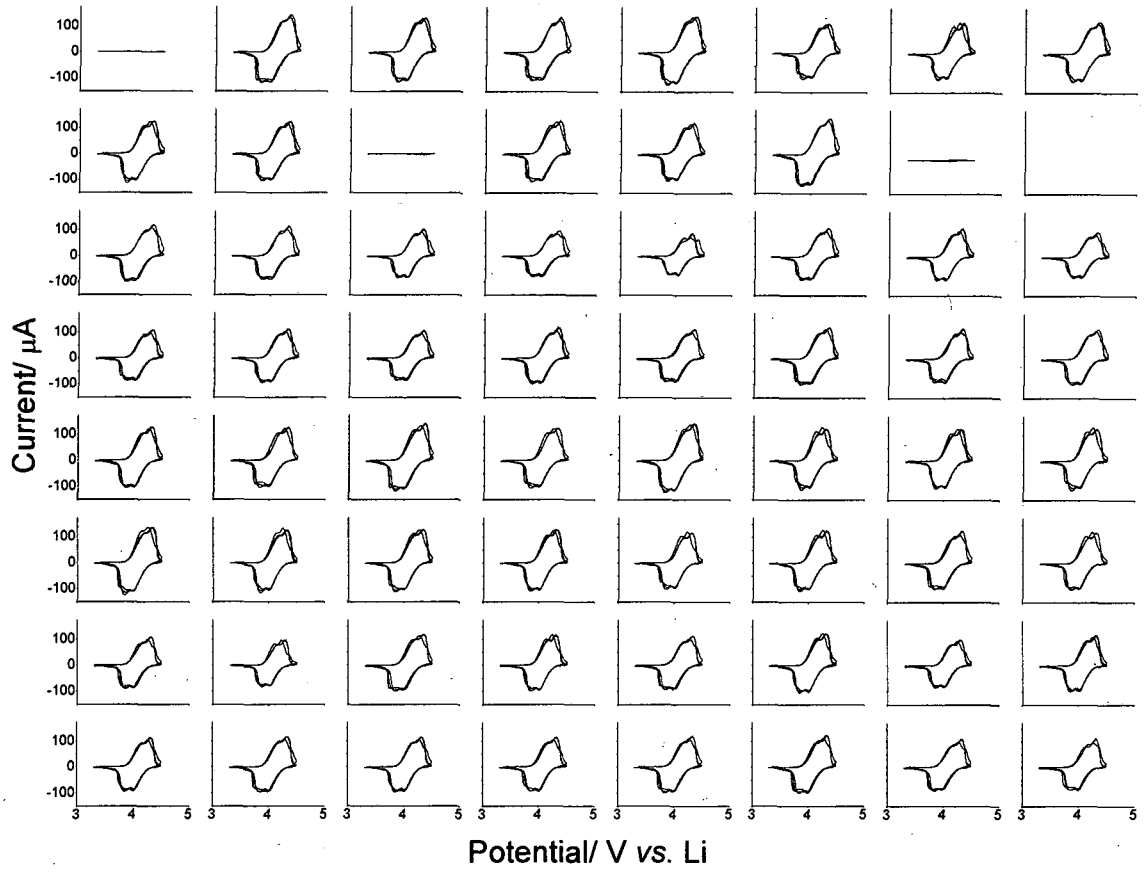

Figure 3-1 64 CVs for $LiMn_2O_4$ *vs.* Li metal. These were cycled between 3.3 and 4.5 V at a scan rate of 0.05 mV s^{-1}. Each electrode film contains 80 % active material 10 % acetylene black (AB) and 10 % PVdF HFP binder, the electrodes were prepared via the ink preparation method. 14 µL of ink was deposited on each electrode, this resulted in an approximate mass of 3 mg. The electrodes had a 6 mm diameter.

The specific capacity of each electrode was then calculated using both real and assumed weights (Figure 3-2). Shown for comparison is the scatter observed for a similar experiment except using 3 mm electrodes with assumed.(1)

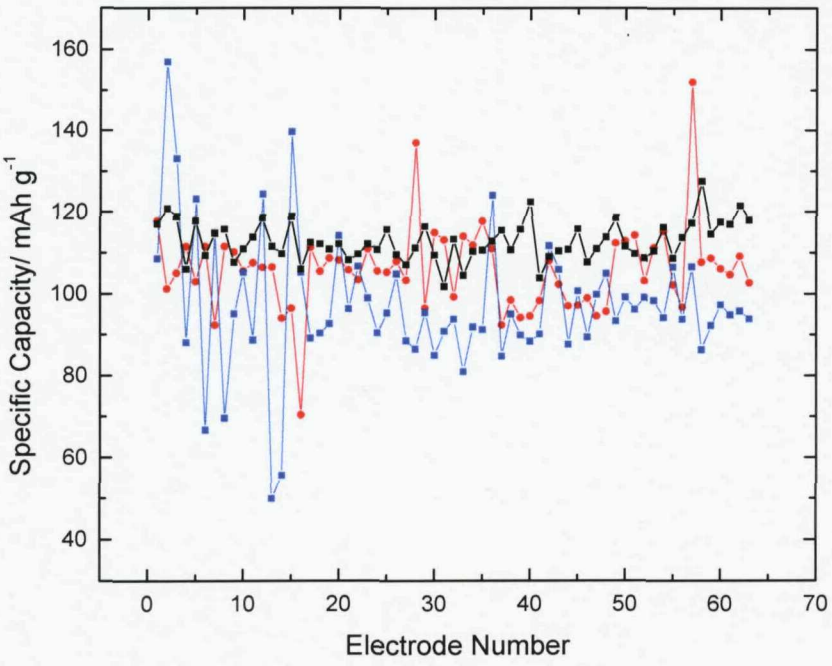

Figure 3-2 The specific capacity of the $LiMn_2O_4$ *vs.* the electrode number for the 64 electrodes on an array; these values are shown for 64 3 mm electrodes (—●—) capacity calculated with an approximate weight, 64 6 mm electrodes (— ■—) capacity calculated with an approximate weight and 64 6 mm electrodes (— ■—) capacity calculated with an accurate weight.

Statistical analysis was performed on the results shown in Figure 3-2 and is reported in Table 3-1. This indicates that the increased electrode size did not improve the scatter in the case where weight is assumed. However a ~3 fold reduction in scatter is seen when accurate weights are measured. The array which has provided the capacity closest to the conventional method is also the 6 mm weighed electrodes, indicating that the method is not only the most accurate but also the most precise. Whilst it may be possible to achieve similar accuracy with weighed 3 mm electrodes, practically the smaller masses would make measurement extremely difficult.

Table 3-1 Average capacity and standard deviation recorded using four different methods.

Method	Average Capacity/ mA h g^{-1}	Standard Deviation/ %
3 mm electrodes with assumed weight	105	12.5
6 mm electrodes with assumed weight	97	17.5
6 mm electrodes of known weight	112	4.5
Conventional small cell test method	118	1

3.1.2 The Reliability of the Automated Liquid Handler

The automated liquid handler (robot) was used extensively in the DISC and IM methods. As reported in the Spong thesis(1) it was not reliable when used with viscous inks, where it frequently delivered inaccurate volumes. The following experiment was designed to evaluate the errors on aqueous mixing.

3.1.2.1 Experimental Details

Using the robot (Perkin-Elmer Life Sciences) volumes of water (1, 0.5, 0.2, 0.1 0.05 0.02 0.01 and 0.005 mL) were deposited into an array of 64 weighed polypropylene vials. Each volume was repeated 8 times and the vials were then reweighed.

3.1.2.2 Results and Discussion

The results are shown below in Figure 3-3.

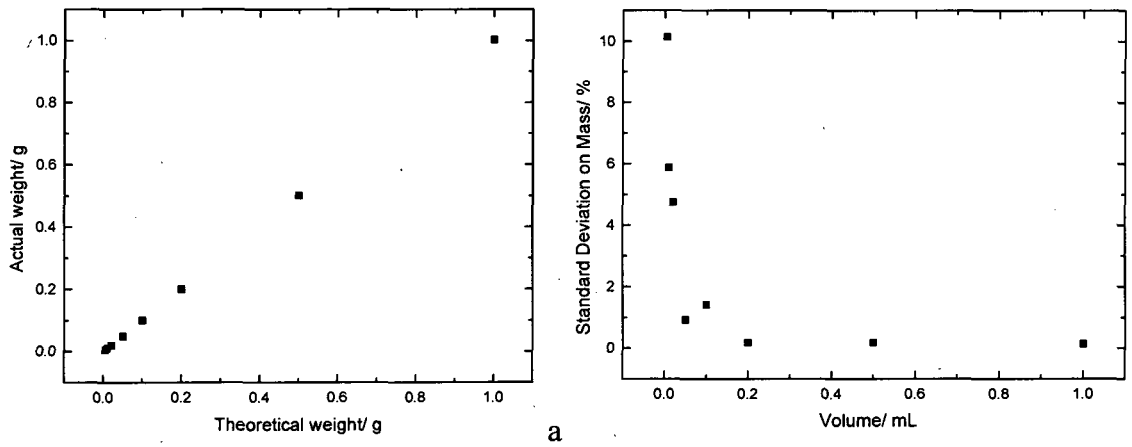

Figure 3-3 (a) The theoretical weight deposited by the robot versus the average weight measured. (b) The percentage standard deviation of repeat measurements versus the volume of solution added.

Figure 3-3a indicates that the robot dispenses accurate volumes; the average addition is exactly as expected. However, Figure 3-3b shows that the standard deviation increases as the dispensed volume decreases so that a 10 % standard deviation is seen when 5 μL additions are made. Errors of this size could affect the structure of the materials prepared. Therefore, when using the robot additions should be kept above 0.05 mL.

3.1.3 Validity of Electrode Testing Without Binder and AB

In the DISC approach materials are synthesised directly onto the surface of a carbon current collector stub and then tested without the addition of AB and binder. These additives are usually included to provide the active material particles with good electronic connectivity and to make the electrode films mechanically strong. To investigate if the DISC conditions provided a fair test of a materials performance, a sample of optimised carbon coated $LiFePO_4$ (Aldrich) was tested with and without the additives.

3.1.3.1 Experimental Details

A 75 μm PTFE electrode was prepared as described in Chapter 2 which contained 75, 20 and 5 % of carbon coated $LiFePO_4$/C, AB and PTFE respectively. A second electrode was prepared using a current collector shown schematically in Figure 3-4 where a single powder can be tested. The well in this current collector was filled with $LiFePO_4$ and compressed using a glass slide, the film thickness was 200 μm (this thickness was chosen as a result of available equipment). The electrodes were then prepared for testing using the small cell approach and cycled galvanostaticaly between 2.5 and 4.5 V *vs.* Li at a rate of C/14.

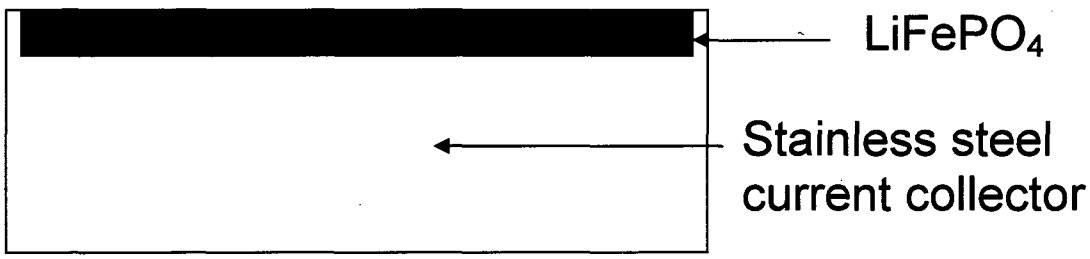

Figure 3-4 Figure showing well design current collector for testing pure powders of active material.

3.1.3.2 Results and Discussion

Below in Figure 3-5 the first cycle charge discharge curves of $LiFePO_4$ can be seen for electrodes prepared with and without AB and Binder. The two preparations show a very different performance. A far greater charge discharge hysteresis is seen in the no additive sample. The lack of AB means the electronic resistance of the electrode increases and the IR drop is far greater. Instead of the flat plateau region on charge and discharge a slope was seen presumably from the increased resistance in the cell. The capacity was also reduced; there are two possible explanations for this; the lack of conducting pathways effectively means some of the material is cut of from discharge, also the increase in IR drop means that the material will need to be charged to higher voltages to extract all the capacity. This evidence suggests that testing in this way will lead to erroneous results.

The DISC method was initially designed to produce thin films of electrode materials (the additive free sample here is not a thin film) that would hopefully not suffer from the problems noted here. However, as discussed in Chapter 1, the electrodes fabricated via DISC are typically large particle agglomerates which will presumably result in a similar performance as shown for the additive free sample in Figure 3-5.

Irreversible capacity can be seen for both electrodes, this is typical for Aldrich $LiFePO_4$ during the first few charge discharge cycles, and as yet remains unexplained.

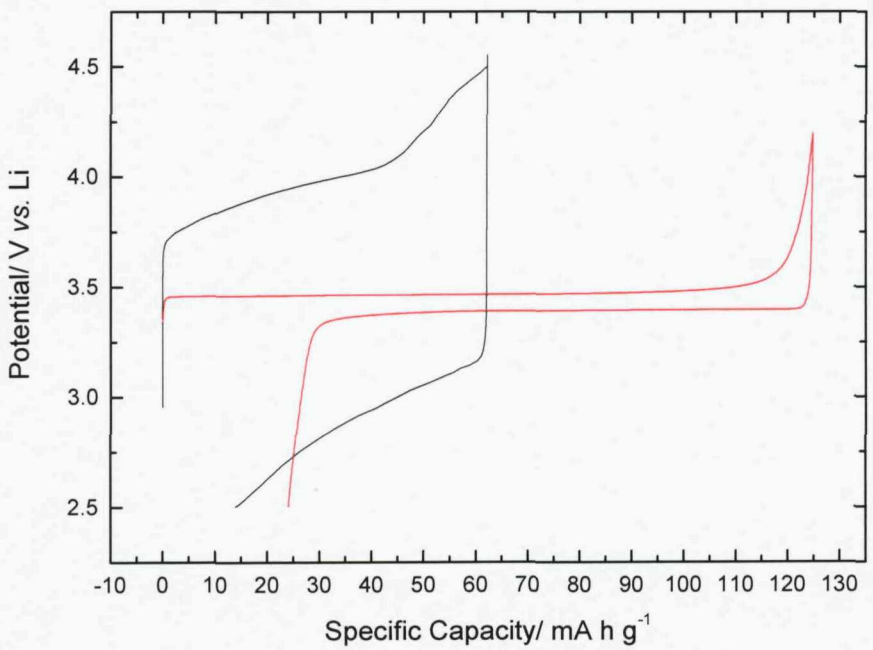

Figure 3-5 Charge and discharge curves for carbon coated $LiFePO_4$ electrodes prepared using PTFE preparation (-) and pure powder preparations (-).

3.1.4 Conclusions

It is clear from the experiments in section 3.1 and the review of DISC in the introduction that several key improvements need to be introduced.

- Accurate active material masses must be recorded for each electrode to achieve percentage standard deviations below 10 %.
- The direct calcinations technique must be modified as electrode adhesion to the current collector is poor and electrochemical evaluation of pure powders without additives will lead to erroneous results.
- Only low viscosity solutions and volumes greater than 5 μL should be used with the robot liquid handler.

3.2 Post Synthesis Array Transfer

3.2.1 Technique Development

To address the reproducibility problems with the DISC and IM methods a new approach was developed. This is shown below in a schematic (Figure 3-6) and is known as Post Synthesis Array Transfer (PoSAT), because it relies on firstly the synthesis of the materials in an array of quartz microtubes followed by the transfer of the active materials to aluminum current collectors.

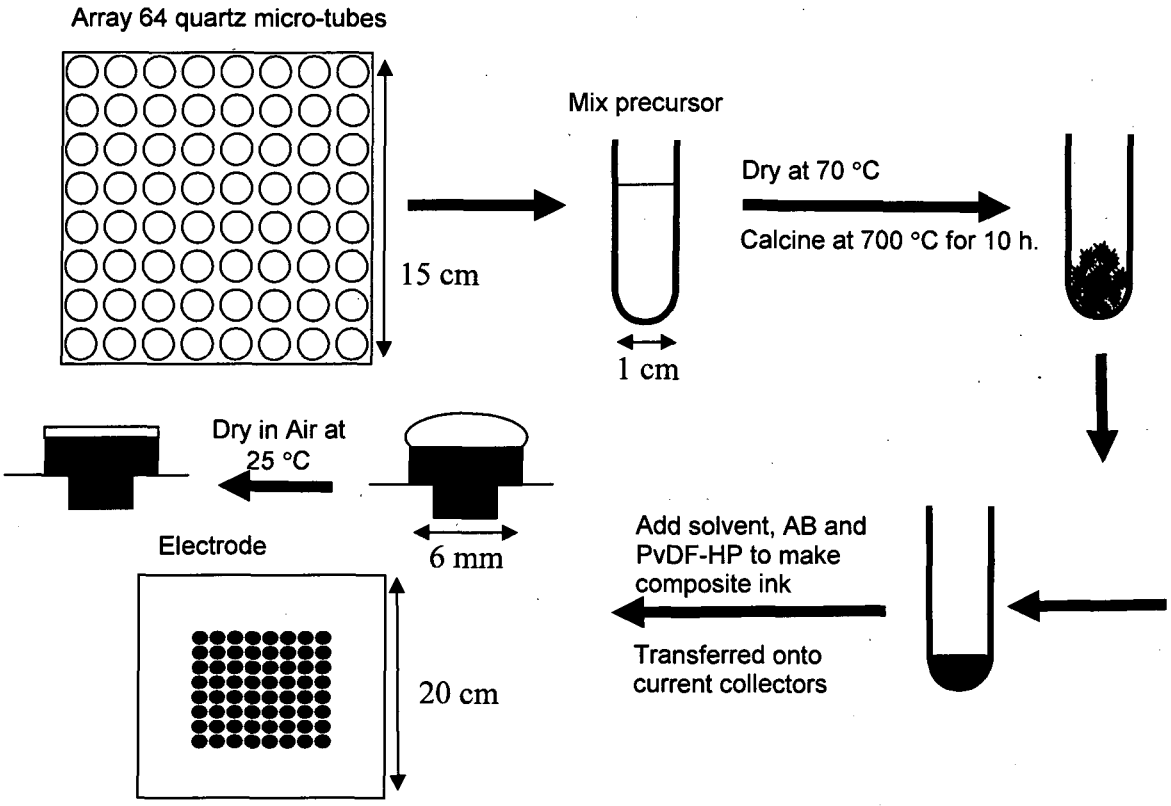

Figure 3-6 Schematic showing the high-throughput technique.

To each quartz micro-tube in the array stiochometric amounts of precursor solutions were added. Then the tubes, contained in two stainless steel racks(Figure 3-7), were placed in an oven a 70 °C for 12 h to remove the water. These two stainless steel racks were then transferred to a large bore (80 mm diameter) tube furnace (Lenton) simultaneously for heat treatment.

Figure 3-7 Photo of one of the two stainless steel racks used to contain the quartz tubes of the array during heat treatment.

The racks were placed in the central portion of the furnace where the heating conditions are assumed to be uniform. The calcination was then undertaken in a controlled atmosphere and temperature. After calcination each active material was crushed to a powder using a glass rod attached to a drill, this sequential task takes less than one hour. (However, in later work this is replaced by the use of ball milling, done by adding the 5 1 mm Zr balls to each sample and then shaking the array on a vibrating table (IKA, VIBRAX VXR basic) for 1 h.) Each tube then had inks of acetylene black (AB) and PVdF-HFP in CP added, also added at this point were 1 mm Zirconia balls (if not added previously for ball milling). These inks were mixed using a vortex mixer (Fisherbrand, Whirlimixer) or shaker table (IKA, VIBRAX VXR basic), the addition of the zirconia balls acted to increase homogenization. 14 μL of each ink was deposited onto 6 mm diameter aluminium current collectors, the ink was spread across the surface to form an even film. The CP was then evaporated at room temperature leaving an array of 64 battery electrodes an example of which is shown in Figure 3-8. Then each of these electrodes was weighed before electrochemical testing.

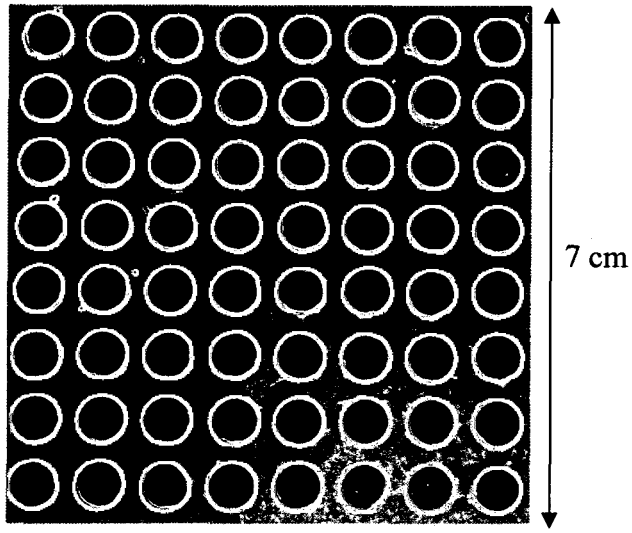

Figure 3-8 Photo showing an array of electrodes prepared using the PoSAT method.

This technique provided arrays of very robust electrode films shown in Figure 3-8. These films were very similar to the composite electrodes formed using standard ink deposition techniques followed by doctor blading. However, the films did not have the shiny polymer like appearance of the conventionally prepared PTFE films, and the grainy particulate nature of the film can still be seen. These films are not compressed and have a thickness of ~100 μm when assembled into the test cell. However, when examined after testing, the electrodes appear compressed with the aforementioned polymer like appearance. This is presumed to be a result of the high pressures which exist within the cell. These electrodes were then constructed into the test cell as described in the Chapter 2. During this fabrication process the electrode weights were monitored carefully by the numerous weighing steps both during the ink additions to the quartz tubes and deposition onto the current collector surface.

To confirm the percentage of active material via high-throughput thermo-gravimetric analysis (HT-TGA)(4) (Figure 3-9) aliquots of the same battery inks as used to construct the electrodes were deposited into an array of ceramic micro-crucibles (Macor).

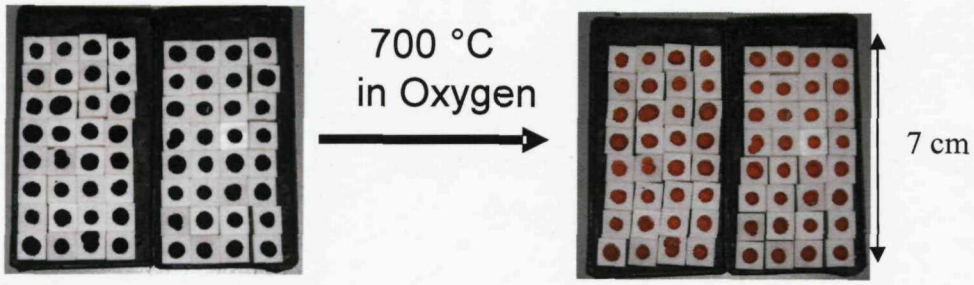

Figure 3-9 Photos showing an array of ceramic micro-crucibles containing $LiFePO_4$ electrodes before and after heat treatment.

As shown in Figure 3-9 the array was heated in oxygen resulting in the combustion of the carbon and PVdF-HFP, this is summarized in Equation 3-2.

$$C + O_2 \rightarrow CO_2$$
$$LiFePO_4 + \tfrac{1}{4}\, O_2 \rightarrow LiFePO_{4.5}$$

Equation 3-2

It was assumed that on heating the PVdF-HFP decomposes into carbon and other volatiles. This was tested by heating a sample in a crucible at 700 °C in oxygen. After heat treatment no residual compounds were found. By undertaking this TGA measurement the error resulting from poor knowledge of electrode composition was reduced.

This PoSAT method has sort to rectify the problems discussed in section 3.1 by the addition of binder and conductive additive and the development of HT-TGA to obtain accurate electrode weights.

3.2.2 Testing and Validation

To test and validate the PoSAT method a simple experiment was performed where 64 identical $LiFePO_4$ electrodes were prepared and tested.

3.2.2.1 Experimental

A 500 mL solution containing 0.625 M of $LiCH_3COO.2H_2O$(*Aldrich*), $Fe(NO_3)_3$ $.9H_2O$(*Aldrich*), H_3PO_4 (85 wt. % in water, *Aldrich*)) and 0.156 M of sucrose was prepared; the sucrose to H_3PO_4 (SPR) ratio was 0.25.(5) 1 ml Aliquots of this solution were then deposited into an array of quartz micro-tubes. This array of solutions was then processed into an array of electrodes and inks in micro-crucibles using the PoSAT approach (section 3.2.1). The synthesis temperature was 700 °C in an inert argon atmosphere for 10 h. The micro-crucible samples were then treated as described in section 3.2.1 using the HT-TGA method. The electrodes were then constructed into the test cell and XRD patterns were recorded. The test cell was cycled between 2.5 and 4.5 V at 0.05 mV s^{-1} 10 times.

3.2.2.2 Results and Discussion

Shown below in Figure 3-10 are the CVs recorded for the prepared array.

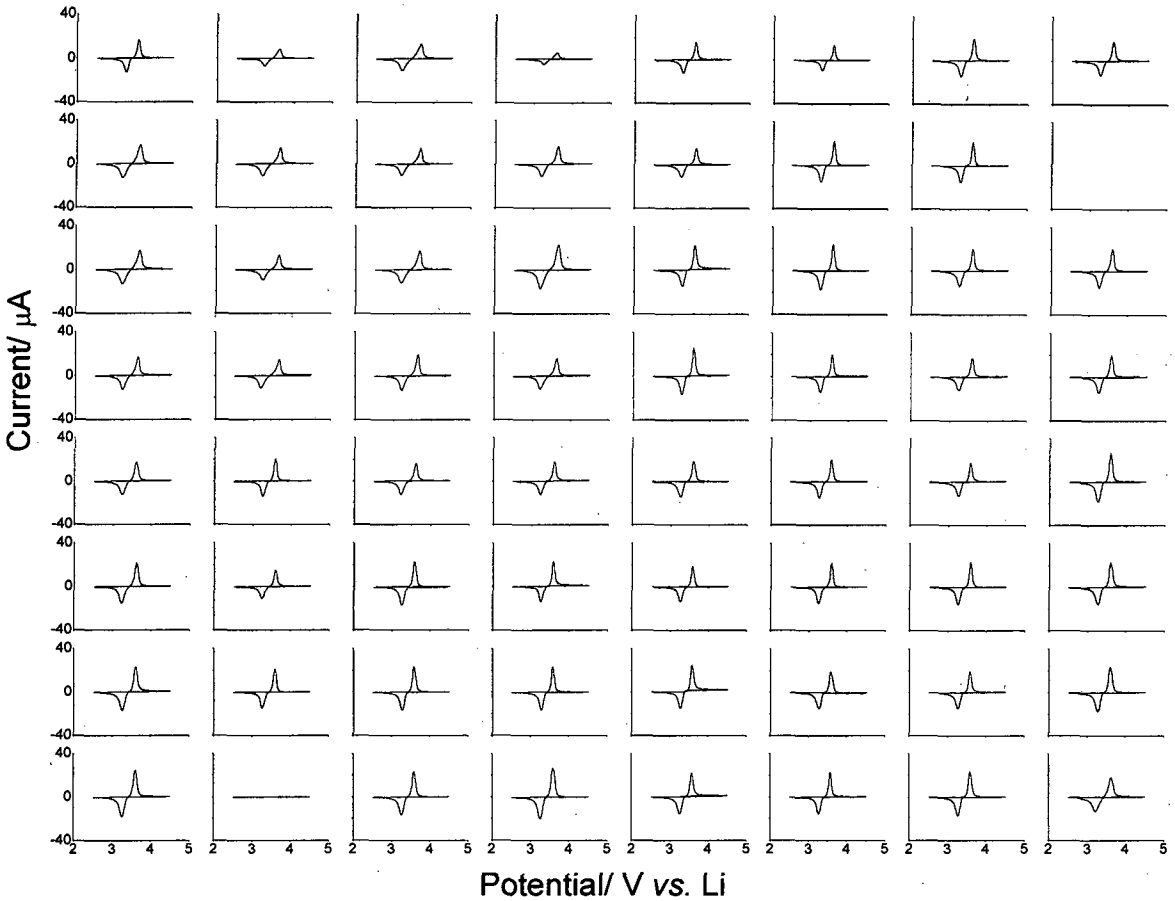

Figure 3-10 64 CVs recorded at 0.05 mV s^{-1} of repeat preparations of $LiFePO_4$ with a sucrose to iron nitrate ratio of 0.25.

The CVs (Figure 3-10) highlight the reproducibility of the PoSAT method. All CVs show the oxidation peak of Fe(II) to Fe(III) at 3.60 V and the reduction peak at 3.25 V. The data quality is generally similar to that of measurements recorded using standard techniques. A slightly irregular variation in the size of the peaks is at least in part attributable to the variations in the active mass as determined by TGA. To characterize the CVs the specific capacity was calculated this is shown below in Figure 3-11. For comparison a result for the same experiment using the DISC method is shown, this was extracted from the thesis of Alan Spong.(1) In this experiment however only 32 measurements were recorded, so for a visual comparison two repeats of each are shown in a randomized the order.

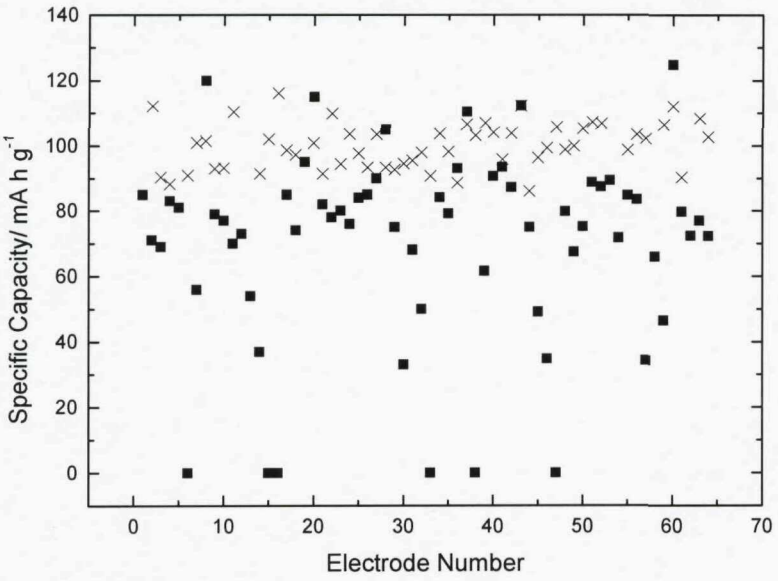

Figure 3-11. Specific capacity measurements for the 64 repeat array for the PoSAT method (X) and the DISC result (■) reproduced from the Spong thesis.(1)

The results in Figure 3-11 show that scatter is significantly reduced for the electrodes prepared using the PoSAT method. The PoSAT result shows an average specific capacity value of 101 mA h g^{-1} and a standard deviation of 8 mA h g^{-1}, whereas the average for the DISC method was 77 mA h g^{-1} and the standard deviation was 29 mA h g^{-1}. This represents a greater than three fold reduction in standard deviation. As a further comparison of the error a statistical plot is shown below in Figure 3-12 this is known as a "box-whisker" diagram, this further highlights the reduction in scatter that can be attributed to the PoSAT method.

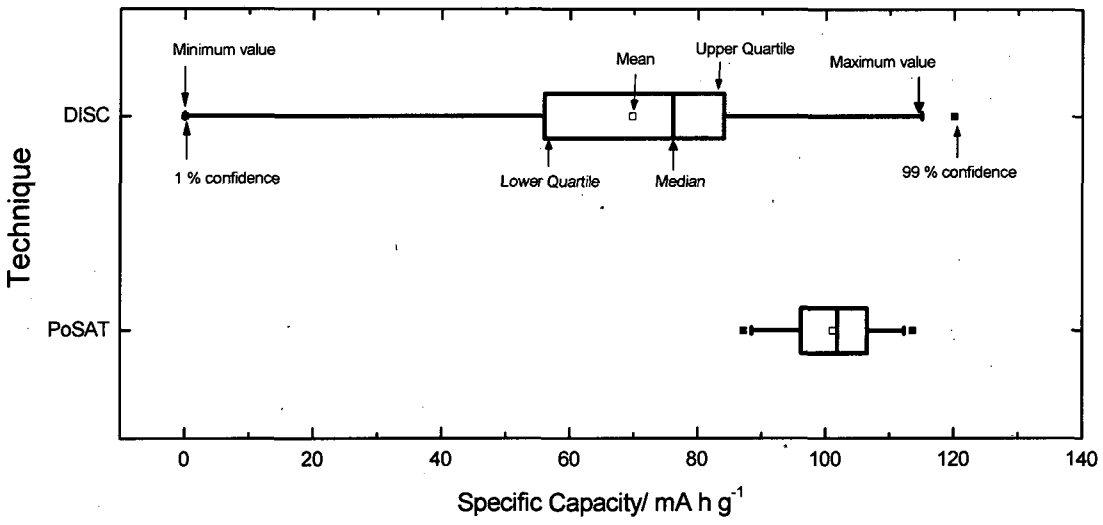

Figure 3-12 A "box-whisker" diagram showing some key statistical data comparing the scatter that exists in the DISC and PoSAT methods.

3.3 Variable Temperature High-throughput Calcination

The synthesis of many battery materials involve high temperatures to allow solid state diffusion of the ions and the formation of the crystal structure(6). Higher synthesis temperatures usually result in the formation of larger crystals, which is not always desirable. However, if the temperature is too low there may not be enough energy to form the desired crystal structure. Also from a commercial point of view lower synthesis temperatures are more energy efficient and therefore more economically viable. To investigate the effect of synthesis temperature an adaptation of the PoSAT high-throughput approach was developed.

3.3.1 The Temperature Gradient in the Tube Furnace

3.3.1.1 Experimental Details

To measure the temperature gradient within the tube furnace (Lenton) a hole was drilled in one of the stainless steel end stoppers and through one of the thermal bungs. A thermocouple was then inserted during heating and moved to different positions to record the temperature (the thermocouple was left at each position for 10 minutes to equilibriate before measurement). The furnace was then set to target temperatures of 900 and 1000 °C (on two separate runs), and was heated using a rate of 5 °C min^{-1} with a gas flow rate of 0.5 L min^{-1}. To make sure the measurements were accurate once the target temperature had been reached the furnace was left to equilibrate for 2 h before any measurements were made.

3.3.1.2 Results and Discussion

Shown in Figure 3-13 is the temperature profile along the tube furnace when the target temperature was set to 900 and 1000 °C. Both show a gradual increase from the edge of the furnace to the centre. When the target temperature was set to 1000 °C the two repeat measurements can be seen to be in good agreement.

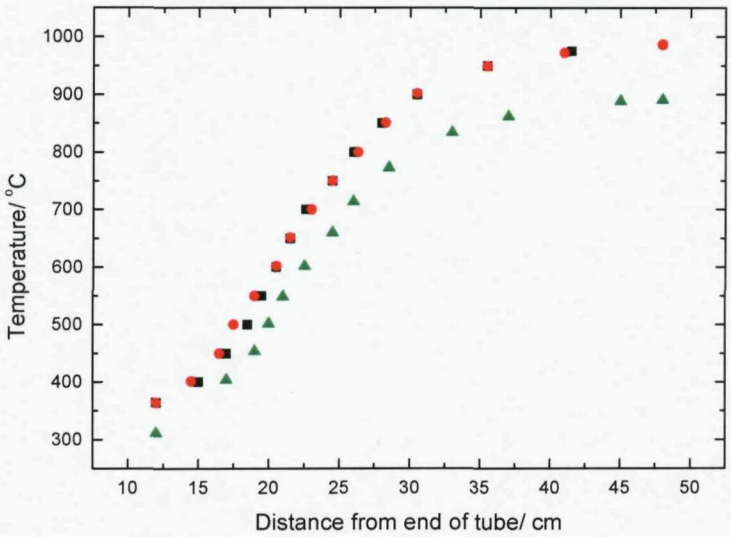

Figure 3-13 Temperature gradient from the end of the tube 1000 °C run 1 (■), 1000 °C run 2 (●) and 900 °C (▲).

Based on the measurements in Figure 3-13 a special rack was designed which is shown below in Figure 3-14. This rack is designed so that when placed with the right end 18.5 cm into the furnace the rows of the array will be exposed to 600, 650, 700, 750, 800, 850, 900 and 950 °C. This rack can only accommodate 32 tubes and the synthesis will have to be performed twice to prepare all 64 samples in a standard array.

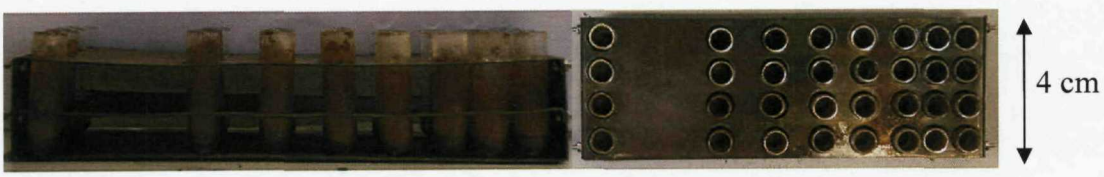

Figure 3-14 HT Furnace Rack.

3.3.2 Validation of the HT Furnace Rack

To confirm the rack exposed each tube to the expected temperatures an experiment was conducted using salts of different melting points.

3.3.2.1 Experimental Details

Three salts were chosen NaCl (*Aldrich*), KBr(*Aldrich*) and KI (*Aldrich*)with various melting points 800.8, 734, 681 °C. 0.5 g samples of salt were placed in each tube so that three columns of the rack were utilised, each column containing a different salt. These tubes were then heated in the thermal gradient by placing the rack at 18.5 cm into the tube and setting the target temperature to 1000 °C, heating rate of 5 °C min^{-1} and an Ar gas flow rate of 0.5 L min^{-1}.

3.3.2.2 Results and Discussion

Below in Figure 3-15 the results from the validation of the HT furnace technique are shown in a colour map. It was determined that a sample had melted if it had changed from its original granular appearance to a single transparent solid after heating.

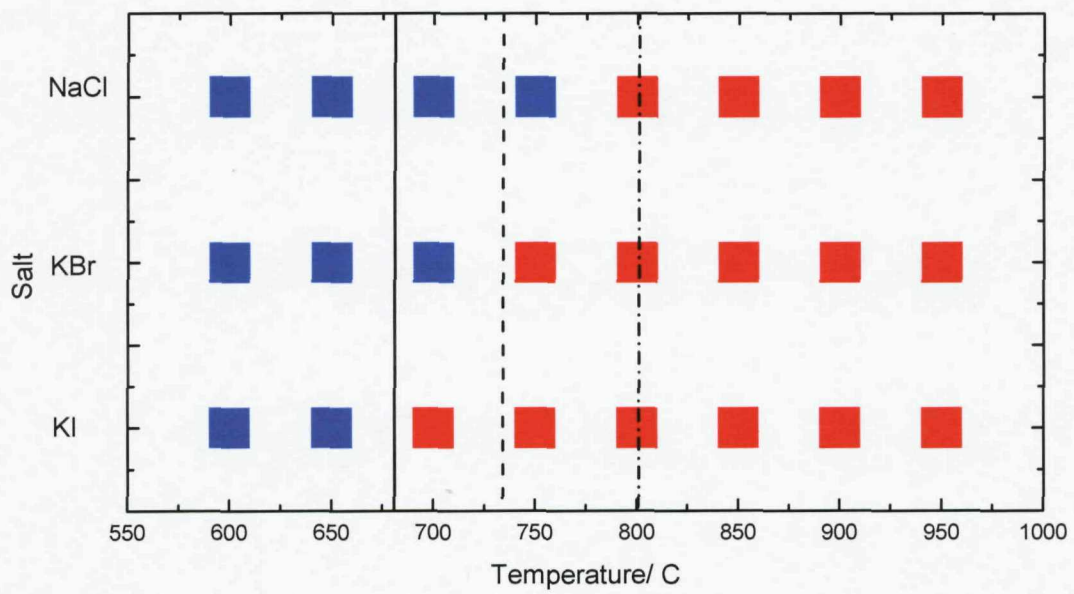

Figure 3-15. Representation of salt melting experiment, the temperature scale indicates the conditions expected. Colored squares show samples which remained solid (■) and samples which melted (■). Also shown are the lines indicating the known melting points for NaCl (-·-) KBr (---) and KI (–).

It can clearly be seen (Figure 3-15) that when the samples were placed in positions where the HT furnace was expected to expose them to temperatures above their melting points the samples melted and when below this temperature remained solid. This technique therefore seems suitable for the preparation of temperature graded arrays.

3.4 High-throughput XRD

The high-throughput XRD (C2) works by placing an array of samples on a movable x, y, z stage, controlling software (GADDS) then moves each sample to a position where the pattern is recorded. However, it is important to understand the validity of these measurements, as the sample height varies and will affect the XRD patterns.

3.4.1.1 Experimental

As a validation of the C2 and to observe detection limits powders of carbon coated $LiFePO_4$ (*Aldrich*), TiO_2 nanopowder (*Aldrich*), PTFE (PTFE, Type: 6C-N, *DuPont*) and AB(acetylene black, *Shawinigan, Chevron Phillips Chemical Company LP*) were mixed in the proportions shown in Table 3-2. In the cases where PTFE and AB were used electrodes were prepared as described in Chapter 2.

Table 3-2. Table showing proportions of $LiFePO_4$, TiO_2, PTFE and AB mixings used to test high-throughput XRD measurement.

Electrode	Percentage $LiFePO_4$	Percentage TiO_2	Percentage PTFE	Percentage AB
A	100	0	0	0
B	74.25	0.75	5	20
C	73.5	1.5	5	20
D	71.25	3.75	5	20
E	67.5	7.5	5	20
F	60	15	5	20
G	37.5	37.5	5	20
H	15	60	5	20
I	7.5	67.5	5	20
J	3.75	71.25	5	20
K	1.5	73.5	5	20
L	0.75	74.25	5	20
M	0	100	0	0

These 13 electrodes/powders were then mounted using adhesive carbon tape (Agar) onto SEM stubs, and placed in a specially designed sample holder. This was then transferred to the C2 difractometer, the sample positions were then imputed into the GADDS software and the 13 XRD patterns were recorded.

3.4.1.2 Results and Discussion

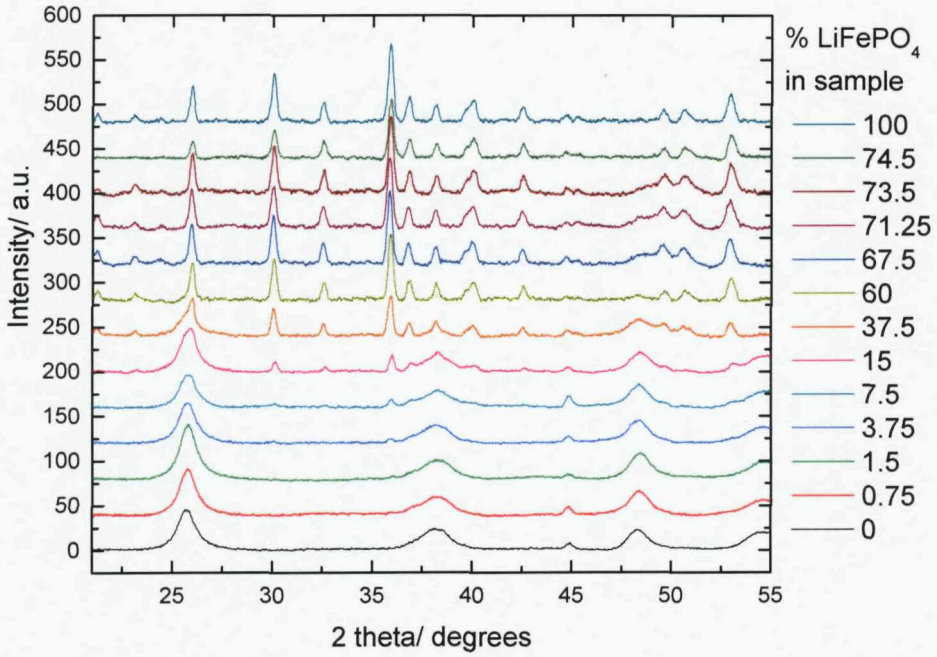

Figure 3-16 XRD patterns of the mixed electrodes containing the compositions indicated on the graph and in Table 3-2.

In Figure 3-16 the $LiFePO_4$ phase can be clearly seen until sample I (7.5 % $LiFePO_4$) and below this the most intense peak at 36 ° can still be seen in sample K(1.5 % $LiFePO_4$). The TiO_2 phase is present until G (37.5 % TiO_2) clearly and in sample F (15 % TiO_2) the most intense peak at 26 ° increases the broadening in one of the $LiFePO_4$ peaks. From this experiment we can conclude that when the phases present in the sample are highly crystalline the fractions can be detected to between 2 and 5 %. However, when the fractions contain broader peaks it is far more difficult to detect there presence below 20 %. To investigate how accurate the 2 theta values are peaks from samples B to G were used for indexing and to calculate the unit cell volume of $LiFePO_4$. The method for this is described in Appendix 3.

3.6 Chapter 3 References

1. A. D. Spong, High-Throughput Discovery of Lithium Battery Materials, in, University of Southampton, Southampton (2005).

2. M. M. Thackeray, *Progress in Solid State Chemistry*, **25**, 1 (1997).

3. G. G. Amatucci, N. Pereira, T. Zheng and J. M. Tarascon, *Journal of the Electrochemical Society*, **148**, A171 (2001).

4. S. F. Yang, Y. N. Song, P. Y. Zavalij and M. S. Whittingham, *Electrochemistry Communications*, **4**, 239 (2002).

5. A. D. Spong, G. Vitins and J. R. Owen, *Journal of the Electrochemical Society*, **152**, A2376 (2005).

6. Weller. M.T, *Inorganic Materials Chemistry*, Oxford University Press (1994).

7. A. K. Padhi, K. S. Nanjundaswamy and J. B. Goodenough, *Journal of the Electrochemical Society*, **144**, 1188 (1997).

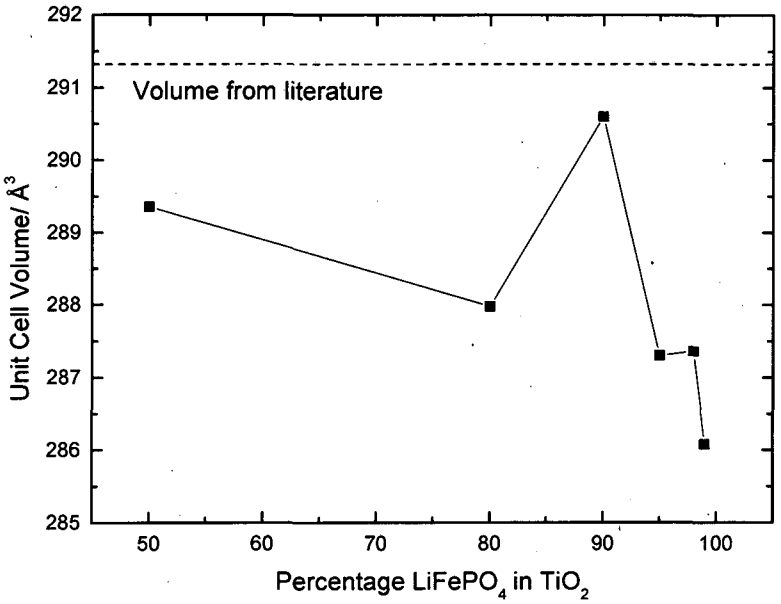

Figure 3-17 Plot showing the unit cell volume as calculated from the XRD patterns B to G. Also shown is a literature value for the volume of $LiFePO_4$.(7)

The results in Figure 3-17 show that the calculated unit cell volume from the XRD patterns in Figure 3-16 are not uniform as expected, and there is a significant degree of scatter. Although the samples seem to be decreasing in volume as the percentage of $LiFePO_4$ in TiO_2 increases it seems unlikely that this is a trend and more probable that this is just random scatter. It can also be seen that the unit cell volume is somewhat smaller than those values calculated in the literature.(7) The unit cell refinement is normally performed via Rietveld refinement; however, when this was tried on the patterns recorded using the C2 the quality was not sufficient for the refinement to be successful, so the determination of the unit cell parameters was done via peak indexing. This could be one of the reasons why the unit cell parameters do not completely match. Therefore this level of scatter should be taken into account when any conclusions are drawn from unit cell parameter determination. From these values the average unit cell volume is 288.11 $Å^3$ and the standard deviation on these results are 1.62 $Å^3$. A typical solid solution study in this work is $LiFe_{1-x}Mn_xPO_x$ where a linear change is seen in the unit cell volume from 292 to 303 $Å^3$ when varying x from 0 to 1.(7) The accuracy of the C2 instrument should be sufficient to observe trends of this magnitude.

3.5 Conclusions Chapter 3

The key areas for improvement in the original method were identified as poor knowledge of electrode weight, poor adhesion of the electrode to the substrate and lack of conductive additive and binder. Because the electrodes are not commercial products it is essential that enough AB and binder are added, so that the material is completely responsible for the performance and not a result of poor composite electrode formation. The PoSAT technique has improved the accuracy of high throughput synthesis by introducing weighing steps to accurately determine the amount of active material on each substrate. The separation of the active material synthesis and electrode fabrication steps has meant that good quality electrodes containing conductive additive and binder are now obtained. Using this approach the electrodes bind well to the surface of the aluminium current collectors. This technique was then trialled with a reproducibility study where 64 identical samples were prepared and tested. The results from this showed a standard deviation of approximately 10 %. This method is therefore seen as a reliable and fast way of characterising possible new cathode materials.

A further development has been the high-throughput method for the preparation of materials at different temperatures. This method has been validated using salts with different temperature melting points and was shown to be effective.

Finally the effectiveness of the high-throughput XRD measurements has been assessed. From this it has been determined that the detection limit for sample impurities is approximately 5 %. The calculation of unit cell information via peak indexing is seen to be only effective within ±2 Å.

The following chapters are further demonstration of these techniques, highlighting the versatility and benefits of the high throughput approach.

Chapter 4 Towards the optimisation of $LiFePO_4$

4.1 Percolation by Carbon Coating

A common method to extract the maximum capacity out of $LiFePO_4$ is to coat the particles in carbon, discussed in the introduction. By using the PoSAT method and the Spong et al.(1) sol-gel synthesis an array was constructed where many samples of $LiFePO_4$ were prepared with incrementing levels of carbon coating.

4.1.1 Experimental details

Array Preparation

A 500 mL solution was prepared containing 0.625 M of $LiCH_3COO.2H_2O$ (*Aldrich*), $Fe(NO_3)_3$ $.9H_2O$ (*Aldrich*) and H_3PO_4 (*Aldrich*). 1 mL aliquots of this solution were then added to each position on an array of quartz micro crucibles. Sucrose (2 M aqueous solution) was then added to give sucrose to phosphoric acid ratios (SPR) equally graded between zero and 0.5 across the array with two repeats at each ratio. The array of precursor solids was then calcined in an argon atmosphere at 700 °C using a large bore (80 mm diameter) tube furnace (Lenton). After cooling, the products were crushed to a powder using a glass rod attached to a drill. Composite electrode preparation began by adding two inks, 4% PVdF-HFP (*Aldrich*, polyvinylidene fluoride-co-hexafluoropropylene) and 4% AB (acetylene black, *Shawinigan, Chevron Phillips Chemical Company LP*) in cyclopentanone (CP) to the active material powders with five 1 mm zirconia beads placed in each tube. The inks were added to give a final mass ratio of 10% PVdF-HFP, 25% AB and 65% active material and then mixed using the vortex mixer. Then 14 µL aliquots of each ink was deposited onto the appropriate position on the array of aluminium current collectors and spread across the surface to form an even film of ink. At the same time, a 40 µL sample of each ink was deposited into an array of alumina micro-crucibles for thermogravimetric analysis as detailed below. The CP was evaporated from both arrays at room temperature before drying at 80 °C followed by evacuation. The

samples on both arrays were then accurately weighed using a computer monitored balance.

Array sample characterisation

This array was then cycled between 2.5 to 4.5 V at the following scan rates; 0.05, 0.1, 0.2, 0.4, 0.8, 1.6 and 3.2 mV s^{-1}. XRD patterns were recorded and TGA analysis performed on each electrode.

Bulk Sample preparation

Several bulk preparations were also undertaken for comparison. The same synthesis method was used as for the array except the volumes were scaled up to give a total volume of 20 mL. The SPRs of the samples prepared were 0.15, 0.22, 0.25, 0.3 and 0.5. These solutions were then dried and placed in ceramic crucibles and heated under the same conditions. The active materials were then prepared into PTFE/carbon films as described in chapter 2 and were cycled galvanostatically at various C-rates between 2 and 4.5 V.

4.1.2 Results and discussion

X-ray Diffraction Patterns

Figure 4-1 shows selected XRD patterns for the array produced by the PoSAT method as described in section 4.1.1. The diffraction patterns were sufficient for phase analysis in all cases. The pattern for 0.10 SPR preparation contained peaks due to a NASICON type phase, and Fe_2O_3 phases as assigned in Figure 4-1b. Although in the 0.10 sample some peaks can be assigned to the olivine phase, the lack of a strong peak at 26 ° indicates that this phase is not present. The NASICON structure is a result of full oxidation of the iron to iron (III) due to the presence of excess nitrate,

e.g. $6\ LiFePO_4 + 3[O] \rightarrow 2Li_3Fe_2(PO4)_3 + Fe_2O_3$ **Formula 1**

For the samples prepared at SPRs above 0.16, all major peaks were assigned to the olivine phase and there was no evidence of any impurities.

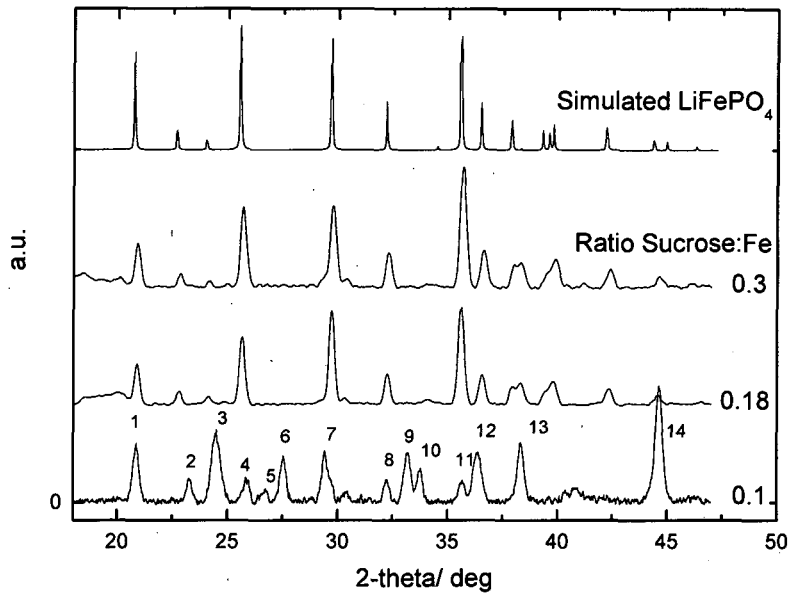

(a)

Compound	Structure	Crystal Class	Peaks
$Li_3Fe_2(PO_4)_3$	NASICON	Monoclinic	1,2,3,4,5,6,7,8,9,10,12
Fe_2O_3	Hematite	Rhombohedral	9,11
PVdF			13
Aluminium metal			14

(b)

Figure 4-1 (a)XRD patterns of $LiFePO_4$ prepared via PoSAT at 700 °C from a solution containing $LiCH_3COO$, $Fe(NO_3)_3$, H_3PO_4, and various amounts of sucrose as shown on the graph, also shown for comparison is a simulated pattern for $LiFePO_4$.(b) A table identifying the probable impurity peaks in the sample prepared with a sucrose:$LiFePO_4$ ratio of 0.1.

Cyclic Voltammograms

The voltammetry result from the array are shown below in Figure 4-2.

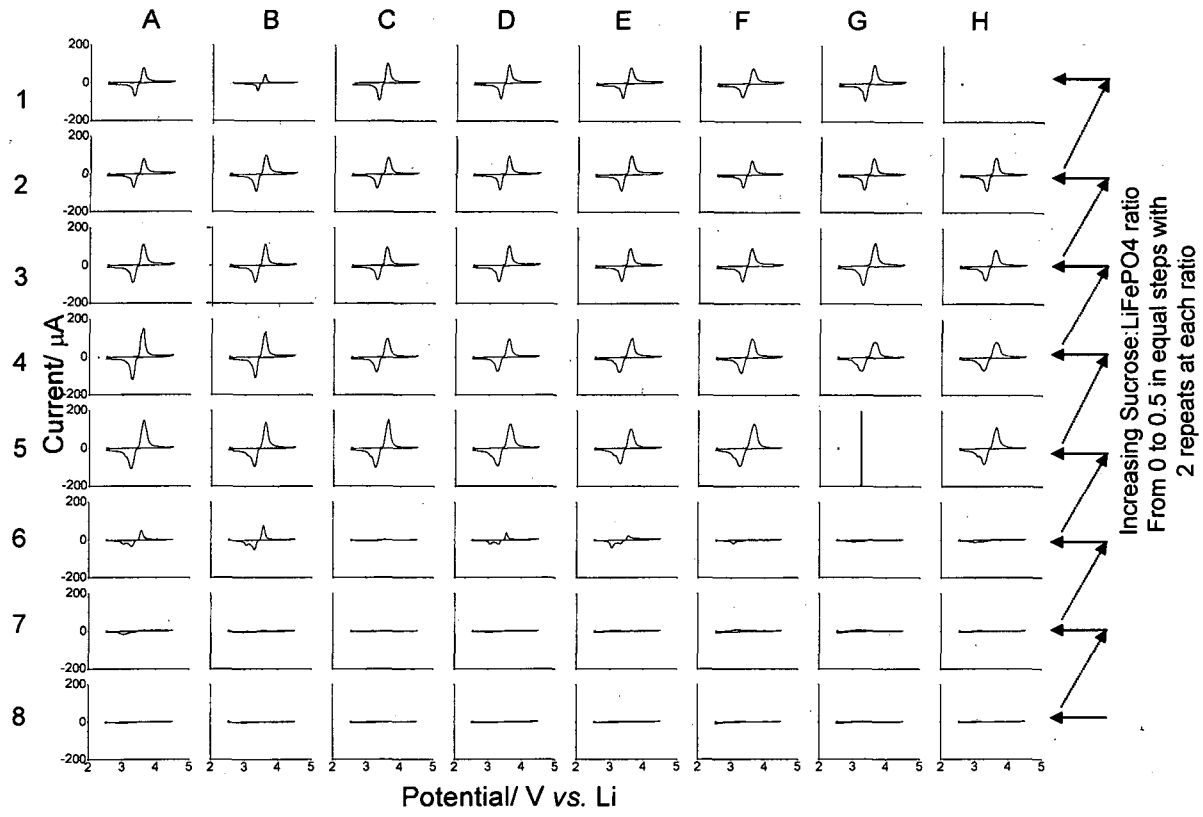

Figure 4-2 CVs (0.05 mV s^{-1}) for the 64 materials prepared as described in the text using the PoSAT methodology.

In the absence of sucrose, none of the voltammograms show any activity due to $LiFePO_4$ despite the presence of the acetylene black and conductive additive. The first sign of increased activity is at position E6, where the sucrose: iron nitrate ratio is 0.14. The peak currents then steadily increase until the CVs appear to be more or less constant beyond position H5 where SPR is 0.20. (A slightly irregular variation in the size of peaks is attributed to the variations in the active mass as determined by TGA). At and above this sucrose level the oxidation peak of Fe(II) to Fe(III) can be seen at 3.60 V and the reduction peak at 3.25 V. Close examination of CVs at lower sucrose levels, e.g. E6-H5, show a secondary anodic peak at 2.9 V, which is the potential associated with $Li_3Fe_2(PO_4)_3$, an impurity phase is seen in the high throughput XRD

measurements. Given the computational difficulties in a full interpretation of each individual CV, the principal quantitative analysis of the results here is based on the average discharge capacity per cycle. These capacity values are shown in Figure 4-3 along with the results from a similar study obtained through DISC(2) and some additional points derived from conventional experiments; the latter highlights the improvement effected by PoSAT.

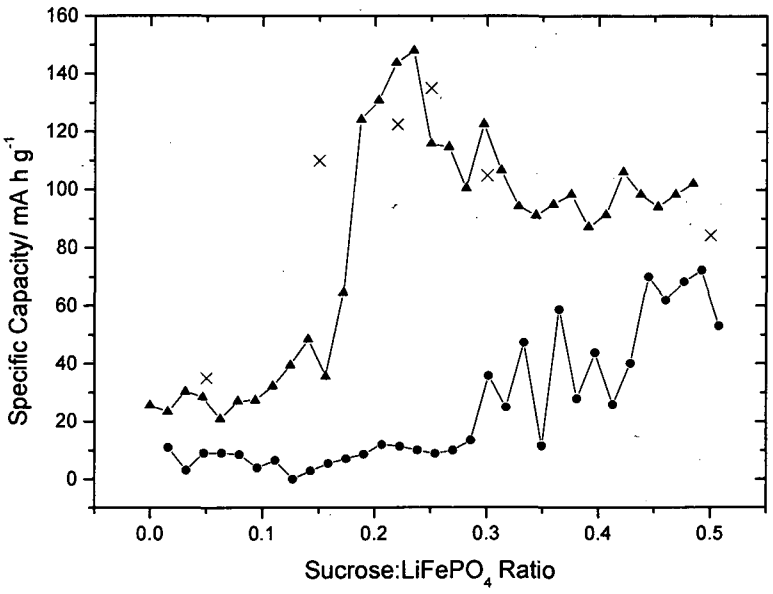

Figure 4-3 Specific Capacity vs. Sucrose:$LiFePO_4$ ratio measured using three techniques: Conventional small cells (X), DISC (-●-) and PoSAT (-▲-).

Three features are apparent from Figure 4-3:

1. In the DISC method the capacity is not significant until sucrose:iron nitrate equals 0.3, as compared by 0.15 in the PoSAT method. This indicates the importance of forming a percolating network of electronic conductivity as well as a partial coating of the electrode surfaces. In the PoSAT case it is the added carbon black that forms the percolating network. The figure of 0.15 closely reflects the amount of sucrose consumed by nitrate according to the following example reaction scheme:

$2C + Fe(NO_3)_3 + CH_3COOLi + H_3PO_4 \rightarrow LiFePO_4 + 4CO_2 + 1.5N_2 + 3H_2O$

Two carbons are required to reduce the reactants to LiFePO4, assuming that the effluent gases are neither oxidizing (e.g., NO_x) nor reducing (e.g., CO). Given the formula $C_{12}H_{22}O_{11}$ for sucrose, it can be deduce that the minimum sucrose:iron nitrate

ratio required should be 0.167. The small discrepancy may have been caused by emission of some organic vapors during sucrose pyrolysis.

2. The rise in activity on increasing the sucrose level above the minimum required for formation of the correct phase is much faster for the PoSAT array. This is likely to result from the different function of the pyrolytic carbon in each case. In the PoSAT array, the added carbon black provides sufficient electronic conductivity across the matrix, the extremely fast rise indicates that only a partial coverage by pyrolytic carbon is required to make a good contact between the particles and the added carbon black. In the DISC case, the pyrolytic carbon is required for long distance conductivity, which first requires percolation and then increases with the cross-sectional area of the current path, which increases with the volume fraction of carbon.

3. The PoSAT results show a decrease in capacity soon after the initial rise. A marked decrease in the available capacity can be observed at higher scan rates (Figure 4-4) although the difference between fast and slow scans is less marked at high sucrose levels. The implications of these results will be discussed below.

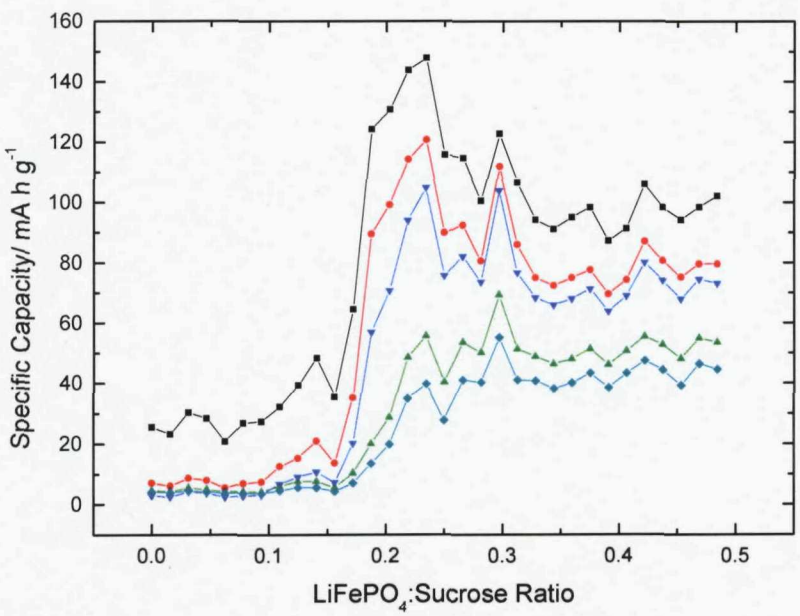

Figure 4-4 Discharge specific capacity vs. Sucrose:$LiFePO_4$ ratio measured using the PoSAT method recorded using the following scan rates are shown 0.05 (■), 0.1 (●), 0.4 (▼), 1.6 (▲) and 3.2 mV s^{-1} (◆).

In Figure 4-4 the percolation threshold (described as the point when the active material becomes sufficiently coated in carbon so as the majority of the theoretical discharge capacity is seen) appears between ratios of 0.17 and 0.2. For the slower scan rates (0.05, 0.1, and 0.4 mV s^{-1}) large capacities (above 125, 95 and 80 mA h g^{-1} respectively) are seen between ratios 0.2 and 0.25, however, above 0.25 the capacity reduces. The reason for this reduction has previously been reported in the literature(3) and is justified as the formation of thicker carbon layer on the particle surface hindering the electrolyte penetration to the particles and also the transfer of lithium ions.

Figure 4-4 also shows that the percolation threshold changes with scan rate, at 0.05 and 0.1 mV s^{-1} it appears at a ratio of 0.18, but at 0.4, 1.6 and 3.2 mV s^{-1} a higher value of 0.22 is required. This could be a result of improved conductivity from increased carbon coating before the layer becomes too thick. At faster scan rates (1.6 and 3.2 mV s^{-1}) this pattern changes so that there is no reduction in capacity after a ratio of 0.25 just a plateau region (at around 50 and 40 mA h g^{-1} respectively).

To try and better understand the regions in Figure 4-4 individual plots of selected CVs are shown in Figure 4-5, Figure 4-6 and Figure 4-7 with rate performance plots.

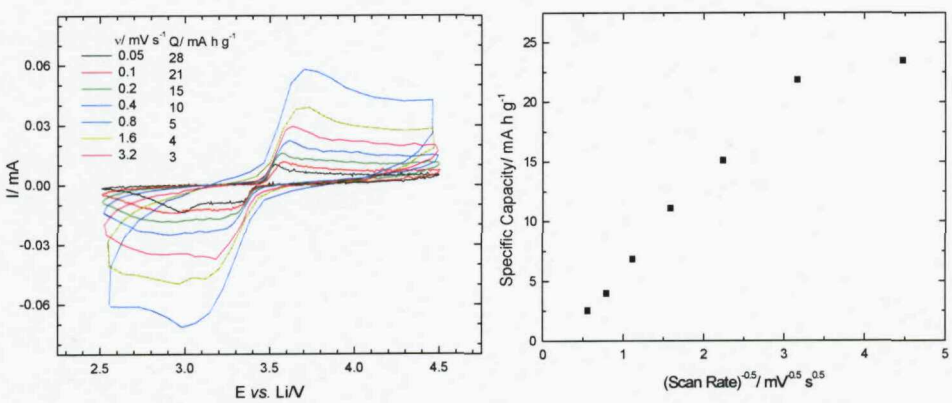

Figure 4-5 Cyclic voltammograms and plots of specific capacity *vs.* (scan rate)$^{-1/2}$ for electrodes with sucrose :iron nitrate ratio 0.16.

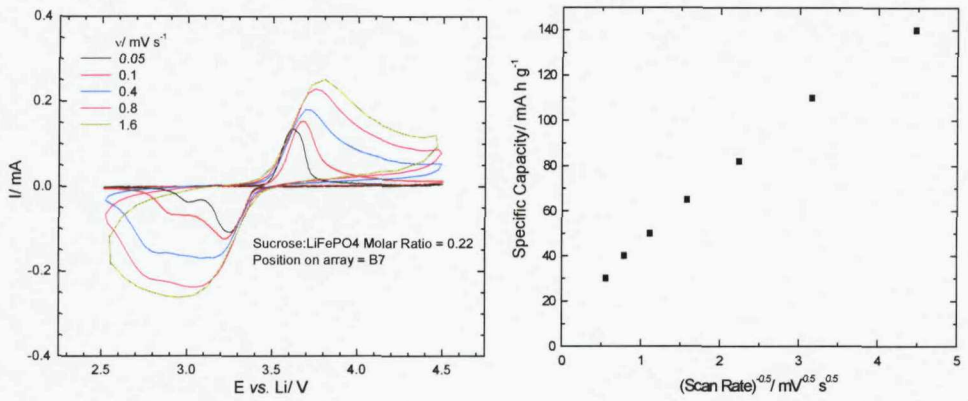

Figure 4-6 Cyclic voltammograms and plots of specific capacity *vs.* (scan rate)$^{-1/2}$ for electrodes with sucrose :iron nitrate ratio 0.22.

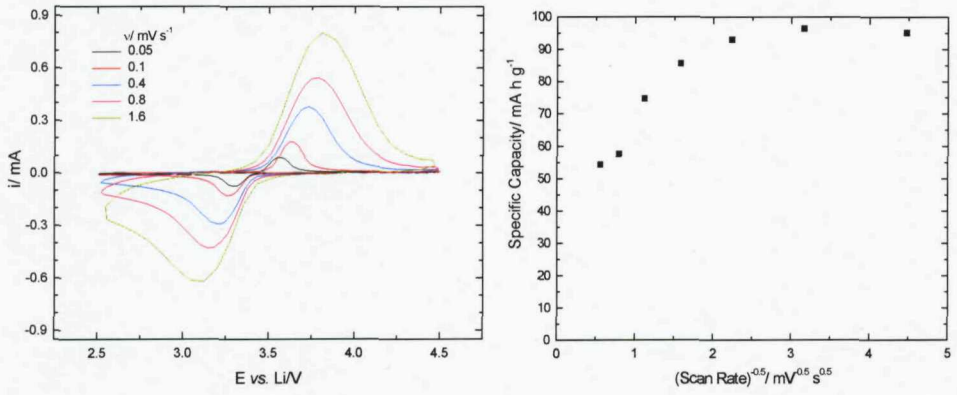

Figure 4-7 Cyclic voltammograms and plots of specific capacity vs. (scan rate)$^{-1/2}$ for electrodes with sucrose :iron nitrate ratio 0.48.

At the lowest sucrose level, Figure 4-5, diffusion-limited behaviour is indicated by low currents, continuing well beyond the scan reversal potential, and a linear relation between capacity and the square root of scan rate in all cases. Although the low purity (indicated by XRD) of this sample reduces the available capacity, it is thought that the main diffusional restriction is the low electron mobility along the path from the outside of the agglomerate, where the carbon black is present, to the inner particles. At the optimum sucrose level of 0.22, Figure 4-6, the currents are much larger but diffusional limitation is apparent even at the low scan rates by decay of the current well before reversal and an almost linear plot of capacity *vs.* (scan rate)$^{-1/2}$. At the highest sucrose level, Figure 4-7, a lower capacity is seen at slow scan rates. However, the CVs show far smaller effects from diffusional limitations with the currents reducing to zero well before the scan reversal potential. The capacity at faster scan

rates is also higher than that seen in the SPR 0.22 sample. To further investigate these materials some SEM images (Figure 4-8) were taken of samples prepared in bulk rather than with the PoSAT method.

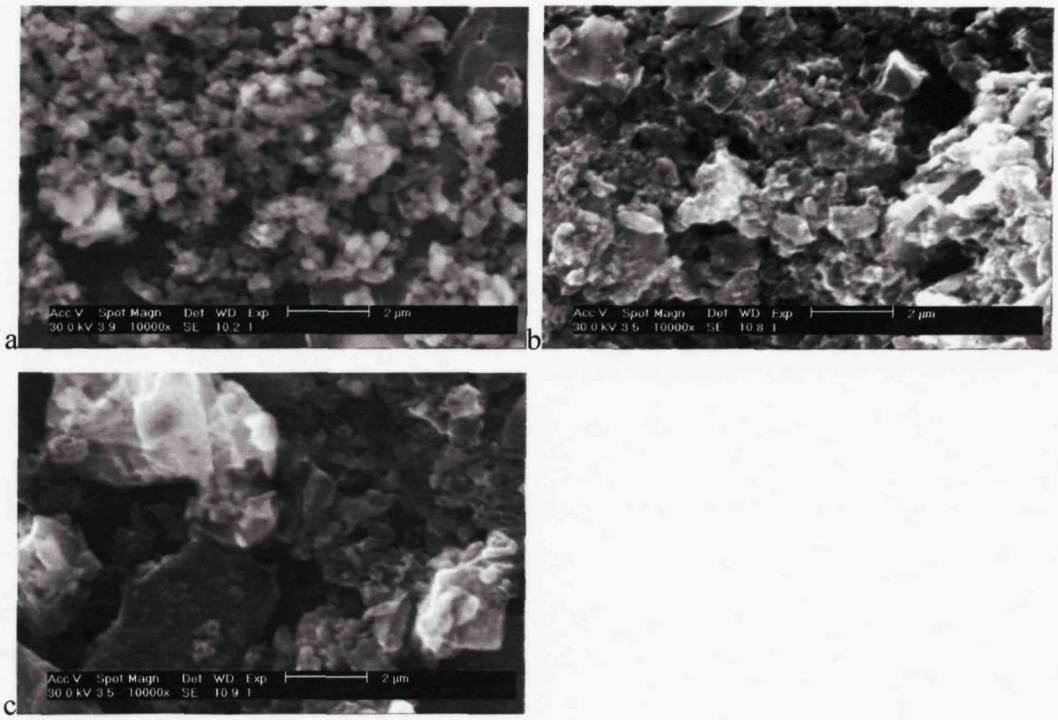

Figure 4-8 SEM images of bulk preparations of $LiFePO_4$ with sucrose to iron nitrate ratios of 0.25(a), 0.5(b) and 1.0(c).

It can be seen in Figure 4-8 that at low sucrose to iron nitrate ratios (0.25) a spherical like particle morphology can be seen around 500 nm in diameter. The samples prepared with higher sucrose ratios (0.5 and 1) have a more angular appearance and the particle size is larger and less uniform (0.5 to 2 and 1 to 5 μm). This suggests that the capacity at higher scan rates is likely limited by the particle size of $LiFePO_4$. However, this does not fit with the previous explanation of increased carbon coating thickness, also this does not explain why the materials prepared with a higher ratio perform better at higher scan rates. One possible explanation is represented below in Figure 4-9.

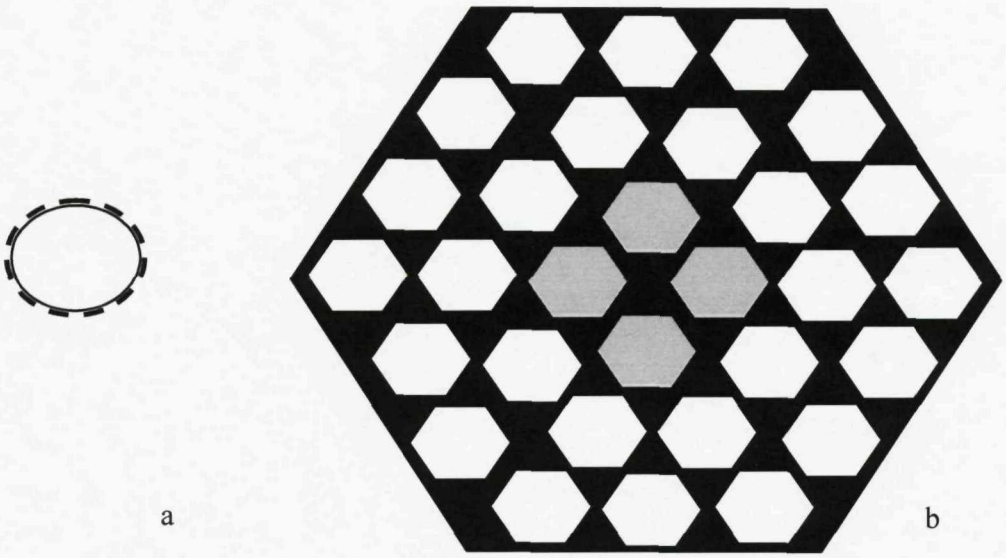

a b

Figure 4-9 Schematic representations of the composite formed during $LiFePO_4$ synthesis with low ratios of sucrose to iron nitrate (a) an high ratios (b).

When low ratios of sucrose (around 0.25) are used (Figure 4-9a) the particles have a thin coating of carbon which is sufficient to extract the maximum capacity at low rates; however, at higher rates the conductivity limits the materials performance. When higher ratios of sucrose (0.3 or above) are used (Figure 4-9b) a large carbon composite is formed containing small pockets of active material each well coated in carbon. The pockets in the centre of this composite are effectively disconnected from the electrolyte and therefore the maximum capacity is reduced. However, at increased rates those particles that are connected have a much improved performance.

4.1.3 Conclusions

Firstly this work has shown how the PoSAT technique has improved the accuracy of high throughput synthesis and capacity measurements in composite electrodes based on LiFePO4 by separating the pyrolytic synthesis from the composite formulation. The method was subsequently used to measure the performance of 64 battery electrodes with different amounts of pyrolytic carbon coatings by cyclic voltammetry at different scan rates. The results indicated an optimum carbon coating with an SPR of 0.22 and the detailed form of the results suggested new insights into the effects of the carbon coating on capacity and rate performance.

4.2 The effect of ball milling on $LiFePO_4$

Ball milling is a technique employed to reduce the particle size in of battery materials.(4) An active material powder is placed with balls in a sealed container this vessel is then shaken so that the impaction of the stainless steel balls between each other smashes up the powder, reducing the particle size. The length of the milling time can be important, too short and the technique will have little effect, too long and the crystal structure of the material can be destroyed. This section of work investigates the effect of milling time on the performance of $LiFePO_4$ and demonstrates another use of high-throughput method.

4.2.1 Experimental details

Array Preparation

Firstly a sample of $LiFePO_4$ was prepared via the sucrose pyrolysis method. A 50 mL solution containing 0.625 M of $LiCH_3COO.2H_2O$ (*Aldrich*), $Fe(NO_3)_3$ $.9H_2O$ (*Aldrich*), H_3PO_4 (*Aldrich*) and 0.156 M of sucrose was prepared. The solution was dried to form a solid precursor and then heated to 700 °C in flowing argon. This was then gently ground to a powder using a pestle and mortar. This preparation should provide an optimal carbon coated sample as investigated in section 4.1. A further sample of carbon coated $LiFePO_4$ was obtained from Aldrich for comparison. 0.5 g samples of each were sealed in stainless steel containers with approximately the same volume of 1 mm diameter stainless steel balls and around 10 mL of isopropanol (IPA) which formed an ink. These containers were then placed in a ball miller (Retsch MM200) and shaken for 10 mins, then 4 small (~0.3 ml) aliquots of the ink were removed from each container and transferred into the first column of an array of polypropylene vials, $LiFePO_4$ prepared via sucrose pyrolysis samples were placed in the top four rows and the Aldrich material in the bottom four rows. This process was then repeated for increasing milling times so that samples were removed after being milled for 0.5, 1, 1.5, 2.5, 4, 5 and 6 h. Once the 2.5 h sample was retrieved there was little sample left and the amount removed was reduced to ~ 0.1 mL for the 4 and 5 h

removal and ~0.05 mL for the 6 h removal. Composite electrode preparation began by adding two inks, 4% PVdF-HFP (*Aldrich*, polyvinylidene fluoride-co-hexafluoropropylene) and 4% AB (acetylene black, *Shawinigan, Chevron Phillips Chemical Company LP*) in cyclopentanone (CP) to the active material powders with five 1 mm zirconia beads placed in each tube. The inks were added to give electrodes with a composition of 65 % Active material (AM) 25 % AB and 10 % PVdF HFP. (However, the reduction in amount of active material from the 4 and 5 h samples meant the compositions were changed to 40 % AM, 50 % AB and 10 % PVdF HFP. The sample from 6 h had to be prepared in a composition altered still further of 20 % AM, 70 % AB and 10 % PVdF-HFP. The reason for these alterations in electrode compositions was to make it possible to process the inks into electrodes.) Then 14 μL aliquots of each ink was deposited onto the appropriate position on the array of aluminium current collectors and spread across the surface to form an even film of ink. At the same time, a 40 μL sample of each ink was deposited into an array of alumina micro-crucibles for thermogravimetric analysis as detailed below. The CP was evaporated from both arrays at room temperature before drying at 80 °C followed by evacuation. The samples on both arrays were then accurately weighed using a computer monitored balance.

Array Sample characterisation

Thermogravimetric Analysis and High Throughput X-ray Diffraction measurements were performed on the array of samples as described in Chapter 2. The High throughput electrochemical cell was also constructed as described in Chapter 2. The array was then cycled between 2.5 to 4.5 V vs. Li at the following scan rates: 0.05, 0.1, 0.4, 0.8 and 1.6 mV s^{-1}.

4.2.2 Results and discussion

High-throughput XRD Data

The use of ball milling has been reported to affect the structure and particle size of some materials(4). Particle size effects can be observed via line broadening of the peaks in XRD patterns if the crystallite thickness is reduced to less than 2000 Å(5).

Below in Figure 4-10 (sol-gel prepared $LiFePO_4$) and Figure 4-11 ($LiFePO_4$ purchased from Aldrich) selected XRD patterns from the array prepared are shown for materials milled for 0, 1, 2.5 and 5 h.

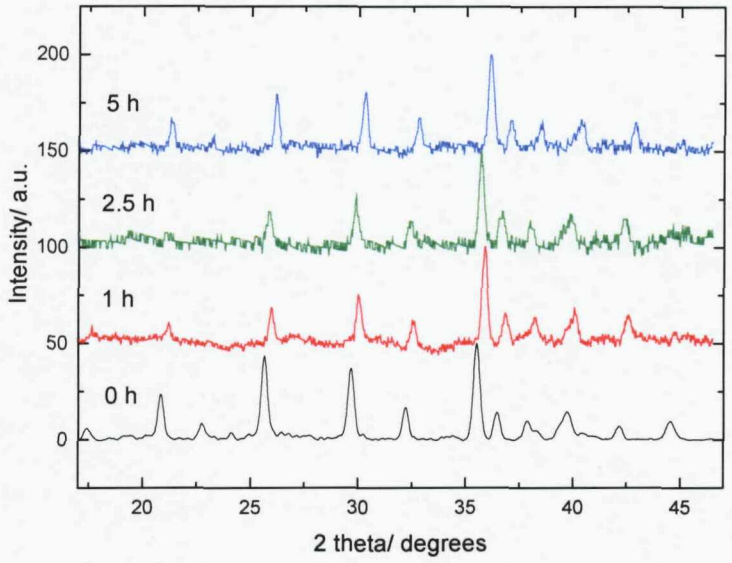

Figure 4-10 Selected XRD patterns from the milled samples (milling times indicated on the graph) of $LiFePO_4$ prepared using the sol-gel method.

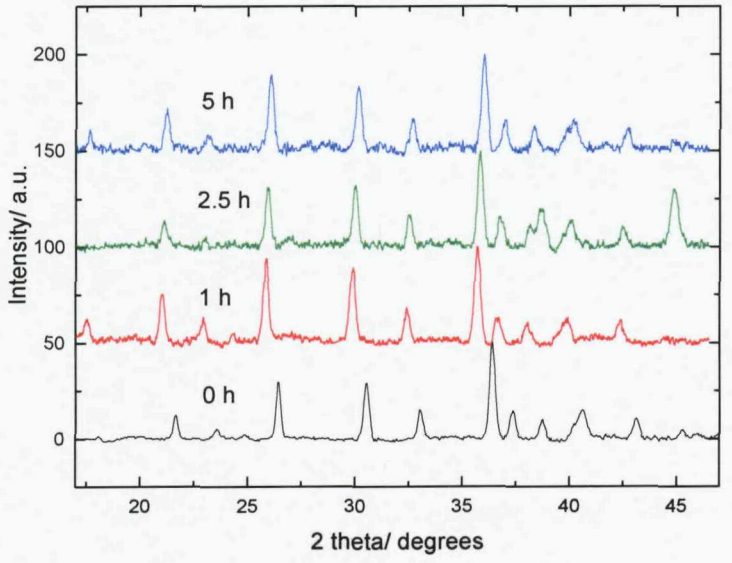

Figure 4-11 Selected XRD patterns from the milled samples (milling times indicated on the graph) of $LiFePO_4$ obtained from Aldrich.

The XRD patterns shown in Figure 4-10 and Figure 4-11 indicate no change in the structure of the material as a result of ball milling. No line broadening can be resolved and the milling has therefore not reduced the particle size to less than 2000 Å. In several of the patterns (0 h and 2.5 h Aldrich $LiFePO_4$ and 2.5 and 5 h sol-gel $LiFePO_4$) a peak is missing at around 15 degrees this is a result of an instrumental effect caused by the low angle portion of the general area detector being masked. Another unusual feature which has been seen in other data sets are peaks for the Aluminium substrate at 39 and 45 degrees which can be seen in the Aldrich sample after 2.5 h milling. Random shifts in the 2 theta values of the peaks can also be seen, this is presumably a result of the slight changes in sample height resulting from the high-throughput measurement.

High-throughput Electrochemical Characterisation

Below in Figure 4-12 the CVs (scan rate 0.05 mV s^{-1}) recorded for powders of $LiFePO_4$ which had been ball milled for increasing time periods are shown. Generally peaks for charge and discharge of $LiFePO_4$ can be seen at around 3.4 V. The low currents observed at higher milling times can be explained as the lower mass loading of active material in the composite electrode discussed above in the experimental details. In the case of the sol-gel prepared $LiFePO_4$ at milling times of 0.167 and 0.5 h, lower currents are also observed; these did not result from active mass changes; this indicates the improved performance in the 1 and 1.5 h samples. No obvious performance enhancement can be seen for the milled Aldrich $LiFePO_4$.

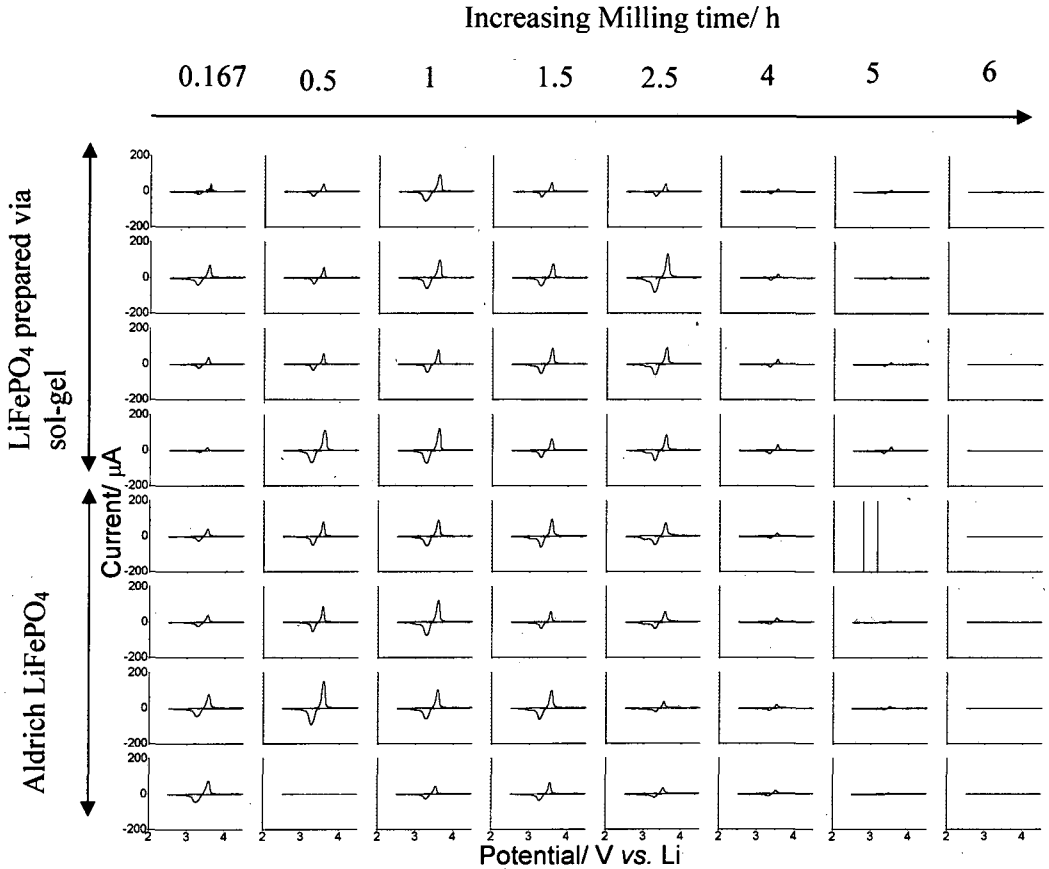

Figure 4-12 CVs from an array of ball milled $LiFePO_4$ samples recorded at 0.05 mV s^{-1}.

To examine the performance effects of ball milling more closely the CVs shown and others recorded at 0.1, 0.4, 0.8, 1.6, and 3.2 mV s^{-1} were used to calculate the specific capacities the results of this are shown in Figure 4-13 for sol-gel prepared $LiFePO_4$ and Figure 4-14 for the Aldrich obtained $LiFePO_4$.

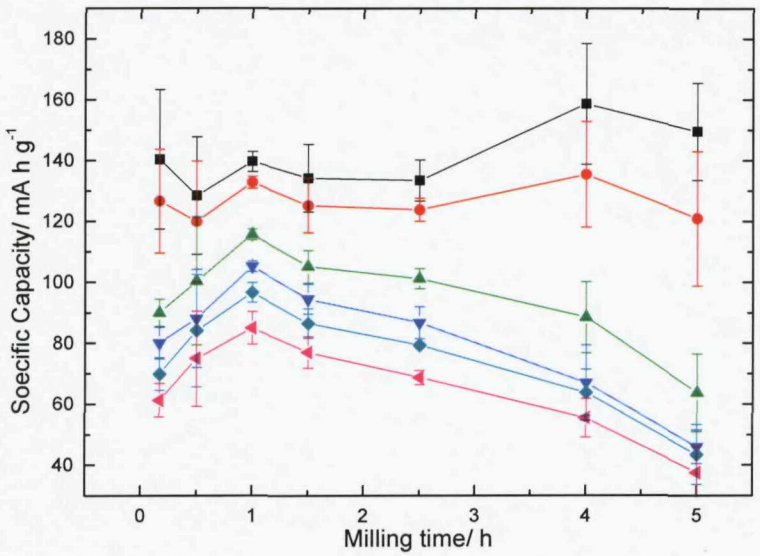

Figure 4-13. Capacity of $LiFePO_4$ prepared via the sucrose pyrolysis method with a SPR of 0.25 and exposed to various milling times. The capacity is shown for the following scan rates 0.05 (-■-), 0.1 (-●-), 0.4 (-▲-), 0.8 (-▼-), 1.6 (-◆-), and 3.2 mV s^{-1} (-◀-). Capacities were averaged for 4 repeat samples and error bars shown are 1 standard deviation calculated based from the 4 repeat samples.

In Figure 4-13 at slow scan rates (0.05 mV s^{-1}, 0.1 mV s^{-1}) all the samples (samples prepared with 6 h of milling are not shown as the extremely low mass loading resulted in immeasurable currents) show capacities of approximately 140 mA h g^{-1} within error bars. At faster scan rates (> 0.4 mV s^{-1}) the materials exposed to milling times greater than 1.5 h and less than 0.5 h show significantly lower capacities than the other samples. The material which was milled for 1 h performed the best with a capacity of ~80 mA h g^{-1} at 3.2 mV s^{-1}; whereas, the worst materials which were milled for 0.167, 4 and 5 h showed significantly reduced capacities of around 60 mA h g^{-1}.

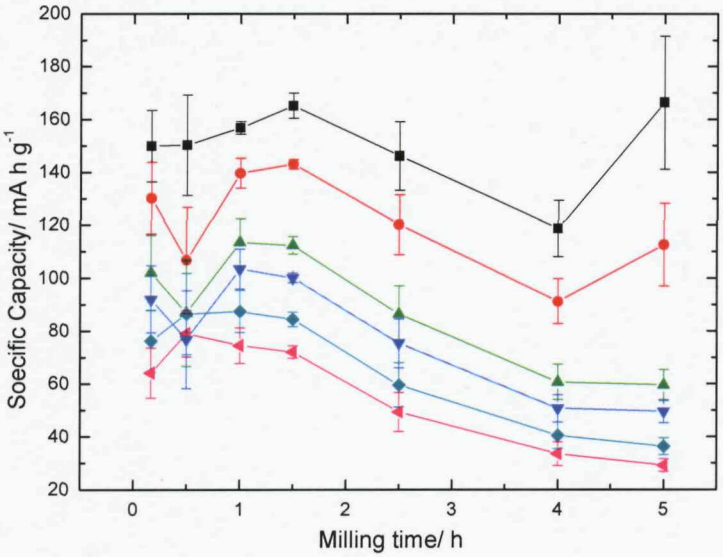

Figure 4-14. Capacity of $LiFePO_4$ obtained from Aldrich after being exposed to various milling times. The capacity is shown for the following scan rates 0.05 (-■-), 0.1 (-●-), 0.4 (-▲-), 0.8 (-▼-), 1.6 (-◆-), and 3.2 mV s^{-1} (-◀-).

The results shown in Figure 4-14 indicate that at slow scan rates that the material with the highest capacity was milled for the shortest times between 0.167 and 1.5 h (~150 mA h g^{-1}); longer milling times resulted in a lowering capacities. No significant improvements at higher rates are seen for any degree of milling. Further analysis of these materials will not be presented as no interesting improvements are seen.

To better understand the performance enhancement seen in the samples of sol-gel $LiFePO_4$ the CVs for milling times of 0.167, 1 and 5 h recorded at 3.2 mV s^{-1} are shown below in Figure 4-15.

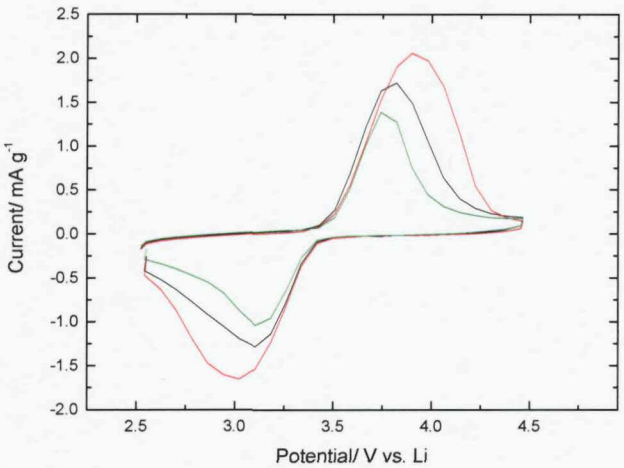

Figure 4-15 CVs recorded at a scan rate of 3.2 mV s^{-1} for $LiFePO_4$ prepared via the sol-gel route for samples milled for 0.167(—), 1(—) and 4 h (—).

There is little difference in the shape of the CVs shown in Figure 4-15; the initial IR drop region shows the same resistance for all materials, all samples return to zero current before the scan reversal potential. This analysis therefore gives little insight into the ball milling performance enhancement. However, the larger currents seen for the 1 h milled samples confirm the improvement.

SEM images

The high resolution FEG-SEM images shown below in Figure 4-16 and Figure 4-17 were recorded to investigate the effect of any change in sample morphology and particle size with milling time.

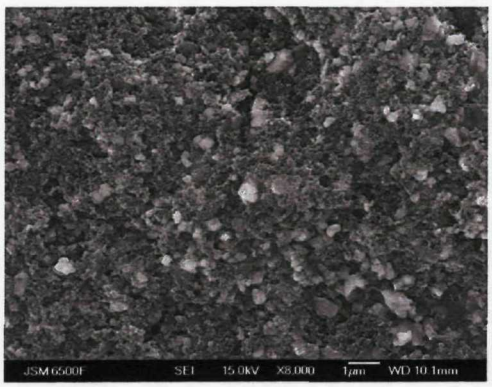

0.167 h a

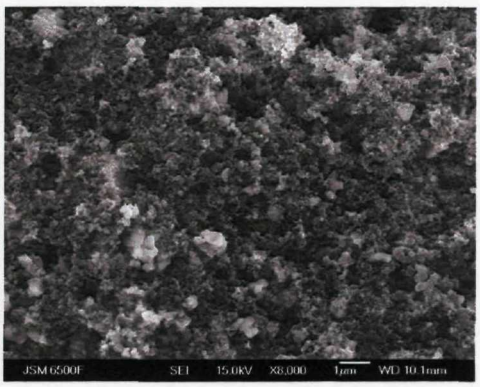

1 h a

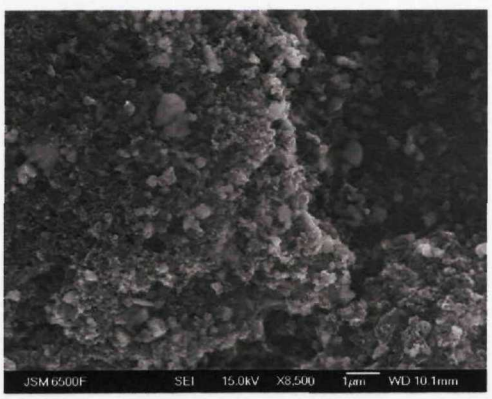

5 h a

Figure 4-16 SEM images (magnification 8500) of sol-gel prepared $LiFePO_4$ which had been exposed to the indicated ball-milling times.

The 8500 times magnification images shown in Figure 4-16 show a small sharp edged sample morphology. The typical particle size seen is approximately 100 nm, however samples as large as 1 μm can be seen. A very rough estimation to determine whether the milling is having an effect on the particle size is to count the number of particles greater than 500 nm in the samples milled for various time periods. The sample milled for 0.167, 1 and 5 h show >30 (accounting for a ~12% of the volume fraction of all the particles), ~15(~3.3%) and ~15(~3.3%) particles greater than 500 nm respectively.

This measurement whilst somewhat subjective does lead to the conclusion that the ball milling is breaking down some of the larger agglomerates in the initial material and causing a reduction in particles size. Also it suggests that in the 0.167 h milled sample ~12 % of the sample will be stored in large particles which will have a slower particle time constant discussed below.

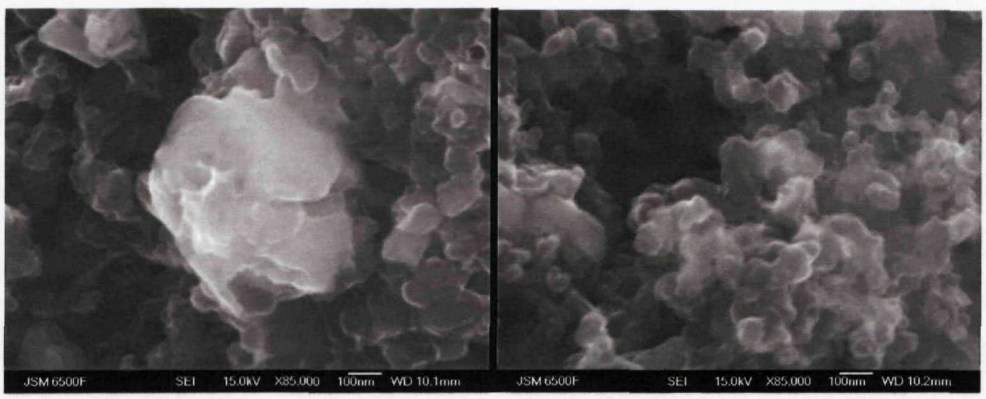

0.167 h b 1h b

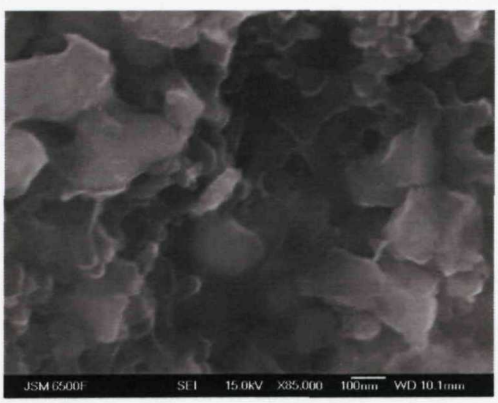

5h b

Figure 4-17 SEM images(magnification 85000) of sol-gel prepared $LiFePO_4$ which had been exposed to the indicated ball-milling times.

The SEM images shown in Figure 4-17 are of the same samples as in Figure 4-16 but at much high magnification (×85000), the three images show the same general sample morphology. However, the particle size of the 1 h milled sample (~100 nm) is smaller than the 0.167(~300 nm) and 5 h (~200 nm) samples. In the sample milled for 0.167 h a mixed morphology is seen; a central large particle surrounded by smaller fragments. In the case of the 1 h sample only the smaller were fragments were observed as shown in Figure 4-17. In the 5 h milled samples the agglomerates appear to have disappeared, however, the global particle size has also increased. These observations are

summarised as the volume fraction of material corresponding to each particle size in Table 4-1.

Table 4-1 Volume fraction of various particle sizes determined from SEM images in Figure 4-16 and Figure 4-17.

	Percentage of volume contain in particles:			
Milling time/ h	>500 nm (~600 nm)	<500 but >100 nm (~200 nm)	<100 (~100 nm)	Average particle size/nm
0.167	~10	~10	~80	160
1	~3	~0	~87	105
5	~3	~87	0	192

The SEM images suggest that the improved performance of the sol-gel preparation is likely to be because of the optimisation of sample morphology and particle size. This can be explained by examining what effects the time constant of discharge of a particle, summarised by Equation 4-1(6).

$$\tau = \frac{l^2}{D}$$

Equation 4-1

τ = Particle time constant/ s

l = Particle radius/ cm

D = Diffusion coefficient/ $cm^2\ s^{-1}$

According to this equation a reduction in the average particle radius will result in a smaller average time constant of discharge for the electrode. This explains why the sol-gel $LiFePO_4$ which was milled for 1 h performs the best as it has the smallest average particle size (Table 4-1). The material which shows the next best performance at high rates of those examined using the SEM is the 0.167 h sample. This sample contains large and small particles therefore having a large spread of time constants; however, the average particle size is the second smallest (Table 4-1). This means that whilst a limited portion of the material becomes effectively disconnected at higher

rates in the larger particles; the smaller particles still perform as well as the 1 h milled sample. In the case of the sample milled for 5 h the average particle size is the largest and therefore at higher rates the material will on average perform worse than in the 1 h milled sample as seen in Figure 4-13.

In the case of the Aldrich $LiFePO_4$ no effect from milling is seen. The reason for this may lie in the fact that this is a commercially available product sold as battery grade i.e. it is likely that it has already been optimised before sale and any further milling has little effect. The poor performance at higher milling times might also result from increased particle size or possibly the excessive milling removes the intimate carbon layer on the surface of the particles reducing the material conductivity and performance.

4.2.3 Conclusions

This work has shown how studies of this nature into the processing of active material can be performed on the high throughput array, highlighting the versatility of the method. The work has shown that this aspect of electrode fabrication can have an effect on the material performance. The sol gel prepared electrodes showed an increased rate performance when a 1 h milling time was used and detrimental effects were seen at longer milling times; this milling time compares well with a report from the literature(4). However, the material obtained from Aldrich showed no improvement from the milling process presumably a result of optimisation before purchase.

4.3 Composite Electrode Fabrication

As discussed in Chapter 1 a cathode electrode is made up of a composite structure containing active material, acetylene black conductive additive and polymer binder. The amount of AB needed must be optimised such that the electrode is above the percolation threshold and the charge discharge reaction is not limited by the electronic conduction from the particles to the current collector. However, an excess of AB should not be added as this will reduce the gravimetric and volumetric capacity of the material unnecessarily. This study aims to find the required amount of AB needed to achieve this in the case of $LiFePO_4$.

4.3.1 Experimental details

Array Preparation

Two inks were prepared, the first containing 5 wt. % $LiFePO_4$ (Aldrich, carbon coated, 99.5+ %, battery grade) with 0.5 wt. % of PVdF-HFP and the second 5 wt. % AB with 0.5 wt. % PVdF-HFP. In an array of 64 polypropylene vials these inks were mixed (using *Finnpipette* adjustable-volume digital pipettes) such that the percentage of AB within the solids in each ink were 0, 1, 2, 3, 4, 5, 6, 7.5, 9, 10, 12.5, 15, 18, 20, 25 and 30 %, 4 repeats of each percentage were made. Then 14 μL aliquots of each ink was deposited onto the appropriate position on the array of aluminium current collectors and spread across the surface to form an even film of ink. The CP was evaporated from both arrays at room temperature before drying at 80 °C followed by evacuation. The samples on both arrays were then accurately weighed using a computer monitored balance. The electrodes were then used to construct a cell before being cycled between 2.5 to 4.5 V at 0.05 mV s^{-1}.

4.3.2 Results and discussion

Below in Figure 4-18 the CVs recorded for the array described above are shown. The CVs of the electrodes prepared with less than 15 % AB show clear signs of resistance limitation. These CVs show a slow increase in current during the potential sweep with the peak currents being seen at higher voltages. The CVs for electrodes containing greater than 15 % show the usual shape for $LiFePO_4$(7) with no obvious distortion.

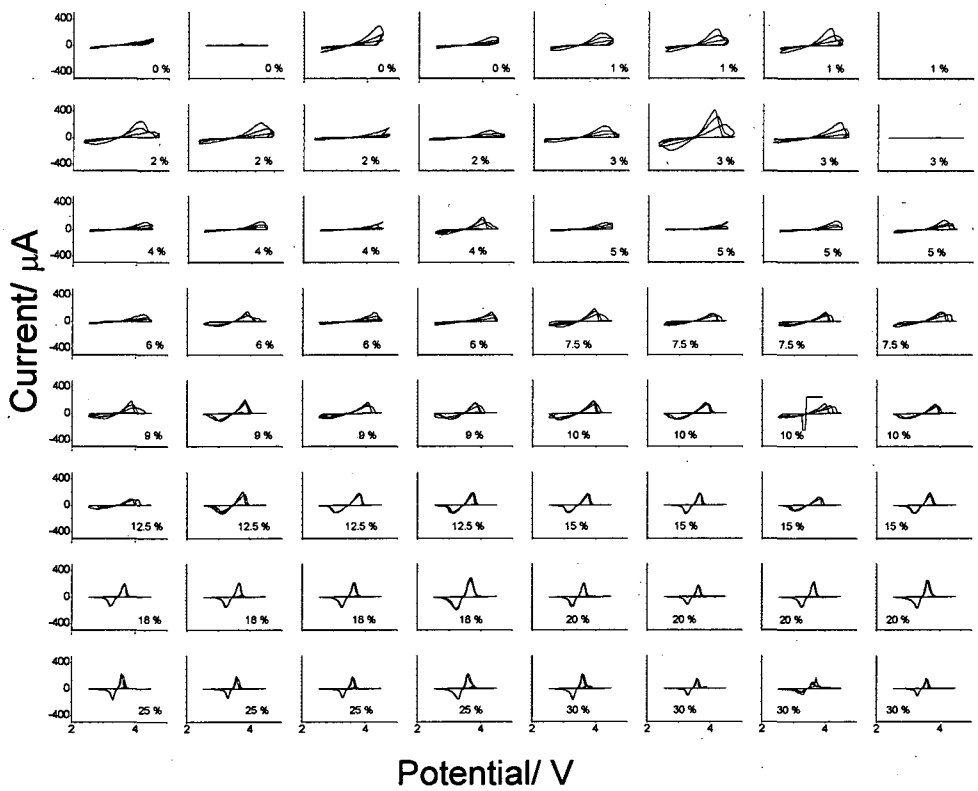

Figure 4-18 CVs from the array of electrodes investigating the effect of AB additive on electrode performance. The percentage of AB in each electrode is also shown here.

Using the CVs in Figure 4-18 the charge and discharge capacities were calculated and are shown for the first 2 cycles in Figure 4-19, the capacity values were averaged for each 4 electrodes containing the same carbon content.

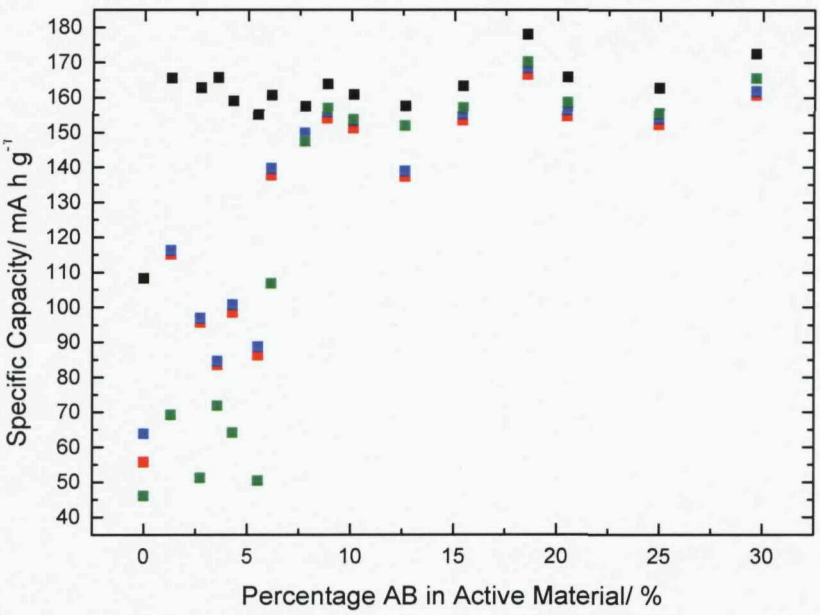

Figure 4-19 Capacities calculated from the array of CVs shown in Figure 4-18. Each point represents the average value of the four repeat electrodes on the array. Capacity values are shown for the first 2 cycles charge and discharge: cycle 1 charge(■), cycle 1 discharge(■),cycle 2 charge (■)and cycle 2 discharge(■).

The amount of carbon required to obtain the maximum capacity or percolation threshold can be seen in Figure 4-19 to be 2.5 % for the first cycle and 7.5 % for those cycles there after. Presumably, the capacity reduction at low carbon on continued cycling is due to a break down in the connectivity of the AB linking the current collector to the particle possibly as a result of volume contraction on the extraction of Li. To highlight the effect of the carbon content selected CVs are shown in Figure 4-20.

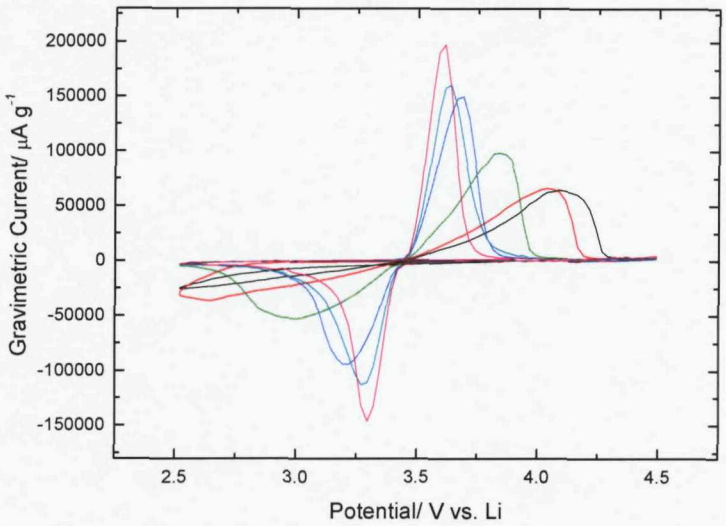

Figure 4-20 CV's of $LiFePO_4$ electrodes containing 10 (——), 12.5 (——), 15 (——), 18 (——), 20 (——) and 30 (——) % percent AB in the electrode.

The shape of the CVs is determined by a number of parameters. The cell resistance results in an IR drop seen in the CV as the gradient approaching the peak currents both on charge and discharge. The low carbon loading samples show (Figure 4-20) the smallest gradients indicating a resistance limitation; the cell resistance has been calculated from this gradient and is shown in Figure 4-21. This shows that a sharp decrease in resistance is seen when greater than 17.5 % AB is used. The resistances of the discharge peaks are higher than those of the charging peaks. This could relate to a breakdown in connectivity in the composite as a result of shrinkage in the AM during charging (from lithium ion extraction).

Figure 4-20 and Figure 4-21 also show that even between those electrodes above the percolation threshold increased amounts of carbon still reduce the cell resistance. This suggests that whilst all the capacity maybe extracted with relatively small amounts of carbon the galvanostatic discharge plateau maybe distorted and the rate performance of these electrodes may be affected. This leads to the conclusion that when an electrode is made the application needs to be considered and the appropriate amount of AB added. Therefore, high carbon contents should be used to fabricate electrodes for PoSAT arrays as these are intended to test the performance of the material and not make commercial battery electrodes.

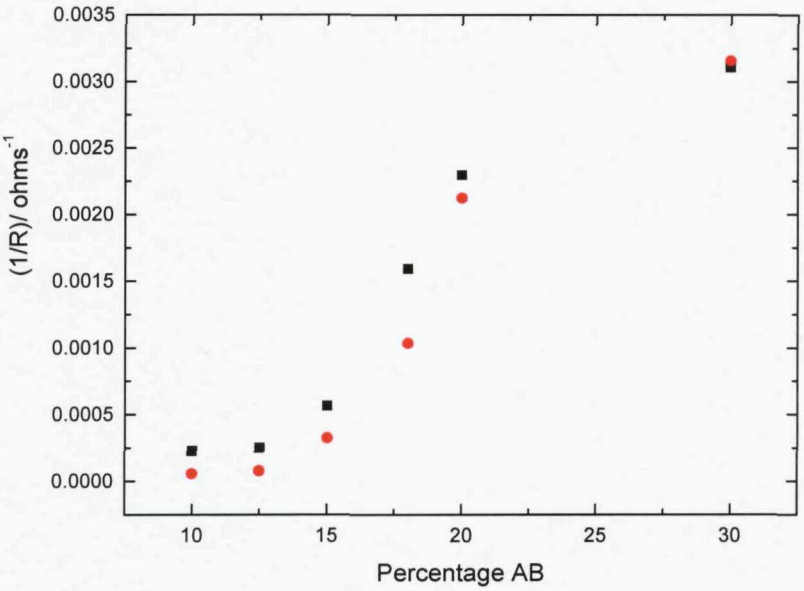

Figure 4-21 Resistances calculated from the CVs in Figure 4-20. The rising slope on the charge peak (■) and the falling slope on the discharge peak (●) were used to calculate the resistances.

4.3.3 Conclusions

This work has shown the importance of optimising the amount of carbon used to percolate the battery electrodes. To extract the maximum capacity out of the material as little as 7 % AB is required, however, if less than 20 % is used some resistance limitations can still be observed in the shape of the CVs.

4.4 Conclusions Chapter 4

Three material systems have been studied in this chapter which highlight three applications of the high-throughput method. The technique was first used to fabricate new active materials and optimise the synthetic route, secondly milling methodologies showed how the technique could be used to investigate material processing, and finally the method was applied to the method of electrode fabrication.

The results for the carbon coating of $LiFePO_4$ materials showed that an optimal level of carbon coating is required to improve the conductivity. However, if too much sucrose is used the large particle agglomerates are formed resulting in a reduced capacity. This work also confirmed that the investigation of $LiFePO_4$ materials via the PoSAT method can be relied upon to give results comparable with those seen in bulk measurements.

The second and third studies into milling and the amount of AB are closely related, as they are both associated with the electrode fabrication procedure. It was found that by using a 1 h milling time for the sol gel prepared $LiFePO_4$ a material which exhibited a higher rate performance could be obtained. The SEM images of the milled powders showed that the 1 h samples resulted in the smallest agglomerate particle size. Investigations into the amount of AB required to obtain the highest rate performance material was determined to be around 20 %. If lower amounts of AB are used the recorded CVs showed significant resistance limitations. However, at low rates almost all the capacity could still be extracted when only 7 % AB was used.

4.5 References Chapter 4

1. A. D. Spong, G. Vitins and J. R. Owen, *Journal of the Electrochemical Society*, **152**, A2376 (2005).

2. A. D. Spong, High-Throughput Discovery of Lithium Battery Materials, in, University of Southampton, Southampton (2005).

3. R. Dominko, M. Bele, M. Gaberscek, M. Remskar, D. Hanzel, S. Pejovnik and J. Jamnik, *Journal of the Electrochemical Society*, **152**, A607 (2005).

4. J. M. Tarascon, M. Morcrette, J. Saint, L. Aymard and R. Janot, *Comptes Rendus Chimie*, **8**, 17 (2005).

5. A. R. West, *Solid State Chemistry and its Application*, John Wiley & Sons Ltd. (1984).

6. J. R. Owen, *Chemical Society Reviews*, **26**, 259 (1997).

7. D. Y. W. Yu, C. Fietzek, W. Weydanz, K. Donoue, T. Inoue, H. Kurokawa and S. Fujitani, *Journal of The Electrochemical Society*, **154**, A253 (2007).

Chapter 5 Compositional variations $LiMPO_4$

The $LiMPO_4$ (M =Fe, Ni, Mn and Co) materials have received much attention within the literature. In this chapter the materials $LiFe_{1-x}Mn_xPO_4$, $LiFe_{1-x}Mg_xPO_4$, $Li_{1-x}Mg_{x/2}FePO_4$ and $LiMn_{1-x}Mg_xPO_4$ are studied using the PoSAT method.

5.1 $LiFe_{1-x}Mn_xPO_4$

The substitution of Fe for Mn in $LiFePO_4$ would increase the energy density of the material as a portion of the discharge would occur with an increased voltage. However, this material suffers from poor conductivity which limits the practical capacity obtained during charge and discharge. The aim of this study was to investigate the effect of Mn substitution for Fe while varying the degree of carbon coating.

5.1.1 Experimental Details

PoSAT Array Preparation

Two 500 mL solutions were prepared the first containing 0.625 M of $LiCH_3COO.2H_2O$ (Aldrich), $Fe(NO_3)_3$ $.9H_2O$ (Aldrich) and H_3PO_4 (85 wt. %, Aldrich), and the second 0.4 M $LiCH_3COO.2H_2O$ (Aldrich), $Mn(CH_3COO)_2.4H_2O$ (Aldrich) and H_3PO_4 (85 wt. %, Aldrich). Aliquots of the two solutions were mixed down the rows of an array of quartz tubes, so that each row contained a different value of x in $LiFe_{1-x}Mn_xPO_4$, x = 0, 0.1, 0.2, 0.3, 0.5, 0.7, 0.9, 1. A 100 mL solution of 2 M sucrose was then prepared, this was added in different amounts to each column so that from left to right they contained a sucrose to metal ion (Fe + Mn) ratio of 0.10, 0.15, 0.2, 0.22, 0.24, 0.27, 0.30, 0.35. These solutions were then agitated using a *Fischer* "Whirlimix" Vortex mixer to ensure homogeneity before being placed in an oven at 70 °C for 12 h to remove the water. The array of precursor solids was then calcined in an argon atmosphere at 700 °C using a large bore (80 mm diameter) tube furnace (Lenton). After cooling, the products were crushed to a powder using a glass rod attached to a drill. Composite electrode preparation began by adding two inks, 4%

PVdF-HFP (*Aldrich*, polyvinylidene fluoride-co-hexafluoropropylene) and 4% AB (acetylene black, *Shawinigan, Chevron Phillips Chemical Company LP*) in cyclopentanone (CP) to the active material powders with five 1 mm zirconia beads placed in each tube. The inks were added to give a final mass ratio of 10 % PVdF-HFP, 25 % AB and 65 % active material and then mixed using the vortex mixer. Then 14 μL aliquots of each ink was deposited onto the appropriate position on the array of aluminium current collectors and spread across the surface to form an even film of ink. At the same time, a 40 μL sample of each ink was deposited into an array of alumina micro-crucibles for thermo-gravimetric analysis as detailed below. The CP was evaporated from both arrays at room temperature before drying at 80 °C followed by evacuation. The samples on both arrays were then accurately weighed using a computer connected balance.

Array sample characterisation

This array was then cycled between 2.5 and 4.5 V at the following scan rates; 0.05, 0.1, 0.2, 0.4, 0.8, 1.6 mV s^{-1}. XRD patterns were recorded and TGA analysis was performed on each electrode prepared on the array.

Bulk sample preparation

Several bulk preparations were also undertaken for comparison. The same synthesis method was used as for the array except the volumes were scaled up to give a total volume of 20 mL. $LiFePO_4$, $LiFe_{0.7}Mn_{0.3}PO_4$, $LiFe_{0.5}Mn_{0.5}PO_4$ and $LiMnPO_4$ were all prepared with an SPR of 0.25. These solutions were then dried and placed in ceramic crucibles and heated under the same conditions. The active materials were then prepared into PTFE films as described previously and were cycled galvanostatically at various C-rates between 2 and 4.5 V.

5.1.2 Results and Discussion

X-ray Diffraction Patterns

The XRD patterns recorded for the array indicated a pure olivine phase had been formed in all samples of $LiFe_{1-x}Mn_xPO_4$ ($x<0.5$) when an SPR value greater than 0.15 was used. In samples prepared where $x>0.5$ pure phase materials were seen for all SPR ratios.

Below in Figure 5-1 a selected series of XRD patterns are shown for materials formed using 0.35 SPR.

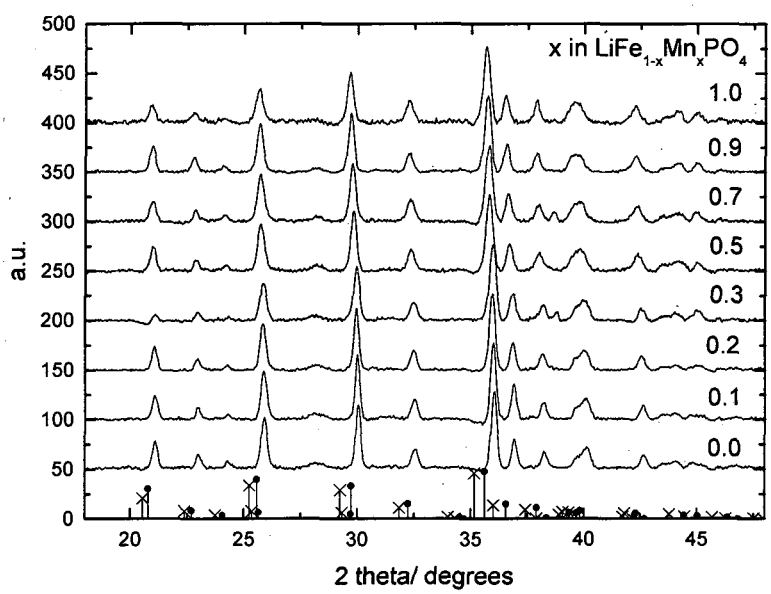

Figure 5-1 X ray diffraction pattern for products formed from selected samples. The SPR used in this column was 0.35. The value of x in $LiFe_{1-x}Mn_xPO_4$ is shown. Also shown are the standard measurements of (•)$LiFePO_4$ (1) and (×)$LiMnPO_4$(2).

Figure 5-1 shows that as x is increased from 0 to 1 there is a gradual shifting of the peak position. This relates to a change in the unit cell parameters. To quantify this effect the peaks were indexed and the unit cell volume calculated; the results are shown in Figure 5-2.

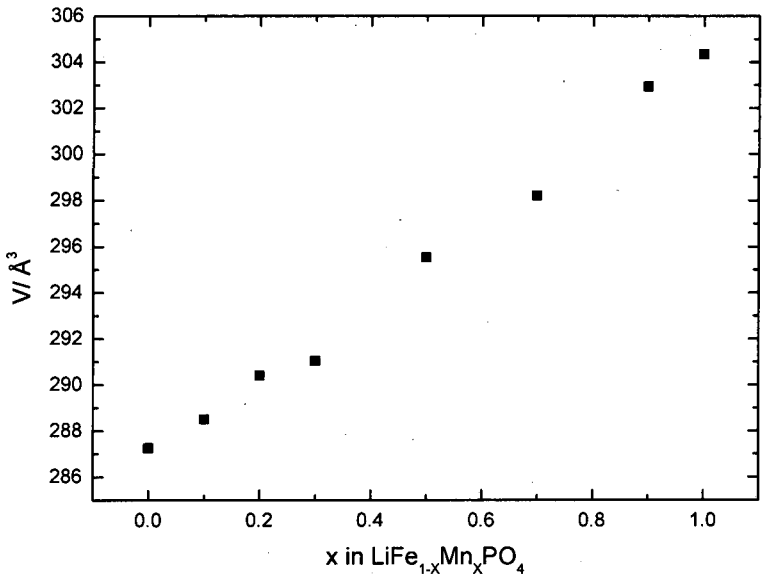

Figure 5-2 Unit cell volume of $LiFe_{1-x}Mn_xPO_4$.

The linear increase of the unit cell volume with x is seen in Figure 5-2 indicating a Vegard's shift(3) and suggests solid solution mixing of the iron and maganese. In the literature Yamada et al.(4) and Padhi et al.(5) report a similar result, however, their unit cell volumes do differ slightly from this result; 292 to 304 and 291 to 303 respectively. This is attributed to the problems of scatter in the high-throughput method disscused in Chapter 3.

High-throughput Electrochemical Measurements

The CVs (scan rate 0.05 mV s^{-1}) for the array are shown below in Figure 5-3. The highest currents were observed for samples containing high amounts of carbon (SPR > 0.2) and low amounts of Mn ($x \leq 0.5$). At high manganese contents ($x > 0.5$) a larger SPR is required to see the maximum currents even though the correct phase has formed. This is assumed to be because of a reduction in conductivity reported in the literature(6).

As previously discussed the sucrose role in this reaction is not only to coat the particles in carbon but also to reduce the Fe(III) to Fe(II). Shown as blue regions in Figure 5-3 are the samples above the threshold amount of sucrose required to form pure phase materials as observed via XRD measurements. The regions below the threshold (green) are also indicated.

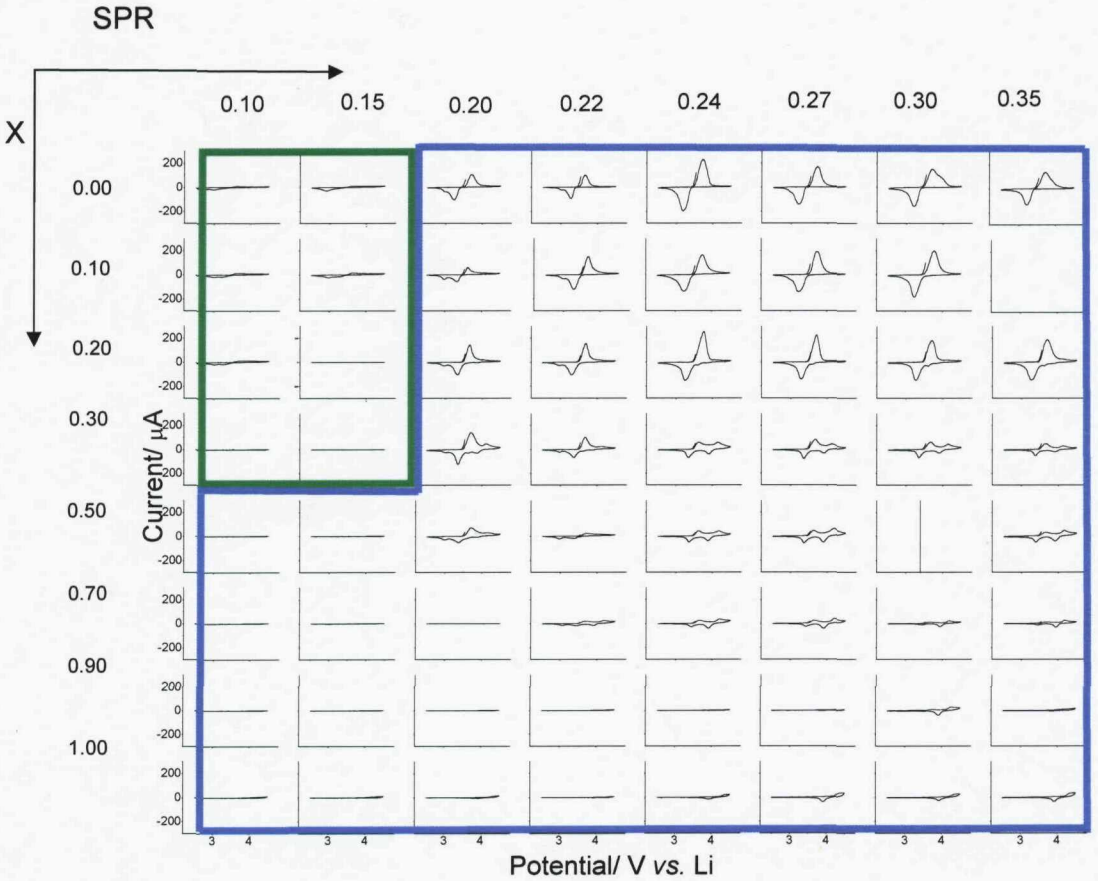

Figure 5-3 CVs (0.05 mV s^{-1}) for the 64 $LiFe_{1-x}Mn_xPO_4$ materials.

Using the CVs in Figure 5-3 the specific capacities of each material was calculated. The effect of sucrose on selected materials capacity (percolation profiles) is shown in Figure 5-4. When x was increased a reduction in the maximum capacity was observed. The amount of sucrose required to cause a significant increase in observed capacity (or percolation) also increases with x. This result is presumed to be related to the reduced electronic conductivity of the $LiMnPO_4$ (as the Mn content increases the conductivity decreases). As a reference the conductivity of $LiFePO_4$ is reported by Delacourt et al.(6) as ~1.5×10^{-9} at 25 °C whereas $LiMnPO_4$ is ~3×10^{-9} at 300 °C. In the $LiFe_{0.7}Mn_{0.3}PO_4$ material as the SPR is increased beyond the percolation threshold the capacity decreases. It is believed that this effect is related to the random errors on the measurement rather than a real effect.

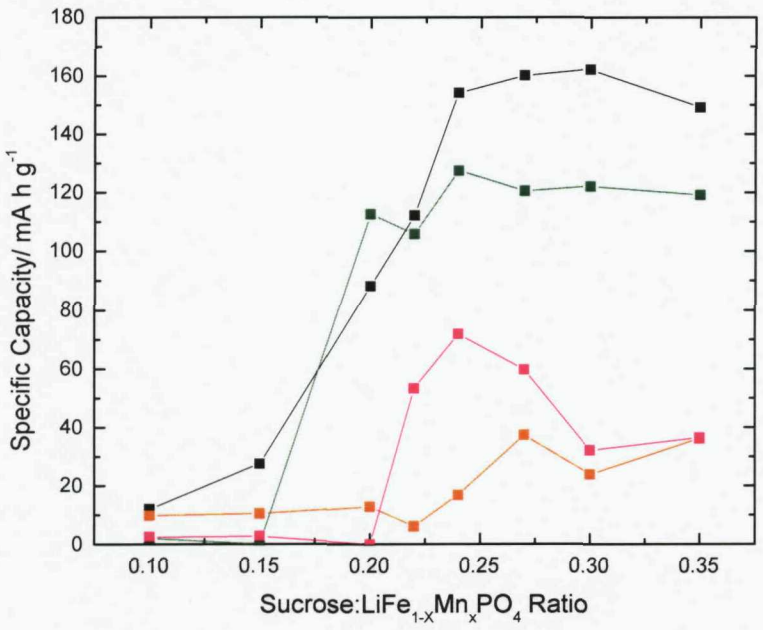

Figure 5-4 Specific Capacity vs. Sucrose:$LiFe_{1-x}Mn_xPO_4$ ratio for x values 0(—), 0.3(—), 0.7(—) and 1(—) to investigate the percolation threshold of these materials. These capacities were calculated from the CVs shown in Figure 5-3.

The trend of decreasing observed capacity with Mn content is shown below in Figure 5-5, showing a drop from 160 to 10 mA h g^{-1} with x changing from 0 to 1.

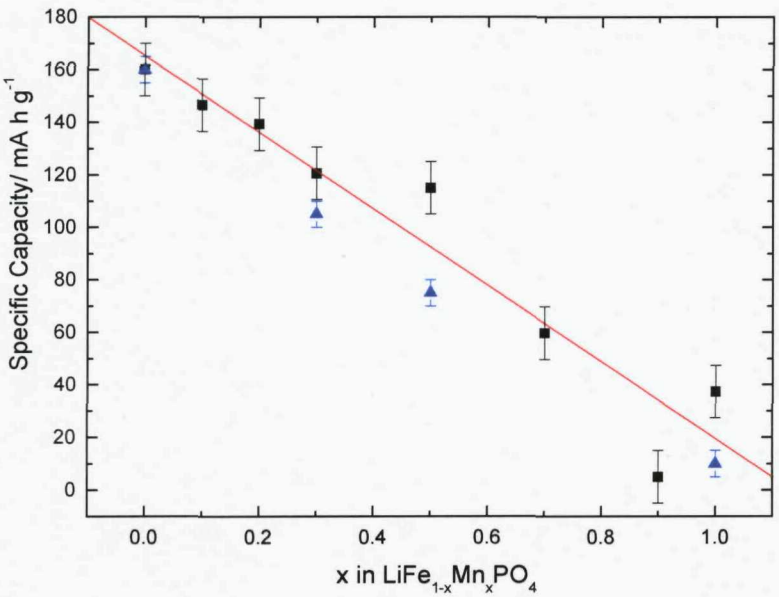

Figure 5-5 Specific capacity *vs.* x in $LiFe_{1-x}Mn_xPO_4$ measured using standard battery techniques (SPR 0.25) (▲) and combinatorial techniques (SPR 0.3) (■). Also shown is a line of best fit for the *combinatorial measurements* (—). The standard materials were cycled between 2.5 and 4.5 V under galvanostatic control at a rate of C/10.6. The cyclic voltammograms used to make the combinatorial measurements were cycled between 2.5 and 4.5 V at a scan rate of 0.05 mVs^{-1}; this equates to an approximate rate of C/11.1.

Also shown in Figure 5-5 is a series of points recorded using the standard small cell test method from materials prepared in the bulk. An identical trend is seen, and confirms that the combinatorial method can be relied upon to generate data of a similar quality to that of conventional methods.

For selected electrodes on the array expanded versions of the CVs at various scan rates are shown in Figure 5-6.

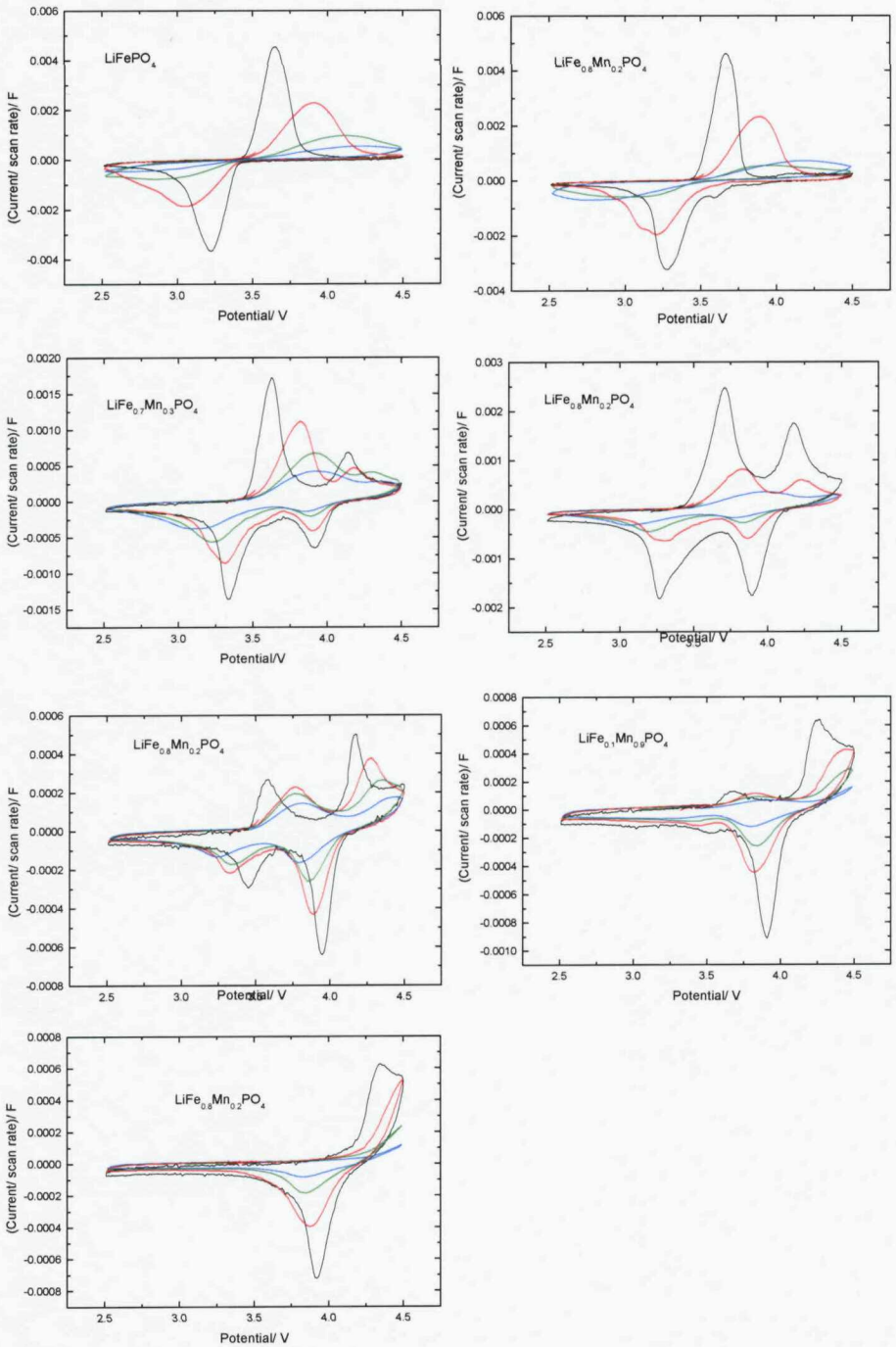

Figure 5-6 CVs $LiFe_{1-x}Mn_xPO_4$ divided by scan rate and shown for 4 different scan rates 0.05 (——), 0.2 (——), 0.4 (——) and 0.8 (——) mV s^{-1}. The SPR used for these preparations was 0.35.

The CVs in Figure 5-6 show charge and discharge peaks around 3.4 and 4.1 V for Fe^{2+}/Fe^{3+} and Mn^{2+}/Mn^{3+} respectively with varying peak heights dependent on the degree of manganese substitution. The ratio between the Mn and Fe peak heights corresponds to the composition. This is confirmed in Figure 5-7, where a linear trend is seen which has a gradient of approximately 1 and intercepts the axis at the origin.

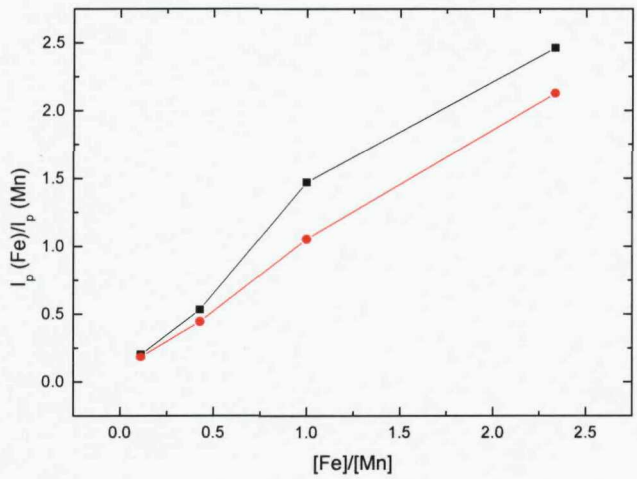

Figure 5-7 The linear relationship of the ratio of peak heights for the Fe (I_p (Fe)) and Mn (I_p (Mn)) *from CVs recorded at 0.05 mV s^{-1} and the ratio of composition. This relationship is shown for* both the charge (-■-) and discharge (-●-) peaks.

A notable change in peak shape of the Fe^{2+}/Fe^{3+} redox with increased substitution of Mn is also noted from Figure 5-6 as the sharp charge discharge peaks around a voltage point change such that the extraction and insertion of Li^+ occur over the same voltage range. This is believed to result from a change in discharge reaction from 2 phase to 1 phase on substitution of Fe for Mn proposed by Yamada et. al., who showed a phase diagram reproduced in Figure 5-8(4). A change in peak shape is also seen in the Mn^{2+}/Mn^{3+} peaks, however, it is believed to be a result of severe electronic conductivity limitations which distorts the CV particularly on charging in the pure Mn material.

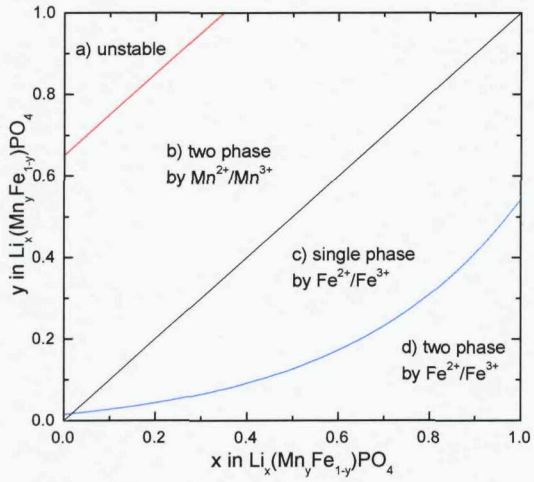

Figure 5-8 The (x, y) two-dimensional phase diagram of the $Li_x(Mn_yFe_{1-y})PO_4$ ($0 \leq x,y \leq 1$) system obtained using XRD and Mössbauer spectroscopy. Information is simply given on the single-phase or two phase matter together with the valence states of Mn and Fe. The map is divided into four areas: (a) the unstable region close to the point (x, y) = (1, 0); (b) the two-phase region by Mn^{2+}/Mn^{3+} ($y > x$); (d) the two-phase region by Fe^{2+}/Fe^{3+} (a part of $y < x$); and (c) the single-phase region by Fe^{2+}/Fe^{3+} connecting (b) and (d). Reproduced from reference(4).

According to the information shown in Figure 5-8 the pure $LiFePO_4$ and $LiMnPO_4$ both discharge according to an exclusively 2 phase reaction. Figure 5-8 also indicates that the charge from the Mn^{2+}/Mn^{3+} in $Li_x(Mn_yFe_{1-y})PO_4$ should always discharge via a 2 phase reaction. However, the mechanism of charge or discharge from Fe^{2+}/Fe^{3+} should change with y. The substitution of even small amounts of Mn for Fe will result in the discharge mechanism being mixed. However, when 60 % of the Fe is replaced by Mn the charge from the Fe^{2+}/Fe^{3+} will be extracted by a completely 1 phase reaction.

To explain how this difference would be seen in the electrochemical measurements two schematics for the behaviour of 1 phase and 2 phase materials are shown in Figure 5-9. The one phase reaction has a very different shape, the charge and discharge peaks appear in an overlapping voltage with a Gaussian like distribution of currents around the average discharge potential, the peaks should completely overlap, ignoring any diffusional or resistance limitations. The two phase reaction is typically characterised by a sharp charge current increase to a peak in the CV followed by an exponential decay to zero, then on discharge a reflection of the charge peak is seen starting at a lower voltage, the two peaks do not overlap the same voltage range.

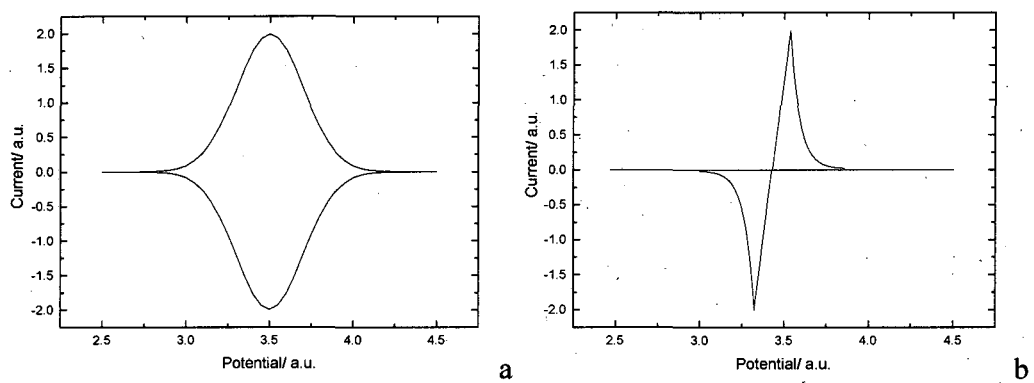

Figure 5-9 Schematic drawings of typical 1(a) and 2(b) phase behaviour.

Using the information from Figure 5-8 and Figure 5-9 the CVs from the array can be interpreted to observe these changes in the reaction mechanism. Below in Figure 5-10 CVs for the selected compositions are shown. Also shown as a guide for the readers eye are example CVs simulated by linear combination of the 2 end member CVs recorded experimentally ($LiFePO_4$ and $LiMnPO_4$); this assumes that both the charge from the Fe and the Mn is extracted via a 2 phase reaction.

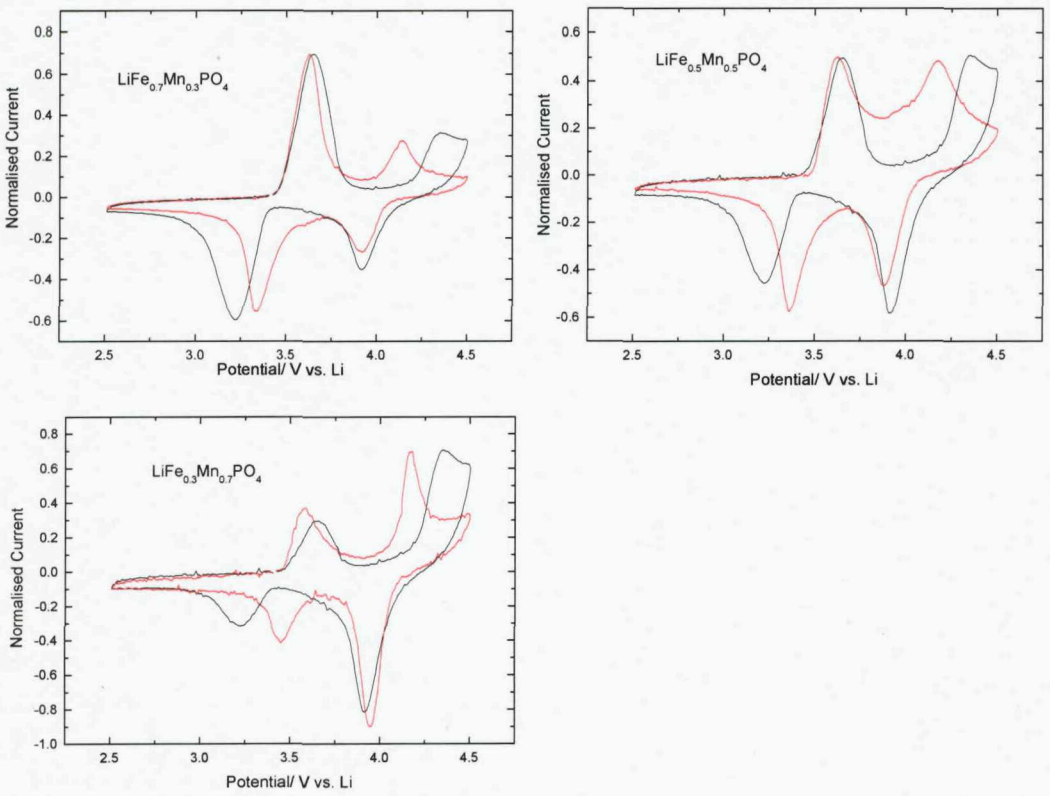

Figure 5-10 CVs $LiFe_{1-x}Mn_xPO_4$ (exact composition indicated on the graph). To indicate the change in shape of Fe^{2+}/Fe^{3+} and Mn^{2+}/Mn^{3+} discharge peaks in the solid solution CVs were simulated by combining the CVs for the pure $LiFePO_4$ and $LiMnPO_4$ and normalising the peak heights of each according to the amount of Fe or Mn. According to the phase diagram of Yamada et. al.(4) the pure materials should discharge based on a 2 phase discharge mechanism. Simulated CVs are shown in black (——) and real CVs are shown in red (——).

Figure 5-10 shows that as the percentage of Mn is increased the redox peaks from Fe^{2+}/Fe^{3+} become broader and the peak positions change. The voltage separation of the charge and discharge peaks is 430 mV in the pure $LiFePO_4$ and 290, 250 and 140 mV in $LiFe_{1-x}Mn_xPO_4$ where x = 0.3, 0.5 and 0.7 respectively. This indicates the change in phase reaction of discharge that is undergone in $LiFe_{1-x}Mn_xPO_4$ as the percentage of Mn increases the peak shapes change from something similar to Figure 5-9b to Figure 5-9a.

The $LiFe_{0.7}Mn_{0.3}PO_4$ sample is particularly interesting as according to the work of Yamada et al. the Fe^{2+}/Fe^{3+} reaction occurs under both a 1 and 2 phase mechanism. In

$Li_yFe_{0.7}Mn_{0.3}PO_4$ when $0.8<y<1$ the charge or discharge should follow a 2 phase reaction, however, if $0.3<y<0.8$ the reaction should be 1 phase. This can be seen in the CV for this material; the charge proceeds as expected with an initial 2 phase behaviour of a sharp linear increase to the peak current as seen for the pure $LiFePO_4$. However, on discharge instead of the same reaction the current increases gradually with an almost exponential shape to the peak, this is the result of the initial 1 phase behaviour that is seen when inserting Li into the material. The same feature can be seen to a lesser extent for the $LiFe_{0.5}Mn_{0.5}PO_4$ material which should also discharge under both 1 phase and 2 phase mechanisms.

5.1.3 Conclusions

Although this work has not shown any significant improvements in the performance of these materials the data has provided useful insights into the discharge such that the structural characterisation conducted by Yamada et. al. has been related directly to the electrochemical measurements. This work also highlights the application of the high-throughput approach where the fabrication of many electrodes was useful in studying the complicated mechanisms of discharge in this material.

5.2 Doping with Mg $Li_{1-x}Mg_xFe_{1-y}Mg_{1-y}PO_4$

Several reports in the literature have suggested improvements in electrochemical performance from substituting Mg for both Fe(7-12) and Li(13-15), in $LiFePO_4$. The aim of this work is to use the PoSAT high-throughput method to investigate the effect of these two substitutions.

5.2.1 Experimental details

Electrode Array Preparation by Post Synthesis Array Transfer (PoSAT)

Four 250 mL aqueous solutions A, B, C and D were prepared with the chemical compositions reported in Table 5-1.

Table 5-1. Showing solutions used to prepare a graded composition array.

Solution	Chemical Concentrations
A	0.625 M $Fe(NO_3)_3.9H_2O$ (*Aldrich*, 1.25 M) 0.625 M $LiCH_3COO.2H_2O$ *(Aldrich,* 2.5 M) 0.625 M H_3PO_4 (85 wt. % *Aldrich*)
B	0.625 M $Fe(NO_3)_3.9H_2O$ (*Aldrich*, 1.25 M) 0.5875 M $LiCH_3COO.2H_2O$ *(Aldrich,* 2.5 M) 0.625 M H_3PO_4 (85 wt. % *Aldrich*) 0.01875 M $Mg(CH_3COO)_2.4H_2O$ (*Aldrich*)
C	0.5 M $Fe(NO_3)_3.9H_2O$ (*Aldrich*, 1.25 M) 0.625 M $LiCH_3COO.2H_2O$ *(Aldrich,* 2.5 M) 0.625 M H_3PO_4 (85 wt. % *Aldrich*) 0.125 M $Mg(CH_3COO)_2.4H_2O$ (*Aldrich*)
D	2 M sucrose

Appropriate aliquots of each solution were dispensed into 64 quartz micro tubes (2 mL capacity) using hand-automated pipettes (*Finnpipette* adjustable-volume digital pipettes) so that the first four rows top to bottom on the array had increasing values of x in $Li_{1-x}Mg_{x/2}FePO_4$ (x = 0, 0.02, 0.04 and 0.06) and the bottom four rows y increased in $LiFe_{1-y}Mg_yPO_4$ (y = 0.05, 0.1, 0.15, 0.2). (These compositions are shown in Table 5-2 along with the specific capacity for each assuming the Mg is inactive.)

Table 5-2. Compositions of prepared materials including theoretical specific capacity assuming the Mg is inactive. The location of each sample on the array is also indicated.

$Li_{1-x}Mg_{x/2}FePO_4$				
	Row 1	Row 2	Row 3	Row 4
X	0	0.02	0.04	0.06
Specific Capacity/ mA h g^{-1}	169.9	166.4	162.9	159.38
$LiFe_{1-y}Mg_yPO_4$				
	Row 5	Row 6	Row 7	Row 8
X	0.05	0.1	0.15	0.2
Specific Capacity/ mA h g^{-1}	163.0	156.0	148.9	141.6

In the columns of the array from left to right the SPR was increased (0.05, 0.1, 0.15, 0.2, 0.22, 0.25 and 0.30). These solutions were then agitated using a Fischer "Whirlimix" Vortex mixer to ensure homogeneity before being placed in an oven at 70 °C for 12 h to remove the water. The array of precursor solids was then calcined in an argon atmosphere at 700 °C using a large bore (80 mm diameter) tube furnace (Lenton). After cooling, the products were crushed to a powder using a glass rod attached to a drill. Composite electrode preparation began by adding two inks, 4% PVdF-HFP (Aldrich, polyvinylidene fluoride-co-hexafluoropropylene) and 4% AB (acetylene black, Shawinigan, Chevron Phillips Chemical Company LP) in cyclopentanone (CP) to the active material powders with five 1 mm zirconia beads placed in each tube. The inks were added to give a final mass ratio of 10 % PVdF-HFP, 25 % AB and 65 % active material and then mixed using the vortex mixer. Then 14 µL aliquots of each ink was deposited onto the appropriate position

on the array of aluminium current collectors and spread across the surface to form an even film of ink. At the same time, a 40 μL sample of each ink was deposited into an array of alumina micro-crucibles for thermo gravimetric analysis as detailed in Chapter 3. The CP was evaporated from both arrays at room temperature before drying at 80 °C followed by evacuation. The samples on both arrays were then accurately weighed using a computer monitored balance.

Array Sample characterisation

Thermo gravimetric Analysis and High Throughput X-ray Diffraction measurements were performed on the array of samples as described in Chapters 2 and 3. High throughput electrochemical evaluation of the array was also performed as described in Chapter 2. The array was cycled between 2.5 to 4.5 V vs. Li at the following scan rates: 0.05, 0.1, 0.4, 0.8and 1.6 mV s^{-1}.

Bulk preparation of samples $LiFePO_4$, $LiFe_{0.9}Mg_{0.05}PO_4$ and $LiFe_{0.9}Mg_{0.1}PO_4$

The same preparation was used as on the PoSAT array except the solution volumes were scaled up so the total precursor volume was 20 mL. A ratio of 0.25 SPR was used in all three cases.

X-ray phase analysis on bulk samples

X-ray powder diffraction patterns were recorded for the bulk samples using a Bruker D5000 diffractometer. X-ray patterns were collected for the 2θ range 15 to 50° at a scanning rate of ca. 0.07 °/min using a $CuK\alpha_1$ radiation.

Scanning electron microscopy on bulk samples

Samples of the active materials were studied by scanning electron microscopy (SEM) using a Philips XL30ESEM at an accelerating voltage between 10 and 15 kV using the secondary electron and backscattered electron detectors.

Electrochemical testing of bulk samples

Electrode pellets containing 75 wt% of active material, 20 wt % of acetylene black (Shawinigan Black, 100%-compressed, Chevron AB) and 5 wt% poly-

tetrafluoroethylene (PTFE, Type: 6C-N, DuPont) binder were prepared as described in Chapter 2. The mass of the pellets was in the range 13–17 mg, with a thickness in the range 0.08–0.11 mm. Cells were then prepared as described in Chapter 2.

Bulk preparations of carbon free samples of $LiFePO_4$ and $LiFe_{0.9}Mg_{0.1}PO_4$

Carbon-free materials were synthesized using a conventional, solid-state reaction. Stoichiometric amounts of Li_2CO_3 (Aldrich), $FeC_2O_4 \cdot 2H_2O$ (Aldrich), $(MgCO_3)_4.Mg(OH)_2.5H_2O$ (Aldrich) and 85 wt % H_3PO_4 (Aldrich) were first mixed to give the desired atomic ratios for $LiFePO_4$ and $LiFe_{0.9}Mg_{0.1}PO_4$. The product, a yellow slurry, was transferred to an alumina boat and calcined (10°/min) in argon for 5 h at 700°C under a slow flow of argon gas without rigorous air exclusion. The red-brown products were ground in the mortar and heat-treated again in flowing 10 % H_2 in Argon at 500°C for another 3 h (heating rate 5°/min); the lower reaction temperature being used to avoid the formation of Fe_2P. The final products were grey powders, characteristic of $LiFePO_4$.

Conductivity Measurements

The pellets used for the electronic conductivity measurements were prepared by die-pressing carbon free $LiFePO_4$ and $LiFe_{0.9}Mg_{0.1}PO_4$ powder samples (using a pressure 1.5 ton/cm^2). Both sides of these pellets were then coated with an Ag conducting paste. The pellets had a 1.1 cm diameter and were ~0.2 cm thick. The impedance of these samples was measured between 30 and 140 °C at ~5 °C intervals using a Solartron 1250 frequency response analyzer with a Solartron 1287 electrochemical interface and a frequency range from 65 kHz to 10 Hz.

5.2.2 Results and discussion

High throughput structural Characterisation

The High-throughput XRD patterns recorded for the prepared materials fell into two groups, depending on whether there was sufficient sucrose or carbon present to reduce all the iron(III) to iron (II) after consuming all the nitrate. Despite the effect of a little substitution of magnesium acetate (reducing) for iron (III) nitrate (oxidizing) across

the array, the threshold SPR remained between 0.15 and 0.20, consistent with the previously found value of around 0.16 for undoped materials. Figure 5-11 shows selected XRD patterns in that reduction was complete for all samples prepared at an SPR of 0.20 and above, and that above this value the olivine phase was deemed to be pure.

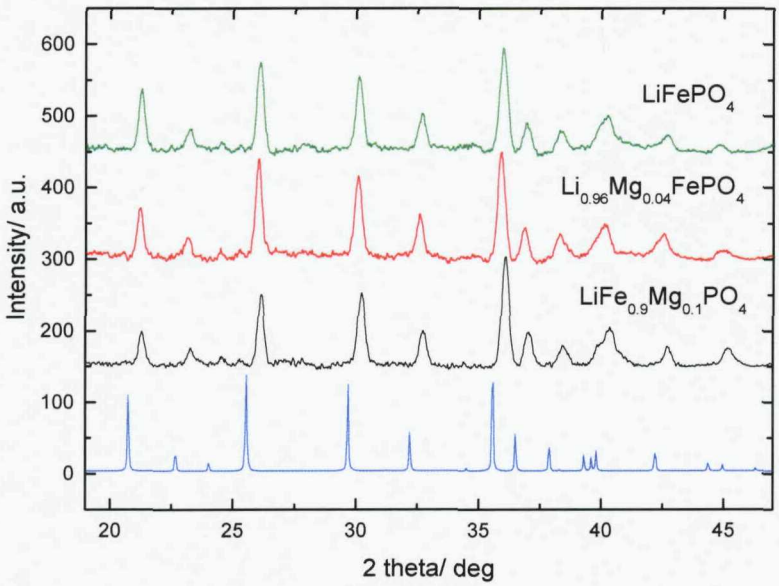

Figure 5-11. Graph showing XRD patterns for array of $LiFePO_4$ where Mg had been substituted for both Li and Fe. Shown here are patterns where sufficient sucrose has been added to reduce all the Fe(III) to Fe(II). Also shown for comparison is a simulated pattern for $LiFePO_4$.

The HT-XRD method does not give extremely accurate diffraction angles as discussed in Chapter 3, any observed differences in the values of 2θ between the selected patterns are affected by small variations in sample height. The patterns were indexed as described in Appendix 3 and an attempt was made to extract the unit cell parameters and volume. The values extracted for $Li_{1-x}Mg_{x/2}FePO_4$ materials showed no trends only scatter in the unit cell volume around 288 $Å^3$ as the degree of lithium substitution was too small to invoke a significant change in the unit cell. However, for $LiFe_{1-y}Mg_yPO_4$ although the results showed a high degree of scatter, by averaging the unit cell volumes for all the materials with an SPR of greater than 0.2 (where phase pure material is thought to exist) a consistent variation in the unit cell parameter was seen, and is shown in Figure 5-12.

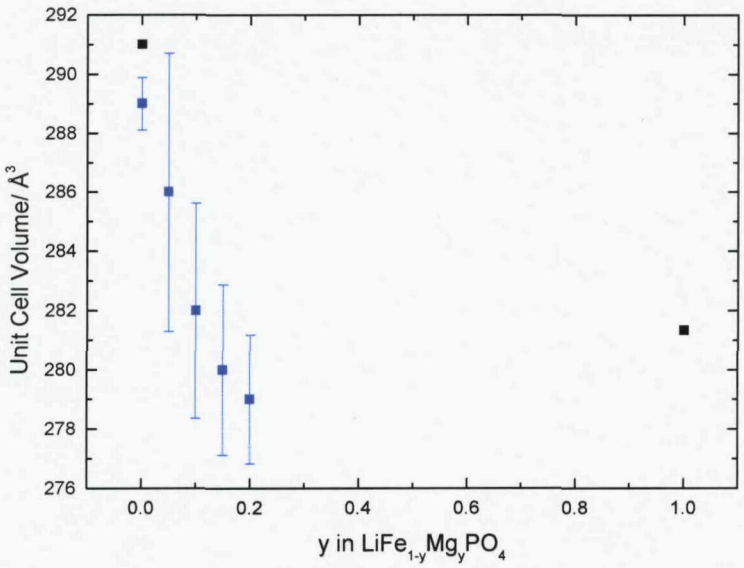

Figure 5-12. Variation of unit cell volume with change y in $LiFe_{1-y}Mg_yPO_4$. The volume for $LiMgPO_4$ is obtained from the literature(16).

The actual values of the unit cell volume shown in Figure 5-12 are clearly not reliable. However, the general trend of decreasing cell volume with increasing Mg substitution is consistent with that expected as shown by the two points for $LiFePO_4$ (measured from a bulk sample and Retvied refinement discussed later) and $LiMgPO_4$ (a value extracted from the literature(16)) is correct. This leads to the qualitative conclusion that the substitution of Mg for Fe results in a change in lattice parameters presumably from a Vegard's shift.

High throughput Electrochemical Characterisation

Below in Figure 5-13 the CVs for the array are shown, the variation in composition in the rows and SPR in the columns are indicated.

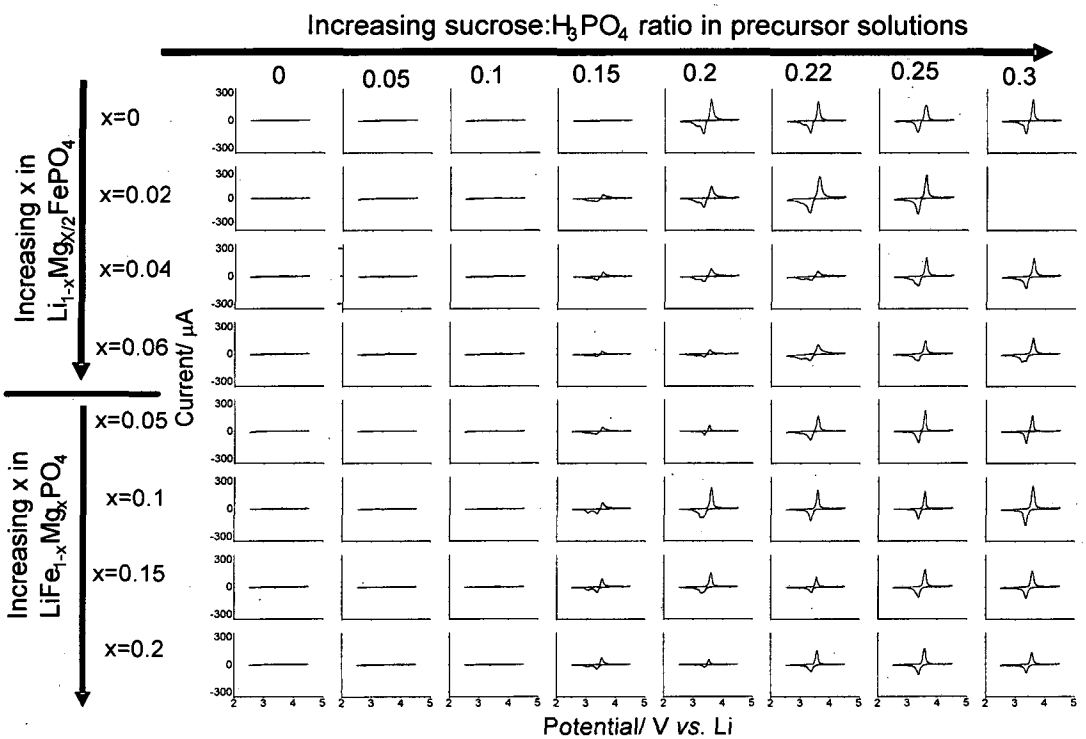

Figure 5-13. CVs for array of LiFePO4 where Mg had been substituted for both Li and Fe

On examination of the CVs shown in Figure 5-13 the currents are negligible for samples with 0, 0.05 and 0.1 SPR but begin to increase at 0.15 where all oxidants have been reduced and the olivine products are coated with a minimal amount of carbon. An impurity peak, occasionally seen around 2.9 V due to a Nasicon-type impurity, $Li_3Fe_2(PO_4)_3$, indicates a small inhomogeneity of the sample at this low sucrose level. For 0.2 SPR and above at this slow scan rate, most of the voltammogram shapes are similar; the rising transients show a resistive limitation of about 1 kΩ which is probably due to the lithium counter electrode interface with the electrolyte, while the falling transients show a time constant on the order of 3000 s, corresponding to ambipolar lithium diffusion out of the particles at the rate of approximately 1C. The different heights of the peaks are therefore mainly due to

changes in the proportion of active material that is in effective contact with the carbon network.

The increases in the discharge capacity at 0.05 mV s^{-1} are expressed in Figure 5-14 (substitution of lithium) and Figure 5-15 (substitution of iron) *vs.* SPR as the percentage of theoretical charge capacity released during a positive potential scan up to 4.5 V and back to the zero current point. There is tentative evidence of capacity increases in both doping schemes at the 0.15 SPR. For the Fe-substituted samples this may be due to the lower nitrate levels rather than a true doping effect. The main effects of increasing amounts of carbon are seen from 0.2 to 0.3 SPR, where the formation of a percolating conductivity network becomes increasingly probable in all cases, as was observed in Chapter 4.

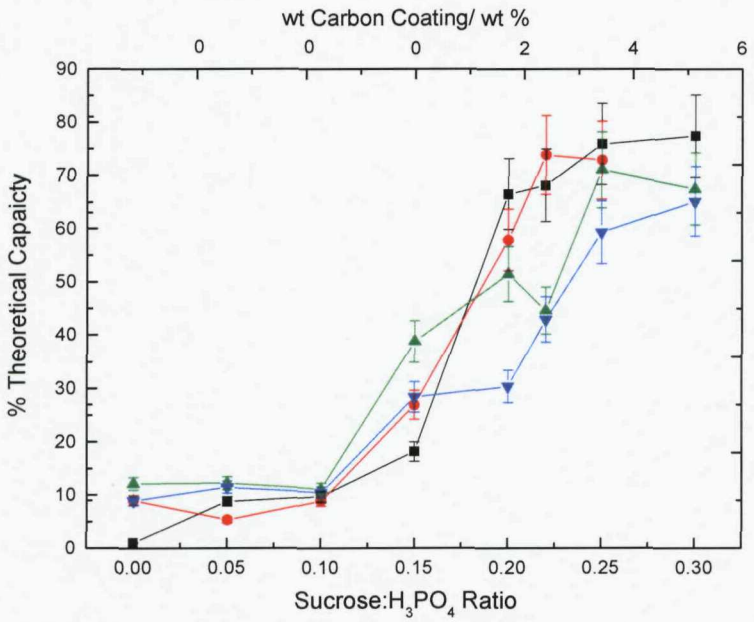

Figure 5-14. Performance $Li_{1-x}Mg_{x/2}FePO_4$ (x= 0(-■-), 0.02(-●-), 0.04(-▲-) and 0.06(-▼-)) prepared with various SPRs. % theoretical capacities were calculated for CVs recorded a 0.05 mV s^{-1} and the specific capacities in Table 5-2. The axis for carbon coating is calculated based on experimental observations.

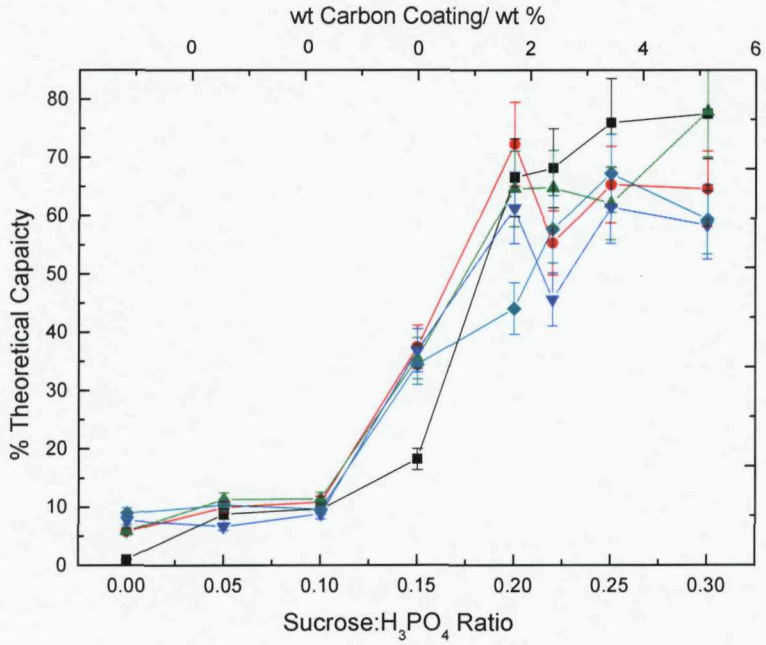

Figure 5-15. Performance $LiFe_{1-x}Mg_xPO_4$ (x= 0(-■-), 0.5(-●-), 0.1(-▲-), 0.15(-▼-) and 0.2(-◆-)) prepared with various SPRs. Specific capacities were calculated for CVs recorded a 0.05 mV s^{-1} and the specific capacities in Table 5-2.

Close examination of Figure 5-14 shows that substitution of Mg for Li is detrimental to the performance of material at SPR values above 0.15, i.e. when the carbon network is fully formed, with capacities decreasing from 70 % to 40 % theoretical as x increases from zero to 0.06. Such an effect is not seen for substitution of Mg for Fe in Figure 5-15, where the results above 0.2 SPR are more closely grouped together with the undoped material – i.e. magnesium substitution for iron does not reduce the charge extracted per iron atom at or below C rates of 1 h^{-1}.

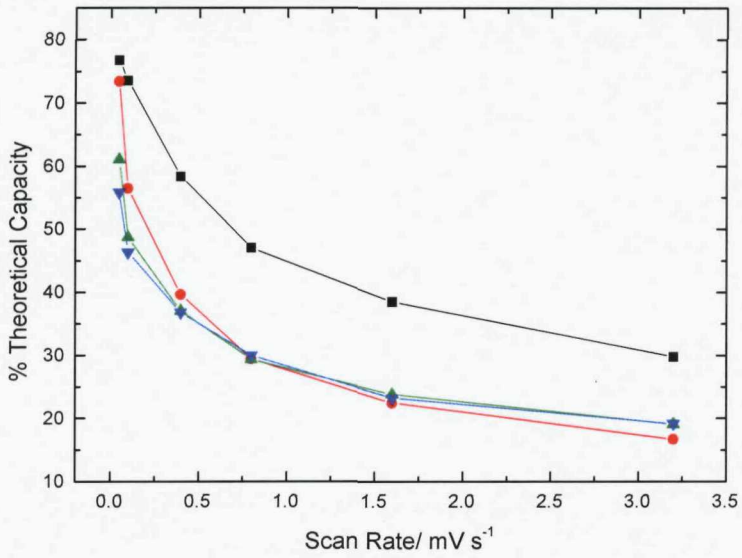

Figure 5-16. Percentage theoretical capacity *vs.* scan rate for $Li_{1-x}Mg_{x/2}FePO_4$ materials where x = 0(■), 0.02(●), 0.04(▲) and 0.6(▼). These are averaged capacity values for each material prepared with 0.22, 0.25 and 0.3 SPR. For each x value one set of sucrose ratio capacities deviating the most from the other two was removed as an outlier.

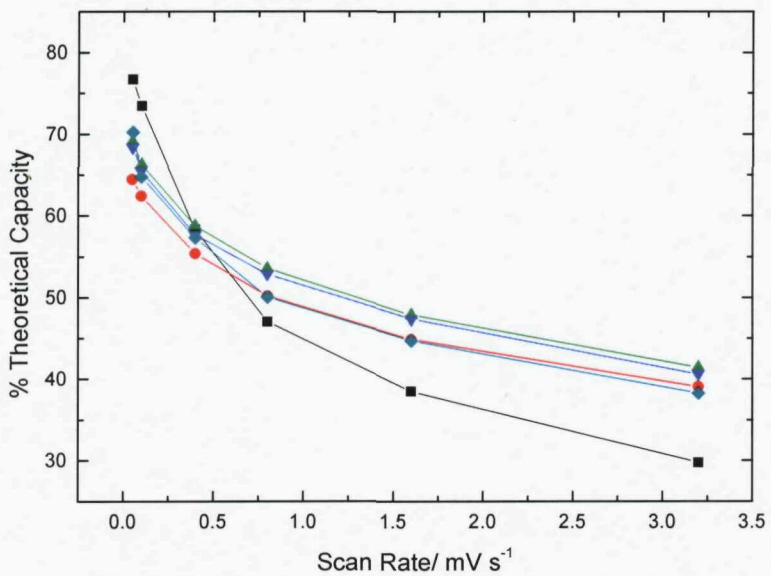

Figure 5-17. Percentage theoretical capacity *vs.* scan rate for $LiFe_{1-y}Mg_yPO_4$ materials where y = 0(■), 0.05(●), 0.1(▲), 0.15(▼) and 0.2(◆). These are averaged capacity values for each material prepared with 0.22, 0.25 and 0.3 sucrose to H_3PO_4 ratio. For each y value one set of sucrose ratio capacities deviating the most from the other two was removed as an outlier.

Figure 5-16 and Figure 5-17 show the proportions of theoretical capacity obtained at higher rates. In the case of magnesium substitution for lithium, the high rate capacities

decrease faster than the pure material. However, the Mg-substituted samples uniformly performed better than the pure material at scan rates 0.8 mV s^{-1} and above (corresponding to C-rates up to about 5 h^{-1} based on the average currents divided by the total charges). Higher actual specific capacities were observed for y = 0.05 and 0.1 at 0.8 mV s^{-1} and also y = 0.15 at 1.6 mV s^{-1} (~3 C) and all samples at 3.2 mV s^{-1} (~5 C). The result is, in fact, consistent with the previous publications(9-12) although it is obtained under a different condition, where the formation of an effective electronic conducting carbon network is well established in all cases and the only differences are the substitution of magnesium in the precursor.

To ascertain the origin of the performance improvement a comparison of the original voltammograms is shown in Figure 5-18.

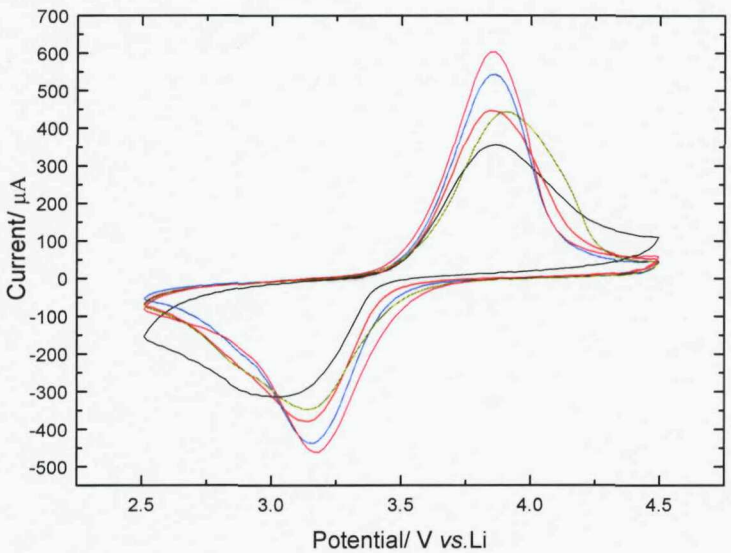

Figure 5-18. CV's of $LiFe_{1-x}Mg_xPO_4$ (x= 0(—), 0.05(—), 0.1(—), 0.15(—) and 0.2(—)) from array during cycling at 0.8 mV s^{-1}. Materials prepared with an SPR ratio of 0.25.

The CVs in Figure 5-18 highlight the differences between the peak shapes for different samples. The effects of increasing the Mg content are as follows:

1) increasing slopes for the rising transients during charge
2) increased peak height
3) decreased decay time constants.

The first effect is consistent with an increased electronic conductivity, under which the contact resistance with the carbon network is decreased. The second and third effects show an increased ambipolar lithium diffusion coefficient, which depends on either the ionic or the electronic conductivity, whichever is lower. Since it is less probable that the substituent increases both conductivities than one, the effect is more likely to originate in the electronic conductivity.

To summarise the results of the High Throughput measurements, enhanced rate capability when the magnesium was substituted for iron in the precursor mixture was seen, but the same was not true when magnesium was substituted for lithium.

Characterisation of $LiFe_{1-x}Mg_xPO_4$ sample from bulk preparations

Samples from sucrose pyrolysis bulk preparations of $LiFePO_4$, $LiFe_{0.9}Mg_{0.1}PO_4$ and the solid state carbon free preparation of $LiFe_{0.95}Mg_{0.05}PO4$ were examined using the Bruker D5000 X-ray diffractometer. The recorded patterns are shown below in Figure 5-19.

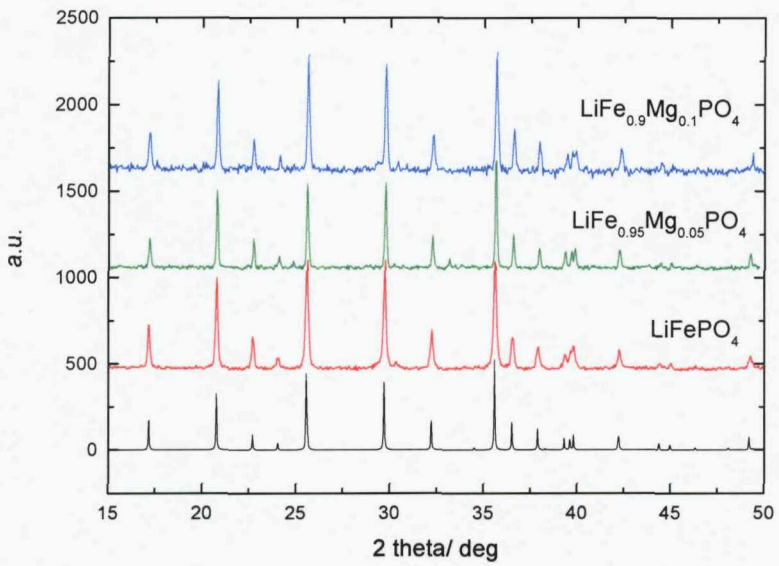

Figure 5-19. XRD patterns $LiFePO_4$, $LiFe_{0.9}Mg_{0.1}PO_4$ (sucrose pyrolysis method) and $LiFe_{0.95}Mg_{0.05}PO_4$ (carbon free solid state reaction prep) recorded using the D5000 on bulk samples. Shown for comparison in black is a simulated $LiFePO_4$ pattern(1).

Reitveld refinement (PowderCell 2.4) of these patterns based on an ordered olivine (orthorhombic) structure using space group *Pnma* gave the unit cell volumes, shown as a function of Mg substitution in Figure 5-20 with a literature value for $LiMgPO_4$(16) for comparison.

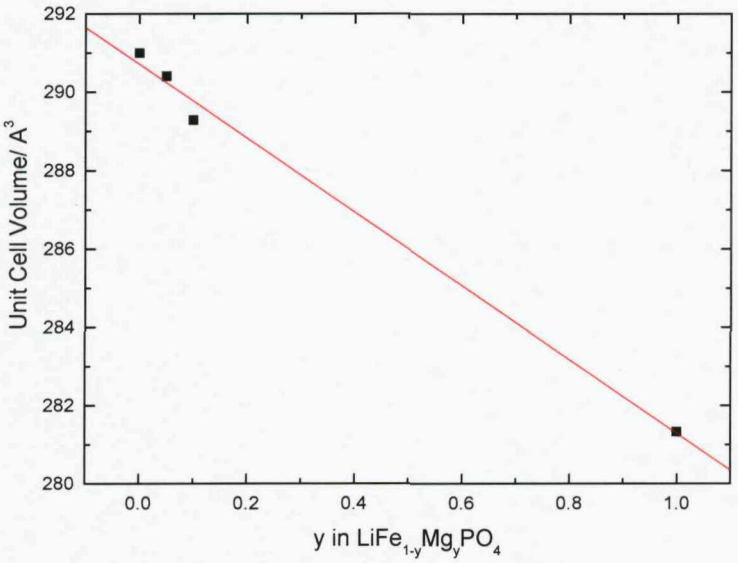

Figure 5-20. Variation of unit cell volume with y in $LiFe_{1-y}Mg_yPO_4$. The volume for $LiMgPO_4$ is obtained from the literature(16).

Solid solution formation is indicated in Figure 5-20 from the decrease in the unit cell volume with magnesium substitution resulting from a Vegard's shift.

Conductivity Measurements of Carbon free $LiFePO_4$ and $LiFe_{0.8}Mg_{0.2}PO_4$.

A single but rather depressed semicircle in the Nyquist plot, peaking at around 100 Hz can be seen for both materials in Figure 5-21. An equivalent circuit that may be used to interpret these impedance data is shown in Figure 5-22. However, this is clearly too complicated as it is difficult to extract information about the 6 components from these single semi circles. Impedance at 10^{-3} Hz and measurement of the current response with potential steps confirmed that there was little dispersion at very low frequency. The low frequency impedance was therefore interpreted as the electronic resistance (R_e). The semicircle was broadly consistent with an electronic resistance coupled to a instrumental capacitance (this simplified circuit is shown in Figure 5-23). This is confirmed in Figure 5-24 where the inverse frequency at the semi circle maximum is

plotted against the low frequency resistance and shows a linear relationship expected from Equation 5-1.

$$R = \frac{1}{2\pi f^* C}$$

Equation 5-1

R	=	lowest frequency resistance/ Ω
f^*	=	frequency at semi circle maximum/ Hz
C	=	Capacitance/ F

Using this analysis the proposed circuit diagram in Figure 5-23 suggests a constant capacitance (~1.8e-11 F for both $LiFePO_4$ and $LiFe_{0.9}Mg_{0.1}PO_4$; the fact that this value is independent of the sample suggests that this is an instrumental artefact) with a temperature dependent resistance. The absence of an increase in the imaginary part at low frequency indicates that the measured resistance is purely electronic and that the ionic resistance is not detected in this experiment.

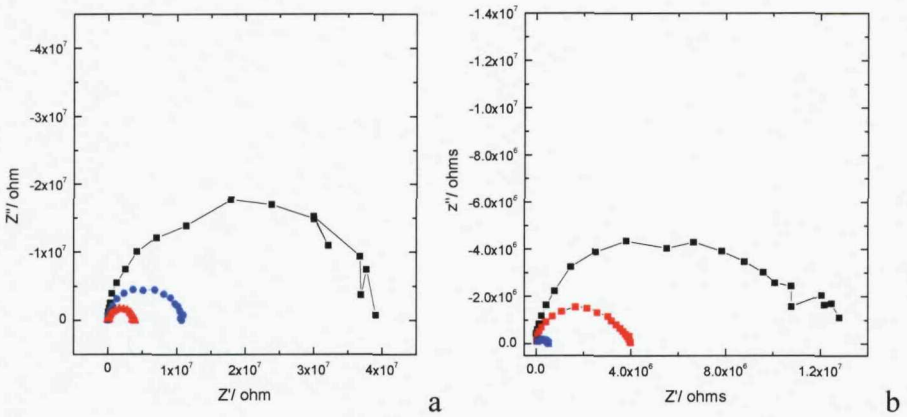

Figure 5-21 Nyquist plots of (a) $LiFePO_4$ at different temperatures 84 °C (-■-), 102 °C (-●-) and 124 °C (-▲-) and (b) $LiFe_{0.9}Mg_{0.1}PO_4$ black 28 C(-■-), red 42 C(-●-), blue 84C(-▲-).

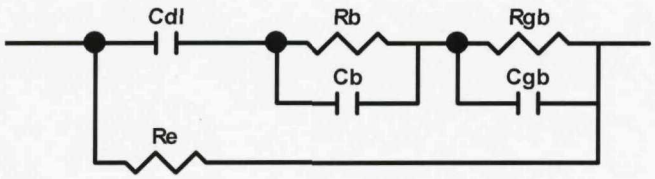

Figure 5-22 Equivalent circuit for polycrystalline solid: Rgb, Cgb- grain boundaries; Rb, Cb- bulk crystals; Re- electronic resistance; Cdl-electrode double-layer capacitance(3).

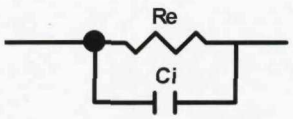

Figure 5-23 A simplified equivalent circuit for this polycrystalline solid. Re- electronic resistance; Ci- instrumental capacitance.

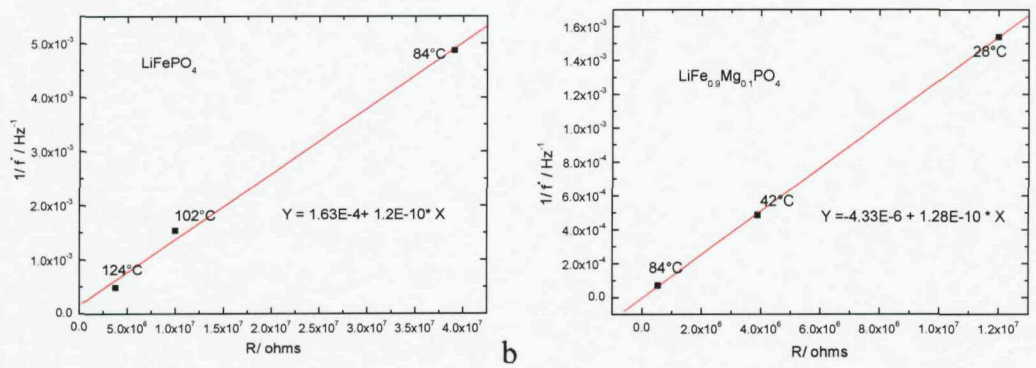

a b

Figure 5-24 Frequency at semi circles maximums in Figure 5-21 a and b vs lowest frequency resistance

The extrapolated low frequency resistance was used to determine the electronic conductivity with knowledge of the sample dimensions. These conductivities from measurements made at a number of different temperatures were used to draw an Arrhenius plot (Figure 5-25, drawn according to the Arrhenius equation shown below in Equation 5-2) to extract the conductivities at 25 °C and the activation energy (shown in Table 5-3).

$$\sigma = A\exp\left(\frac{-E_m}{kT}\right)$$

Equation 5-2

σ = conductivity/ S cm^{-1}

A= pre-exponential factor/ S cm^{-1}

k = Boltzman Constant/ eV K^{-1}

T= absolute temperature/ K

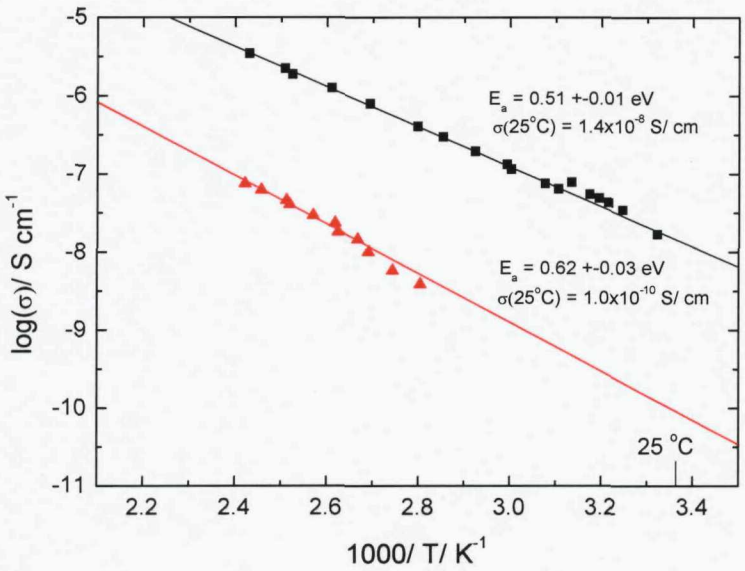

Figure 5-25. Arrhenius plot to extract the conductivity and activation energy values. $LiFePO_4$(▲) and $LiMg_{0.1}Fe_{0.9}PO_4$(■).

Table 5-3 Showing conductivities of carbon free samples of $LiFePO_4$ and $LiFe_{0.9}Mg_{0.1}PO_4$.

	$LiFePO_4$	$LiFe_{0.9}Mg_{0.1}PO_4$
σ/ S cm^{-1} (25°C)	1×10^{-10}	1.4×10^{-08}
Ea/ eV	0.62 ± 0.03	0.51 ± 0.01

The electronic conductivity results (Table 5-3) indicate improvements of about 2 orders of magnitude in the measured conductivity between the pure and Mg doped samples. A reduction in the activation energy is also seen for the Mg doped material.

SEM Images of $LiFePO_4$ and $LiFe_{0.9}Mg_{0.1}PO_4$ Samples Prepare via Sucrose Pyrolisis

Another possibility for this improved performance could result from a change in sample morphology, below in Figure 5-26 SEM images of bulk preparations of $LiFePO_4$ and $LiFe_{0.9}Mg_{0.1}PO_4$ (prepared via sucrose pyrolysis method) are shown.

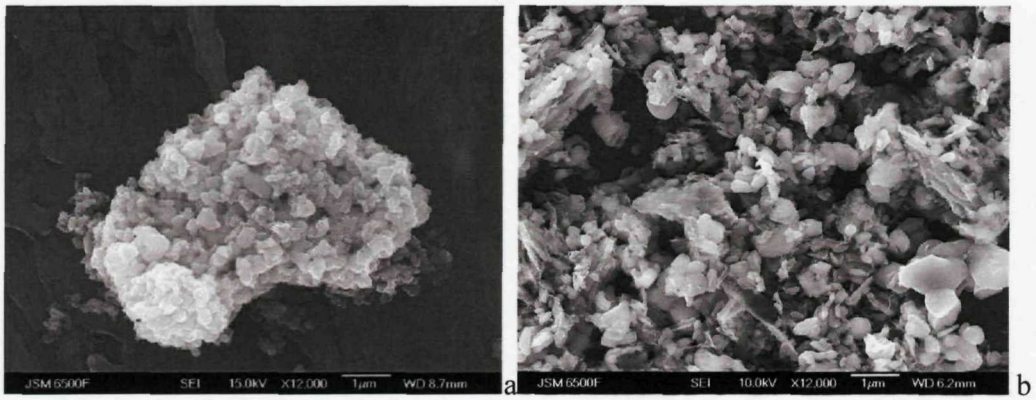

Figure 5-26. SEM images of $LiFePO_4$(1) and $LiFe_{0.9}Mg_{0.1}PO_4$ prepared by 700°C heat-treatment of a solution containing LiCH3COO, $Mg(CH_3COO)_2$, Fe(NO3)3, H3PO4, and sucrose.

The SEM images shown in Figure 5-26 indicate that the $LiFe_{0.9}Mg_{0.1}PO_4$ has a similar particle size to the $LiFePO_4$, around 300-500 nm. However, the particle morphology is different; the particles in $LiFe_{0.9}Mg_{0.1}PO_4$ are more dispersed and not held together in large agglomerates, also the particles appear to be flatter more disc like than those in the $LiFePO_4$.

Therefore, contributions to improved properties from morphological effects cannot be ruled out, as discussed earlier the large agglomerate of particles shown in Figure 5-26a appears to be broken up into the individual particle in Figure 5-26b. Therefore, it is likely that both the morphological change and the electronic conductivity improvement contribute to the improved material performance at higher rates.

Bulk Measurements Using Galvanostatic Cycling

To confirm these results the bulk preparations of $LiFePO_4$ and $LiFe_{0.9}Mg_{0.1}PO_4$ (prepared via sucrose pyrolysis method) were prepared and cycled galvanostatically; the results of this are shown below in Figure 5-27.

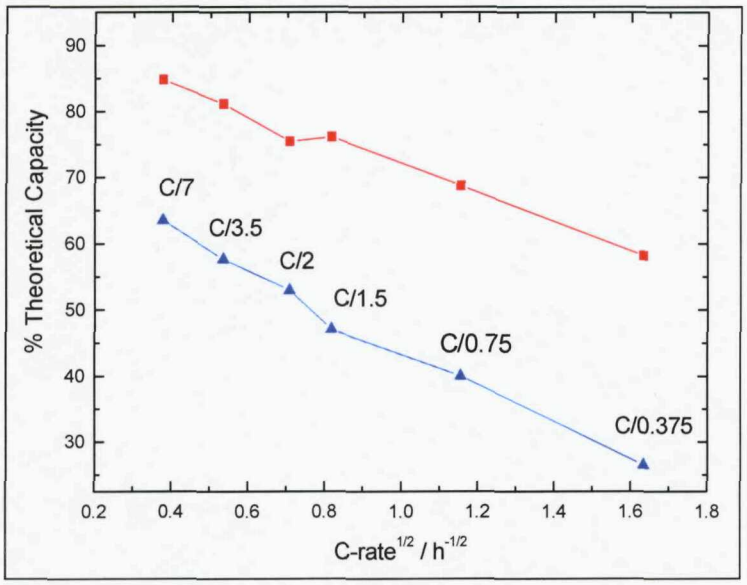

Figure 5-27. Specific capacity for $LiFePO_4$ (-▲-) and $LiFe_{1-y}Mg_yPO_4$ (-■-) *vs.* the square root of discharge rate. The discharge rate is expressed as the "C-rate," i.e., the ratio of discharge current to the theoretical charge ("capacity").

There is a large improvement in performance for $LiFe_{0.9}Mg_{0.1}PO_4$ from the $LiFePO_4$ at all C-rates. The low C-rate behaviour contrasts with slow scan rate results obtained in the high-throughput test and probably reflects the effects of compaction (a result of electrode film rolling used in this testing) on the electronic percolation.

5.2.3 Conclusions

In samples of $Li_{1-x}Mg_{x/2}FePO_4$ we saw that higher SPRs were required to fully percolate the material with increasing x. The maximum observed capacity was also significantly reduced by the increase of x, and no improvement in rate capability was observed.

In samples of $LiFe_{1-y}Mg_yPO_4$ a slight decrease in the amount of carbon that was required to percolate the material was observed. The required carbon coating which gave optimal performance was determined for each material to be greater than the 0.22 SPR seen for pure $LiFePO_4$. By observing the rate performance of materials prepared with a high SPR an improvement in extractable capacity when Fe is replaced by Mg has been shown. This is attributed to an improvement in electronic conductivity within the active material particle, and a slight modification in sample morphology which reduces the build up of large agglomerates of small particles.

This work has highlighted the use of the PoSAT high-throughput method to discover improvements in material performance as a result of compositional variations.

5.3 $LiFe_{1-x-y}Mn_xMg_yPO_4$

The limitation of the $LiFe_{1-x}Mn_xPO_4$ materials as discussed in section 5.1 was assumed to be the electronic conductivity, this has also been suggested in the literature(6). Therefore the natural progression after seeing the improvement in performance for the $LiFePO_4$ with Mg substitution is to try the same approach with the $LiFe_{1-x}Mn_xPO_4$ materials. The aim of this study was to improve the extractable capacity from $LiMnPO_4$ and $LiFe_{0.5}Mn_{0.5}PO_4$. These two compositions were chosen as initial tests to see if the Mg substitution had any effect.

5.3.1 Experimental details

Electrode Array Preparation by Post Synthesis Array Transfer (PoSAT)

Solutions of $LiCH_3COO$ (2.5 M, 250 mL), $Fe(NO_3)_3$ $9H_2O$ (1.25 M, 250 mL), $Mg(CH_3COO)_2.4H_2O$ (1.25 M, 250 mL), $Mn(NO_3)_2$ (1.25 M, 250 mL) and H_3PO_4 (1.25 M, 250 mL) were prepared. The array of quartz was divided into two sides of 32 tubes, the left hand side was used to prepare $LiMn_{1-x}Mg_xPO_4$ and the right hand side to prepare $LiFe_{0.5-y/2}Mn_{0.5-y/2}Mg_yPO_4$. In the columns of each side the values of x and y was altered such that samples containing y = 0, 0.05, 0.1 and 0.2 were prepared. In the rows of the array from top to bottom the amount of sucrose used in each preparation was increased, SPR ratios of 0.16, 0.25, 0.4 and 0.6 (the extremely high levels of sucrose were chosen in a further attempt to reduce the conductivity limitations of this material) were investigated, two repeats of each sucrose level was made. The prepared solutions were then mixed to from precursor solutions (2 ml) in the quartz tubes using the automated liquid handler (Perkin-Elmer Life Sciences) to obtain the correct stiochiometry for these preparations. These solutions were then agitated using a *Fischer* "Whirlimix" Vortex mixer to ensure homogeneity before being placed in an oven at 70 °C for 12 h to remove the water. The array of precursor solids was then calcined in an argon atmosphere at 700 °C using a large bore (80 mm

diameter) tube furnace (Lenton). After cooling, the products were crushed by the addition of five 1 mm zirconia beads to each tube followed by placing the whole array on a vibrating table (IKA VIBRAX VXR BASIC). Composite electrode preparation began by adding two inks, 4 % PVdF-HFP (Aldrich, polyvinylidene fluoride-co-hexafluoropropylene) and 4 % AB (acetylene black, Shawinigan, Chevron Phillips Chemical Company LP) in cyclopentanone (CP) to the active material powders in each tube. The inks were added to give a final mass ratio of 10 % PVdF-HFP, 25 % AB and 65 % active material and then mixed using the vortex mixer. Then 14 μL aliquots of each ink was deposited onto the appropriate position on the array of aluminium current collectors and spread across the surface to form an even film of ink. At the same time, a 40 μL sample of each ink was deposited into an array of alumina micro-crucibles for thermo gravimetric analysis as detailed in Chapter 3. The CP was evaporated from both arrays at room temperature before drying at 80 °C followed by evacuation. The samples on both arrays were then accurately weighed using a computer connected balance.

Array Sample characterisation

Thermogravimetric Analysis and High Throughput X-ray Diffraction measurements were performed on the array of samples as described in Chapter 2. High throughput electrochemical evaluation of the array was also performed as described in section Chapter 2. The array was cycled between 2.5 to 4.5 V vs. Li at the following scan rates: 0.05, 0.1, 0.4, 0.8and 1.6 mV s^{-1} .

Bulk preparation of samples $LiMn_{0.8}Mg_{0.2}PO_4$ and $LiMnPO_4$

The same preparation was used as on the PoSAT array except the solution volumes were scaled up so the total precursor volume was 20 mL. A ratio of 0.6 sucrose to H_3PO_4 was used in both cases.

X-ray phase analysis on bulk samples

X-ray powder diffraction patterns were recorded for the bulk samples using a Bruker D5000 diffractometer. X-ray patterns were collected for the 2θ between 15 and 50° at a scanning rate of ca. 0.07 °/min using a $CuK\alpha_1$ radiation.

Electrochemical testing of bulk samples

Electrode pellets containing 75 wt% of active material, 20 wt % of acetylene black (Shawinigan Black, 100%-compressed, Chevron AB) and 5 wt% poly-tetrafluoroethylene (PTFE, Type: 6C-N, DuPont) binder were prepared as described in Chapter 2. The mass of the pellets was in the range 13–17 mg, with a thickness in the range 0.08–0.11 mm. Two-electrode cells were assembled as described in Chapter 2. The cells were cycled galvanostatically at a range of different currents between 2.0 and 4.5 V using a 16-channel potentiostat (VMP2, Princeton Applied Research; Biologic-Science Instruments).

5.3.2 Results and discussion

High-throughput XRD results

The array is split into two halves the $LiMn_{1-x}Mg_xPO_4$ and the $LiFe_{0.5-y/2}Mn_{0.5-y/2}Mg_yPO_4$ materials. The analysis of these two will be treated separately. Below in Figure 5-28 the XRD patterns for $LiMn_{0.8}Mg_{0.2}PO_4$ materials with the various different SPR values are shown, these were representative of all the $LiMn_{1-x}Mg_xPO_4$ materials. This indicates that when an SPR greater than or equal 0.25 is used the major phase present is olivine. The materials synthesised with an SPR of 0.16 shows no peaks resulting from olivine the majority of the peaks corresponding to the material $Mn_2(P_2O_7)$. This impurity phase can also be resolved in all the other patterns shown in Figure 5-28, however, the intensity of the peaks do decrease with increasing amounts of sucrose. This indicates that this method of synthesis does not give a pure phase material until large amounts of sucrose are used; presumably the high levels of sucrose produce a more homogenous precursor which leads to the formation of the target material. This is in contrast with the $LiFePO_4$ preparations seen in Chapter 3 and in the early section of this chapter, the reason for this difference is unknown. However, the preparations of $LiMnPO_4$ in Section 5.1 were performed with a manganese acetate precursor, whereas, in this preparation manganese nitrate has been used. This will result in a change in the reaction as the nitrate is more oxidising than the acetate and therefore more sucrose would be required.

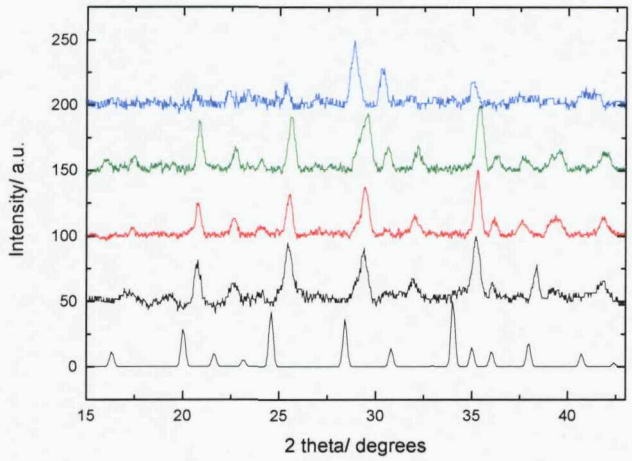

Figure 5-28 Selected high-throughput XRD patterns from the array of $LiMn_{0.8}Mg_{0.2}PO_4$ with SPR values of 0.16(—), 0.25(—), 0.4(—) and 0.6(—). Shown for comparison in black is a database pattern of $LiMnPO_4$.

The XRD patterns of $LiFe_{0.4}Mn_{0.4}Mg_{0.2}PO_4$ materials with different SPR values are shown below in Figure 5-29, these were considered representative of all the $LiFe_{0.5-y/2}Mn_{0.5-y/2}Mg_yPO_4$ materials. The peaks for the olivine phase can be seen in all the samples with no obvious impurity peaks. In the sample prepared with an SPR of 0.16 a peak at approximately 37 degrees is seen resulting from the aluminium substrate. The Fe in the preparation seems to stabilise the synthesis better than in the $LiMn_{1-x}Mg_xPO_4$ preparations as no impurity phases were detected.

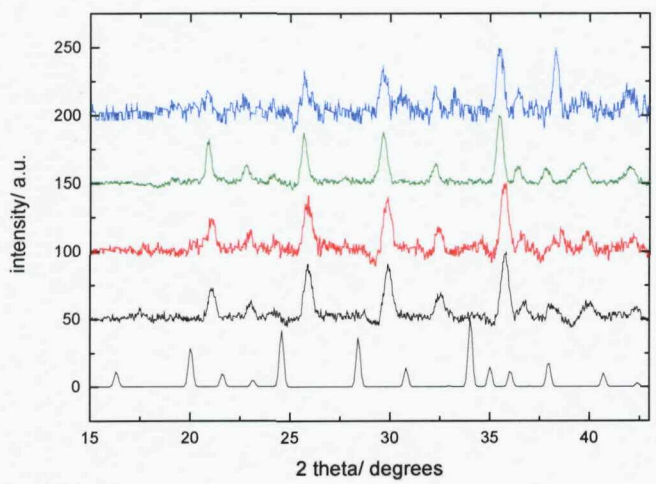

Figure 5-29 Selected high-throughput XRD patterns from the array of $LiFe_{0.4}Mn_{0.4}Mg_{0.2}PO_4$ with SPR values of 0.16(—), 0.25(—), 0.4(—) and 0.6(—). Shown for comparison in black is a database pattern of $LiMnPO_4$.

High-throughput Electrochemical Results

The CVs recorded from the array are shown in Figure 5-30. These CVs indicate that the materials require a much larger amount of sucrose to observe the maximum currents than pure $LiFePO_4$; this is assumed to be because these materials have much lower conductivities this was previously noted in section 5.1. In both the $LiMn_{1-x}Mg_xPO_4$ and $LiFe_{0.5-y/2}Mn_{0.5-y/2}Mg_yPO_4$ material the highest currents were seen when an SPR ratio of greater than 0.4 was used.

The $LiMn_{1-x}Mg_xPO_4$ materials show the charge and discharge peaks for Mn^{2+}/Mn^{3+} around 4.1 V when an SPR >0.4 was used. The currents increase significantly on increasing x suggesting an improved performance from the Mg substitution.

Peaks at 4.1 V are also seen for the Mn^{2+}/Mn^{3+} and also at 3.4 V for Fe^{2+}/Fe^{3+} in the $LiFe_{0.5-y/2}Mn_{0.5-y/2}Mg_yPO_4$ materials when an SPR >0.4 was used. However, in these materials the currents do not increase significantly on increasing y.

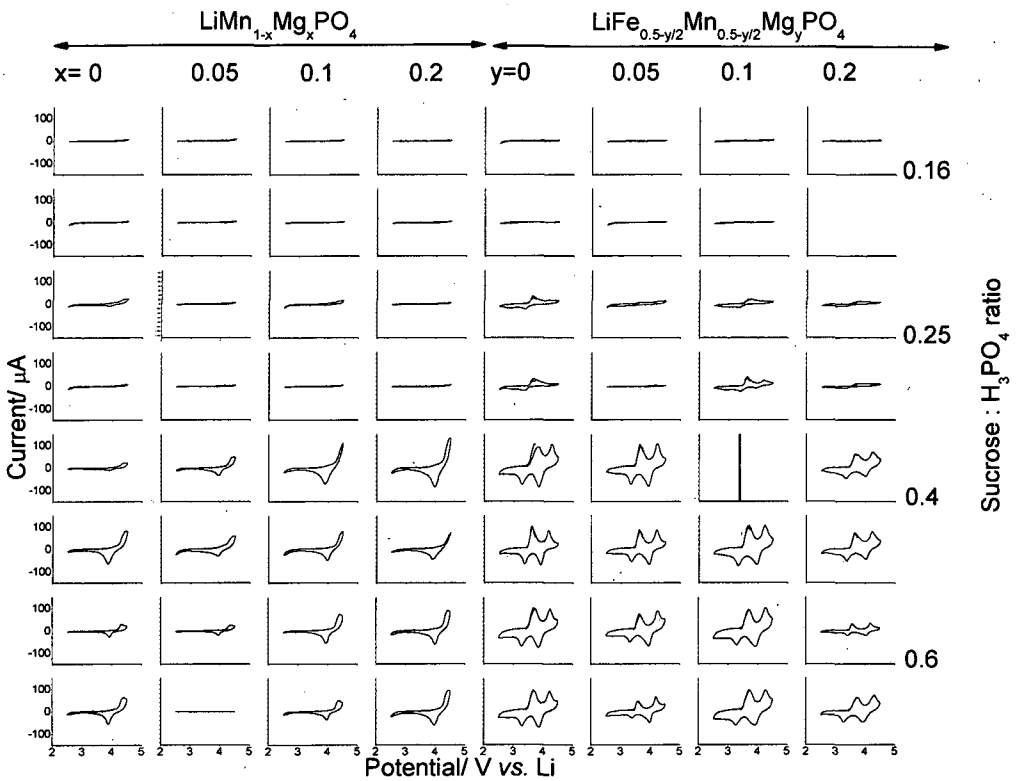

Figure 5-30 CVs electrode compositions are indicated. Potential swept from 2.5 to 4.2 V vs. Li at 0.05 mV s^{-1}.

Using the CVs shown in Figure 5-30 the specific capacities were calculated and are shown in Figure 5-31 and Figure 5-32.

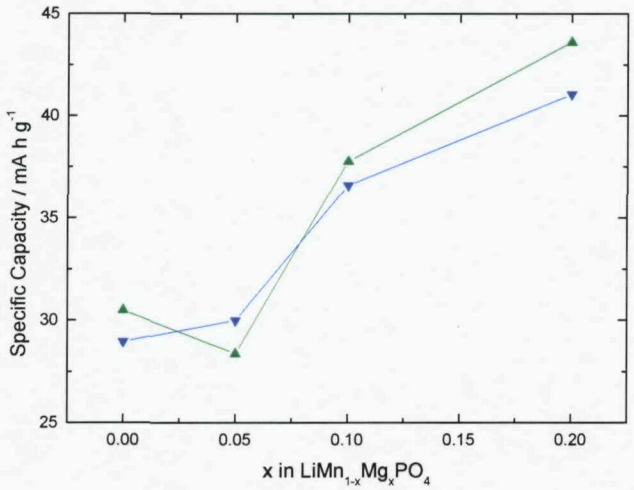

Figure 5-31 Capacity with increased Mg substitution for Mn in $LiMnPO_4$. The SPR ratios were 0.4(-▲-) and 0.6(-▼-).

In Figure 5-31 the extractable capacity increases markedly with the amount of Mg substituted for Mn. Whilst the capacity was still low (<50 mA h g^{-1}) an almost 15 mA h g^{-1} increase was seen in the $LiMn_{0.8}Mg_{0.2}PO_4$ sample. The capacities were only slightly increased when SPR values were changed from 0.4 to 0.6.

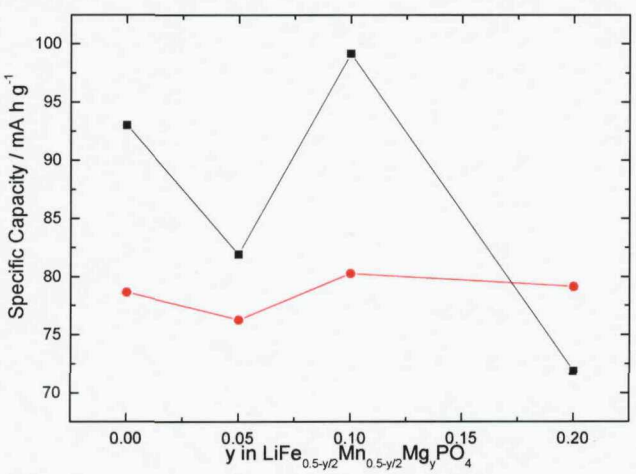

Figure 5-32 Capacity with increased Mg substitution for Fe and Mn in $LiFe_{0.5}Mn_{0.5}PO_4$. The SPR ratios were 0.4(-▲-) and 0.6(-▼-).

In Figure 5-32 the effect of Mg substitution is shown to have no significant improvement on the capacity, the actual specific capacities are almost twice that seen for the pure $LiMnPO_4$, but the lack of any improvement means that $LiFe_{0.5-y/2}Mn_{0.5-y/2}Mg_yPO_4$ materials will not be further studied.

To examine the improvement that is seen for the $LiMn_{1-x}Mg_xPO_4$ samples the CVs are shown in more detail for all the increments of Mg substitution for SPR values of 0.4 (Figure 5-33) and 0.6 (Figure 5-34). To obtain these graphs the 2 CVs measured for the repeat electrodes were averaged to try and reduce any scatter.

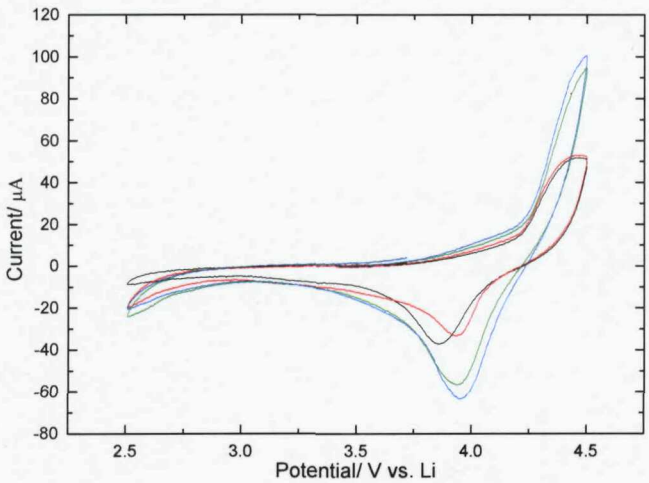

Figure 5-33 Averaged CVs for the two repeats of each $LiMn_{1-x}Mg_xPO_4$ electrode where x = 0(—), 0.05(—), 0.1(—), 0.2(—). The SPR value for these electrodes was 0.4.

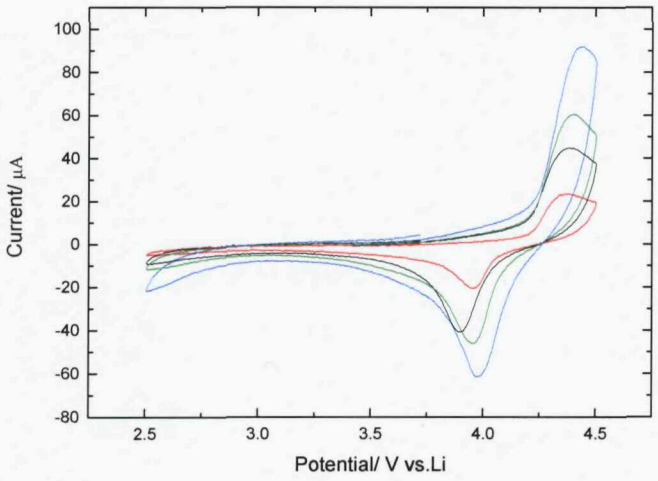

Figure 5-34 Averaged CVs for the two repeats of each $LiMn_{1-x}Mg_xPO_4$ electrode where x = 0(—), 0.05(—), 0.1(—), 0.2(—). The SPR value for these electrodes was 0.6.

In Figure 5-33 and Figure 5-34 the currents are seen to increase with the amount of Mg in the material (however, the $LiMn_{0.95}Mg_{0.05}PO_4$ does not fit this trend in both cases; this is presumed to be a result of scatter within the data). Another feature is that when electrodes were prepared with a higher SPR (Figure 5-34) the charging current appears to have reached a clear peak before the scan reverse potential, whereas, the currents in Figure 5-33 appear to still be increasing at this point. This indicates that there may be some improved conductivity in the higher carbon coated materials although only slight as it does not significantly affect the capacity. On close examination of the discharge peaks in both Figure 5-33 and Figure 5-34 a shift to higher peak potentials is seen with increasing amounts of Mg. This indicates an improvement in electronic conductivity and a reduction in the IR drop. The peak potentials have been plotted against composition below in Figure 5-35; the highest potential is seen for $LiMn_{0.8}Mg_{0.2}PO_4$ prepared with an SPR value of 0.6.

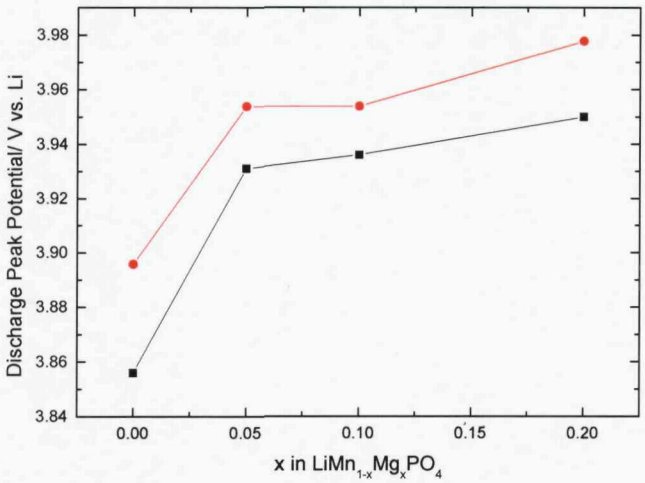

Figure 5-35 Discharge peak potential as a function of x in $LiMn_{1-x}Mg_xPO_4$. The SPR values were 0.4 (-■-) and 0.6 (-●-).

From this work the material which shows the highest capacity and best performance is the $LiMn_{0.8}Mg_{0.2}PO_4$ prepared with an SPR of 0.6. To further confirm this result a bulk sample of $LiMn_{0.8}Mg_{0.2}PO_4$ and for comparison $LiMnPO_4$ were prepared both with an SPR of 0.6.

Bulk XRD patterns

The XRD patterns for $LiMnPO_4$ and $LiMn_{0.8}Mg_{0.2}PO_4$ are shown below in Figure 5-36. The major phase present is the olivine indicated by comparisons between the experimental data and the shown database $LiMnPO_4$ pattern.(2) Indicated by (*) is the impurity phase $Mn_2P_2O_7$ which is present in both samples.(17)

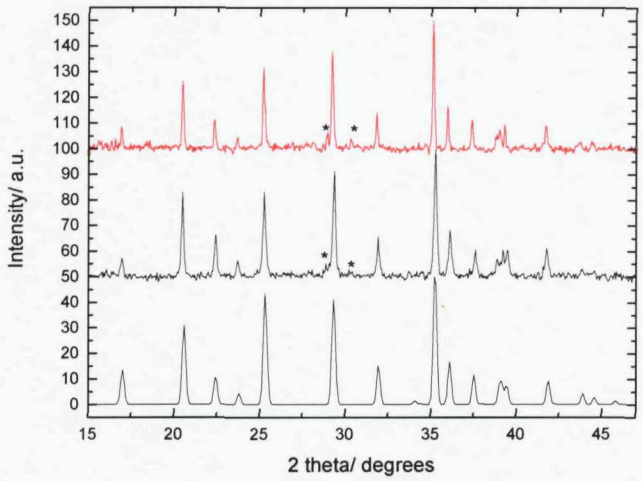

Figure 5-36 XRD patterns of $LiMnPO_4$/C (—) and $LiMn_{0.8}Mg_{0.2}PO_4$/C (—) prepared at 700°C in Ar. Shown for comparison is a simulated $LiMnPO_4$ pattern from the literature.(2) Asterisks mark the most intense lines of $Mn_2P_2O_7$.(17)

The patterns in Figure 5-37 were used to perform Rietveld refinement (*PowderCell 2.3*) based on an ordered olivine (orthorhombic) structure using space group *Pnma* to obtain the unit cell volumes. The results of which are shown as a function of Mg substitution in Figure 5-37 with a literature value for $LiMgPO_4$ for comparison. This is a good indication that a solid solution has formed as the linear decrease in the unit cell volume with magnesium substitution is in accordance with Vegard's law.

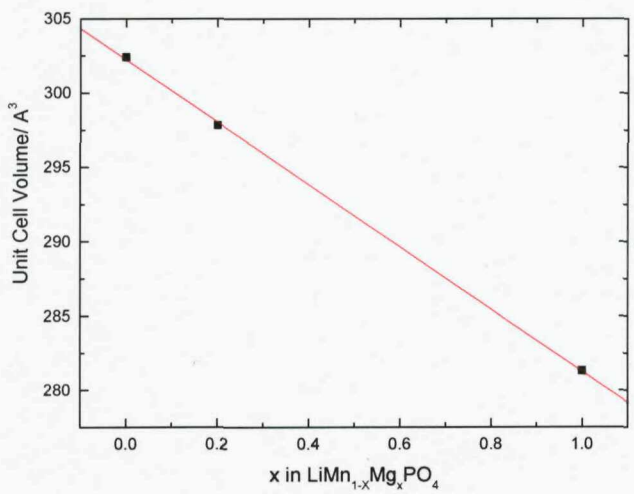

Figure 5-37 Variation of unit cell volume with change y in $LiFe_{1-y}Mg_yPO_4$. The volume for $LiMgPO_4$ is obtained from the literature(16).

Bulk Measurements Using Galvanostatic Cycling

Shown below is the galvanostatic cycling performance of $LiMn_{0.8}Mg_{0.2}PO_4$ and $LiMnPO_4$ prepared using the as described bulk route. The improvement in performance when the Mg doping is used is dramatic even at this relatively fast scan rate (~C/7). The Mg doped material has a charge and discharge capacity of ~75 and 55 mA h g^{-1}, which is still low in comparison to the best reported in the literature for this material. (At comparable rates the best performing materials reach between 70 and 140 mA h g^{-1}(18-21).) However, no attempt has been made to control the particle size or morphology which has been shown to be extremely important in other preparations.

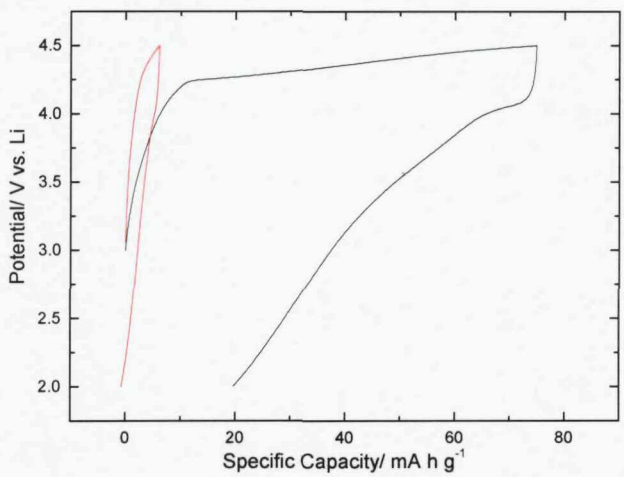

Figure 5-38 The galvanostatic cycling performance of $LiMn_{0.8}Mg_{0.2}PO_4$ and $LiMnPO_4$ at a rate of ~C/7.

5.3.3 Conclusions

The conclusion from this work is that the Mg doping does have a dramatic improvement on the electrochemical performance of $LiMnPO_4$. However, further work is required to try more synthetically challenging routes which might yield smaller particle sizes. The improved performance from both the small particles, Mg doping and carbon coating could be combined to obtain a material with a much better rate performance than those seen in the literature.

5.4 Conclusions Chapter 5

This chapter has been used to demonstrate the high-throughput method applied to compositional variations in $LiFePO_4$ materials. Insights have been provided into several uses for the high-throughput technique. The studies of $LiFe_{1-x}Mn_xPO_4$ materials have highlighted the use of the method in studies where the charge and discharge profiles are dramatically changed by composition. This has resulted in a situation where whilst the average discharge voltage is increased with Mn substitution the capacity is also reduced. It was speculated that this resulted from the reduced conductivity of the material reported in the literature. This study also gave insights into the charge and discharge mechanism which changes with x. Materials where x was greater than 0.3 a shift in behaviour of the Fe^{2+}/Fe^{3+} reaction from 1 phase to 2 phase was seen. This interpretation of the electrochemical measurements corresponds well with the work of Yamada et. al.(4) who studied the same system using structural characterisation. This has highlighted how the acquisition of data from compositional spreads can give fast insights into complicated changes in material performance.

The second study into the substitution Mg for both Fe and Li in $LiFePO_4$ has shown how the method can examine compositional changes affecting material conductivity. This approach highlighted improved conductivity when samples were prepared with Mg substituted for Fe. This was later confirmed with the preparation and testing of a bulk material. The preparation of carbon free samples and ac impedance measurements also showed that there was an improvement in electronic conductivity as a result of the Mg substitution. However, a secondary effect was believed to be related to a change in sample morphology seen using SEM.

The final study conducted in this chapter led on from the previous two. The reduced capacity with increasing x in $LiFe_{1-x}Mn_xPO_4$ was believed to be related to a drop in electronic conductivity. This led to the hypothesis that the same improvement in conductivity seen in $LiFe_{1-x}Mg_xPO_4$ might be reproduced for $LiFe_{1-x-y}Mn_xMg_yPO_4$ materials. This work showed that significantly improved performance of $LiMnPO_4$ could be obtained by using Mg doping (from <10 to ~60 mA h g^{-1}), presumably

because of an improvement in conductivity. However, the results showed no performance improvement for $LiFe_{0.5-y}Mn_{0.5-y}Mg_yPO_4$ materials.

5.5 References Chapter 5

1. A. D. Spong, G. Vitins and J. R. Owen, *Journal of the Electrochemical Society*, **152**, A2376 (2005).
2. O. Garcia-Moreno, M. Alvarez-Vega, F. Garcia-Alvarado, J. Garcia-Jaca, J. M. Gallardo Amores, M. L. Sanjuan and U. Amador, *Chemistry of Materials*, **13**, 1570 (2001).
3. A. R. West, *Solid State Chemistry and its Application*, John Wiley & Sons Ltd. (1984).
4. A. Yamada, Y. Kudo and K. Y. Liu, *Journal of the Electrochemical Society*, **148**, A1153 (2001).
5. A. K. Padhi, K. S. Nanjundaswamy and J. B. Goodenough, *Journal of the Electrochemical Society*, **144**, 1188 (1997).
6. C. Delacourt, L. Laffont, R. Bouchet, C. Wurm, J. B. Leriche, M. Morcrette, J. M. Tarascon and C. Masquelier, *Journal of The Electrochemical Society*, **152**, A913 (2005).
7. J. Barker, M. Y. Saidi and J. L. Swoyer, *Electrochemical and Solid-State Letters*, **6**, A53 (2003).
8. J. Hong, C. Wang and U. Kasavajjula, *Journal of Power Sources*, **162**, 1289 (2006).
9. T. H. Teng, M. R. Yang, S. H. Wu and Y. P. Chiang, *Solid State Communications*, **142**, 389 (2007).
10. D. Wang, H. Li, S. Shi, X. Huang and L. Chen, *Electrochimica Acta*, **50**, 2955 (2005).
11. C. Wang and J. Hong, *Electrochemical and Solid-State Letters*, **10**, A65 (2007).
12. G. X. Wang, S. Bewlay, J. Yao, J. H. Ahn, S. X. Dou and H. K. Liu, *Electrochemical and Solid-State Letters*, **7**, A503 (2004).
13. S. Y. Chung, J. T. Bloking and Y. M. Chiang, *Nature Materials*, **1**, 123 (2002).
14. Z. P. Guo, H. Liu, S. Bewlay, H. K. Liu and S. X. Dou, *Synthetic Metals*, **153**, 113 (2005).
15. G. X. Wang, S. L. Bewlay, K. Konstantinov, H. K. Liu, S. X. Dou and J. H. Ahn, *Electrochimica Acta*, **50**, 443 (2004).
16. F. Hanic, M. Handlovic, K. Burdová and J. Majling, *Journal of Chemical Crystallography*, **12**, 99 (1982).
17. T. Stefanidis and A. G. Nord, *Acta Crystallographica C*, **40**, 1995 (1984).
18. H. S. Fang, L. P. Li and G. S. Li, *Chemistry Letters*, **36**, 436 (2007).
19. X. Y. Chang, Z. X. Wang, X. H. Li, Q. Kuang, W. J. Peng, H. J. Guo and Y. H. Zhang, *Acta Physico-Chimica Sinica*, **20**, 1249 (2004).
20. G. H. Li, H. Azuma and M. Tohda, *Electrochemical and Solid State Letters*, **5**, A135 (2002).
21. N.-H. Kwon, T. Drezen, I. Exnar, I. Teerlinck, M. Isono and M. Graetzel, *Electrochemical and Solid-State Letters*, **9**, A277 (2006).

Chapter 6 Investigations of $LiNi_{1-x-y}Co_xMn_yO_2$ cathodes

6.1 Preparation conditions $LiNi_{1/3}Co_{1/3}Mn_{1/3}O_2$

The literature is replete with synthetic routes to prepare $LiNi_{1/3}Co_{1/3}Mn_{1/3}O_2$(1-4). The published results suggest that the preparation route significantly affects the electrochemical performance. The aim of this section is to examine different solution based preparations, varying precursor components and synthesis temperatures to obtain a suitable method for high-throughput compositional studies.

6.1.1 Experimental Details

Electrode Array Preparation by PoSAT

Solutions of $LiCH_3COO$ (2.5 M, 250 mL), $Co(NO_3)_2.6H_2O$ (1.25 M, 250 mL), $Ni(NO_3)_2.6H_2O$ (1.25 M, 250 mL), $Mn(NO_3)_2.6H_2O$ (Alfa Aesar, 1.25 M, 250 mL), $Ni(CH_3COO)_2.4H_2O$ (0.625 M, 250 mL), $Mn(CH_3COO)_2$ (0.625 M, 250 mL), $Co(CH_3COO)_2.4H_2O$ (0.625 M, 250 mL), Sucrose (2 M, 100 mL), Ammonium hydroxide(28 wt. % aqueous solutions, 100 mL), Brij 78(4 wt. % aqueous solutions, 100 mL, referred to as just Brij), Ethylene glycol and Citric acid (2 M, 100 mL) were prepared. The precursor salt solutions were then mixed as shown in Table 6-1 to form the $LiNi_{1/3}Co_{1/3}Mn_{1/3}O_2$ stiochoimetries with the automated liquid handling robot (Perkin-Elmer Life Sciences). Using hand automated pipettes the various additives were then dispensed into the appropriate positions on the array. In the case of the hydroxide precipitation method, small (4 × 2 mm) magnetic stirrer bars were added to each tube prior to the ammonia hydroxide addition. The solutions were then stirred at 60 °C for 12 h after the addition of ammonium hydroxide to each tube. For the ethylene glycol and citric acid(5) preparations the additive was dispensed at room temperature and the samples were then heated to 90 °C for 10 mins and then 40 °C for

10 h. All other preparations were simply dried to solids at 60 °C. Then 32 precursors at a time were placed within a rack designed to utilise the thermal gradient in the tube furnace such that each row in the array was exposed to a different temperature; 600, 650, 700, 750, 800, 850, 900 and 950 °C. This synthesis was performed in an oxygen atmosphere. After cooling, the products were crushed by adding five 1 mm zirconia beads to each tube followed by placing the whole array on a vibrating table (IKA VIBRAX VXR Basic). Composite electrode preparation began by adding two inks, 4% PVdF-HFP (*Aldrich*, polyvinylidene fluoride-co-hexafluoropropylene) and 4% AB (acetylene black, *Shawinigan, Chevron Phillips Chemical Company LP*) in cyclopentanone (CP) to the active material powders in each tube. The inks were added to give a final mass ratio of 10 % PVdF-HFP, 25 % AB and 65 % active material and then mixed using the vortex mixer. Then 14 µL aliquots of each ink was deposited onto the appropriate position on the array of aluminium current collectors and spread across the surface to form an even film of ink. At the same time, a 40 µL sample of each ink was deposited into an array of alumina micro-crucibles for thermo gravimetric analysis as detailed below. The CP was evaporated from both arrays at room temperature before drying at 80 °C followed by evacuation. The samples on both arrays were then accurately weighed using a computer monitored balance.

Table 6-1 Table showing the preparation mixtures used to prepare $LiNi_{1/3}Co_{1/3}Mn_{1/3}O_2$. Total volume precursor salt solutions 1 mL.

	Array	Columns	Precursors Salts	Precipitation Additive	Additive to stop Crystallization
Nitrates only	1	1, 2	$LiCH_3COO$, $Ni(NO_3)_2$, $Mn(NO_3)_2$, $Co(NO_3)_2$		
Nitrates + Sucrose	1	3, 4	$LiCH_3COO$, $Ni(NO_3)_2$, $Mn(NO_3)_2$, $Co(NO_3)_2$		31.2 µL 1 M Sucrose
Hydroxide	1	5, 6	$LiCH_3COO$, $Ni(NO_3)_2$, $Mn(NO_3)_2$, $Co(NO_3)_2$	0.473 mL 28 % Ammonium hydroxide	
EG Citrate	1	7, 8	$LiCH_3COO$, $Ni(NO_3)_2$, $Mn(NO_3)_2$, $Co(NO_3)_2$		70 µL Ethylene glycol and 0.625 mL of 2 M Citric acid
Brij	2	1, 2	$LiCH_3COO$, $Ni(NO_3)_2$,		1 mL 4 wt. %

			$Mn(NO_3)_2$, $Co(NO_3)_2$		aqueous Brij 78
Brij + EG and citrate	2	3, 4	$LiCH_3COO$, $Ni(NO_3)_2$, $Mn(NO_3)_2$, $Co(NO_3)_2$		1 mL 4 wt. % aqueous Brij 78, 70 µL Ethylene glycol and 0.625 mL of 2 M Citric acid
Acetates only	2	5, 6	$LiCH_3COO$, $Ni(CH_3COO)_2$, $Mn(CH_3COO)_2$, $Co(CH_3COO)_2$		
Acetates + sucrose	2	7, 8	$LiCH_3COO$, $Ni(CH_3COO)_2$, $Mn(CH_3COO)_2$, $Co(CH_3COO)_2$		31.2 µL 1 M Sucrose

Array Sample characterisation

Thermo gravimetric Analysis and High Throughput X-ray Diffraction measurements were then performed on the array of samples as described in Chapter 2. High throughput electrochemical evaluation of the array was also performed as described in Chapter 2. The arrays were cycled between 2.5 to 4.2 V vs. Li at the following 0.05 mV s^{-1}.

Bulk Sample Preparation

Samples of $LiNi_{1/3}Co_{1/3}Mn_{1/3}O_2$ were prepared via the nitrate only method using the same solutions and mixing ratios as that used for the PoSAT array except the solution volumes were scaled up so the total precursor volume was 20 mL. Two samples were prepared; the solution was then removed to leave solid precursors. These two samples were then heat treated at 700 and 900 °C for 10 h in flowing air 0.5 L min^{-1} respectively.

X-ray phase analysis on bulk samples

X-ray powder diffraction patterns were recorded for the bulk samples using a Bruker D5000 diffractometer. X-ray patterns were collected for the 2θ between 15 and 50° at a scanning rate of ca. 0.07 °/min using a $CuK\alpha_1$ radiation.

Scanning electron microscopy on bulk samples

Samples of the active materials were studied by scanning electron microscopy (SEM) using a Philips XL30ESEM at an accelerating voltage between 10 and 15 kV using the secondary electron and backscattered electron detectors.

Electrochemical testing of bulk samples

The electrodes (thickness ~70 μm) and cells were prepared as described in the Chapter 2 and were then cycled galvanostatically at currents corresponding to C/7 between 2 and 4.2 or 4.5 V potential limits using a 16-channel potentiostat (VMP, Princeton Applied Research; Biologic-Science Instruments).

6.1.2 Results and Discussion

Properties of the dried precursors

The properties of the dried precursor solids varied significantly shown in Figure 6-1. In the case of the nitrates only (A), acetates (G) and acetates with sucrose (H) preparations homogeneous dense purple solids were formed after drying. When nitrates and sucrose (B) were used a homogeneous porous brown solid is formed. When the hydroxides were precipitated a fine black powder was seen which coated the side of the tube and cannot be seen clearly in photo C. The ethylene glycol citric acid preparation (D) formed a brown translucent solid which resulted from the formation of a gel as the citric acid acts as a chelating agent binding to the metal ions before polymerising with the ethylene glycol. After high temperature calcinations no visual difference could be seen between any of the samples.

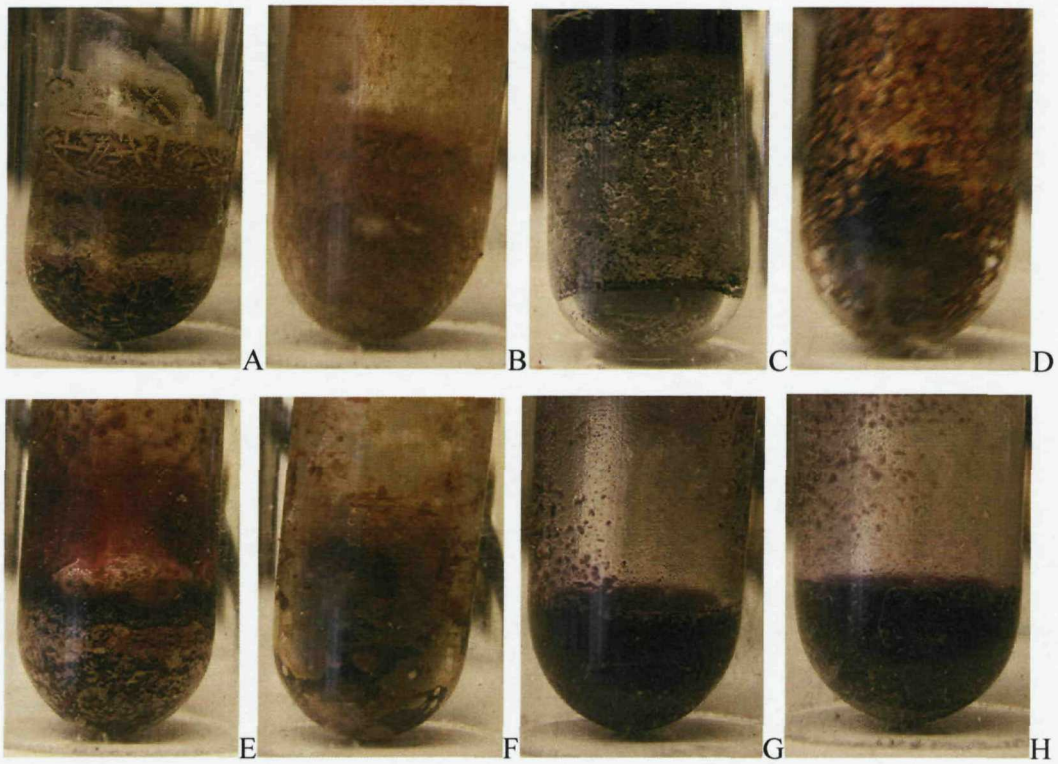

Figure 6-1 Dried $LiCo_{1/3}Ni_{1/3}Mn_{1/3}O_2$ precursors prepared via the following routes: A nitrates only; B nitrates with sucrose; C hydroxide preparation; D EG and Citric acid; E Brij; F EG, Citric acid and Brij; G acetates only; H acetates with sucrose.

High-throughput XRD analysis

The XRD patterns for 800 °C preparations are representative of the trends seen for all synthesis temperatures and are shown in Figure 6-2. All patterns except those belonging to the acetates and acetates with sucrose preparations showed patterns corresponding to pure $LiCo_{1/3}Ni_{1/3}Mn_{1/3}O_2$. In the acetate preparations a unidentified impurity peak (2 theta = 43.5 °) can be seen. This may have been due to a lack of precursor homogeneity; as the MnAc is not stable in solution for long, forming a dark brown precipitate. For several of the patterns the intensity of the peak at ~38 ° varies from the database pattern. This is attributed to a peak at 38 ° in the PVdF-HFP binder material present in all electrodes. In some of the samples the intensity of the peak at 45 ° appears larger relative to the other peaks as observed in the literature; this peak is for aluminium sometimes seen from the substrate below. A 2 theta shift between

samples prepared using the different routes can also be noted, this is likely to result from slight variations in sample height during measurement.

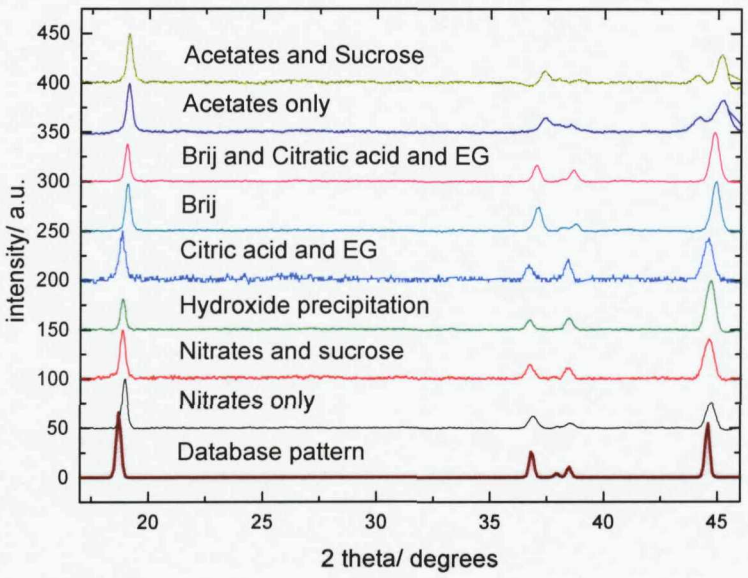

Figure 6-2 XRD patterns of $LiNi_{1/3}Co_{1/3}Mn_{1/3}O_2$ prepared using the following precursors nitrates only (—), nitrates with sucrose (—), hydroxides (—), citrates and EG (—), Brij (—),Brij with citrates and EG (—), acetates only (—) and acetates and sucrose (—). Also shown for comparison is a database result (—)(6).

XRD patterns for all temperature preparations using the nitrate only method are shown in Figure 6-3. This is representative of the patterns obtained for each different route.

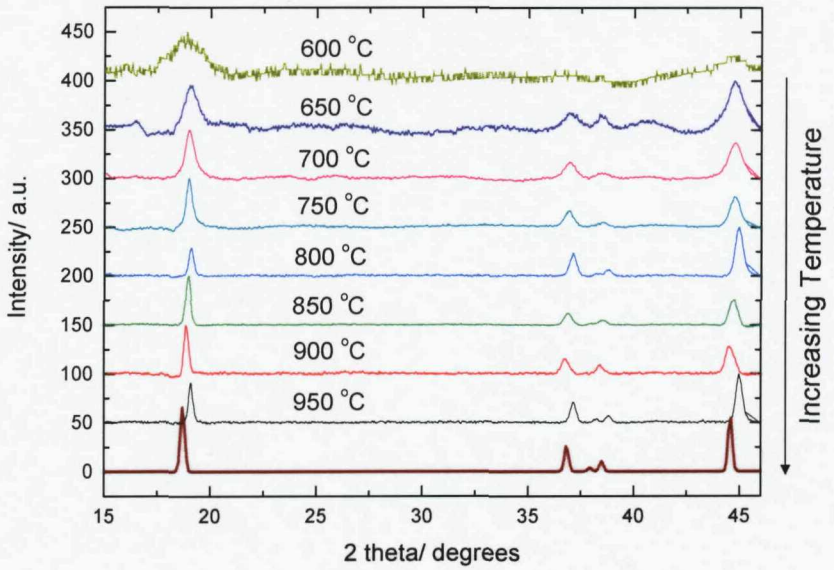

Figure 6-3 XRD patterns of $LiNi_{1/3}Co_{1/3}Mn_{1/3}O_2$ prepared via the nitrates only preparation method at 600 (—), 650(—), 700(—), 750(—), 800(—), 850(—), 900(—) and 950(—). Also shown for comparison is a database result (—)(6).

In Figure 6-3 no detectable impurity peaks are seen in any of the samples. In some samples the same variations from the pure material resulting from Al and PVdF-HFP can be seen as in Figure 6-2. Significant line broadening is seen in preparations below 800 °C, this effect is typically reported as a reduction in the crystallite thickness.(7, 8) The lower temperature means that there is not sufficient energy to form large crystals. Using the Scherrer formula (Equation 6-1) this broadening can be interpreted to give the crystallite thickness shown in Figure 6-4.

$$t = \frac{0.9\lambda}{B\cos\theta_B}$$

Equation 6-1

t = Crystal size/ nm

λ = X-ray wavelength/ nm

Θ_B = Bragg angle/ °

B = factor determining the degree of line broadening

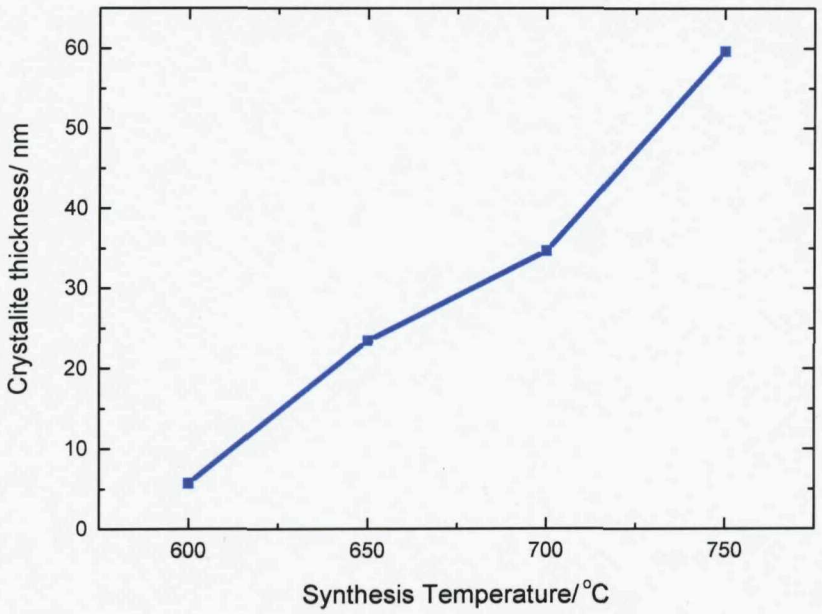

Figure 6-4 Crystallite thickness of $LiNi_{1/3}Co_{1/3}Mn_{1/3}O_2$ when calcined at different temperatures.

High-throughput electrochemical measurements

The first cycle CVs (scan rate 0.05 mV s^{-1}) recorded for all the preparations are shown below in Figure 6-5 and Figure 6-6. In general the CVs show charge discharge peaks around 4 V which is characteristic for this material.(9) The peak shape is characteristic of a 1 phase material with the charge and discharge peaks occurring in the same voltage range. The CVs with the highest currents in both arrays appear to be the nitrates only preparation, hydroxide precipitation, EG and Citrate and EG, Citrate and Brij. The nitrates with sucrose and both acetate preparations have significantly lower currents. In the case of the sucrose this is explained as the TGA results showed significantly lower amounts of AM in the composite than expected by the addition of the inks. The quartz tubes used for the sucrose preparations had active material coated on the surface of the tube rather than falling to the bottom, it is presumed that this resulted in less material being transferred to the composite ink. In the case of the acetates the lack of phase purity as confirmed via XRD measurements is likely to explain the poor electrochemical performance.

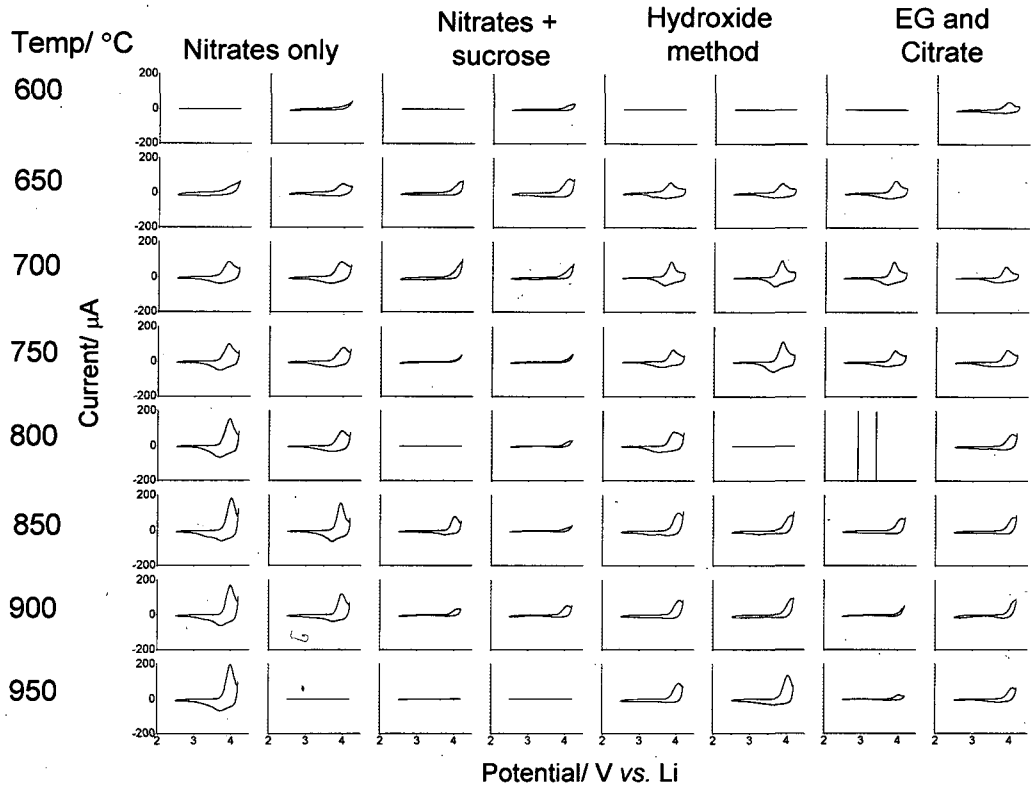

Figure 6-5 First cycle CVs Array 1, preparation conditions are indicated. Potential swept from 2.5 to 4.2 V at 0.05 mV s^{-1}.

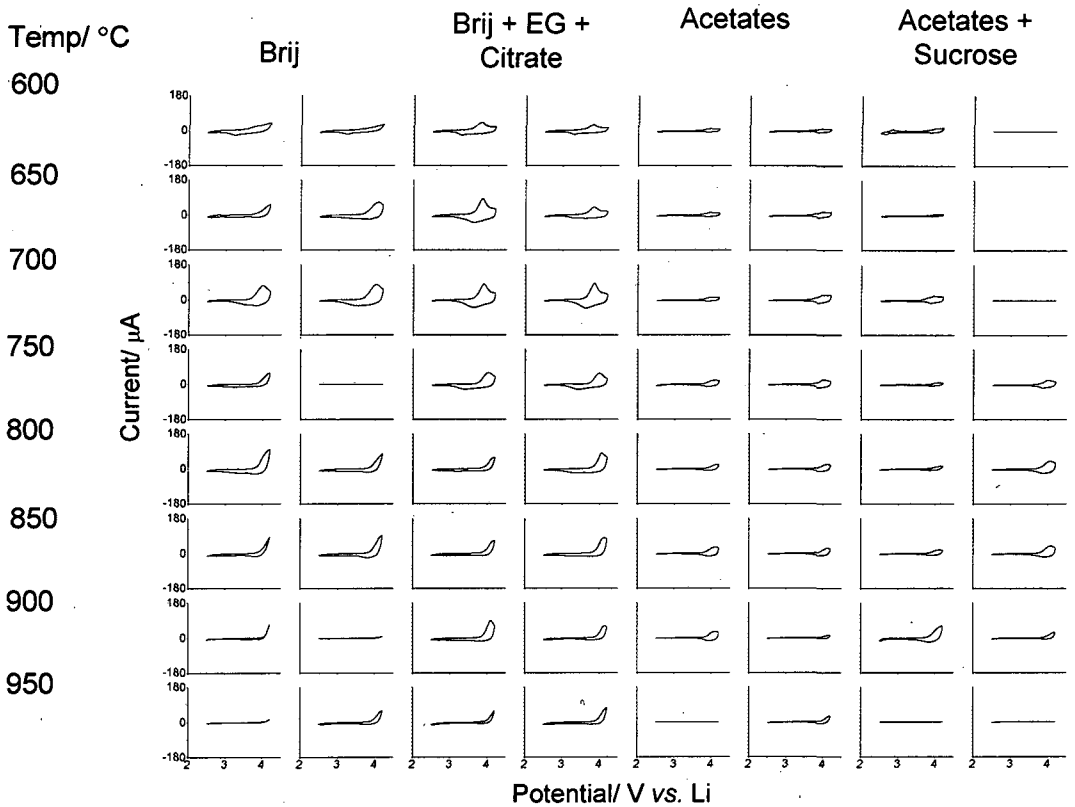

Figure 6-6 First cycle CVs array 2, preparation conditions are indicated. Potential swept from 2.5 to 4.2 V at 0.05 mV s^{-1}.

To quantify the performance of these materials the capacity per cycle was calculated and is shown below in Figure 6-7 and Figure 6-8. The duplicate samples on the array were used to average this result so as to reduce the error, only the 700, 800 and 900 °C preparations are shown for simplicity.

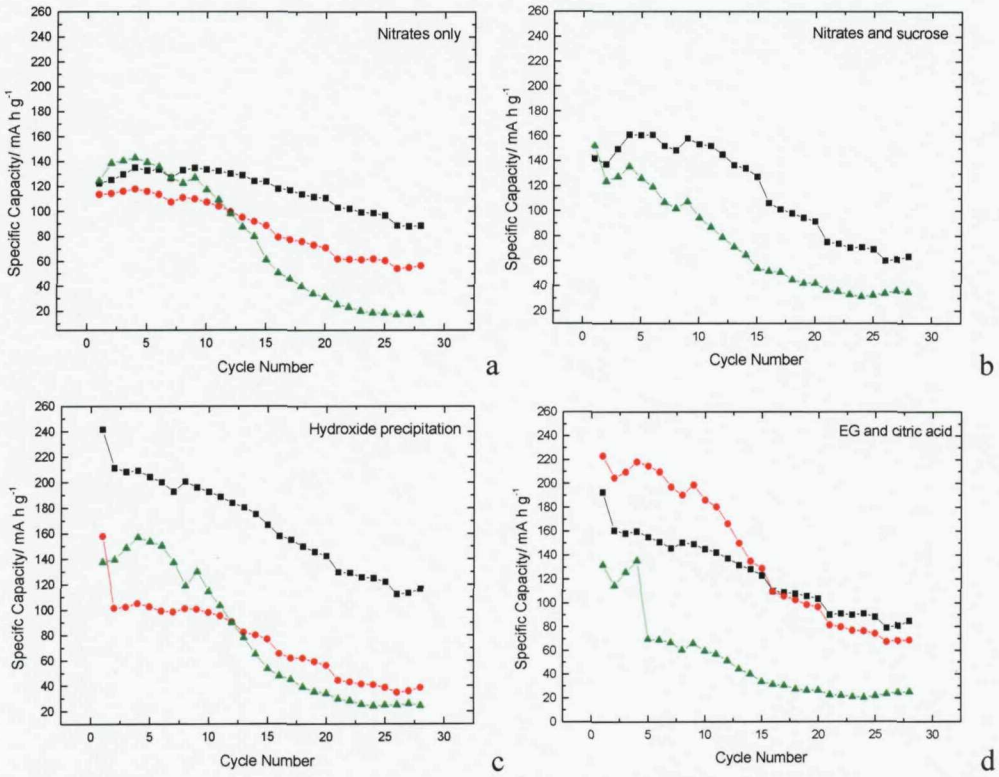

Figure 6-7 Retention of capacity on cycling for selected temperatures 700 (-■-) 800 (-●-) and 900 °C (-▲-) for the preparations of $LiNi_{1/3}Co_{1/3}Mn_{1/3}O_2$; (a) nitrates only, (b) nitrates and sucrose, (c) hydroxide precipitation and (d) ethylene glycol and citric acid.

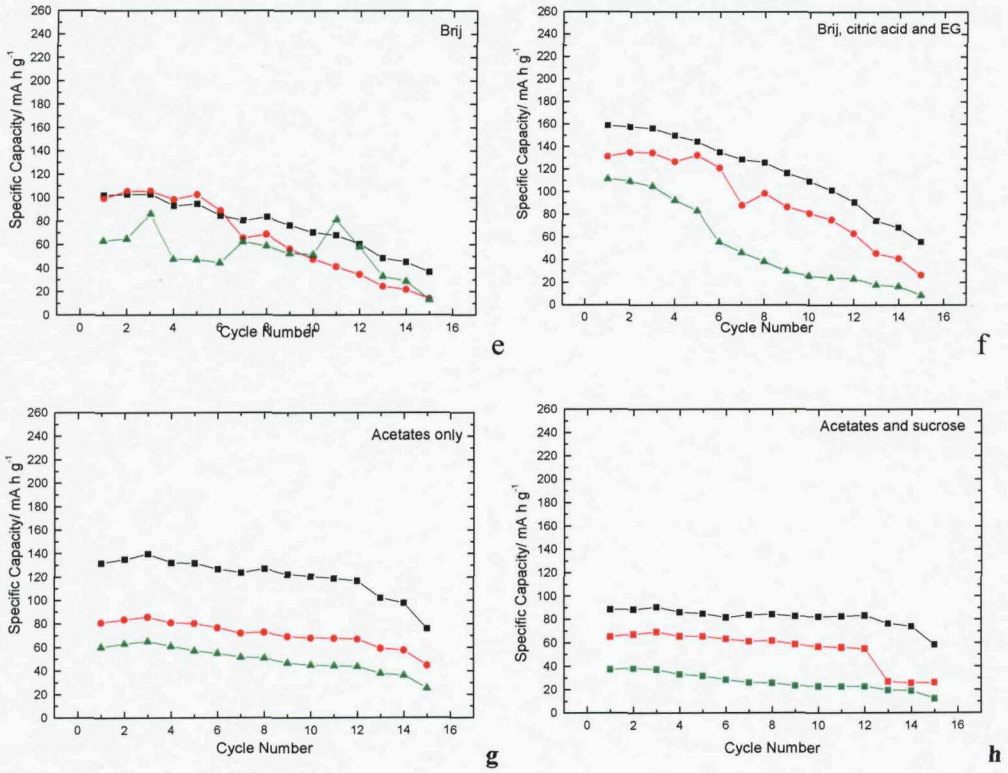

Figure 6-8 **Retention of capacity on cycling for selected temperatures 700 (-■-) 800 (-●-) and 900 °C (-▲-) for the preparations of $LiNi_{1/3}Co_{1/3}Mn_{1/3}O_2$; (e) Brij, (f) Brij and ethylene glycol and citric acid, (g) acetates only (h) acetates and sucrose.**

The initial capacities shown in Figure 6-7 and Figure 6-8 for the materials vary from 60 to 240 mA h g^{-1}, the highest being seen for the hydroxide precipitated materials synthesised at 700 °C. Typically values of 200 mA h g^{-1} are quoted within the literature(2, 9), however, this is normally seen when charging the material to 4.6 V rather than the limited voltage range used in this work. This restricted charging voltage was chosen so as not to damage the material by extraction of all or most of the Li which is reported to result in poor cycle life in $LiCoO_2$.(10) The cycle life of this material was of particular interest as it is indicated in the literature to be the most significant drawback of this material.(11-13) Figure 6-7 and Figure 6-8 show that for the capacity retention of materials prepared at 900 °C is extremely poor, all materials dropping below 40 mA h g^{-1} after 20 cycles, this was also true for the materials prepared at 950 and 850 °C. The materials synthesised at 800 °C also show a significant, however, less dramatic capacity loss, the best performing of which are the

nitrates only and EG and citrate preparations but still only retain 60 mA h g^{-1} after 30 cycles. The materials synthesised at 700 °C showed the highest retention on cycling the best of which were the nitrates only (90 mA h g^{-1} after 30 cycles), hydroxide precipitation (110 mA h g^{-1} after 30 cycles) and EG and citric acid (80 mA h g^{-1}) preparations. Of these materials the hydroxide and EG and citric acid preparation show significant capacity losses during the 30 cycles, however, the high initial capacities leads to the high final capacity. However, the nitrate only preparation has a maximum capacity of 130 mA h g^{-1} and a final capacity of 90 mA h g^{-1} making it the most stable of the materials.

Characterisation of bulk samples

The aim was to find a simple synthetic route which gave a material with a good electrochemical performance. In terms of retention of initial capacity on cycling the nitrates only, hydroxide precipitation and EG and citric acid method at 700 °C performed the best. However, in terms of the preparation simplicity the nitrates only mixing method is the most straightforward and most suitable for further compositional studies using the high-throughput methods. The reason the hydroxide preparation in particular was discounted at this point (when the results above appear to be the best), is because using stirrer bars in all 64 samples on the array as required for the preparation is extremely difficult. To confirm the performance of the nitrate materials some bulk samples of $LiNi_{1/3}Co_{1/3}Mn_{1/3}O_2$ were prepared using the nitrate only preparation method at both 700 and 950 °C. Below in Figure 6-9 the XRD patterns for these materials are shown.

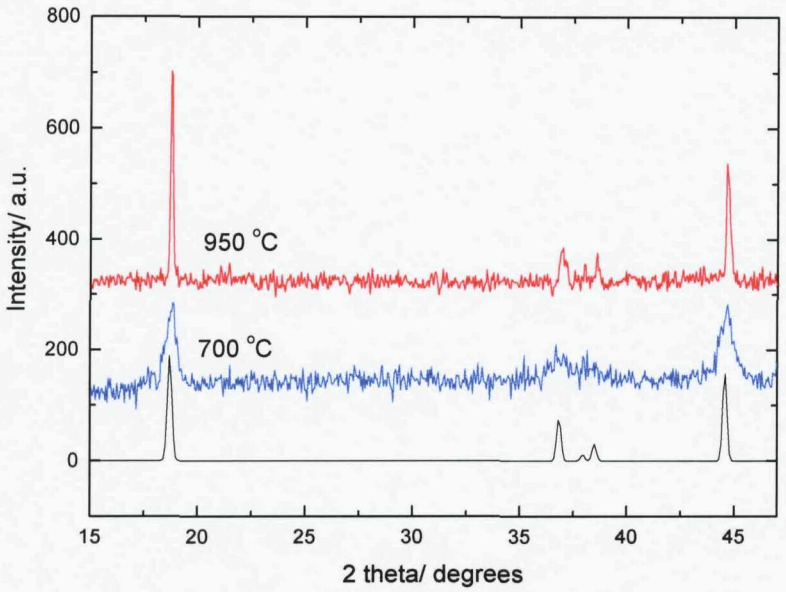

Figure 6-9 XRD patterns of nitrate only prepared $LiNi_{1/3}Co_{1/3}Mn_{1/3}O_2$ synthesised at both 950 and 700 °C indicated on the graph. Also shown for comparison is a literature pattern(6)

The XRD patterns in Figure 6-9 show that there are no detectable impurity peaks in either material as seen in the high-throughput measurements. The same line broadening in the sample prepared at only 700 °C is also seen.

The galvanostatic cycling data is shown below in Figure 6-10 and Figure 6-11, to see the effect that the depth of discharge has on the cyclability of the materials the potential limits for the experiments depicted in the two graphs were 2 to 4.2 and 2 to 4.5 V respectively.

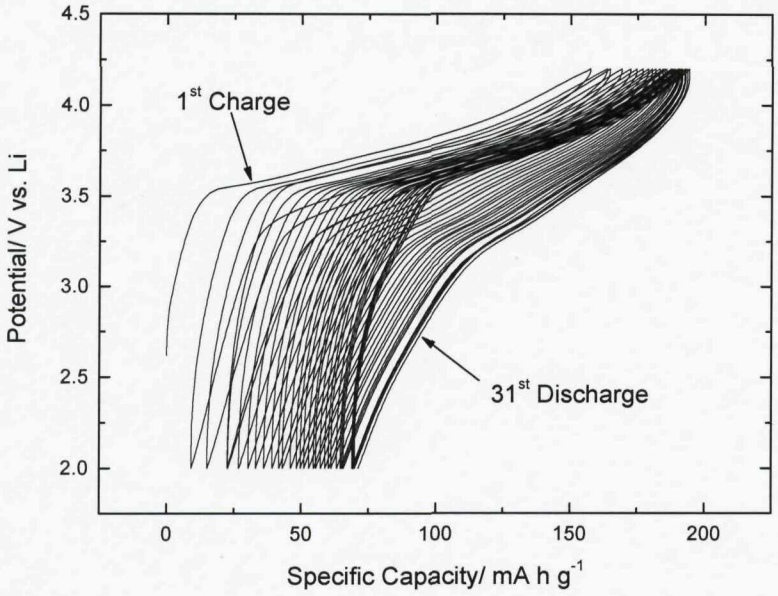

Figure 6-10 Galvanostatic cycling profile (C/7) for $LiNi_{1/3}Co_{1/3}Mn_{1/3}O_2$ prepared from nitrate only precursor at 700 °C.

In Figure 6-10 the material shows an initial discharge capacity of 146 mA h g^{-1} which drops to 121 mA h g^{-1} by the 32nd cycle. The shape of the charging curve stays consistent for all cycles, with an area of activity seen above 3.6 V during which approximately 75 % of the charging capacity is delivered. There is a significant hysteresis between charge and discharge curve seen in Figure 6-10 which gets larger on increased cycling. The size of the hysteresis is probably rate dependent (although this was not studied) and therefore a kinetic or mass transport effect, e.g. due to the deterioration of contacts between particles and the carbon network. During discharge a voltage plateau can be seen between approximately 4.2 and 3 V where around 60 % of the discharge capacity is delivered and then around 40 % of the capacity is seen at lower potentials, this general shape is maintained for all 30 cycles. A significant charge discharge capacity imbalance can also been seen.

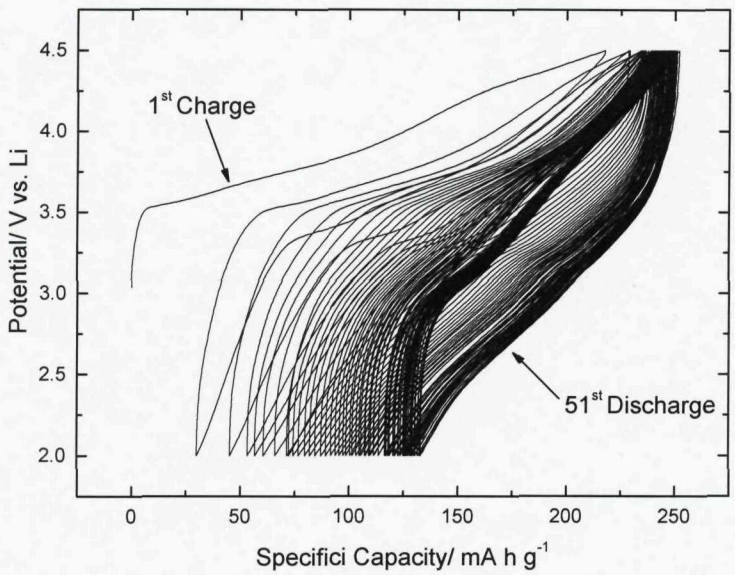

Figure 6-11 Galvanostatic Cycling profile for $LiNi_{1/3}Co_{1/3}Mn_{1/3}O_2$ prepared from nitrate only precursor at 700 °C.

The galvanostatic cycling data in Figure 6-11 shows a marked change from the restricted potential window cycling seen in Figure 6-10. Initially a similar voltage charge plateau is seen between 3.5 and 4.5 V, however, over the subsequent 10 cycles this plateau region changes to between 3 to 4.5 V. The hysteresis seen between charge and discharge is greater than seen in Figure 6-10, and there is a much larger charge imbalance seen over the first few cycles. The discharge curve shows a similar pattern to that seen in Figure 6-10 over the first few cycles with a plateau seen between 4.5 and 3 V. However, after ~ 4 cycles 80 % of the discharge capacity is delivered between 3.5 and 2.25 V, this is possibly indicating an increased resistance in the material resulting from continued cycling and therefore an increased IR drop.

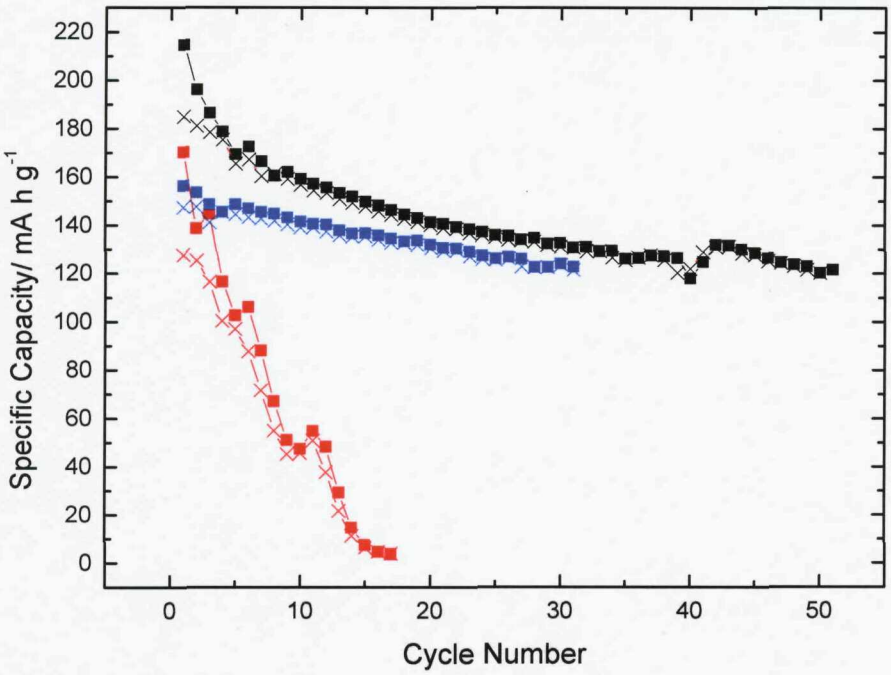

Figure 6-12 Retention of capacity on cycling for $LiNi_{1/3}Co_{1/3}Mn_{1/3}O_2$ prepared at 700 °C (charged to 4.2 V (■) and discharged to 2 V(×) and charged to 4.5 V (■) and discharged to 2 V(×)) and 950 °C (charged to 4.5 V (■) and discharged to 2 V(×)).

The material synthesised at 700 °C has a far greater retention of capacity per cycle than the 950 °C material, this is shown in Figure 6-12. The 950 °C material shows an initial discharge capacity of 130 mA h g^{-1} which decreases to less than 20 mA h g^{-1} after 13 cycles. The 700 °C material which was cycled between 2 and 4.2 V had an initial discharge capacity was 146 mA h g^{-1} which decreased to 121 mA h g^{-1} by the 31st cycle. This corresponds to a percentage of capacity retention per cycle of 99.45 %. This same material when cycled between 2 and 4.5 V shows an initial capacity of 186 mA h g^{-1} which has dropped to only 122 mA h g^{-1} and relates to a percentage of capacity retention per cycle of 98.9 %. Typical values reported in the literature for capacity retention per cycle are 99.9(initial capacity 190 mA h g^{-1}) (2), 99.7 (200 mA h g^{-1}) (9) and 99.6 % (145 mA h g^{-1}) (12). Whilst the performance of the nitrate 700 °C material is not as good as some of these materials it is still competitive. Two of these reports are for slower discharge rates(9) or restricted potential window(12) testing.

SEM images on Bulk Samples

Sample morphology and particle size was investigated as a possible reason for the improved performance of the 700 °C samples. The broadening of the peaks in the XRD data has already indicated a reduction in particle size. To confirm this effect high resolution SEM images were recorded for the 700 and 950 °C nitrates only preparations shown in Figure 6-13 and Figure 6-14 respectively.

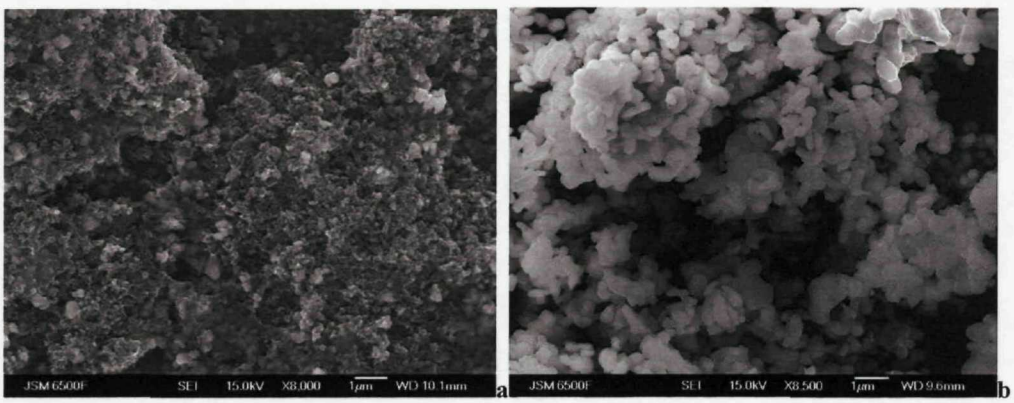

Figure 6-13 SEM images of nitrate only precursor preparations calcined at (a) 700 and (b) 900 °C.

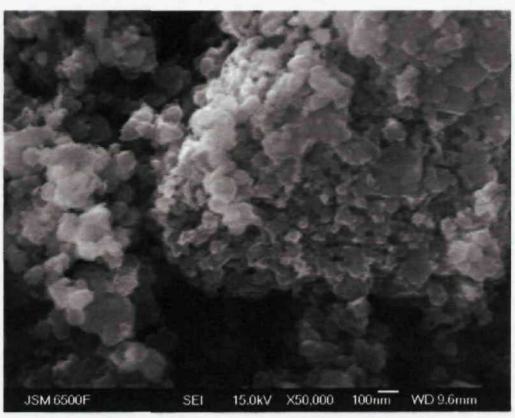

Figure 6-14 Increased magnification SEM image of nitrate only precursor prepared at 700 °C.

In Figure 6-13 and Figure 6-14 the particle size is approximately 100 and 500 nm for the 700 and 950 °C synthesis temperatures respectively. The morphology of the particles is also temperature dependent, the 700 °C preparation shows sharp faceted crystals, whereas the 950 °C preparations show rounded crystals edges, which form large agglomerates. However, although in this work the 700 °C preparation performs best the shape of 950 °C material is more consistent with those preparations reported

within the literature, particularly the material prepared by Shaju et al.(2) who report the highest capacity, rate capability and capacity retention on cycling.

This highlights the importance of sample morphology in obtaining improved capacity retention. However, the very low temperatures for optimal synthesis reported here do not typically match those from the literature. Several studies have been undertaken to try and optimise the synthesis conditions all involving different synthetic routes and all concluding different optimal synthesis temperatures (800(11), 850(14), 900(15), 950(2), 1000(12)), times and precursors. It is therefore difficult to make any statements about this material in general and the materials performance is clearly sensitive to the preparation routes.

Based on the results seen here it is speculated that the reason for the improvements in some materials is related to the stresses and strains that the particle undergoes during charge and discharge. The particle expands and contracts with the insertion and removal of Li from the structure. When a particle is small the stresses and strains which it undergoes are usually homogeneous and the particles do not suffer too many fractures. When a particle is large the volume of the particle can vary from region to region depending on the sample morphology. This could result in inhomogeneous strains possibly causing fractures in the material.

6.1.3 Conclusions

The PoSAT method has been used to investigate a number of different preparation conditions with the introduction of arrays prepared in temperature gradients. This is a novel area for high-throughput work which the PoSAT method can easily be applied to when investigating new systems in the future.

A material has also been identified with an easy synthetic route and good electrochemical performance within a limited potential range. Therefore, this route was deemed the most practical for use in further compositional variation studies on the ternary system $LiCo_{1-x-y}Ni_xMn_yO_2$ investigated in section 6.2. This work has also highlighted how sensitive this material is to sample morphology.

6.2 $LiCo_{1-x-y}Ni_xMn_yO_2$ Graded Composition

The aim of this study was to use the preparation developed in Section 6.1 to investigate a large number of materials in the ternary system $LiCo_{1-x-y}Ni_xMn_yO_2$.

6.2.1 Experimental Details

Electrode Array Preparation by PoSAT

Solutions of $LiCH_3COO$ (2.5 M, 250 mL), $Co(NO_3)_2$ (1.25 M, 250 mL), $Ni(NO_3)_2$ (1.25 M, 250 mL), $Mn(NO_3)_2$ (1.25 M, 250 mL) were prepared. Using the automated liquid handler (Perkin-Elmer Life Sciences) the solutions were then mixed in ratios such that the correct stiochiometry for the materials indicated in Figure 6-15 were prepared in an array of 64 quartz tubes.

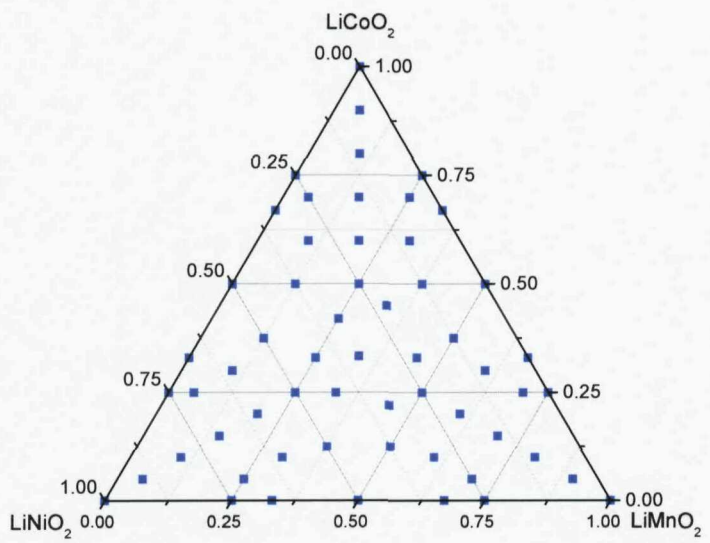

Figure 6-15 Ternary diagram for $LiCo_{1-x-y}Ni_xMn_yO_2$ indicating the samples which were synthesised.

All the preparations were dried to solids at 60 °C. Then the tubes contained within stainless steel racks were placed in a tube furnace (Lenton) and calcined at 700 °C in oxygen. After cooling, the products were crushed by the addition of five 1 mm zirconia beads to each tube followed by placing the whole array on a vibrating table (IKA VIBRAX VXR Basic). Composite electrode preparation began by adding two inks, 4% PVdF-HFP (Aldrich, polyvinylidene fluoride-co-hexafluoropropylene) and 4% AB (acetylene black, Shawinigan, Chevron Phillips Chemical Company LP) in cyclopentanone (CP) to the active material powders in each tube. The inks were added to give a final mass ratio of 10% PVdF-HFP, 25% AB and 65% active material and then mixed using the vortex mixer. A smaller amount than usual of ink (10 μL) was deposited onto each aluminium current collector as better adhesion to the substrate was found. 40 μL samples of each ink were deposited into an array of alumina micro-crucibles for thermo gravimetric analysis as detailed below. The CP was evaporated from both arrays at room temperature before drying at 80 °C followed by evacuation. The samples on both arrays were then accurately weighed using a computer connected balance.

Array Sample characterisation

X-ray Diffraction measurements were performed on the selected samples using the C2 difractometer in single sample mode. The arrays were cycled between 2.5 to 4.2 V vs. Li at 0.05 mV s^{-1}.

6.2.2 Results and Discussion

High-throughput XRD results

Selected XRD patterns from the array are shown in Figure 6-16. The patterns show three groups of peaks at around 20 °, between 35 and 40 ° and 45 ° which correspond to peaks within the patterns of $LiCoO_2$, $LiNiO_2$ and $LiMn_2O_4$. (It is expected that samples which contains one Li to Mn will not form the layered structure but instead the spinel $LiMn_2O_4$. This is also confirmed in the electrochemical data shown later.) The peaks are broad indicating small crystals presumably because of the low synthesis temperatures. No extra impurity peaks can be seen in any of the samples except

$LiCo_{0.25}Mn_{0.75}O_2$. In this sample a small peak is seen at around 21 ° and on the shoulder of another peak at 45°. This could indicate phase separation and the formation of 0.25 $LiCoO_2$ and 0.75 $LiMn_2O_4$. Many of the samples also show severe intensity variations and shifts in the 2 theta values from the displayed database patterns; both discrepancies are believed to result from systematic problems associated with the high-throughput instrument. However, the peak positions do show a general shift from right to left with increasing amounts of Mn and Ni substitution in the $LiCoO_2$ as expected from the database patterns. This leads to the tentative conclusion that the correct phase of target materials have been prepared in most samples, however, it is likely that some phase segregation has occurred in $LiCo_{1-x}Mn_xO_2$ samples.

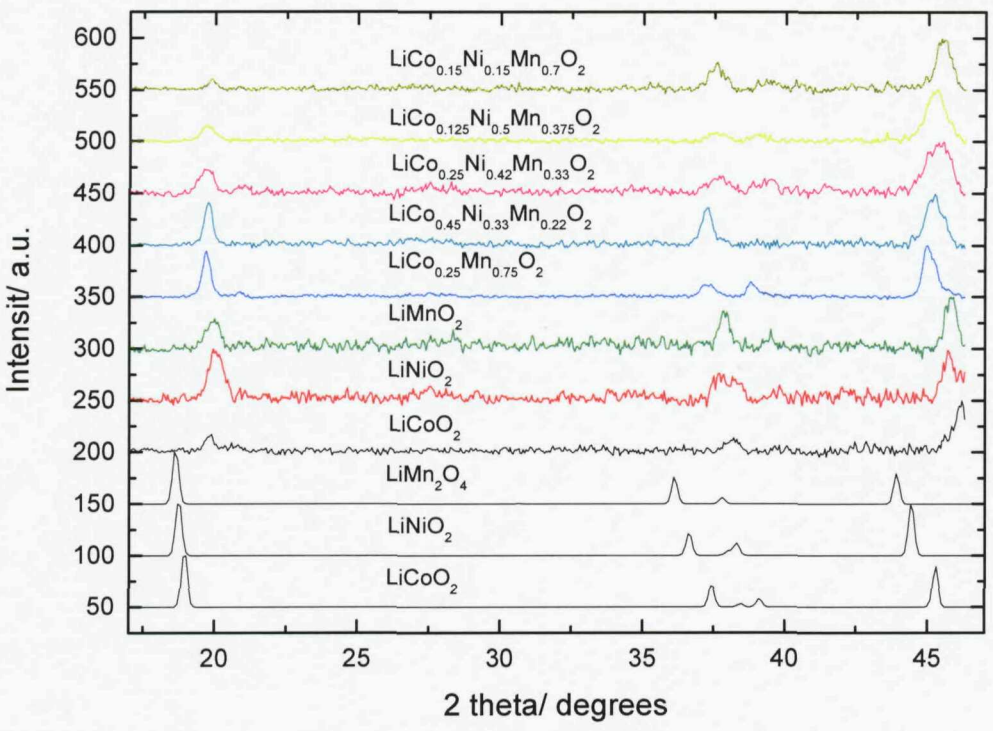

Figure 6-16 Selected XRD patterns from the array. The composition is indicated on the graph. Database patterns for $LiCoO_2$(16), $LiNiO_2$(17) and $LiMn_2O_4$(18) are included as a guide.

High-throughput Electrochemical Results

On the following page a ternary CV diagram (Figure 6-17) shows the general trends in electrochemical performance with composition. The most dramatic feature is that in high Mn samples a lower voltage peak can be seen at around 2.8 V. This corresponds to the discharge behaviour of $Li_xMn_2O_4$ where x equals between 1 to 2. This is summarised below in Equation 6-2 and Equation 6-3.(19, 20)

$$Mn_2O_4 + Li^+ + e^- \leftrightarrow LiMn_2O_4 \quad \text{charge discharge} \sim 4\ V$$

Equation 6-2

$$LiMn_2O_4 + Li^+ + e^- \leftrightarrow Li_2Mn_2O_4 \quad \text{charge discharge} \sim 2.8\ V$$

Equation 6-3

Therefore, the samples showing the 2.8 V peak either have the spinel structure, or the Mn phase has segregated from the other components to form regions of spinel $LiMn_2O_4$ and regions of the layered $LiCo_{1-x}Ni_xO_2$. The highest currents can be seen in the central region of the ternary diagram.

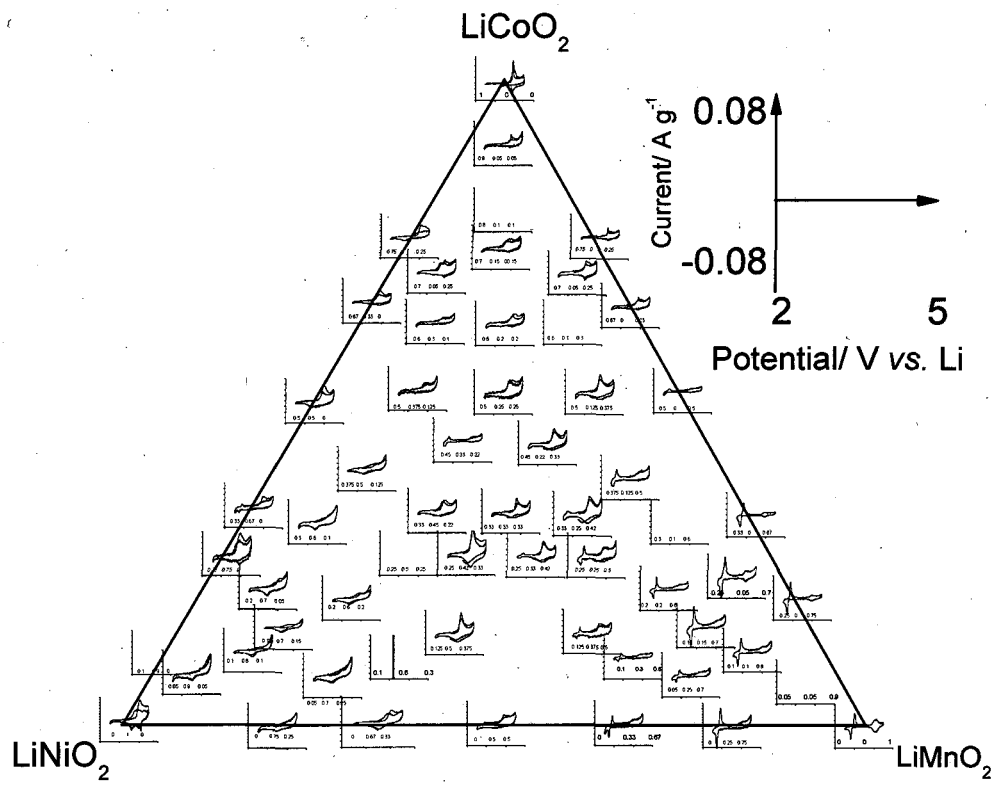

Figure 6-17 CVs from the array investigating $LiCo_{1-x-y}Ni_xMn_yO_2$ materials arranged in the approximately correct positions on the ternary diagram. Numbers are shown on each graph which corresponds to the composition e.g. for $LiCo_{0.4}Ni_{0.1}Mn_{0.5}O_2$ the numbers 0.4 0.1 0.5 would be displayed. Currents have been divided by weight to remove some of the scatter. CVs are shown from the first two cycles and were recorded at 0.05 mV s^{-1}.

In samples where $y < 0.5$ in $LiCo_{1-x-y}Ni_xMn_yO_2$ (i.e. where no spinel behaviour is seen) a similar performance is noted; the majority of the capacity being utilised at voltages higher than 3.5 V. To observe the changes in performance one figure of merit that can be calculated is the discharge capacity. The discharge capacities are shown in a colour mapped ternary diagram in Figure 6-18.

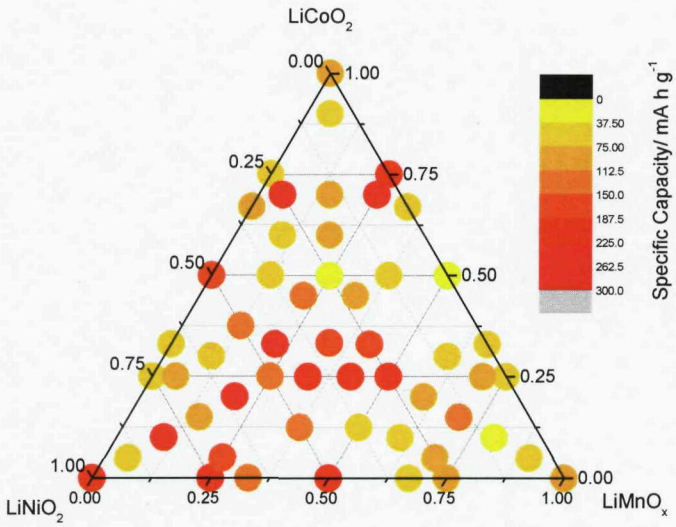

Figure 6-18 Colour map showing capacities of $LiCo_{1-x-y}Ni_xMn_yO_2$ prepared from mixed nitrate solutions calcined at 700 °C. These capacities are for the first discharge of each material at 0.05 mV s^{-1}.

Figure 6-18 shows can be summarised with the following three trends:

1. Materials containing high levels of Co (>0.5) or Mn (>0.5) have the lowest capacities.
2. Compositions with high Ni (>0.5) generally show moderate capacities; with samples containing low amounts of Co performing especially well.
3. Compositions within the range indicated in this formula $LiCo_{0.25-0.5}Ni_{0.25-0.5}Mn_{0.25-0.5}O_2$ generally showed the highest capacities.

After this initial overview a more detail analysis is presented in the following (Figure 6-19 to Figure 6-24) to examine the CVs in Figure 6-17 and capacity trends in Figure 6-18 in more detail. Each figure shows data where a single element composition has been kept constant whilst the other two parameters varied (i.e. $LiCo_x$-$Ni_{0.33}Mn_yO_2$, where the x and y vary). CVs and plots of capacity variation with composition (shown separately for spinel and high voltage capacity for both charge and discharge) are shown in each figure. This method effectively investigates cross sections within the above ternary diagrams.

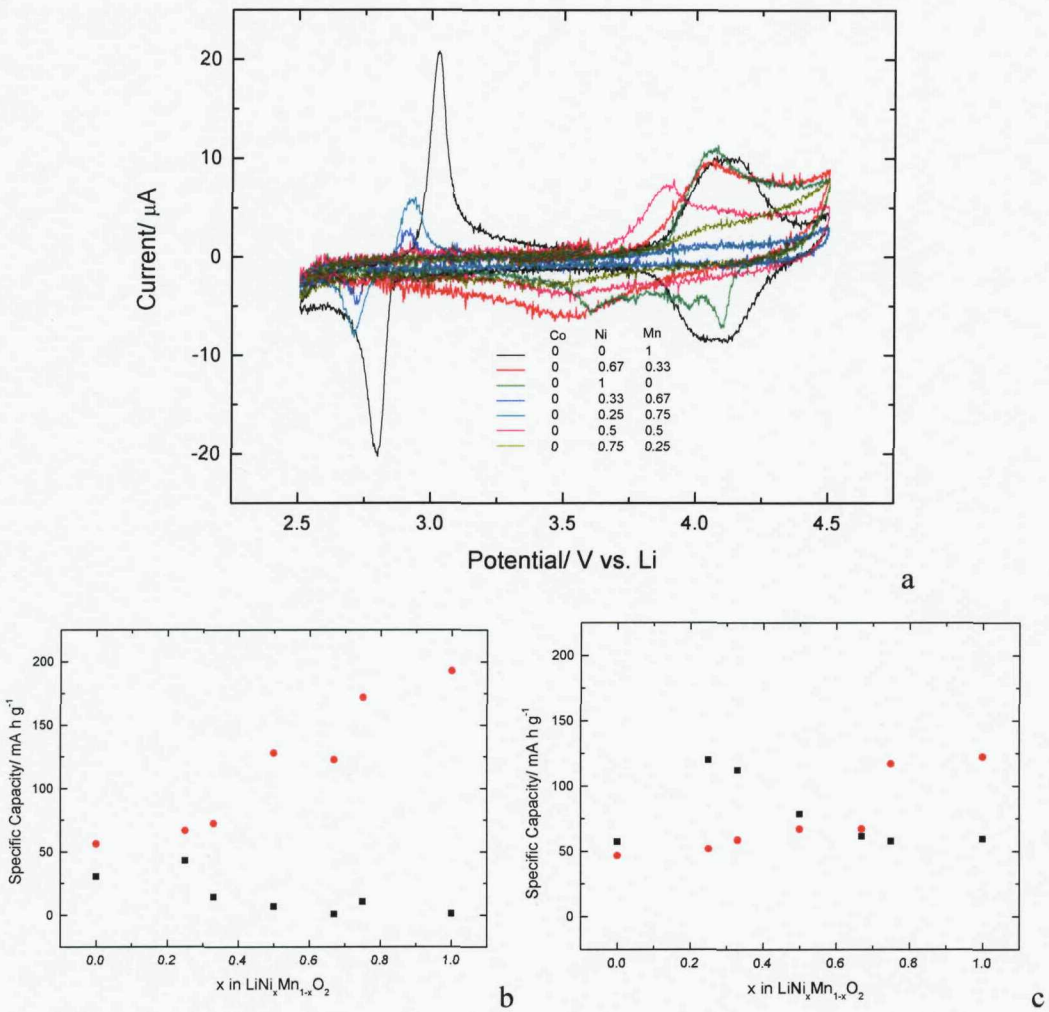

Figure 6-19 (a) First cycle CVs (scan rate = 0.05 mV s^{-1}) from electrodes on the array containing no cobalt. The exact compositions used for each sample is indicated on the graph as the amount of each metal relative to the total metal of M in $LiMO_2$.(b) summary of charge capacities below(■) and above(●) 3.3 V for each material shown in (a), (c) is the same plot as (b) except for discharge capacities.

In Figure 6-19 (a) the CVs show that generally as x decreases in $LiNi_xMn_{1-x}O_2$ the peak current at approximately 4.1 V also decreases. The lower voltage peak (~2.7 V) appears in samples where x is smaller than 0.5; the size of this peak current then increases inversely with x. The same trend can also be seen in the capacity plot(b). The material $LiMn_{1.5}Ni_{0.5}O_4$ has been previously studied in the literature. These reports suggest that a similar reaction as shown in Equation 6-4 occurs in this material(21). It is suggested that the Ni stays in the +2 oxidation state throughout this reaction and that the charge is completely from a Mn^{3+} to Mn^{4+} reaction. The Li

extraction to give $Mn_{1.5}Ni_{0.5}O_4$ (resulting in a change in Ni oxidation number) does not occur within this potential range, being reported around 4.7 V(22). In the samples where $0.5 > x > 0$ in $LiNi_xMn_{1-x}O_2$ a behaviour consistent with the literature reports can be noted. However, the capacity plots show that in the high voltage region some capacity is still seen. Electrolyte decomposition at higher voltages might explain the capacity seen without the presence of an obvious peak. The peak potentials within the low voltage region also shift to lower voltages as the compositions are varied indicating a change in the energy of reaction. However the shift is different to the direction reported in the literature, the reason for this is not clear.

$$LiMn_{1.5}Ni_{0.5}O_4 + Li^+ + e^- \leftrightarrow Li_2Mn_{1.5}Ni_{0.5}O_4 \text{ charge discharge} \sim 3 \text{ V}$$

Equation 6-4

In the high Ni containing samples high capacities can be seen on the charging peak, however, on discharge this capacity is split between both the high and low voltage region. In samples where x is greater than 0.5 this is not resulting from a spinel type behaviour and indicates a severe hysteresis between the charging and discharging. This suggests that there is some increased resistance on discharge and that these materials are therefore not good candidates for further study.

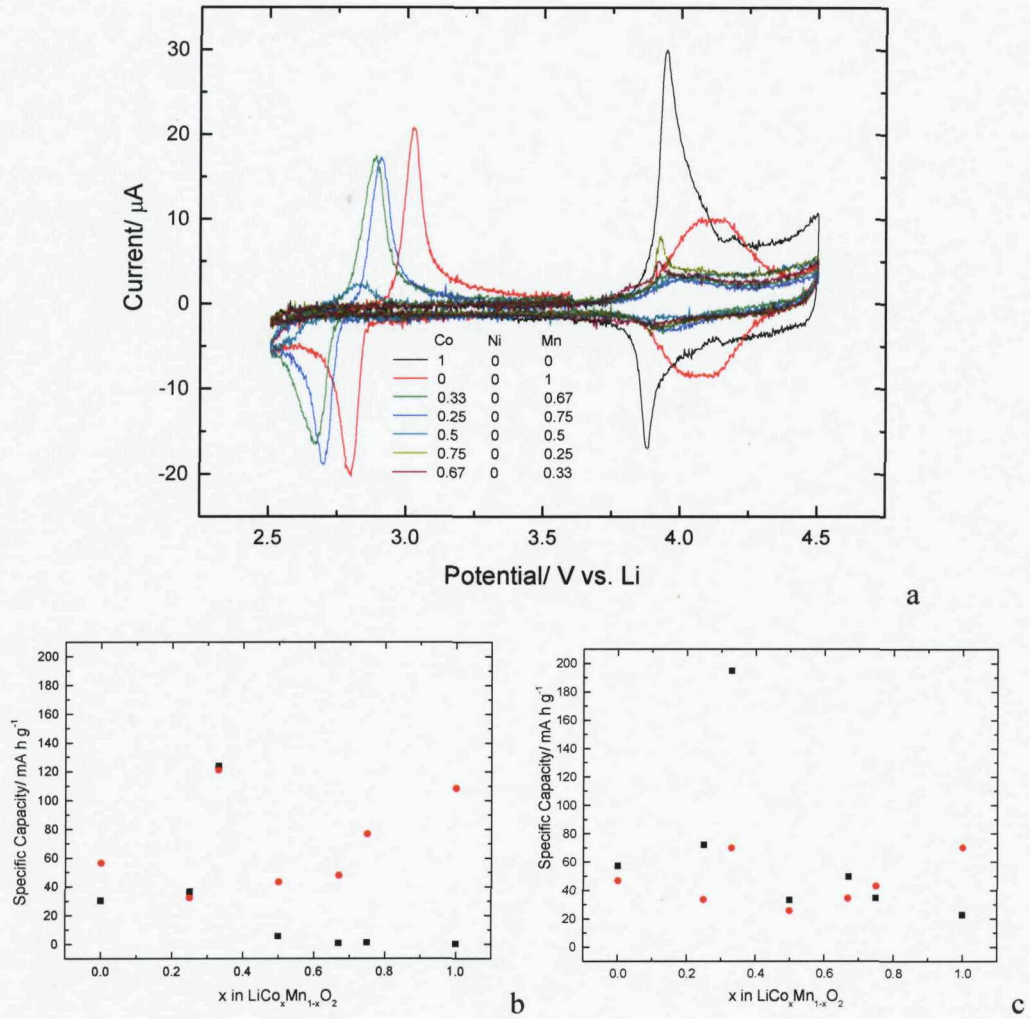

Figure 6-20 (a) First cycle CVs (scan rate = 0.05 mV s^{-1}) from electrodes on the array containing no nickel. The exact compositions used for each sample is indicated on the graph as the amount of each metal relative to the total metal of M in $LiMO_2$.(b) summary of charge capacities below(■) and above(●) 3.3 V for each material shown in (a), (c) is the same plot as (b) except for discharge capacities.

In Figure 6-20 (a) for materials where x is greater than 0.5 in $LiCo_xMn_{1-x}O_2$ charge and discharge peaks can be seen at ~4V, the peak height decreases with increasing Mn and peaks become broader. The pure $LiCoO_2$ material shows a sharp peak at around 3.9 V which tapers off at higher voltages, however, a plateau current is still seen up to 4.5 V until the potential scan is reversed. As seen for the $LiNi_{1-x}Mn_xO_2$ samples the discharge capacities is spread over the whole voltage range rather than in the charging state when all the capacity is seen above 3.3 V. This again indicates that there is a large amount of hysterisis in the cycling behaviour; the fact that so much of

the capacity is seen at lower voltages suggests these materials are not ideal as candidates for cathode materials.

In the samples where x is less than 0.5 in $LiCo_xMn_{1-x}O_2$ peak currents are seen in the higher voltage region; peaks below 3 V usually associated with spinel type materials are also seen, increasing in magnitude with the amount of Mn (indicative of a similar performance seen for the $LiNi_{1-x}Mn_xO_4$ material). The low voltage peak potential also changes in correspondence with increasing Mn, from 2.8 to 3 V for the charge peaks. This is suggesting a change in free energy of reaction and thus the formation of a solid solution in $LiCo_xMn_{2-x}O_4$. However, this material was seen to have significant phase separation in the XRD data; suggesting that the high and low voltage behaviours result from the formation of mixed amounts of $LiCoO_2$ and $LiMn_2O_4$, further investigation of these materials is required to determine the mechanism of this reaction. The capacity plot shows low capacities for all the materials indicating poor performance and suggesting that this composition range (produced under the preparation conditions used here) is also not an obvious candidate as a future cathode material.

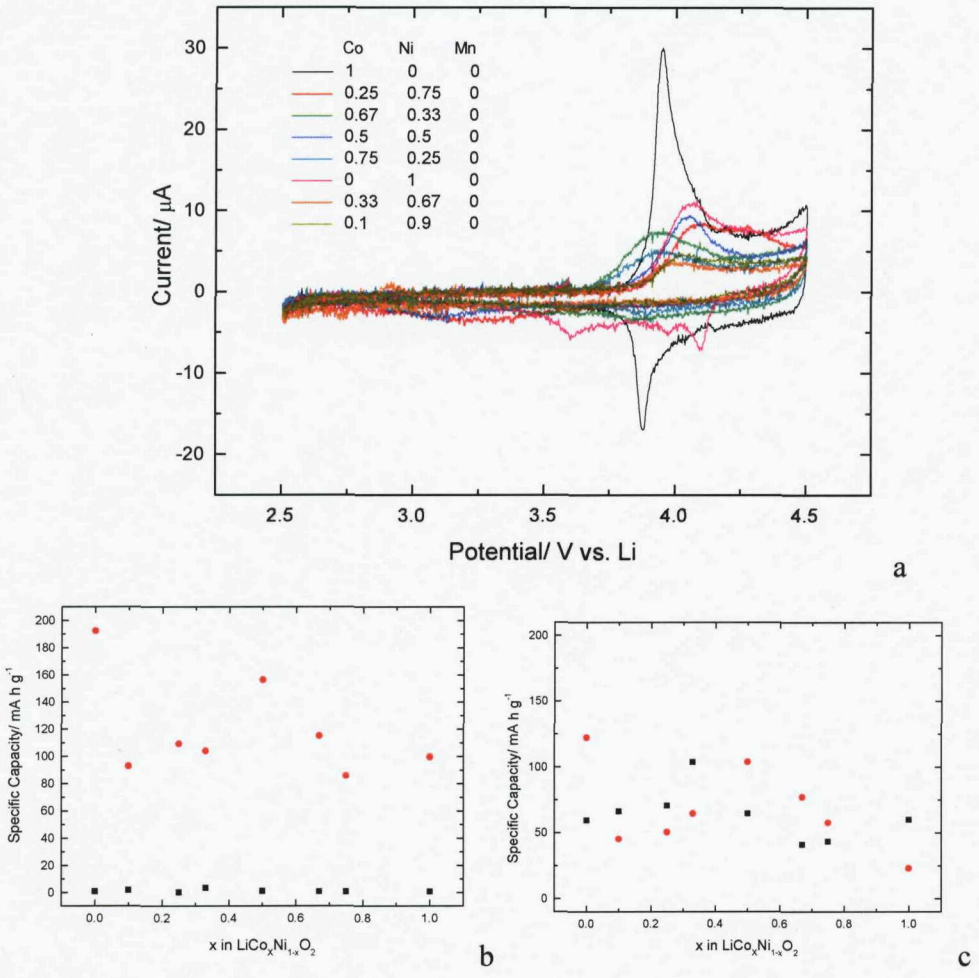

Figure 6-21 (a) First cycle CVs (scan rate = 0.05 mV s^{-1}) from electrodes on the array containing no manganese. The exact compositions used for each sample is indicated on the graph as the amount of each metal relative to the total metal of M in $LiMO_2$.(b) summary of charge capacities below(■) and above(●) 3.3 V for each material shown in a (a), (c) is the same plot as (b) except for discharge capacities.

The CVs seen above in Figure 6-21 (a) for $LiCo_{1-x}Ni_xO_2$ materials show the typical high voltage peak (~4V) seen for layered Co and Ni oxides. When Co is substituted for Ni the charge and discharge peaks become broader, in particular it is difficult to resolve any features in the discharge peak, just a plateau current continuing to 2.5 V; this is emphasised in the capacity plots Figure 6-21b and c, where the capacity on charge can be seen all above 3.3 V and discharge split approximately equally above and below 3.3 V. The peak potentials increase with x in $LiCo_{1-x}Ni_xO_2$ this is again

indicative of a change in the free energy of reaction with the changing composition. The pure $LiNiO_2$ material shows the largest shift in the charging peak potential. However, some strange features are seen in the discharge sweep which can not be easily explained. The capacity plot Figure 6-21 (b) and (c) show an approximately uniform capacity for all the materials. Although several of these materials show a slightly increased capacity over $LiCoO_2$, the charge discharge hysteresis again suggests that these compositions do not stand out as particularly good candidates for further study.

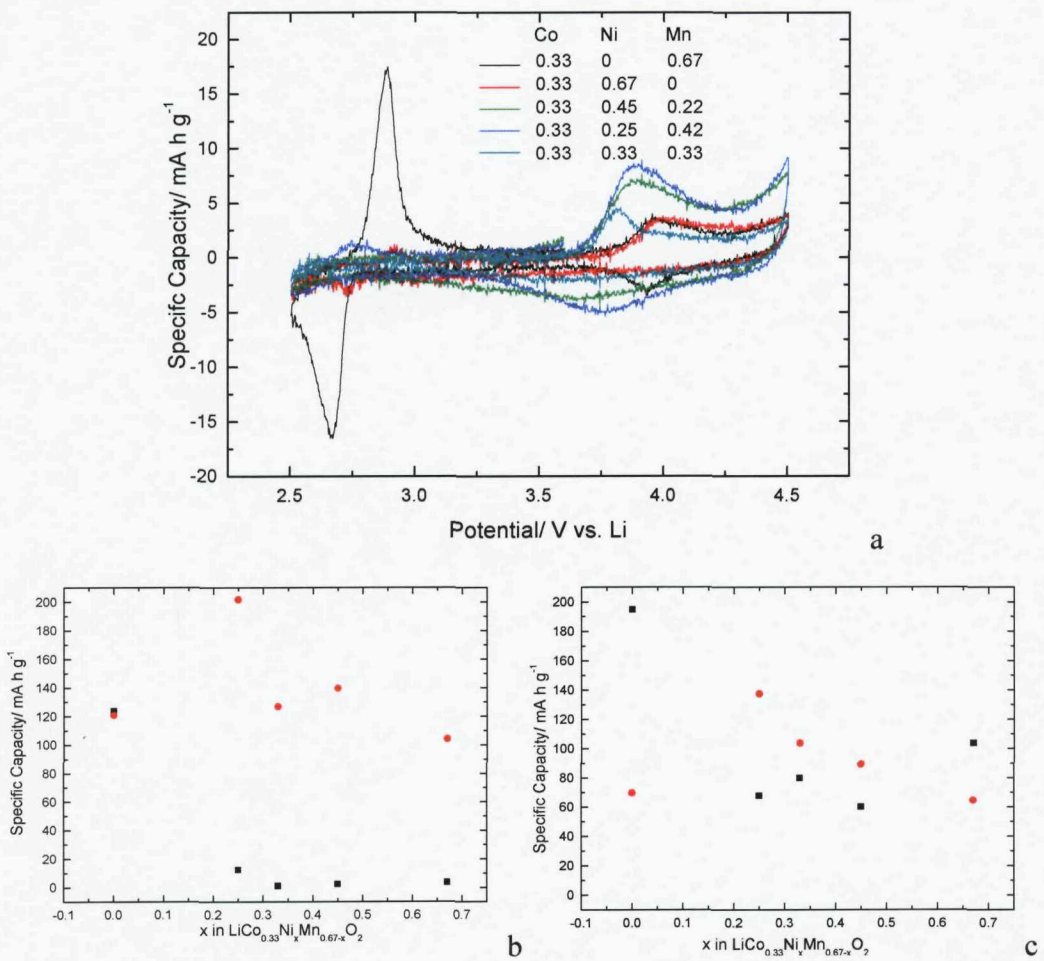

Figure 6-22 (a) First cycle CVs (scan rate = 0.05 mV s^{-1}) from electrodes on the array containing one third Co. The exact compositions used for each sample is indicated on the graph as the amount of each metal relative to the total metal of M in $LiMO_2$.(b) summary of charge capacities below(■) and above(●) 3.3 V for each material shown in (a), (c) is the same plot as (b) except for discharge capacities.

The CVs shown in Figure 6-22 are for $LiCo_{0.33}Ni_xMn_{0.67-x}O_2$ materials. When only small amounts of Ni replace Mn the low voltage peak (a result of spinel like behaviour) is reduced dramatically in comparison with the high voltage peak. A small peak around 2.6 V can still be seen in all the samples except $LiCo_{0.33}Ni_{0.33}Mn_{0.33}O_2$ and $LiCo_{0.33}Ni_{0.45}Mn_{0.22}O_2$. The capacity plot shows that when x equals between 0.25 and 0.45 high capacities are observed for the high voltage charge. Although this charge is not exclusively discharged above 3.3 V the performance of these samples is much better than others studied in terms of this feature. In the samples where no spinel like behaviour is seen the peak potential of the high voltage peak can also be seen to shift to higher voltages with increasing amounts of Ni suggesting the formation of a solid solution. This analysis suggests that the samples of $LiCo_{0.33}Ni_xMn_{0.67-x}O_2$ where x is greater than 0.33 shows a significantly improved performance and would provide interesting further bulk studies.

It should be noted that the $LiCo_{0.33}Mn_{0.66}O_2$ (presumably forming LiM_2O_4 like structure) also performs extremely well with exceptional capacity balance between the high and low voltage peaks on charge; this suggests that 1 Li is being inserted per transition metal (one at high voltage and one at low voltage) as is expected for a LiM_2O_4 material.

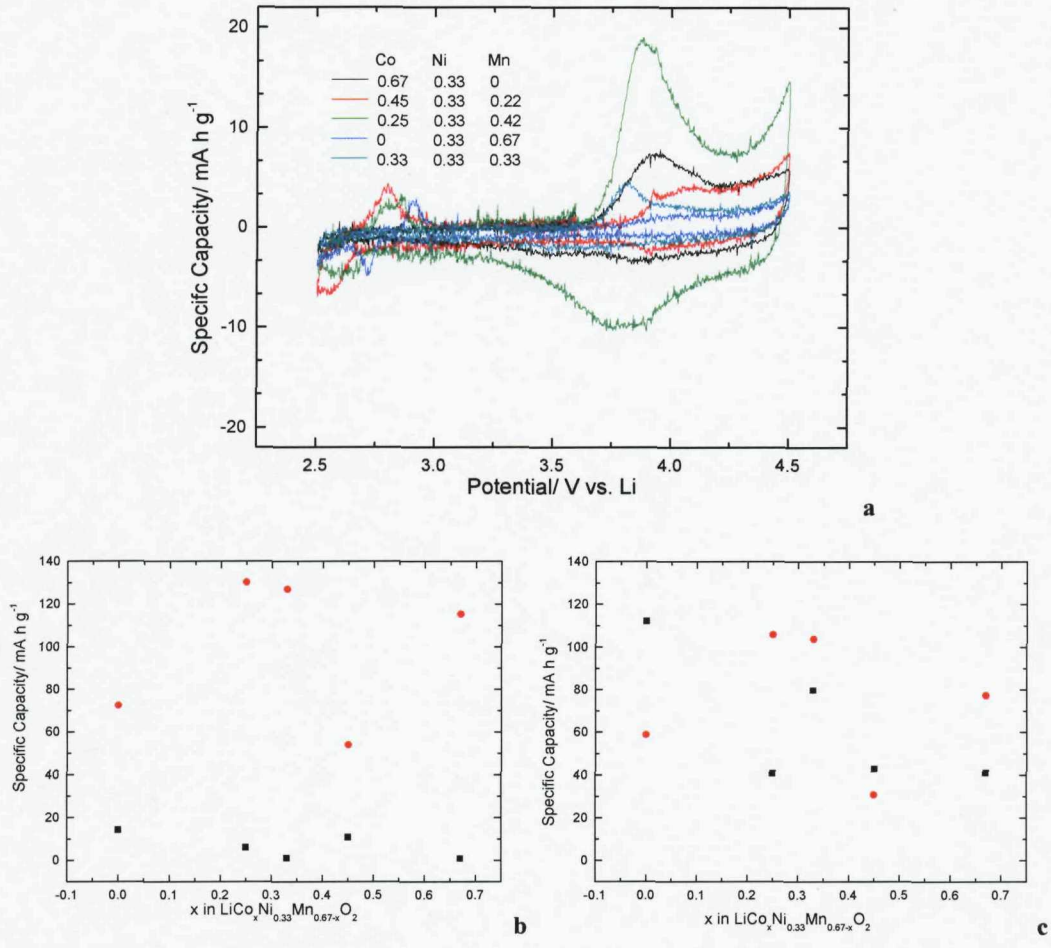

Figure 6-23 (a) First cycle CVs (scan rate = 0.05 mV s^{-1}) from electrodes on the array containing *one third Ni. The exact compositions used for each sample is indicated on the graph as the* amount of each metal relative to the total metal of M in $LiMO_2$.(b) summary of charge capacities below(■) and above(●) 3.3 V for each material shown in (a), (c) is the same plot as (b) except for discharge capacities.

The CVs shown in Figure 6-23(a) are for $LiCo_{0.67-x}Ni_{0.33}Mn_xO_2$ materials. The high voltage and the low voltage peaks can be seen in all except the $LiCo_{0.33}Ni_{0.33}Mn_{0.33}O_2$. However the low voltage peak is extremely small in several of the preparations, possibly indicating that it is a result of a small amount of phase separated $LiMn_2O_4$. As seen in the plot in Figure 6-22 the samples with compositions closest to the central area of the ternary diagram have the highest capacities.

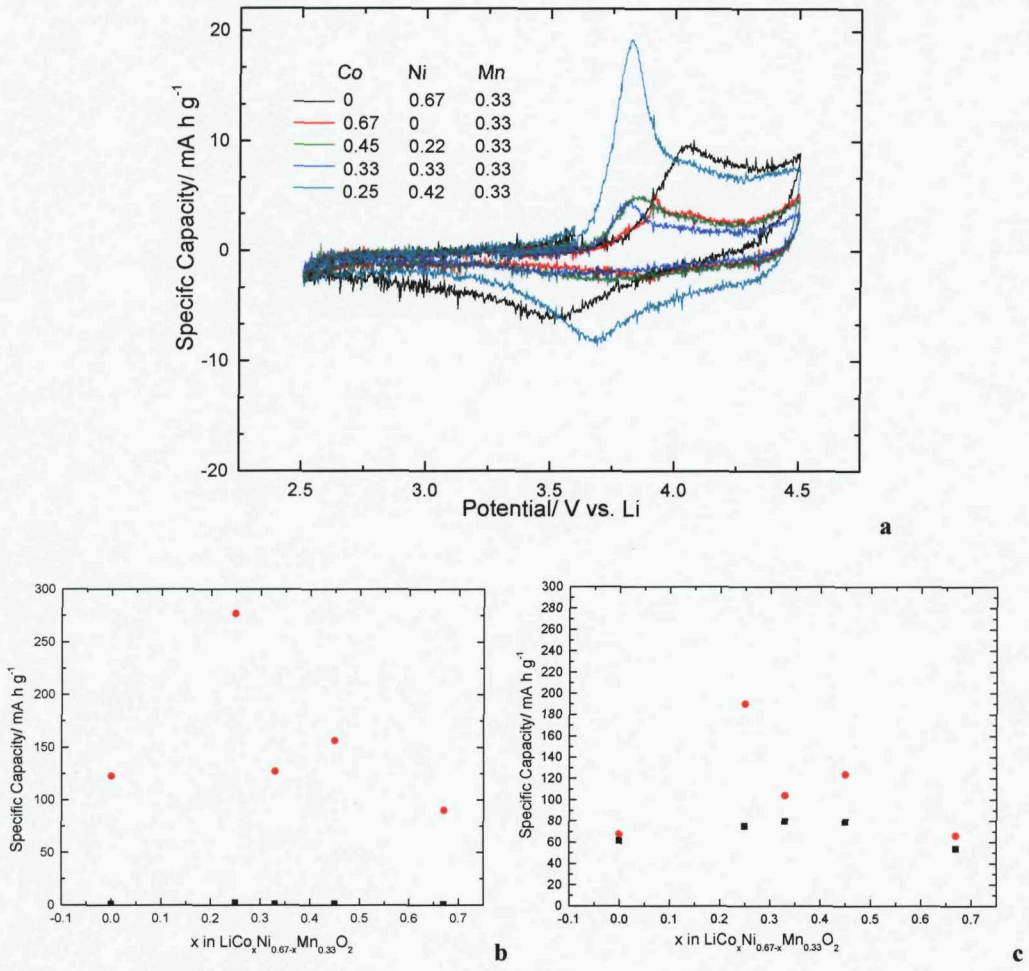

Figure 6-24 (a) First cycle CVs (scan rate = 0.05 mV s^{-1}) from electrodes on the array containing one third Mn. The exact compositions used for each sample is indicated on the graph as the amount of each metal relative to the total metal of M in $LiMO_2$.(b) summary of charge capacities *below*(■) *and above*(●) *3.3 V for each material shown in a* (a), (c) *is the same plot as* (b) *except for* discharge capacities.

The CVs shown in Figure 6-24a are for $LiCo_xNi_{0.67-x}Mn_{0.33}O_2$ materials. None of the materials show any low voltage peaks indicative of spinel like materials suggesting a solid solution of layered metal oxides exists in this whole composition range. There are significant changes in the peak potentials, however, this corresponds to no obvious trend. The highest peak currents and capacities (Figure 6-24b and c) appear for the $LiCo_{0.45}Ni_{0.22}Mn_{0.33}O_2$ material, the shape of the CV also shows the most well defined features of any of the materials examined in this section. This material shows the most promise for further study using bulk methods.

6.2.3 Conclusions

To try and summarise and make clear conclusions on these results a ternary diagram has been drawn and is shown below Figure 6-25 where several sections have been highlighted for further comment.

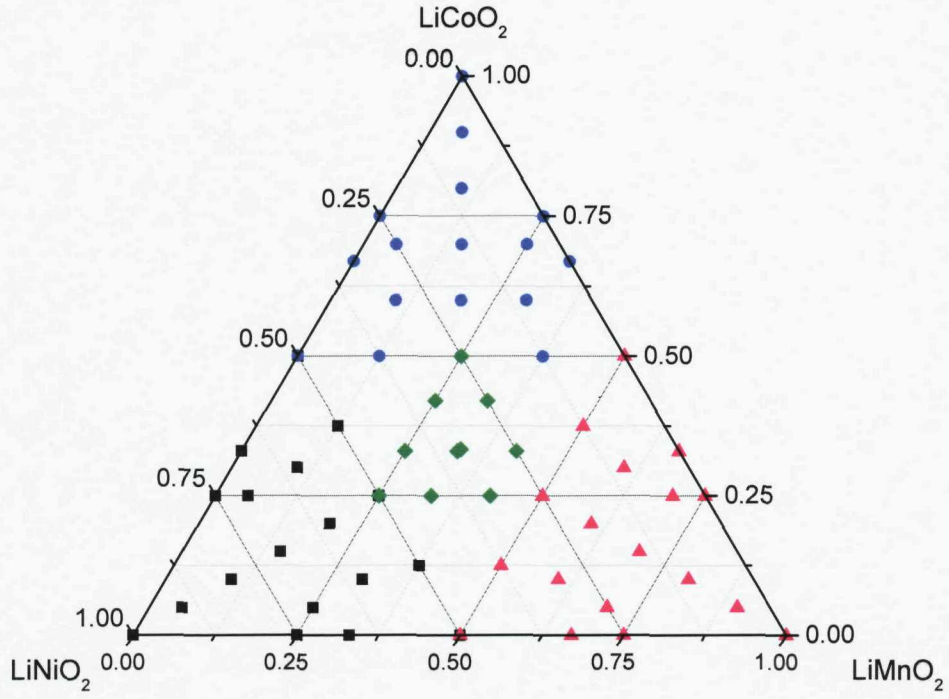

Figure 6-25 Ternary diagram indicating regions of interest of $LiCo_{1-x-y}Ni_xMn_yO_2$ materials. Region 1 (●)contains materials with greater than 50 % Co (% is relative to the M in $LiMO_2$). Region 2 (■)contains materials with greater than 50 % Ni. Region 3 (▲)contains materials with greater than 50 % Mn. Region 3(◆) is the central region where the three metals are all present in amounts greater than 25 %.

The ternary diagram shown in Figure 6-25 is divided into 4 sections which represent regions where the material performance significantly changes. An explanation of these regions is listed below.

- Region 1 (●): the samples contain high amounts of Co, the capacities were usually lowest in this composition range. Typically a single charge peak was seen at around 3.9 V with a discharge occurring with no clear peak over the whole voltage range.

- Region 2 (■): samples contain the highest amounts of Ni and generally recorded the high capacities.
- Region 3(▲): the formation of a spinel phase was suggested as a lower voltage discharge peak was seen. It is difficult to conclude if this is a direct result of phase separation or the formation of a solid solution in the $LiCo_{2-x-y}Ni_xMn_yO_4$ material. However, changes in the spinel peak charge and discharge potentials as a function of composition suggest that there is a change in the free energy of reaction. Future work should be undertaken on many of these to investigate the possibility of the high voltage discharge plateau reported in the literature(22) for $LiMn_{1.5}Ni_{0.5}O_4$.
- Region 4 (◆): the metals were mixed most evenly, all were present in the amounts greater than 25 %. These compositions generally saw the highest currents and capacities on the array. Normally, the charge discharges occurs at around 3.9 V and the shapes of the CVs appear to be that of a 1 phase material. Further work on this region is required to make any more detailed conclusions; however, this can be termed the "hot spot" area of this array. An array which encompasses just these compositions with several repeats of each preparation for greater accuracy is required to make more detailed comment.

This work has shown how the high-throughput method can be applied to a ternary system. The system is very complicated and the PoSAT method has quickly and simply given an overview. This work has also highlighted the limitations of the PoSAT method. When applied to the framework structure of the phosphates the electrochemistry is not so sensitive to the preparation techniques and trends are easier to see. In the case of the oxides as seen here the performance is very sensitive with regards to the preparation conditions, making fixed conclusions about structural changes difficult.

6.3 Conclusions Chapter 6

This chapter differs significantly from the materials studies in chapters 3 and 4. In those chapters work was presented for $LiMPO_4$ and built on much of the early work

developing a suitable synthesis for $LiFePO_4$ conducted by Owen and co-workers(23). This chapter presented a new challenge as first an appropriate synthetic route needed to be identified which would be compatible with the PoSAT method. Then a materials study on a complicated ternary system was undertaken. One noteworthy comment is that the PoSAT method has actually made this study possible as oxides could not be synthesised on the carbon stub electrodes of DISC (which would have been oxidised by the reaction gas at high temperatures).

The initial work in this chapter investigated the effect of precursors on the performance of the active materials. A dramatic effect was seen in performance between different calcination temperatures (the best performing materials prepared at 700 °C), however, several of the different precursor salts showed similar performance. The metal nitrate only preparation at 700 °C was selected for further study as it was felt that this was most compatible for compositional studies with the high-throughput methodology. This preparation formed a material with no detectable impurity phases and broad XRD peaks resulting from a small particle size (50-100 nm). The material had a competitive initial capacity (146 mA h g^{-1}) and was electrochemically stable (capacity retention per cycle of 99.45 %) when cycled within a limited potential window (2 and 4.2 V). When the upper potential limit was increased (to 4.5 V) the stability of the material reduced (capacity retention per cycle of 98.9 %), however, the initial capacity increased (186 mA h g^{-1}). The performance of this material is not as good as some reports in the literature, however, for the purposes of the high-throughput screening method it is deemed acceptable.

The second section of work investigated the effect of changing compositions in $LiCo_{1-x-y}Ni_xMn_yO_2$. Some important trends in performance were seen. The high manganese materials showed a significant change as the performance suggesting a change in the materials structure from layered to a spinel. The high Co containing materials performed significantly worse than all the others. The best performing materials were those containing at least 25 % of each metal and those with high amounts of Co. It is suggested from this work that further more detailed studies of these high performance areas should be undertaken. This work has also highlighted the limitations of the PoSAT method. Although some changes in performance have

been seen it is difficult to judge the reliability of these results given that the preparation conditions of $LiNi_{1/3}Co_{1/3}Mn_{1/3}O_2$ have been shown to be so important in the early part of this chapter. It is conceivable that to assess each composition fairly the preparation conditions of each must first be optimised.

6.4 References Chapter 6

1. T. Ohzuku, M. Ariyoshi, Y. Makimura, N. Yabuuchi and K. Sawai, *Electrochemistry*, **73**, 2 (2005).
2. K. M. Shaju and P. G. Bruce, *Advanced Materials*, **18**, 2330 (2006).
3. J. M. Kim, N. Kumagai, Y. Kadoma and H. Yashiro, *Journal of Power Sources*, **174**, 473 (2007).
4. J. J. Liu, W. H. Qiu, L. Y. Yu, G. H. Zhang, H. L. Zhao and T. Li, *Journal of Power Sources*, **174**, 701 (2007).
5. S. J. Henderson, J. A. Armstrong, A. L. Hector and M. T. Weller, *Journal of Materials Chemistry*, **15**, 1528 (2005).
6. S. C. Yin, Y. H. Rho, I. Swainson and L. F. Nazar, *Chemistry of Materials*, **18**, 1901 (2006).
7. A. R. West, *Solid State Chemistry and its Application*, John Wiley & Sons Ltd. (1984).
8. Weller. M.T, *Inorganic Materials Chemistry*, Oxford University Press (1994).
9. T. Ohzuku and Y. Makimura, *Chemistry Letters*, 744 (2001).
10. M. S. Whittingham, *Chemical Reviews*, **104**, 4271 (2004).
11. J. Guo, L. F. Jiao, H. T. Yuan, H. X. Li, M. Zhang and Y. M. Wang, *Electrochimica Acta*, **51**, 3731 (2006).
12. S. Patoux and M. M. Doeff, *Electrochemistry Communications*, **6**, 767 (2004).
13. K. M. Shaju, G. V. S. Rao and B. V. R. Chowdari, *Electrochimica Acta*, **48**, 145 (2002).
14. X. F. Luo, X. Y. Wang, L. Liao, X. M. Wang, S. Gamboa and P. J. Sebastian, *Journal of Power Sources*, **161**, 601 (2006).
15. L. Q. Zhang, X. Q. Wang, T. Muta, D. C. Li, H. Noguchi, M. Yoshio, R. Z. Ma, K. Takada and T. Sasaki, *Journal of Power Sources*, **162**, 629 (2006).
16. M. Nasir Khan and J. Bashir, *Materials Research Bulletin*, **41**, 1589 (2006).
17. A. Hirano, R. Kanno, Y. Kawamoto, Y. Takeda, K. Yamaura, M. Takano, K. Ohyama, M. Ohashi and Y. Yamaguchi, *Solid State Ionics*, **78**, 123 (1995).
18. C. Wende, K. Olimov, H. Modrow, F. E. Wagner and H. Langbein, *Materials Research Bulletin*, **41**, 1530 (2006).
19. M. M. Thackeray, *Progress in Solid State Chemistry*, **25**, 1 (1997).
20. M. M. Thackeray, A. Dekock, M. H. Rossouw, D. Liles, R. Bittihn and D. Hoge, *Journal of the Electrochemical Society*, **139**, 363 (1992).
21. K. Amine, H. Tukamoto, H. Yasuda and Y. Fujita, *Journal of The Electrochemical Society*, **143**, 1607 (1996).
22. Y. S. Lee, Y. K. Sun, S. Ota, T. Miyashita and M. Yoshi, *Electrochemistry Communications*, **4**, 989 (2002).
23. A. D. Spong, G. Vitins and J. R. Owen, *Journal of the Electrochemical Society*, **152**, A2376 (2005).

Chapter 7 Conclusions and Further Work

7.1 General Conclusions on Combinatorial Methods

The major aim of this thesis was to develop a new method for the high-throughput discovery of new electrode materials. In Chapter 3 results were presented which identified the major drawbacks in the previously developed DISC method (1-3). Poor knowledge of electrode weight, poor adhesion of the active material to the substrate and a lack of conductive additive or binder were identified as the major cause of the high levels of scatter found in the results. The PoSAT method was then presented; in this new approach active materials were first calcined within an array of individual micro-tubes (reacting in quartz tubes instead of on carbon stubs alleviated the need for inert gas atmospheres during synthesis); this was followed by mixing each material with solvent and additives to form inks which were deposited onto an array of current collectors. The separation of these steps allowed the formation of electrodes with conductive additive and binder as done in commercial processes. This improved the adhesion of the electrodes to the current collectors. A series of weighing steps was also incorporated resulting in accurate knowledge of the amount of active material. This new method led to a reduction in scatter, the standard deviation on results was reduced to less than 10 %. The original PoSAT method was later modified so the powders could be crushed in parallel using a ball milling approach, and a method to prepare thermally graded arrays was also developed.

In most cases these new methodologies provided reliable results which allowed for the simple rapid characterisation of material systems. In chapters 4 to 6 several materials studies were undertaken which highlight how the combinatorial method was practically used. In Chapter 6 whilst trends and tentative conclusions could be seen a limitation of the technique was observed. In cases of framework materials such as $LiFePO_4$ the performance of the material is reasonably robust in terms of the preparation conditions. However, in the case of the materials prepared in Chapter 6 the layered metal oxides were seen to be extremely sensitive to variations in synthesis

conditions. This lead to difficulties when trying to resolve real trends over scatter caused by slight variations in temperature or localised changes in the atmosphere resulting from neighbouring quartz tubes gas decomposition.

7.2 Specific Conclusions from the Materials Study

An optimal amount of sucrose (of between 0.22 and 0.28 moles sucrose per iron is used) was found to form a carbon network to percolate $LiFePO_4$ resulting in the best electrochemical performance. A reduction in capacity at slow scan rates (<0.8 mV s^{-1}) was seen when an SPR greater than 0.28 was used. However, at faster scan rates (>0.8 mV s^{-1}) all the samples prepared with an SPR greater than 0.22 showed approximately the same capacity. Analysis of the CVs showed some resistance distortion in samples which were prepared with an SPR less than 0.3. The SEM images show that increased particle sizes are seen for high SPR preparations. A model is suggested where the large particle size of the high carbon preparations restricts ionic diffusion and thus the capacity even at slow scan rates. However, at faster scan rates the low carbon preparations become limited by the electronic conductivity.

Ball milling for 1 h of the solution based preparation of $LiFePO_4$ was found to be an effective method to optimise the performance of the material. SEM micrographs indicate that this milling time resulted in the smallest particle size, it is therefore concluded that this results in reduced time constants for reaction of each particle and improved rate performance in these materials.

Substitution of Mn for Fe in $LiFePO_4$ resulted in a linear decrease in capacity. This result was presumed to be caused by a reduction in electronic conductivity. Interestingly the results showed a change in the reaction mechanism during charge and discharge of the Fe^{2+}/Fe^{3+} redox couple. With increased Mn substitution the reaction changes from 2 phase from of $0<x<1$ in $Li_xFe_{1-y}Mn_yPO_4$ to 1 phase and then back to 2 phase. This was observed by the changing shapes of the CVs and compared well with structural studies performed within the literature(4). This study represented the first application of the PoSAT method to investigation of changes in the atomic

composition of an active material; this covered a large number of compositions and made the observation of this trend relatively simple.

The effect of Mg doping on the Fe and Li site in $LiFePO_4$ was also reported. This was monitored with respect to the amount of carbon coating such that any enhancement from doping on the materials performance could be separated from the sometimes misleading side effects of variable carbon coatings. These results showed no improvement from the Mg on the Li site and no further studies were performed on this material. However, the Mg on the Fe site showed significant performance improvements at high scan rates. This was attributed in part to an increase in electronic conductivity. A second factor which may have influenced this improvement is a change in particle morphology. The results were repeated with bulk sample testing and the same trends were observed. These observations were all made on samples which contained high amounts of carbon such that any variations in the amount should have no effect on performance.

Leading on from the findings of improved conductivity in $LiFePO_4$ with Mg substitution for the Fe the same approach was taken for $LiMnPO_4$ (which typically showed capacities lower than 20 mA h g^{-1}) and $LiFe_{0.5}Mn_{0.5}PO_4$ (100 mA h g^{-1}). No improvement was seen for $LiFe_{0.5}Mn_{0.5}PO_4$. However, the $LiMn_{0.8}Mg_{0.2}PO_4$ sample showed significant performance improvements with ~65 mA h g^{-1} being extracted at rates of C/7. This is attributed to enhanced electronic conductivity, however, further experiments would be required to confirm this.

Investigations of the $LiNi_{0.33}Co_{0.33}Mn_{0.33}O_2$ material have shown that low temperature (700 °C) preparations form materials with the best cyclability. The material prepared from the mixed metal nitrate precursors only was of most interest. The simplicity of this preparation meant that arrays of materials could be easily prepared using the PoSAT method. This material had an initial capacity of 146 mA h g^{-1} and a capacity retention per cycle of 99.45 % when cycled within the 2 to 4.2 V range. When the upper potential limit was increased to 4.5 V the capacity retention per cycle was reduced to 98.9 %, however, the initial capacity increased to 186 mA h g^{-1}. This improved performance over the high temperature preparations is attributed to a

reduction in particle size which may reduce the stresses and strains on a particle during charge and discharge.

Using the metal nitrate preparation at 700 °C the ternary system of $LiNi_{1-x-y}Co_xMn_yO_2$ was investigated. This showed how the PoSAT method could easily be applied to large systems such as this to give a general overview. In samples containing high Mn contents spinel peaks could be seen resulting from materials with a similar performance to $LiMn_2O_4$. The high Co samples had the lowest capacities and generally worst performance. When samples contained roughly equal amounts of each metal (the central part of the ternary system) and also the materials containing high amounts of Ni the highest capacities were found. This led to the conclusion that further work needs to be undertaken investigating these hotspot areas in greater detail.

7.3 Further Work

The study shows an extensive opportunity for future development of the high-throughput method: Specifically to this thesis there is still room for further optimisation of the PoSAT method e.g. adjustment to the cell design such that more repeat measurements, or further increases in electrode size. The application of automated weighing would dramatically improve the method, as several repeats of each weight could be made easily and then averaged. A future aim for this technique is to approach accuracies of the 1 % level normally seen in conventional methods.

New high-throughput methods using similar ideas could also be developed. Work on high-throughput polymer electrolytes has already been started by Owen and co-workers. However, an area which is not well explored is liquid electrolytes, initials techniques and studies have been undertaken by the author, however, are not reported here. This would allow for the study of new Li salts and electrolyte additives. This could be particularly important in assessing how different additives interact.

Several of the material studies require further work using conventional methods to investigate some of the causes of the observed effects. In particular the work on $LiMn_{1-x}Mg_xPO_4$ requires further investigations such as high resolution SEM and

measurements of electronic conductivity. Another interesting experiment here would be to try and synthesise nano sized particles of $LiMn_{1-x}Mg_xPO_4$; in such a material the improvement in conductivity combined with very small particles could potentially lead to a very high performance material. The hot spot areas in the $LiNi_{1-x-y}Co_xMn_yO_2$ ternary diagram should also be investigated in greater detail.

7.4 References Chapter 7

1. A. D. Spong, High-Throughput Discovery of Lithium Battery Materials, in, University of Southampton, Southampton (2005).
2. A. D. Spong, G. Vitins, S. Guerin, B. E. Hayden, A. E. Russell and J. R. Owen, *Journal of Power Sources*, **119**, 778 (2003).
3. M. R. Roberts, A. D. Spong, G. Vitins and J. R. Owen, *Journal of The Electrochemical Society*, **154**, A921 (2007).
4. A. Yamada, Y. Kudo and K. Y. Liu, *Journal of the Electrochemical Society*, **148**, A1153 (2001).

Appendices

Appendix 1

Preparation of Electrodes, TGA and SEM arrays from precursor solutions via standard PoSAT methodologies

This list describes sequentially the processing steps that are used when processing an array of precursor solutions into an electrode, TGA and SEM array. The list below starts at the point where an array of precursor solutions has been prepared within an array of 64 quartz micro-tubes.

1. The array of mixed precursor solutions are then agitated using a *Fischer* "Whirlimix" Vortex mixer to ensure homogeneity before being placed in an oven at 70 °C for 12 h to remove the water.
2. The array of precursor solids is then calcined in controlled gas atmosphere at the required temperature using a large bore (80 mm diameter) tube furnace (Lenton).
3. After cooling, the products are crushed to a powder using a glass rod attached to a drill or in later prepared arrays via ball milling.
4. Then composite electrodes are prepared by adding two inks, 4% PVdF-HFP (*Aldrich*, polyvinylidene fluoride-co-hexafluoropropylene) and 4% AB (acetylene black, *Shawinigan, Chevron Phillips Chemical Company LP*) in cyclopentanone (CP) to the active material powders with five 1 mm zirconia beads placed in each tube. The inks are added to give final mass ratios of 10% PVdF-HFP, 25% AB and 65% active material and then mixed using the vortex mixer.
5. Then 14 μL aliquots of each ink was deposited onto the appropriate position on the array of aluminum current collectors and spread across the surface to form an even film of ink.
6. A second 40 μL sample of each ink was deposited into an array of alumina micro-crucibles for thermogravimetric analysis.
7. A third 3 μL sample of each ink was deposited onto an array of 3 mm aluminium stubs which were used for SEM analysis.

8. The CP was evaporated from all three arrays at room temperature before drying at 80 °C followed by evacuation.
9. The samples on both the electrode and TGA arrays are then accurately weighed using a computer connected balance.

Appendix 2

Data Processing

A large amount of data was generated from the high-throughput method. Typically 40 cycles were recorded for each array, leading to 2560 charge and discharge capacities which need to be calculated. No automated method for this was available and originally it was simply done manually. However, during the course of this PhD a rudimentary automated system for calculating capacity per cycle per channel was developed based on excel logic functions and macros. Using a macro a set of data was copied into a template worksheet. This worksheet used the IF logic function to find the charging currents of each cycle, the integral with respect to time of this was calculated in the same template, the macro then copied the capacities into another results spread sheet. To run a macro to analyse all 40 cycles it would typically take around 30 minutes. This method is not a perfect method and much could be done to improve this, however, a more skilled computer programmer would be required.

Below first an example of the spread sheet template is shown in Figure 1 followed by the associated macro code:

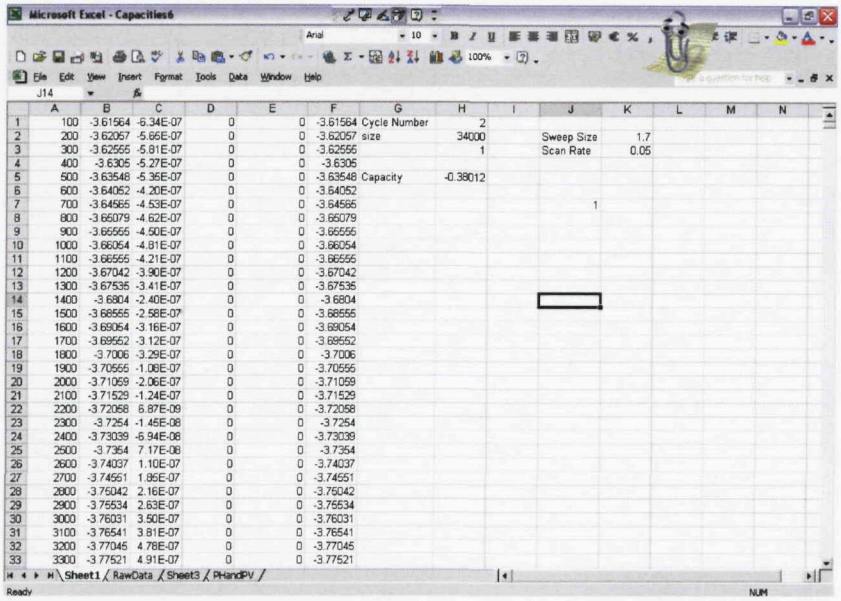

Figure 1 Template data processing spread sheet.

Macro Code

```
Sub Channel1()
'
' Macro1 Macro
' Macro recorded 26/01/2006 by Matthew
'
' C is number of channels
' n is number of cycles
For C = 1 To 63
Range("J7").Select
   ActiveCell.FormulaR1C1 = C
For n = 1 To 40
Sheets("RawData").Select
Columns(2 + C).Select
   Selection.Copy
   Sheets("Sheet1").Select
   Columns("C:C").Select
   Selection.PasteSpecial Paste:=xlPasteValues, Operation:=xlNone, SkipBlanks _
      :=False, Transpose:=False
   Sheets("Sheet1").Select
   Range("H1").Select
   ActiveCell.FormulaR1C1 = n
   Range("H5").Select
   Selection.Copy
   Sheets("Sheet3").Select
   Cells(1 + n, 1 + C).Select
   Selection.PasteSpecial Paste:=xlPasteValues, Operation:=xlNone, SkipBlanks _
```

```
:=False, Transpose:=False
        Sheets("Sheet1").Select
        Range("H9:H10").Select
Selection.Copy
Sheets("PHandPV").Select
Cells(2 + n, 2 * C).Select
Selection.PasteSpecial Paste:=xlPasteValues, Operation:=xlNone, SkipBlanks _
  :=False, Transpose:=True
        Next n
        Next C
        End Sub
```

Appendix 3

Peak Indexing

Peak indexing can be used to obtain the unit cell parameters from XRD patterns. This is done using the formula relating the d spacings to the miller indices and unit cell parameters (Equation 1 shows this equation for an orthorhombic material such as $LiFePO_4$) combined with the Bragg equation (Equation 2). These equations can be solved by relating the XRD peaks to the appropriate set of miller indices (shown for $LiFePO_4$ in Figure 2). The unit cell volume of a orthorhombic material can then be simply calculated using Equation 1.

$$\frac{1}{d^2} = \frac{h^2}{a^2} + \frac{k^2}{b^2} + \frac{l^2}{c^2}$$

Equation 1

h,k,l = miller indices

a,b,c = unit cell parameters

d = the perpendicular distance between adjacent planes

$$2d_{hkl}.\sin\theta = n\lambda$$

Equation 2

λ = wavelength

n = positive integer (usually 1)

d_{hkl} = lattice spacing

θ = X-ray beam angle of incidence

$$V = abc$$

Equation 3

V = unit cell volume

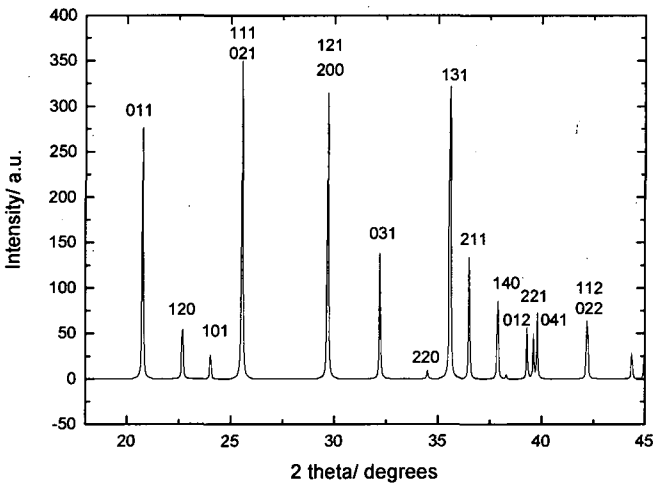

Figure 2 Simulated XRD pattern of $LiFePO_4$ showing miller indices.